Superconducting Properties and Nanostructure of $YBa_2Cu_3O_{7-\delta}$ Coated Conductors Prepared by Chemical Solution Deposition

Dissertation
der Mathematisch-Naturwissenschaftlichen Fakultät
der Eberhard Karls Universität Tübingen
zur Erlangung des Grades eines
Doktors der Naturwissenschaften
(Dr. rer. nat.)

Vorgelegt von
Leopoldo Molina-Luna
(Master of Science in Physics)
aus Valera, Venezuela

Tübingen
2010

Tag der mündlichen Qualifikation: 22.12.2010

Dekan: Prof. Dr. Wolfgang Rosenstiel

1. Berichterstatter: Prof. Dr. Oliver Eibl

2. Berichterstatter: Prof. Dr. Erich Plies

Out of the cradle onto dry land...
here it is standing...
atoms with consciousness...
matter with curiosity.
Stands at the sea...
wonders at wondering... I...
a universe of atoms...
an atom in the universe.

Richard P. Feynman

Summary

Wire fabrication is the enabling technology for superconducting devices in the magnet and energy technology. Up to now no adequate superconducting material for operation at 77 K and magnetic fields larger than 1 T is available. Therefore, there is a fast-growing worldwide interest in the second generation (2G) of high-temperature superconductor (HTS) wires for applications such as fault current limiters and motors. These materials are also known as $YBa_2Cu_3O_{7-\delta}$(YBCO)-coated conductors and are prepared by thin film technologies.

A chemical solution deposition (CSD) prepared YBCO-coated conductor consists of a biaxially textured nickel tungsten substrate (Rolling-Assisted-Biaxially-Textured Substrates - RABiTS) which is dip-coated in a precursor solution, in this way buffer layers and a superconducting YBCO film are deposited on top of the substrate. The biaxial texture is transferred from the substrate up to the superconducting layer forming a small-angle grain boundary network in the YBCO film, which is necessary for obtaining high-critical current densities.

Among the various deposition methods, chemical solution deposition has specific advantages with respect to Physical Vapor Deposition (PVD) and Chemical Vapor Deposition (CVD) such as flexibility in composition and easy up-scaling, allowing the coating of long-length substrates and since it is a non-vacuum method, less expensive equipment is required. Due to these advantages there is a considerable interest in the development of all-solution based processes.

The critical current density is the important figure of merit for determining a high temperature superconducting materials performance. Recently, it has been found that YBCO coated conductors can reach critical currents densities of up to 10 MA/cm^2 at 1 T magnetic field and 77 K by introducing $BaZrO_3$ (BZO) nanocomposites into a YBCO matrix. BZO nanoinclusions incorporate randomly into the matrix and act as pinning centers in the system. For a coated conductor that is 1 cm wide and about 1 µm thick a current density of 1 MA/cm^2 corresponds to a current of 100 A.

Due to the short coherence length of YBCO ($<$10 nm), nano-scaled non-superconducting defects act as efficient pinning centers for magnetic vortices and by the controlled introduction of these the critical current densities of the films can be enhanced. Non-superconducting defects include: twin boundaries, dislocations, interfaces and nano-scaled secondary phases. The micro- and nano-structure strongly influences the critical current density (j_c) and it's anisotropy.

The samples investigated in this work were prepared and characterized for their superconducting properties (T_c, B_{c2} and j_c(B,T)) by partner institutions within the framework of two research projects: (i) the Virtual Institute of the Helmholtz Gemeinschaft "Chemically deposited YBCO superconductors" and (ii) the ELSA project (Entwicklung innovativer Supraleiter mit Schichtarchitektur für die Energie technik).

This dissertation can be subdivided as follows: (i) development of the methodology for quantitative electron microscopy and spectroscopy of YBCO coated conductors assessed by a Zeiss 912 Omega energy-filtered transmission electron microscope (TEM) operating at 120 kV and a Jeol 6500-F scanning electron microscope (SEM); both provided with an Oxford X-ray detector, (ii) electron microscopy characterization of $La_2Zr_2O_7$ (LZO) buffer layers for YBCO coated conductors and (iii) electron microscopy and spectroscopy of complete YBCO coated conductor samples with and without BZO artificial nano-inclusions.

Quantitative electron microscopy and spectroscopy of YBCO coated conductors is challenging due to the multi-layer architecture of the samples, the complex micro- and nanostructure and the difficult TEM specimen preparation. The first step was to study the biaxial texturing and grain growth mechanism

of $La_2Zr_2O_7$ (LZO) thin films since they act as diffusion barriers and transfer the biaxial texture from the nickel tungsten substrate up to the YBCO superconducting layer. The LZO Buffer layer thickness of the samples investigated ranged from 100-200 nm. LZO buffer layers were highly biaxially textured, but non-epitaxial and as a consequence the grain size in the LZO buffer layer (100-200 nm) was much smaller than the grain size found in the nickel tungsten substrate (40 µm). LZO grains 100-200 nm in size and preferentially oriented nanovoids of 10-20 nm in size were found to be distinct features in LZO thin films deposited by chemical solution deposition. In the samples studied, it was shown that the nickel tungsten alloy substrate / LZO interface had a roughness with a wavelength of 60 nm and amplitude of 10 nm.

LZO thin films deposited on nickel tungsten alloy substrates were annealed at temperatures ranging from T = 600-1000°C to study the influence of the annealing temperature on the nanostructure. These LZO thin films were investigated by X-ray diffraction (XRD) and transmission electron microscopy (TEM). A nano-crystalline phase at T = 600°C was found. LZO grain formation starts at 800°C, with grains of 100 nm in size and a polycrystalline phase is reached at T $>$ 1000°C, with grains of 200 nm in size. The texture of the films was analysed by XRD, however, the local texture is more pronounced than over the mm size areas measured by XRD. LZO grain size is limited by the film thickness and the LZO grain boundaries are strongly facetted at T=800°C. Grain facetting decreases with increasing annealing temperature.

Nanovoid formation was found to be a typical feature of LZO thin films that are obtained by organic prescursors and with a reducing forming gas (Ar-5%H_2) and is directly linked to the carbon content in the film. A quantitative TEM-EDX analysis was done on LZO thin films annealed at 600°C, 800°C and 1000°C. Thickness dependent measurements showed that the C content in the films is found as volume and surface impurities. At 600°C the volume fraction dominates, at 1000°C the surface fraction. Nanovoids have preferential {111} crystallographic planes due to the anisotropic surface energy of LZO. This is why nanovoids have an octahedral form in this crystal structure. Even though LZO buffer layers contain nanovoids, they act as effective diffusion barriers.

EDX-spectrocopy in a scanning electron microscope (Jeol 6500-F SEM provided with an Oxford X-ray detector) was performed to determine the LZO film thickness with a lateral resolution of 1 µm. This method is, especially for thin films that are prepared by dip-coating, of great importance because the film thickness of such films is difficult to control. The thereby established method is a fast and reliable alternative to ellipsometry and cross-sectional transmission electron microscopy imaging. The great advantage is that film thicknesses can be determined on different length-scales from 1 µm to $>$ 100 µm. The $La - L\alpha$ and $Zr - L\alpha$ X-ray lines were evaluated quantitatively and as an outcome, obtained calibration curves were used for LZO film thickness determination.

In this dissertation, energy-filtered transmission electron microscopy (EFTEM) was applied extensively for the study of YBCO-coated conductors. EFTEM is a method with a high-spatial resolution that uses inelastically scattered electrons to acquire chemical information from images and spectra. Studies done previously on YBCO coated conductors with the intention of acquiring chemical information with a high-spatial resolution, were mainly obtained by scanning methods (Scanning transmission electron microscopy -STEM) and EDX-spectroscopy. EFTEM has essential advantages over STEM-EDX: (i) EFTEM uses inelastically scattered electrons as the relevant signal, whereas EDX uses characteristic X-ray emissions; (ii) EFTEM is an imaging technique, whereas STEM-EDX is a scanning technique. (iii) EFTEM elemental maps can be acquired in a few seconds, whereas EDX elemental maps require several 10 minutes for yielding a similar quality with respect to noise; the signal to background ratios are more favorable in STEM-EDX. Both methods are key for coated conductors analytics. This thesis contributes substantially to the development of EFTEM methods applied to YBCO coated conductors. Acquisition conditions for EFTEM elemental mapping were established and a chemical phase mapping method was shown. Element distribution images were evaluated quantitatively. Ionization edges that lay at low energies were preferentially used due to the favorable high-signal intensities. Using the three window method for elemental mapping (core-loss ionization edges) Ba N4,5 (99 eV), Y M4,5 (160 eV), La N4,5 (117 eV), Ce N4,5 (102 eV) were chosen and used for elemental mapping by Electron Spectroscopic Imaging (ESI). The goal was to quantify the elemental maps by determining the intensity per pixel in the single elemental maps and relating this to the mole fraction ratios. Therefore, electron energy-loss spectra (EELS) of Ba N4,5 (99 eV), O-K (532 eV) and Zr N4,5 (29 eV) ionization edges were acquired and studied in detail. Differential scattering cross-sections for inelastically scattered electrons with energy-losses near the adjusted ionization edge were calculated using parameterized oscillator strengths. These calculations are based on relativistic Bethe theory and tabulated oscillator strengths values were used. In this way, total and partial differential scattering cross-sections were calculated and correlated with experimental results from electron energy-loss spectrocopy (EELS) and energy-filtering transmission electron microscopy (EFTEM). EFTEM images were quantified with respect to the mole fraction ratio.

The YBCO coated conductor samples, that were investigated in this thesis, had film thicknesses of 200 - 440 nm and critical current densities (j_c) ranging from 0.5 to 1 MA/cm^2 and critical currents (I_c) of 12 to 50 A/cm at 77 K and self-field. The samples studied were prepared with and without BZO nano-inclusions. Electron diffraction showed that in the case of those with, the nano-inclusions incorporate randomly into the YBCO matrix.

In dip-coated prepared YBCO thin films, pinning relevant intrinsic Y_2O_3 precipitates 20-50 nm in size appear and these were imaged by EFTEM phase mapping. From the different phases present in the thin films, electron energy-loss spectra at low ionization energies were obtained. These allow a spectral discrimination of the different phases as chemical finger prints. With these spectra we could establish a imaging method for EFTEM, that allows the chemical phase mapping of pinning relevant Y_2O_3 precipitates and from 200-500 nm in size CuO grains that appear in the YBCO matrix. Especially jump ratio images using the Zr N2,3 (29 eV) and Ba N4,5 (99 eV) ionization edges could be obtained that allow the imaging of $BaZrO_3$ nanocomposites.

Critical current measurements were performed at 77 K by partners on all samples investigated by TEM. T_c was determined by an inductive method (hereby the sample is placed between a primary coil and a secondary coil. Connected to the primary coil is a frequency generator that generates an oscillating current with a frequency of 1 kHz and an amplitude of 500 mV. The current induced in the second coil is then measured in dependence of the temperature). The critical current density (j_c) was determined by transport (resistive) measurements (four-point configuration using a 1µV/cm criterion). The data were correlated to the micro- and nanostructure by TEM investigations and yielded a structure-property correlation. This structure-property correlation is particularly interesting, because only in this way it is possible to identify the limiting mechanisms of the critical current density (j_c). YBCO thin films deposited on single crystalline substrates and accordingly short-length nickel tungsten alloy substrates gave the best results with respect to j_c.

From the samples investigated we found that: (i) YBCO films with BZO nano-inclusions grown on LAO substrates yield better superconducting properties ($j_c > 1$ MA/cm^2) than the same films deposited on RABiTS ($j_c > 0.5$ MA/cm^2) with I_c´s ranging from 20-50 A/cm. (ii) YBCO films without BZO nanoinclusions deposited on RABiTS (short-length, 10 x 10 mm) yield similar results as the same on LAO substrates ($j_c > 1$ MA/cm^2) with 280 nm and 440 nm film thickness). (iii) Values reported in

the literature of 10 MA/cm^2 with 200 nm film thickness and T=77 K have not been yet reproduced on long-lengths. The low values of j_c and I_c of the samples studied in this work compared to those from the literature are due to the not optimized long-length dip-coating technology, sample quality and the large degree of freedom in the chemical composition of the samples. The electron microscopy techniques presented in this thesis elucidate the current limiting causes in the microstructure and will be used in the future for a systematic study of nano-engineered YBCO-coated conductors since further improvement is still needed for a reliable long-length chemical solution deposition YBCO-coated conductor technology.

Zussamenfassung

Die Drahtherstellung ist die Schlüsseltechnologie um Anwendungen der Supraleitung in der Magnet- und Energietechnik umzusetzen. Bis jetzt ist kein supraleitendes Material verfügbar, das einen Einsatz bei 77 K und Magnetfeldern größer 1T ermöglicht. Deshalb wird weltweit intensiv an Leitern der zweiten Generation geforscht, die unterschiedliche Anwendungen bei 77 K und höheren Magnetfeldern ermöglichen werden. Diese Materialien werden als $YBa_2Cu_3O_{7-\delta}$(YBCO) coated conductors bezeichnet und mittels Dünnfilmtechnologie hergestellt.

Ein über Tauchbeschichtungsverfahren hergestellter YBCO coated conductor wird auf ein biaxial texturierte Ni Substrat abgeschieden. Dazu wird unmittelbar auf das Susbstrat zunächst eine Pufferschicht abgeschieden, auf diese Pufferschicht dann die supraleitende YBCO Schicht. Mittels der Pufferschicht wird die biaxiale Textur vom Substrat in die supraleitende Schicht übertragen. Damit ist sichergestellt, dass in der Supraleiterschicht ein Netzwerk von Kleinwinkelkorngrenzen, aber keine Großwinkelkorngrenzen erzeugt werden. Großwinkelkorngrenzen begrenzen die kritische Stromdichte in YBCO dramatisch und dürfen in für Anwendungen relevanten Leitern nicht auftreten, Kleinwinkelkorngrenzen können toleriert werden.

Unter den verschiedenen Beschichtungsverfahren für coated conductors bietet das Verfahren der Tauchbeschichtung besondere Vorteile gegenüber Vakuumverfahren wie physikalischen und chemischen Beschichtungsverfahren: Freiheitsgrade bei der Einstellung der chemischen Zusammensetzung, einfachere Hochskalierung zur Herstellung von Drähten langer Länge, aber auch Reduktion der Leiterkosten. Deshalb besteht ein großes Interesse, das Tauchbeschichtungsverfahren für die Herstellung der coated conductor einzusetzen.

Die kritische Stromdichte ist die relevanteste Zielgröße, um supraleitende Eigenschaften von Materialien für Anwendungen zu klassifizieren. Für YBCO coated conductors konnten vor kurzem kritische Stromdichten von 10 MA/cm^2 bei 1 T und 77 K erreicht werden, wenn $BaZrO_3$ (BZO) Nanoausscheidungen in die YBCO Matrix eingebracht wurden. BZO Nanoausscheidungen können sich statistisch verteilt in der YBCO Matrix ausbilden und wirken als Flusslinien-Verankerungszentren. Mit einer Breite von 1 cm und einer Schichtdicke von 1 µm entspricht einer kritischen Stromdichte von 1 MA/cm^2 ein kritischer Strom von 100 A.

Nicht-supraleitende Kristallbaufehler wirken als Verankerungszentren für magnetische Flusslinien und führen damit zu einer Erhöhung der kritischen Stromdichte. In YBCO sind diese Kristallbaufehler Zwillingsgrenzen, Versetzungen und nanoskalige Ausscheidungen. Maßgeschneiderte Mikro- und Nanostruktur von YBCO coated conductor enthalten ausschließlich Kleinwinkelkorngrenzen und nanoskalige Kristallbaufehler, die zur Flußlinien-Verankerung beitragen.

Proben, die in dieser Arbeit untersucht wurden, wurden im Rahmen von folgenden zwei Forschungsprojekten von Partnerinstitutionen hergestellt und bezüglich der supraleitenden Eigenschaften (T_c, B_{c2} and j_c (B,T)) vermessen: (i) einem virtuellen Institut der Helmholtz Gemeinschaft “Chemically deposited YBCO superconductors” und (ii) einem Projekt namens ELSA (Entwicklung innovativer Supraleiter mit Schichtarchitektur für die Energietechnik).

Diese Doktorarbeit wird wie folgt unterteilt: (i) methodische Arbeiten für die quantitative Elektronenmikroskopie und Spektroskopie für YBCO coated conductors, (ii) Untersuchungen zu $La_2Zr_2O_7$ (LZO) Pufferschichten für YBCO coated conductors und (iii) Elektronenmikroskopie und Spektrokopie von vollständig prozessierten YBCO coated conductor proben, die mit und ohne BZO Nanoausscheidungen hergestellt wurden.

Quantitative Elektronenmikrokopie und Spektroskopie von YBCO coated conductors ist anspruchsvoll

wegen des Schichtaufbaus der Proben, der komplizierten Mikro- und Nanostruktur und der schwierigen TEM-Probenpräparation. Ein wichtiger Schritt war die Untersuchung der biaxialen Texturbildung und des Kornwachstums von $La_2Zr_2O_7$ (LZO) Pufferschichten. Sie wirken als Diffusionsbarrieren und übertragen die biaxiale Textur des Ni-Substrats auf die supraleitende YBCO Schicht. Die Schichtdicken dieser Pufferschichten lagen zwischen 100-200 nm. LZO Pufferschichten wachsen biaxial texturiert, jedoch nicht epitaktisch auf den Ni-Substraten. Die Korngröße in den LZO Pufferschichten ist mit 100-200 nm wesentlich kleiner als die Korngröße der Ni Substrate, die ca. 40 µm betrug. LZO Korngrößen von 100-200 nm und Nanoporen mit Durchmessern von 10-20 nm, die durch planare Grenzflächen berandet werden, sind charakteristische Merkmale dieser Pufferschichten; sie treten immer auf, unabhängig von den detaillierten Bedingungen der Tauchbeschichtung. Die Rauhigkeit der Ni/LZO Grenzfläche wurde mit 10 nm Amplitude und 60 nm Wellenlänge bestimmt.

LZO Dünnfilme wurden auf Ni-Substrate abgeschieden und bei unterschiedlichen Temperaturen zwischen 600 und 1000°C getempert, um den Einfluß der Temperatur auf die Nanostruktur zu untersuchen. Die LZO Dünnfilme wurden mittels Röntgentexturanalyse und darüber hinaus auch mit TEM untersucht. Bei 600°C wird eine röntgenamorphe nanokristalline Struktur gefunden, Korngröße < 5 nm. LZO Kornwachstum beginnt bei Temperaturen von 800°C, die Körner erreichen Durchmesser von ca. 100 nm. Bei Tempertemperaturen von 1000°C wurden Korngrößen von 200 nm bestimmt. Die Textur der Filme wurde über die Röntgentexturanalyse bestimmt, jedoch ist die lokale Textur wesentlich weniger ausgeprägt als die über mm-große Bereiche gemessene Röntgen-Textur. Die LZO-Korngröße ist durch die Filmdicke begrenzt und die Korngrenzen sind bei 800°C Temperung stark facettiert. Die Facettierung der Korngrenzen nimmt mit zunehmender Tempertemperatur ab.

Die Bildung von Nanoporen findet in LZO Dünnfilmen statt, die über organische Precursoren hergestellt werden, und steht direkt mit dem Kohlenstoffanteil der Schicht in Verbindung. Quantitative TEM-EDX-Untersuchungen wurden an den LZO-Dünnfilmen durchgeführt, die bei 600°C, 800°C und 1000°C getempert wurden. Mittels dickenabhängiger Messungen konnte nachgewiesen werden, dass C als Volumen- und Oberflächenverunreinigung vorliegt; bei 600°C dominiert der Volumenanteil, bei 1000°C der Oberflächenanteil. Nanoporen werden durch planare Grenzflächen, die auf $\{111\}$ kristallographischen Ebenen begrenzt, dies ergibt sich aufgrund der deutlichen Anisotropie in der Oberflächenenergie. Deshalb haben Nanoporen in dieser Kristallstruktur oktaedrische Form. Obwohl LZO Pufferschichten Nanoporen enthalten, wirken sie dennoch als effektive Diffusionsbarrieren.

EDX-Spektroskopie im REM wurde angewandt, um die Filmdicke von LZO Dünnfilmen mit einer lateralen Auflösung von 1 µm zu bestimmen. Dies ist besonders für Dünnfilme, die mittels Tauchbeschichtung hergestellt werden, von großer Bedeutung, da mit diesem Beschichtungsverfahren die Schichtdicke nicht einfach zu kontrollieren ist. Die dabei etablierte Methode ist eine schnelle und zuverlässige Alternative zur Ellipsometrie und zu TEM-Querchnittsabbildung. Der große Vorteil besteht darin, dass Filmdicken auf unterschiedlichen lateralen Längenskalen von 1 µm bis $>$ 100 µm bestimmt werden können. Die $La - L\alpha$ and $Zr - L\alpha$ Röntgenlinien werden zur Dickenbestimmung quantitativ ausgewertet und daraus über Kalibrierkurven Filmdicken bestimmt.

In dieser Arbeit wurde energiegefilterte Transmissionselektronenmikroskopie (EFTEM) intensiv für die Untersuchung von YBCO coated conductors eingesetzt. Die EFTEM ist ein Verfahren, um mit hoher Ortsauflösung mittels inelastisch gestreuter Elektronen chemische Information in Bildern und Spektren zu akquirieren. Untersuchungen ergebnisse zu YBCO coated conductors, die chemische Information mit hoher Ortsauflösung zum Ziel haben, werden nahezu ausschließlich mittels Rastermethoden (STEM) und EDX-Spektroskopie erhalten. EFTEM hat gegenüber STEM-EDX wesentliche Vorteile: (i) EFTEM verwendet inelastisch gestreute Elektronen als Meßsignal, STEM-EDX verwendet hingegen charakteristische Röntgenstrahlung; (ii) EFTEM ist eine abbildende Methode, STEM-EDX eine Rastermethode (iii) EFTEM Elementverteilungsbilder können in wenigen Sekunden akquiriert werden, hingegen benötigen EDX Elementverteilungsbilder Akquisitionszeiten von mehr als 10 Minuten, um vergleichbare Signal-zu-Rausch Verhältnisse zu erreichen; Die Signal-zu-Untergrund Verhältnisse sind für STEM-EDX günstiger. Beide Methoden sind Schlüsselmethoden für die Untersuchung von coated conductors. Diese Arbeit liefert einen wesentlichen Beitrag, um die Möglichkeiten des EFTEM für die coated conductor Analytik aufzuzeigen. Akquisitionsbedingungen für Elementverteilungsbilder wurden etabliert und eine Phasenabbildungsmethode vorgestellt. Auch wurden die Elementverteilungsbilder quantitativ ausgewertet. Es kamen vorzugsweise Ionisationskanten bei niedrigen Ionisationsenergien zum Zuge, weil dort sehr günstige, d.h. hohe Signalintensitäten vorliegen. Für die Dreifenster-Methode wurden die Ba N4,5 (99 eV), die Y M4,5 (160 eV), die La N4,5 (117 eV) und die Ce N4,5 (102 eV) Ionsiationskanten ausgewählt und damit Elementverteilungsbilder erhalten. Das Ziel war, diese Elementverteilungsbilder zu quantifizieren und die Intensitäten bezüglich Atomzahlanteile auszuwerten. Dazu wurden Elektronen-Energieverlust-Spektren der Ba N4,5 (99 eV), der O-K (532 eV) und der Zr N4,5 (29 eV) Ionisationskanten aufgenommen und detailliert untersucht. Differentielle Wirkungsquerschnitte für inelastisch gestreute Elektronen mit Energieverlusten nahe der eingestellten Ionisationskanten wurden mittels parametrisierter Oszillatorstärken berechnet. Diese Rechnungen basieren auf der Bethe Theorie, tabellierte Werte für die Oszillatorstärken wurden dazu verwendet. Damit konnten sowohl totale, als auch einfach differentielle Wirkungsquerschnitte berechnet und mit den experimentellen Ergebnissen der Elektronen-Energieverlust-Spektroskopie und der EFTEM korreliert werden. EFTEM Elementverteilungsbilder können dann bzgl. der Atomzahlanteile quantifiziert werden.

Die YBCO coated conductor Proben, die in dieser Arbeit untersucht wurden, hatten Filmdicken von 200 – 440 nm, wiesen kritische Stromdichten von 0.5 to 1 MA/cm^2 und kritische Ströme von 12 bis 50 A/cm bei 77 K und Eigenfeld auf. Es wurden auch Proben mit BZO Nanoausscheidungen untersucht. Elektronenbeugung zeigte, dass diese BZO Nanoausscheidungen ohne Vorzugsorientierung in die YBCO Matrix eingebaut wurden.

In den mittels Tauchbeschichtung hergestellten Dünnfilmen treten Y_2O_3 Ausscheidungen mit Größen von 20-50 nm auf und wurden mittels EFTEM Phasenabbildung abgebildet. Von den in den Dünnfilmen auftretenden Phasen wurden Elektronen-Energieverlust-Spektren bei niedrigen Energieverlusten aufgenommen, sie erlauben die spektrale Unterscheidung der verschiedenen Phasen ähnlich einem Fingerabdruck. Mit diesen Spektren wurden Abbildungsmethoden für EFTEM erarbeitet, die die Phasenabbildung von Y_2O_3 Ausscheidungen zeigen, die relevant für das Flußlinien-Pinning sein können, und von CuO Körnern, die in einer größe vom 200-500 nm innerhalb der YBCO Matrix auftreten. Insbesondere konnten Quotientenbilder an der Zr N2,3 (29 eV) and Ba N4,5 (99 eV) Ionisationskante erhalten werden, die die BZO Ausscheidungen abbilden.

Messungen der kritischen Stromdichte (j_c) und T_c bei 77 K wurden an allen Proben durchgeführt, die mittels TEM untersucht wurden. Diese Messungen wurden entweder mittels einer induktiven Methode (hierbei befindet sich die Probe zwischen einer Primärspule und einer Sekundärspule. Die Primärspule ist an einen Frequenzgenerator angeschlossen, der eine Wechselspannung mit einer Frequenz von 1 kHz und einer Amplitude vom 500 mV erzeugt. Es wird dann die in der Sekundärspule induzierte Spannung in Abhängigkeit von der Temperatur gemessen) oder über eine Transportstrommessung durchgeführt (Vierpunktmessung mit einem 1µV/cm Kriterium). Die Werte wurden mit der Mikro- und Nanostruktur aus TEM-Messungen korreliert und ergaben dann eine Struktur-Eigenschaftskorrelation. Diese Struktur-Eigenschaftskorrelation ist besonders interessant, weil nur so die Begrenzungsmechanismen der kritischen Stromdichte identifiziert werden können. Dünnfilme abgeschieden auf Einkristallen bzw. auf kurzen Ni-

Substraten ergaben die besten Ergebnisse in Bezug auf j_c.

Aus den Untersuchungen lassen sich folgende Schlußfolgerungen ableiten: (i) YBCO Filme mit BZO Ausscheidungen, die auf LAO abgeschieden wurden, ergaben höhere kritische Stromdichten $j_c > 1$ MA/cm^2 als Dünnfilme, die auf RABiTS Ni-Substraten abgeschieden wurden ($j_c > 0.5$ MA/cm^2). Die kritischen Ströme lagen dabei bei 20-50 A/cm. (ii) YBCO Dünnfilme ohne BZO Nanoausscheidungen, die auf RABiTS Ni-Substraten (Kurzproben, 10 x 10 mm) abgeschieden wurden, ergeben ähnliche Werte wie solche auf LAO Substraten abgeschiedene ($j_c > 1$ MA/cm^2 mit Filmdicken zwischen 280 nm und 440 nm). (iii) Stromdichten von 10 $MA/BaZrO_3cm^2$ bei 77 K mit 200 nm Filmdicken, wie sie aus der Literatur bekannt sind, konnten nicht reproduziert werden. Die niedrigen Werte für j_c and I_c der Dünnfilme, die in dieser Arbeit untersucht wurden, ergeben sich aufgrund der noch nicht optimierten Technologie, wie sie für lange Längen bei der Tauchbeschichtung eingesetzt wird. Die elektronenmikroskopischen und spektroskopischen Methoden, die in dieser Arbeit zur Anwendung kommen, zeigen die strombegrenzenden Ursachen der Nanostruktur und werden in Zukunft angewendet werden, um auf der Nanoskala maßgeschneiderte YBCO coated conductor systematisch zu untersuchen.

Chapter preview

Chapter 1 is an introduction to the materials science of high-temperature superconductors. The structural and physical properties of the YBCO high temperature superconductor will be treated and a brief review on YBCO-coated conductor technology will be given. Critical current density, current limiting mechanisms and the mechanism of pinning by non-superconducting phases in a YBCO superconducting matrix will be discussed.

Chapter 2 deals with electron microscopy and -spectroscopy of HTS materials. The main challenges for YBCO-coated conductor characterization by electron microscopy will be presented. A review of the theory of electron scattering in solids will be given for both elastic and inelastic scattering. The definition the differential scattering cross-section for inelastic scattering will be discussed in detail and the method for calculating scattering cross-sections of elements relevant for a chemical quantification of YBCO coated conductors is discussed. The experimental implementation of the electron microscopy techniques used in this work for the characterization of YBCO-coated conductors is presented.

Chapter 3 presents results on the the film growth and microstructure of chemically deposited $La_2Zr_2O_7$ (LZO) buffer layers for YBCO-coated conductors investigated by scanning electron microscopy (SEM), X-ray diffraction (XRD) and diffraction contrast imaging by conventional transmission electron microscopy (TEM). LZO grain size and nanovoid size were determined.

Chapter 4 discusses the effect of the annealing temperature on the microsctructure of LZO buffer layers for YBCO coated conductors. The mechanism of biaxial texturing and nanovoid formation is discussed. Imaging of in-plane and out- of plane rotations of LZO grains by Moiré contrast is shown. Precise measurements of C-K by quantitative EDX in the transmission electron microscope performed on a temperature series of LZO buffer layers annealed at temperatures ranging from 600-1000°C are shown.

Chapter 5 presents results on LZO film thickness estimation by EDX in a scanning electron microscope (SEM). A precise and quick film thickness estimation method is crucial for the development and monitoring of coated conductor technology in an industrial environment, since film homogeneity over large samples areas ($>$ meters) is important for the deposition of the superconducting layer. EDX spectroscopy is a fast and reliable alternative to ellipsometry and cross-sectional transmission electron microscopy (TEM), which is very time consuming, for the measurement of film thicknesses and homogeneity of LZO buffer layers. Calibration curves were obtained and an empirical film thickness estimation technique was established.

Chapter 6 is a nano-scaled chemical analysis of chemical solution deposition (CSD) prepared YBCO coated conductors by energy-filtering transmission electron microscopy (EFTEM). The application of electron energy-loss spectroscopy (EELS) and the use of the low-loss and core-loss regions of the spectra is discussed and results are presented. The low-loss region was used for a chemical phase mapping technique for the imaging of pinning relevant Y_2O_3 precipitates and other phases. Differential scattering cross-sections for elements relevant to YBCO coated conductors were calculated and implemented. The three window technique was used for elemental mapping using core-loss ionization edges. Results are given and theoretical results are compared with the experiments. The intensity per pixel in the elemental maps was calculated and used for the estimation of mole fraction ratios in the elemental maps.

Chapter 7 deals with EFTEM and EDX-spectroscopy of pinning relevant (10-20 nm in size) extrinsic $BaZrO_3$ nanocomposites in a TFA-YBCO matrix. The determination of the nanodot density, the use of low-loss EELS for chemical phase mapping, elemental mapping by means of the three window method using relevant core-loss ionization edges, EDX spectroscopy of single $BaZrO_3$ nano-dots and STEM-EDX mapping results are presented.

Chapter 8 gives a final assessment on the structure-property correlation of the YBCO coated conductor samples investigated in this thesis.

Contents

Chapter 1

Materials science of high-temperature superconductors

1.1 Introduction

Ever since the discovery of cuprate high-temperature superconductors in 1986 by Georg Bednorz and Alexander Müller [1], not only an effort is being made in understanding the basic physical mechanisms that govern the phenomenon, but also intensive research activities in universities and institutions worldwide has been devoted to the study and development of such materials for technological and industrial purposes.

This has proven to be an arduous and challenging task, but as well as the race for even higher transition temperatures in high-Tc superconducting materials during the end of the 1980´s was an exciting time for physics worldwide, nowadays the search and development of potential high-Tc materials for industrial applications has also become an exciting and expanding interdisciplinary field of its own. Superconducting materials considered in energy and magnet technology are hard type-II superconductors, i.e. materials that show a strong hysterectic behavior in magnetization above B_{c1}.

The physical properties of these superconducting materials are governed extensively by their micro and nanostructure and the effect of various extended crystal defects on their physical properties, particularly transport properties, is complex. It requires a throughout understanding of the nature of the extended defects, their length scales and the effect they exhibit on electrons and phonons. In the case of advanced functional materials for devices technology, the precise control of phase formation, grain size and density of nano-scaled extended defects plays a crucial role in improving the physical properties, as in the case for nano-engineered superconductors for power applications.

Materials based on high-temperature superconductors are currently developed for applications in high-power devices such as transformers, power transmision cables, motors, magnetic applications and generators. These have to meet several requirements in order to be competitive with normal conductors or low temperature superconductors. The main considerations taken into account consider if the materials present high enough critical currents, are simple to fabricate and have low DC and AC losses [2].

Figure 1.1 is a plot of the applied magnetic field in function of the critical current density needed for current applications like AC and DC power transmission lines, squids, magnetic storage devices, motors and generators [3]. Also shown are materials based on BSCCO and YBCO thin films. As seen in the

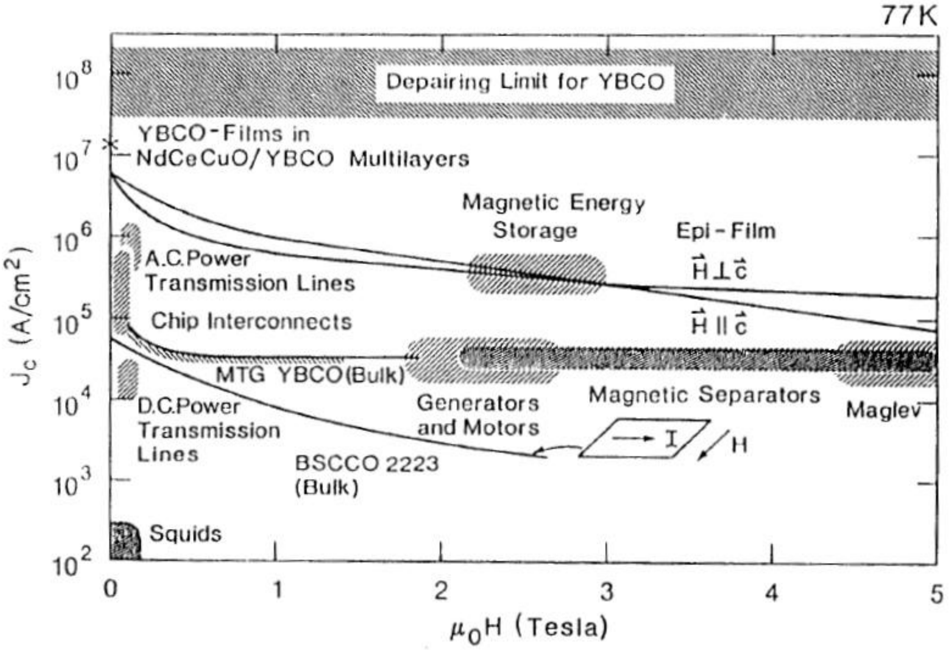

Figure 1.1: Schematic diagram showing the applied magnetic field in function of the critical current density (j_c) for several high temperature superconducting materials and their potential applications [3].

figure, YBCO thin films can reach high critical current densities of over $10^6 A/cm^2$.

A material of choice for fabricating nano-engineered superconductors is $YBa_2Cu_3O_{7-\delta}$ (YBCO). This cuprate high temperature superconductor exhibits properties that makes it an outstanding material for practical superconducting applications, since it presents a critical temperature above 77 K, has a high upper critical field and has the potential for high critical currents if suitable pinning centers are present [4]. Efforts have been made in recent years to develop YBCO coated conductors, also known as second generation superconducting materials for electric power systems [5].

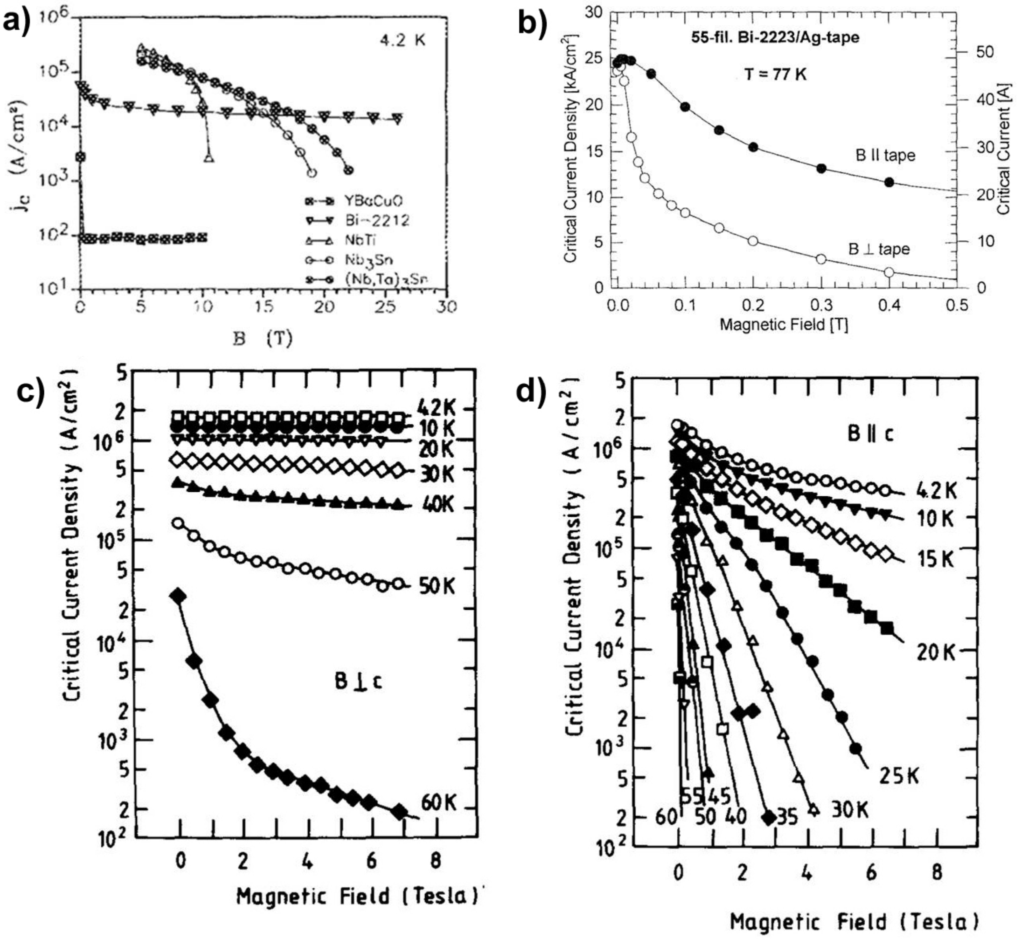

Figure 1.2: (a) Critical current density (j_c) in dependence of applied magnetic field $B(T)$ of up to 30 T at 4.2 K for various HTS materials [6]. (b) Critical current density (j_c) and critical current (A) for a 55 filament Bi-2223/Ag-tape at 77 K [7]. (c) Magnetic field dependence of the critical current density for the B perpendicular to c direction at different temperatures [8]. (d) Magnetic field dependence of the critical current density for the B parallel to c direction at different temperatures [8].

Figure 1.2 (a) shows the critical current density (j_c) in dependence of the applied magnetic field $B(T)$ of various HTS materials at 4.2 K as it was in 1990. Nb_3Sn and $NbTi$ are metallic superconductors which were used to make wires by the powder in the tube or the multifilament method [9], however due limitations beacuse of cooling (at 4.2 K) they were not suitable for comercial applications. The critical current density is limited in these materials by a flux-flow mechanism. As can be seen, the critical current density of YBCO ceramics was only $100\,A/cm^2$ and was limited by weak-links [6]. Another material showed a high critical current density and stable behavoiur over large applied magnetic-fields; Bi-2223/Ag-tapes, but were limited by thermally activated flux-flow which is magnetic-field orientation dependent as can seen in figures 1.2 (b-d), where the critical current decreases from $10^6 A/cm^2$(42 K) to $100 A/cm^2$(60 K), this is due to thermallly activated flux flow [8].

1.2 Superconducting properties of type II superconductors

Figure 1.3 shows the magnetization in function of the applied magnetic field for type II superconductors. According to London [10], the applied magnetic field penetrates the superconductor over a mean distance λ_L, known as the London penetration depth. In 1950, Ginzburg and Landau introduced a theory describing the superconducting electrons involved defining a complex wavefunction $\psi(\vec{r})$, where $n_s = \left|\psi(\vec{r})\right|^2$ is the density of the superconducting electrons. The Ginzburg-Landau theory yields two characteristic lengths, the Ginzburg-Landau penetration depth λ_{GL} and the Ginzburg-Landau coherence length ξ_{GL}. The penetration depth, is the characteristic length for the decay of the magnetic field in a superconductor and the coherence length is the length scale over which the order parameter varies. Pinning defects found in HTS materials have this length scale. Abrikosov [11] found that solutions of the Ginzburg-Landau equations fall into two different categories according to the ratio $\kappa = \frac{\lambda_{GL}}{\xi_{GL}}$. In the case for $\kappa < \frac{1}{\sqrt{2}}$, the superconductor allows the magnetic flux to penetrate at and beyond the critical field H_c. Changing from the Meissner state to the normal state with a direct loss of superconductivity. This corresponds to type I superconductivity, which corresponds to pure metallic elements. The current carrying capacity of type I superconductors is low, thus such materials have have limited potential in large-scale magnetic and electric applications.

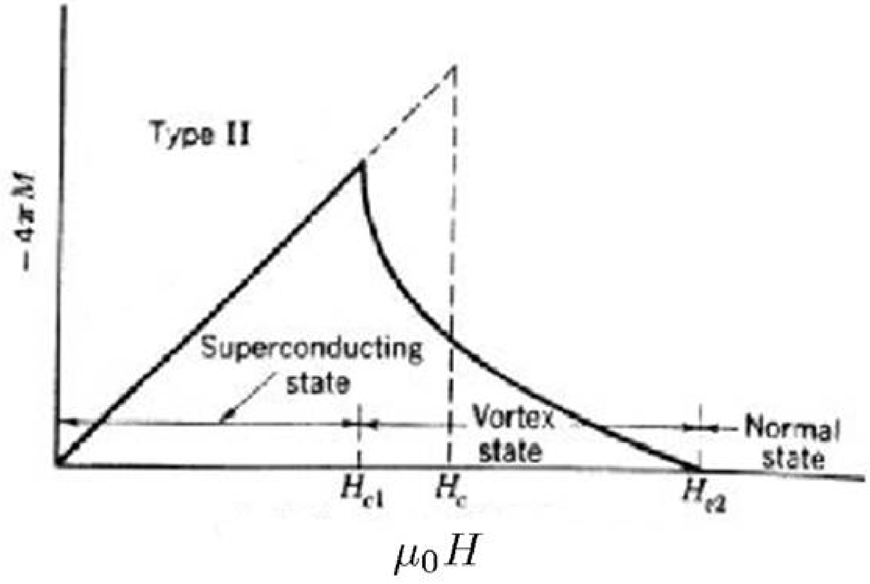

Figure 1.3: Phase diagram of type II superconductors

The case $\kappa > \frac{1}{\sqrt{2}}$,corresponds to type II superconductors, where the Meissner state is followed by the mix state (Shubnikov phase) and with increasing magnetic field, the flux penetrates into the material at a lower critical field H_{c1}, and flux penetration increases until the magnetic field reaches an upper critical field H_{c2} where the superconductor is fully penetrated, before it restores to the normal state (See figure 1.3). The flux penetrates the superconductor in form of Abrikosov vortices. Type II superconductors are metal alloys and compounds which have a much higher current-carrying capacity and are more attractive for power applications [12, 9].

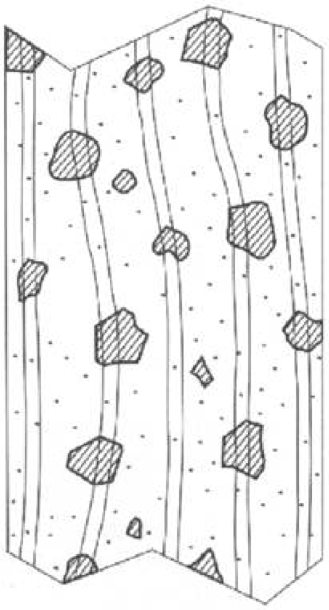

Figure 1.4: Schematic of a superconducting matrix where magnetic vortices with quantized flux ϕ_0 and spacing $a_0 = \sqrt{\frac{\phi_0}{B}}$ are pinned by nanoscaled defects to resist the force $\vec{F} = \vec{I} \times \vec{B}$ produced by the interaction of the vortex field [13].

Figure 1.4 is a schematic of a superconducting matrix where magnetic vortices with a quantized flux ϕ_0 are pinned by nano-scaled defects. The spacing between the vortices is given by $a_0 = \sqrt{\frac{\phi_0}{B}}$. Defects are pinned by nano-scaled defects to resist the force $\vec{F_L} = \vec{I} \times \vec{B}$ produced by the interaction of the vortex field, where I is the transport current and B the magnetic field. The defects are non-superconducting phases or crystal defects that are in the order of the coherence length of YBCO (<10 nm).

1.3 Critical current density of superconductors

The critical current density j_c is reached when the current in the superconductor falls at an electrical field 1µV/cm as shown schematically in figure 1.5. This is the most important figure of merit when choosing superconducting materials for applications.

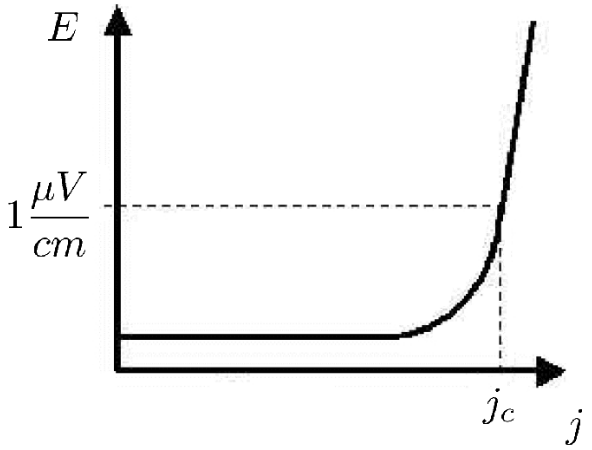

Figure 1.5: Critical current density of a 1 cm long sample.

1.3.1 The current limiting mechanisms

Important current limiting mechanisms in HTS include (i) decoupling of weak-links, (ii) depinning and (iii) thermally activated flux-flow (TAFF) [3].

(i) *Decoupling of weak-links* are relevant for polycrystalline materials, which consist of a statistical order of crystals with different crystal orientations, because of these differences grain boundaries are formed. At the grain boundaries the CuO planes in YBCO no longer match, so that the grain boundary acts like a barrier or isolator, these are called “weak-links”.

(ii-*a) Depinning-* The defects act as pinning centers detaining the vortice from moving, in order to free the vortice an energy is needed and this gives rise to the concept of pinning force ($F_{pinning}$). The current transport gives rise to a Lorentz force (F_L). The pinning force acts when the vortices at large transport current cannot move, so that their is no current decay. When the Lorentz force is as large as the pinning force the critical current density is reached, this is known as deppining and originates flux-flow resistance.

(ii-b) *Depinning by thermally activated flux-flow* occurs due to the strong anisotropy in Bi-2212 and Bi-2223. Because of the 2-D character of the CuO planes, the vortices form “pancake vortices”. At the same temperature the movement of warmth is enough to free the vortices through thermal energy from their pinning potential. At similar temperature the Lorentz force is much weaker than the pinning force and loss-free current transport is not possible.

1.3.2 The grain-boundary problem

In 1988, Dimos *et al.* [14] investigated the orientation dependence of grain boundary critical currents in $YBa_2Cu_3O_{7-\delta}$ bicrystals. The critical current densities across grain boundaries were measured in function of the misorientation angle in the basal plane of bicrystals of $YBa_2Cu_3O_{7-\delta}$. For small misorientation angles, the ratio of the grain-boundary critical current density to the bulk critical current density was found to be proportional to the inverse of the misorientation angle and for large angles, this ratio saturated to a value of about $\frac{1}{50}$. These results showed that achieving a high degree of texture both normal to and within the basal plane is important for obtaining very high critical current densities in pure polycrystalline samples. Thus, this paper is the landmark for the development of YBCO-coated conductor technology.

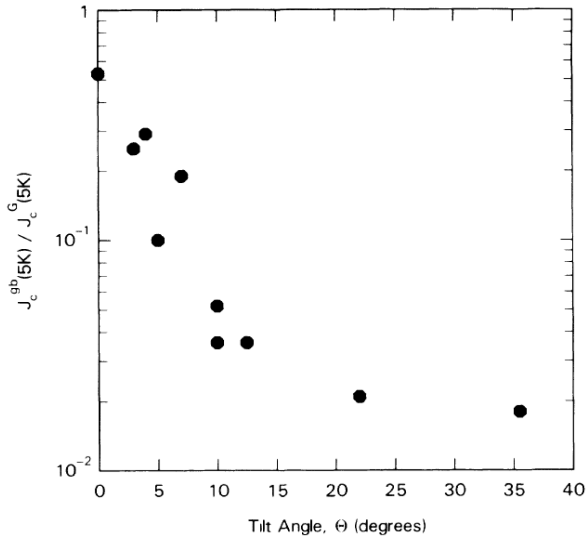

Figure 1.6: Plot of the ratio of the grain-boundary critical current density to the average value of the critical current density in the two grains at 4.2-5 K vs. the misorientation angle in the basal plane [14].

Figure 1.6 is the original plot from Dimos [14] where a strong correlation of the ratio of the grain-boundary critical current density to the average value of the grain critical current density, J_c^{gb}/J_c^G with the misorientation angle (θ) was found.

1.4 Structural properties of YBCO

Structurally, the $YBa_2Cu_3O_{7-\delta}$ (YBCO) compound is a ceramic material very similar to a perovskite structure. It is composed of an orthorombic unit cell, consisting of three perovskite units stacked along the c-axis (Figure 1.7). The central unit cell contains an yttrium cation and the other two contain a Ba atom. Along the c-axis CuO_2 planes are found which are believed to be responsible for superconductivity. The CuO_2 planes act as charge carrier reservoirs. The oxygen content can vary along the CuO_2 planes and depending on the oxygen content the structure can be tetragonal, which is the non- superconducting phase, or orthorombic at $T = 92K$, which is the superconducting phase. The compound parameters for both the orthorombic and the tetragonal phase are given in Table 1.1. The atomic positions of superconducting orthorhombic YBCO are given in Table 1.2.

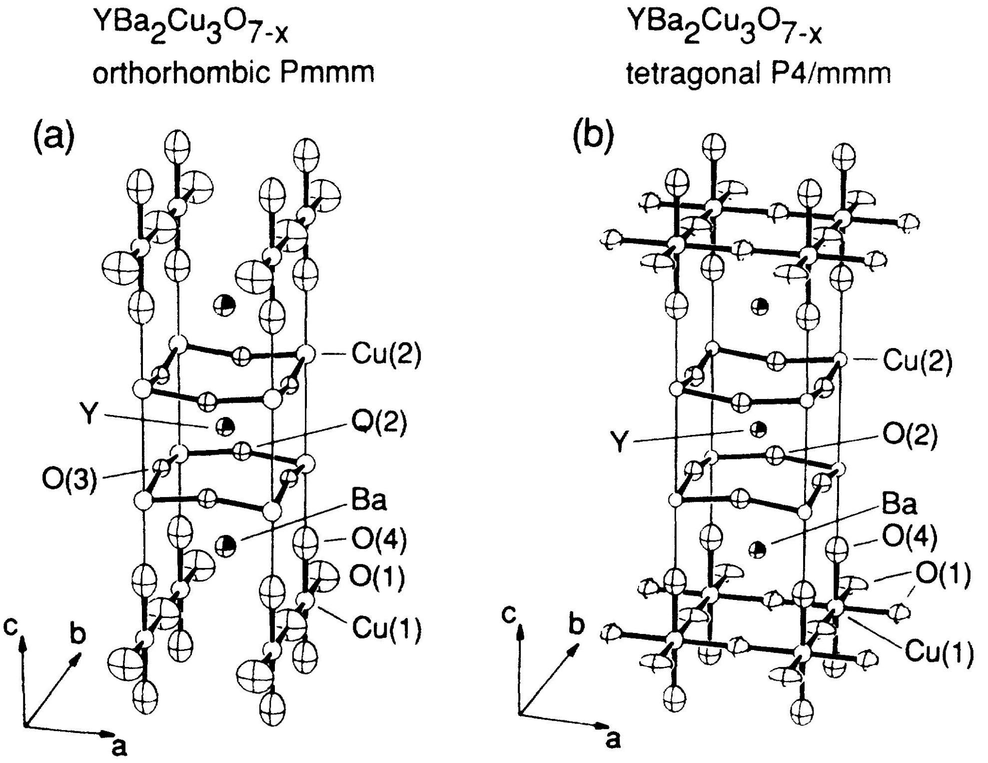

Figure 1.7: (a) Orthorhombic and (b) tetragonal structures of YBCO. The 0(1) site in the tetragonal phase (b) is not fully occupied [14].

Compound	oxygen content $(7-\delta)$	Lattice constant (nm)	Space group	T_c
$YBa_2Cu_3O_\delta$	$\delta = 0.05$	0.382, 0.388, 1.17	Pmmm (Orthorhombic)	92 K Superconducting
$YBa_2Cu_3O_\delta$	$\delta = 1$	0.390, 0.390, 1.94	P4/mmm (Tetragonal)	-

Table 1.1: Important parameters for YBCO.

These data were obtained by J. Jorgensen and collaborators using a Rietveld refinenment of Neutron powder diffraction data [15]. They observed the orthorhombic-tetragonal phase transition when varying the oxgyen doping of the atmosphere. It was possible to obtain detailed structural data on the oxygen lattice site ocupation. Electron diffraction experiments provided information on the ordering phenomena of the oxygen occupied lattice sites. Table 1.2 shows the atomic positions according to [15]. In the orthorhombic phase of YBCO various secondary phases are formed and crystal defects are found, characteristic for YBCO are twin boundaries, were the tetragonal [100] direction is parallel to the orthorhombic direction [100] and they are rotated 90° to each other. The orthorhombic crystal structure corresponds to space group Pmmm (No.47) and the lattice parameters are given in table 1.1.

Atoms	x	y	z
Ba	0.5	0.5	0.1843
Y	0.5	0.5	0.5
Cu(1)	0	0	0
Cu(2)	0	0	0.3546
O(1)	0	0.5	0
O(2)	0	0	0.1572
O(3)	0.5	0	0.3781
O(4)	0	0.5	0.3777

Table 1.2: Atomic positions in YBCO

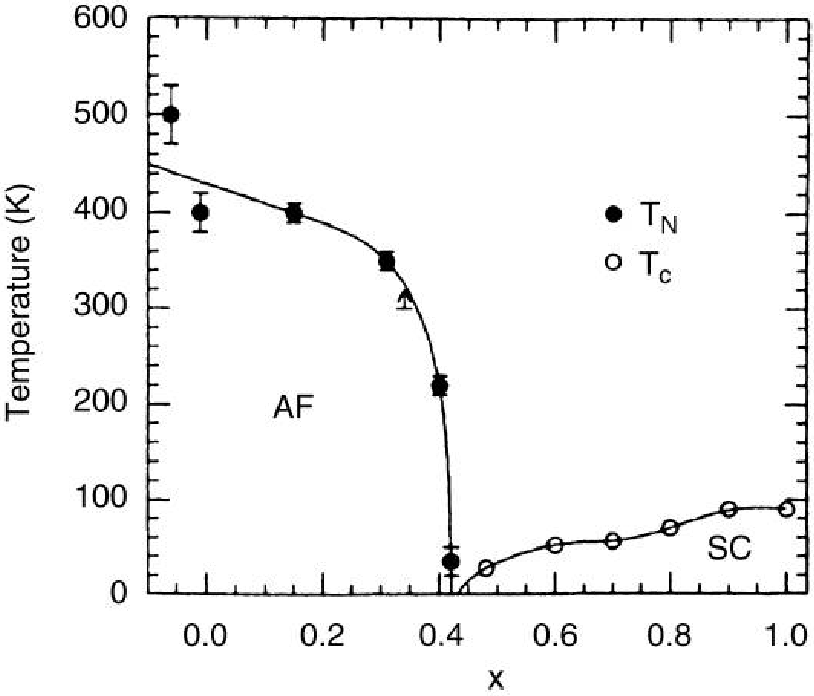

Figure 1.8: Phase diagram (temperature versus oxygen content x) of the cuprate YBCO. In the state “AF” the material is ordered antiferromagnetically and is electrically insulating. In the region “SC” the material is superconducting [9].

Shown in figure 1.8 is the phase diagram of YBCO, showing temperature in function of oxygen content. In the state “AF”, the material is ordered antiferromagnetically and is electrically insulating. In the region “SC” the material is superconducting

1.5 YBCO coated conductors

In 1996 Goyal *et al.*[16] presented a method to obtain long lengths of flexible, biaxially oriented substrates with smooth, chemically compatible surfaces for epitaxial growth of high-temperature superconductors. The technique was based on a well established, industrially scalable, thermomechanical processes to impart a strong bixial texture to a base metal. This was followed by vapor deposition of epitaxial layers to yield chemically compatible surfaces. Epitaxial YBCO films grown on such substrates had critical current densities exceeding $10^5 A/cm^2$ at $77\,K$ in zero field and had field dependencies similar to epitaxial films on single crystal ceramic substrates.

A YBCO coated conductor consists of a highly biaxially textured substrate upon which one or more buffer layers are deposited followed by a superconducting layer. The main role of the buffer layers is to prevent ion diffusion from the metallic substrate into the superconducting film and at the same time allow the transfer of the biaxial texture i.e. both in-plane and out-of plane texturing of the grains, minimizing weak link effects and forming low-angle grain boundaries in the superconducting layer. This can be achieved quite well on small scales, using deposition techniques that can produce highly epitaxial films on single crystalline crystals, but the realization on long lengths using polycrystalline substrates is a much greater challenge [17, 18, 19]. Figure 1.9 is a schematic diagram of a YBCO coated conductor.

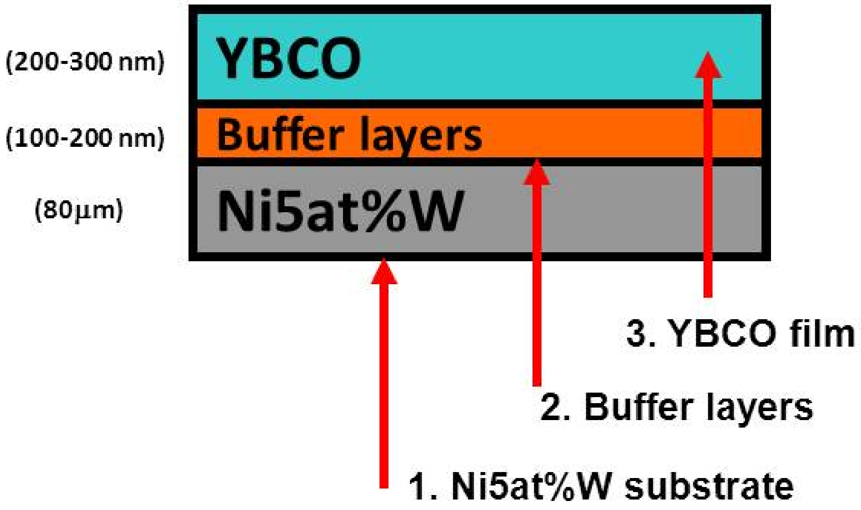

Figure 1.9: Schematic diagram of a YBCO-coated conductor prepared by chemical solution deposition.

1.5.1 Review of YBCO coated conductors

Second generation (2G) HTS coated conductors consists of a substrate upon which one or more buffer layers are deposited followed by a superconducting layer. The basic requirement that a coated conductor must fullfill is that the superconducting layer that is deposited on top must be biaxially textured [19]. There are two mayor approaches for fabricating buffered metallic substrates [20] (i) Starting from untextured metallic substrate tapes e.g. hastealloys and (ii) RABiTS (Rolling assisted biaxially textured substrate process): biaxially textured metallic susbstrates by thermo-mechanical processing [21].

The mayor differences between both methods is that untextured tapes require thicker buffer layers, but need lower deposition temperatures as compared to nickel tapes. The RABiTS technique involves heavy deformation of a metal ingot (in many cases a nickel alloy) via rolling followed by various annealing steps to obtain the desired texture. Ni is especially suitable as a substrate material due to the easy formation of a sharp cubic texture and its high oxygen resistance, however it is magnetic, whereas hastealloys are non-magnetic. Biaxially textured Ni alloy substrates are now days available in hundred meter lengths. For the production of meter to kilometer length coated conductors using flexible substrates.

The film deposition methods include (i) inclined substrate deposition (ISD) [22], (ii) ion-beam assited depostition (IBAD) [17, 18] and chemical solution deposition (CSD) [23], the latter has raised large interest due to the relatively easy and inexpensive fabrication process.

1.5.2 Requirements for applications

YBCO thin films can be used in high-field applications at 77 K such as (i) as permanent magnets with high remanent field in nuclear magnetic resonance devices (NMR) (ii) magnetic energy storage devices (iii) tapes as coils for magnetic applications. DC and AC losses play an important role for choosing adequate materials for superconducting devices. Two other energy loss mechanisms are also relevant (i) ohmic losses i.e. the loss of electric energy when a current flows through a resistance due to conversion into heat and (ii) cooling losses i.e. energy dissipation due to cooling.

For practical aplications, such as magnet winding, superconducting tapes should be mechanically flexible and relatively inexpensive to produce and it has to be possible to scale up to long lengths. This immediately highlights the great advantage of metallic substrates over single crystal substrates. Film deposition techniques should be cheap and easy to realize. There are various film deposition methods available, which are be divided in two types: (i) physical and (ii) chemical deposition methods.

Chemical methods such as the chemical solution deposition (CSD), which is method by which the samples studied in this work were prepared, are relatively inexpensive and easy to deposit on various length scales, but films are less perfect than those prepared by physical deposition methods and present a high density of defects and chemical inhomogenities, both in the superconducting and in the buffer layers [24, 25].

A microstructural and chemical investigation of the buffer layers is essential for understanding and optimizing the biaxial texture transfer to the superconducting layer and the YBCO layer itself, which is rich in secondary phases. However, high current density performances in the MA/cm^2 range at liquid nitrogen temperature (77 K) have been reported for thick chemically deposited YBCO films on flexible metal substrates.

1.5.3 CSD processed YBCO-coated conductors

The coated conductors studied in this work were prepared by colleagues at the IFW-Dresden and at Zenergy Power at Rheinbach. The currently preferred architecture consists of a biaxially textured nickel-tungsten substrate upon which two LZO buffer layers are deposited followed by a thin layer of CeO_2, both deposited by chemical solution deposition followed by a superconducting film. Films had maximum jc´s of $1MA/cm^2$at 77 K and zero field.

The superconducting films are prepared by the trifluroacetate (TFA) process, as described in [26]. The layered architecture of CSD based coated conductors is composed of (i) the highly biaxially textured nickel tungsten alloy substrate (Ni5at%W), (ii) the buffer layers LZO and CeO_2 and (iii) the TFA-YBCO superconducting film. The steps needed for chemical solution deposition of the buffer layers include: (i) mixing starting substances in addition to solvents and heat yield a precursor solution (ii) the nickel alloy tungsten substrate is then dip coated in the solution and removed with a certain velocity (iii) substrate and precursor film are then subject to a heat treatment in a tube furnace [20].

Nickel is the material of choice for fabricating Rolling Assited biaxially textured Substrates (RABiTS) as explained in [21, 27, 28]. The main fabrication procedure involves rolling of the substrate and a recrystallization process for obtaining the biaxially textured substrate. This occurs in a two step process with temperatures of 700°C and 1000°C repectively and with rate of 400 K/h and 100K/h. Afterwards an oven cooling in a Ar+5%H2 atmosphere is made. This avoids the oxidation of the substrate. Advantages of nickel based substrates over other materials are mainly (i) the similar expansion coefficient with respect to (ii) a high temperature stability (iii) a high deformability (iv) and a very good texturing. The nickel substrate thickness is 80 µm.

1.6 Tailored coated conductors

Chemical solution deposition (CSD) grown YBCO coated conductors impose great scientific and technological challenges due to the route by which these films are formed and due to the large degree of freedom with respect to their chemical composition [29, 25]. A coated conductor consists of a biaxially textured substrate upon which one or more buffer layers are deposited followed by a superconducting layer. The basic requirement that it must fullfil is that the superconducting layer that is deposited on top must have both in-plane and out-of-plane texturing of the grains in the film.

Coated conductors present a multilayer architecture. The properties of the superconducting YBCO layers are governed not only by the oxygen stoichiometry, but also by the texture, the micro and nanostructure and the effect of various extended crystal defects.

Effort was spent to the study of CSD $La_2Zr_2O_7$ buffer layers deposited on rolling assisted biaxially textured nickel tungsten substrates (RABiTS) and results are summarized. The buffer layer growth was studied at different temperatures and buffer layers plus their substrate interfaces were carefully studied by TEM show exciting structural features (i) the biaxial texture on substrates with large misfit and atomically rough surfaces, (ii) high-density of small-angle grain boundaries yielding grain sizes in the buffer layer of 100 nm compared to 40 µm in the substrate, (iii) the nanoporosity and (iv) C content.

Afterwards, full chemical solution deposition (CSD) grown YBCO coated conductors with a YBCO-CeO_2-$La_2Zr_2O_7$-Ni5at.%-W substrate layer architecture, both with and without artificial nanoinclusions were investigated and the nano- and microstructure and chemical composition obtained under various deposition and solution concentration conditions was correlated to the superconducting properties.

1.7 Structure-property-chemistry correlation

By the advancement of methods for assuring a high-biaxial texturing and low-angle grain boundaries in YBCO the values of j_c of increased into the MA/cm^2 range at 77 K and zero field. Nowdays, YBCO has become the material of choice for fabricating HTS tapes and by introducing artificial pinning centers j_c values have increased up to $10\,MA/cm^2$ for films prepared solely by chemical solution deposition methods [30].

This has further encouraged the development of YBCO coated conductors for up-scaling [31]. The use of the trifluroacetate (TFA) process to prepare chemically deposited YBCO thin films as been shown by Falter et.al. [26]. The TFA prepared YBCO superconducting films studied in this thesis included (i) multiphase standard chemically deposited TFA-YBCO and (ii) and $BaZrO_3$ doped TFA-YBCO films with BZO nanocomposites of 10- 20 nm in size. BZO nanoinclusions are of interest because introducted into the TFA-YBCO matrix they increase the critical current density (j_c) by an order of 10.

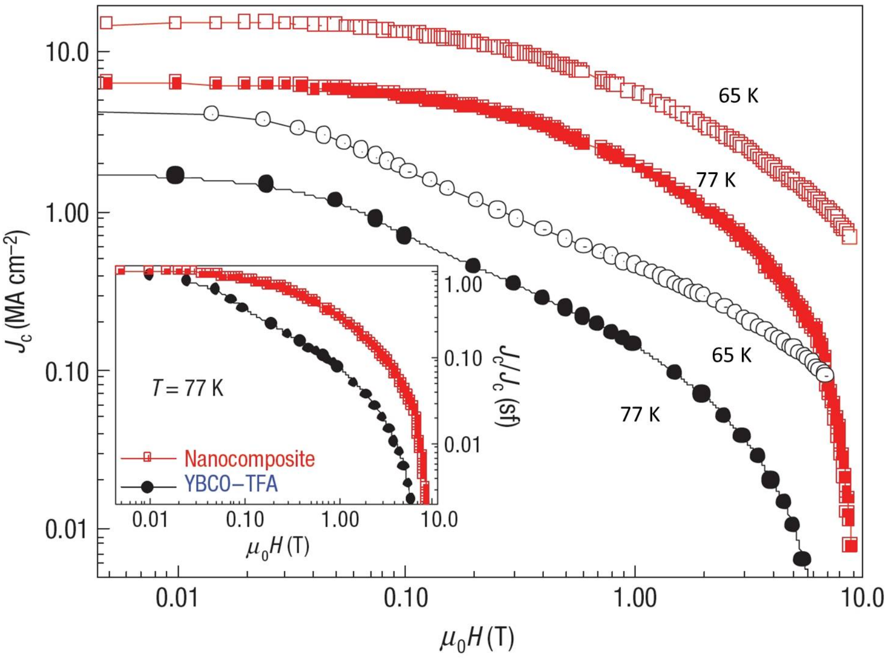

Figure 1.10: Magnetic-field dependence of the critical current density (J_c). Red squares are $J_c(B)$ dependances of TFA-YBCO with artificial pinning centers (10% mol BZO nanocomposites) at 77 K (empty squares) and 65 K (filled squares). Black curves are $J_c(B)$ dependances of standard TFA-YBCO at 77 K (empty circles) and 65 K (filled circles). The inset shows the field dependence of the normalized $J_c(B)/J_c(0)$ at 77 K for standard and nanocomposite films [30].

Shown in figure 1.10 are magnetic-field dependences of the critical current densities (J_c) of TFA-YBCO samples with and without BZO nanoinclusions. Samples were 200 nm thick and had an I_c of 200 A per cm. Red squares are $J_c(B)$ dependances of TFA-YBCO with artificial pinning centers (10% mol BZO nanocomposites) at 77 K (empty squares) and 65 K (filled squares). Black curves are $J_c(B)$ dependances of standard TFA-YBCO at 77 K (empty circles) and 65 K (filled circles).

The inset shows the field dependence of the normalized $J_c(B)/J_c(0)$ at 77 K for standard and nanocomposite films.

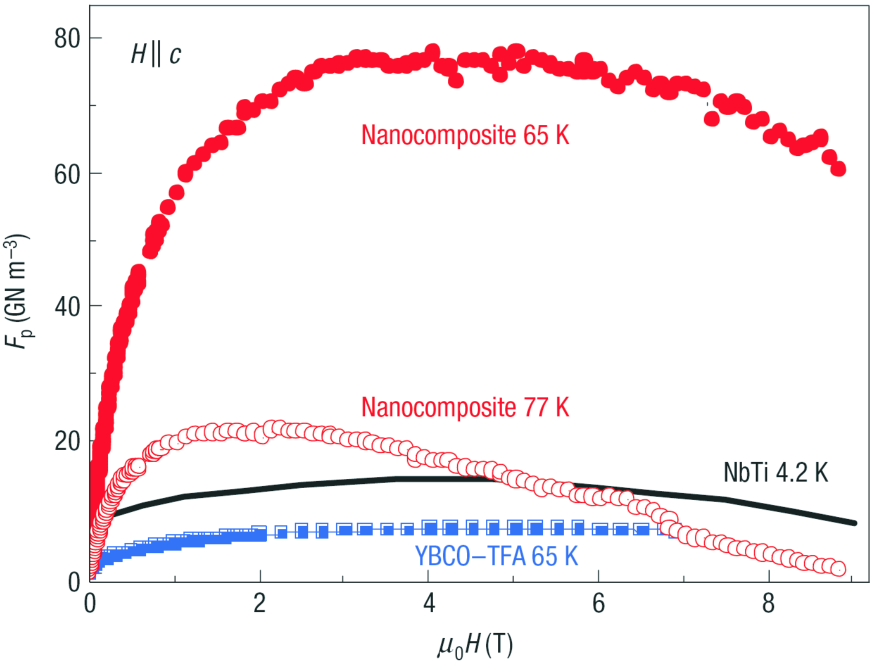

Figure 1.11: Pinning force, $Fp(H)$, curves of a BZO nanocomposite film at 65 and 77 K, compared with a standard YBCO–TFA film at 65 K and NbTi wires at 4.2 K [30]

Figure 1.11 shows the Pinning force, $Fp(H)$, curves of a BZO nanocomposite film at 65 and 77 K, compared with a standard YBCO–TFA film at 65 K and NbTi wires at 4.2 K [30]. This immediately highlights the spectacular effect of introducing BZO nanodots into a YBCO film.

In this chapter we briefly reviewed the fundamental physical properties concerning YBCO coated conductors, discussed the actual state of coated conductor technology, emphazising the chemical solution deposition method and made an overview of the requirements needed for applications, outlining the technological relevance of YBCO coated conductors.

For a reliable control of the film thickness and homogeneity, a quick non-destructive quantification method with a high spatial resolution is necessary. SEM-EDX is the method of choice (spatial resolution < 1 μm). We present optimal acquisition conditions for analysing LZO buffer layers deposited on nickel-tungsten substrates. Since the intensity of the excited X-ray lines increases with film thickness they can be used for quantification.

However, effects from absorption and fluorescence have to be taken into consideration. In order to obtain a calibration curve, we analysed four samples of different buffer layer thicknesses previously measured by alternative methods, i.e. ellipsometry, which provides a poor spatial resolution and cross-sectional transmission electron microscopy, which is very time-consuming. We established two different SEM-EDX film thickness determination methods: (a) current dependent and (b) current independent. Method (a) requires knowledge of the primary electron beam current and requires futher considerations.

For fully CSD processed coated conductors CeO_2 and YBCO layers were grown on the LZO buffer layers and the nanostructure was carefully studied and differs from that of PVD deposited films (i) a larger number of secondary phases on various length scales and (ii) surface segregation of secondary phases relevant for multilayer deposition. A new and efficient chemical mapping method yielding high accuracy was established by FIB prepared TEM lamellae in combination with EFTEM. A complete set of efficient and quantitative SEM and TEM methods were used and applied for CSD grown coated conductors that yield a fast and thorough characterization on various length scales.

TFA-YBCO coated conductor samples with BZO nanoinclusions were investigated by EFTEM and EDX spectroscopy. Pinning relevant Y_2O_3 intrinsic nanoinclusions and BZO nanodots were chemically imaged and quantified.

Chapter 2

Electron microscopy and -spectroscopy of HTS materials

2.1 Introduction

Electron microscopy techniques have proven to be essential in the understanding and design of devices based on high-Tc materials. For device relevant work electron microscopy methods have to cover different length scales from several tenth micrometers to nanometers. Conventional transmission electron microscopy (CTEM) techniques i.e. bright-field, dark-field imaging and selected area diffraction (SAD) were used for grain size determination and defect identification and required imaging under two-beam conditions. Chemical mapping techniques were used for phase formation studies in chemically grown YBCO films and involved EDX-mapping in an SEM, STEM-EDX mapping and electron spectroscopic imaging (ESI) in a transmission electron microscope (TEM) with an energy filter. Electron energy-loss spectroscopy (EELS) together with energy dispersive X-ray micro-analysis (EDX) played an important role for the study of chemical solution deposition (CSD) prepared YBCO coated conductors.

Modern electron microscopy methods are crucial for establishing a structure-property-chemistry correlation of CSD grown coated conductors and contribute strongly to the understanding of the growth and microstructure of CSD coated conductors [25] and are the central topic of this dissertation.

2.2 Electron scattering in solids

The theory of electron scattering describes the interaction of fast electrons with a specimen, relativistic corrections are necessary to calculate the corresponding wave-lengths (λ). When the electrons pass through a solid they are scattered by the interaction with the atoms of the solid. The interaction involves mainly Coulomb forces, since the incident electrons, the nucleus and the atomic electrons are charged particles. Electron scattering can be divided in elastic and inelastic scattering. Elastic scattering deals with the interaction of an incident electron with an atom, where the energy-loss to the sample is less than some experimental resolution limit, whereas inelastic scattering rises from the Coulomb interaction between incident electrons and atomic electrons and there is a measurable energy-loss of the primary electron.

U (keV)	λ(pm)	γ	$\lvert\vec{k_0}\rvert = \gamma m_0 v/\hbar$ (nm^{-1})	$T = \frac{1}{2} m_0 v^2$ (keV)
120	3.399	1.2345	1874	87.94
200	2.507	1.3909	2503	123.6
300	1.977	1.5870	3187	154.1

Table 2.1: Quantities as function of the primary energy U(keV) of electrons λ is the de-Brolglie wavelength, γ the mass correction factor, $\vec{k_0}$ the incident wave vector and T the primary energy.

In table 2.1 relevant electron quantities are calculated in function of the primary energy U(keV).

2.2.1 Elastic scattering

In elastic scattering the energy-loss during the scattering event is zero. The mechanism of the elastic scattering process is fundamental for image formation in a TEM. During electron scattering, however, the wave properties of the electrons are the most important.

The length of the wave vector of the incoming wave is given by $\left|\vec{k_0}\right| = \frac{1}{\lambda}$. $\left|\vec{k_0}\right|$ is then equal to the scattered wave so that $\left|\vec{k_0}\right| = \left|\vec{k_1}\right|$. For the wave vector we have that $\vec{p} = h\vec{k}$, where $\vec{p}$ is the momentum of the free electron and λ the de Broglie wave length. The wave vector of the incoming wave is $\vec{k_0}$ and that of the scattered wave is $\vec{k_1}$, the difference is then equal to $\vec{q}$, as seen in figure 2.1 (a).

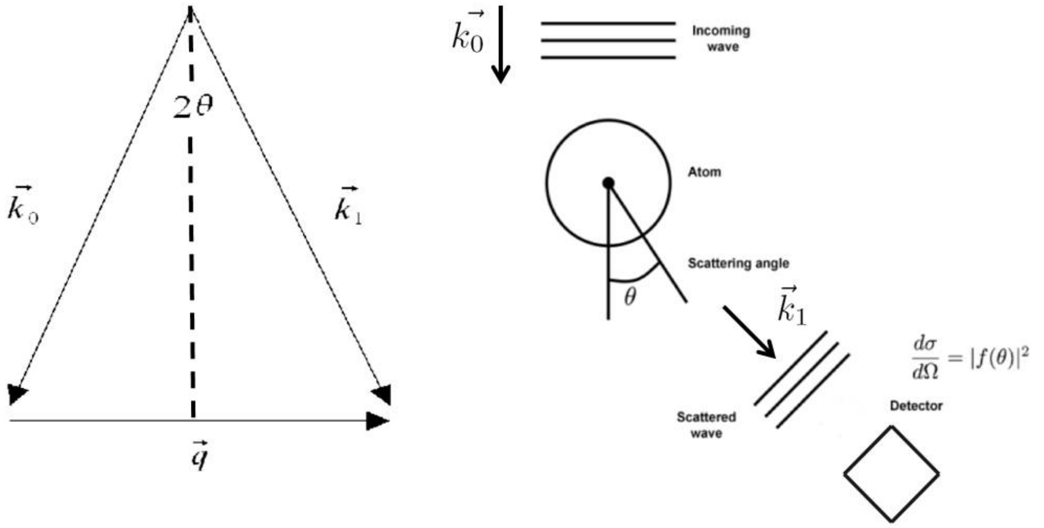

(a) (b)

Figure 2.1: (a) Schematic diagrams of the scattering triangle and (b) elastic scattering of an atom, showing incoming wave, scattering center (atom) and detector.

Using simple trigonometry it can be shown that the relationship between the the length of the scattering vector $\vec{q}$ and the scattering angle θ is given by:

$$sin\theta = \frac{|\vec{q}|\,\lambda}{2} \tag{2.1}$$

Using the small-angle approximation we obtain:

$$2\theta = |\vec{q}|\,\lambda \tag{2.2}$$

The scattering amplitude emitted from an atom is described by the atomic scattering factor $f(\theta)$.

Figures 2.1 (b) illustrates the scattering of a wave from an atom. A detector that measures the intensity of the scattered wave is placed far away from the scattering center. The intensity measured is proportional to the absolute squared of the atomic scattering factor. This quantity is known as the simple differential scattering cross-section:

$$\frac{d\sigma}{d\Omega} = |f(\theta)|^2 \tag{2.3}$$

Atomic scattering factors for electrons are simple functions that are tabulated in the literature [32] and correspond to the fourier transform of the atomic potential, they increase with increasing atomic number (Z) of an atom.

Equation 2.3 describes how to obtain the kinematical scattering factors for electrons according to a relativistic Hartree-Fock atomic wave function calculation given by Coultard *et al.* [33]:

$$f(s) = \frac{8\pi^2 m_0 e}{h^2} \int_{\infty}^{0} r^2 V(r) \frac{\sin(4\pi s r)}{(4\pi s r)} dr \tag{2.4}$$

s is defined as:

$$s = \frac{\sin\theta}{\lambda} \left[\mathring{A}^{-1}\right] \tag{2.5}$$

and $V(r)$ is the atomic potential. The analytical approximation for $f(s)$ is given by:

$$f(s) = \gamma \cdot \sum_{i=l}^{n} a_i \exp(-b_i s^2) + c \tag{2.6}$$

a_i and b_i are fitting factors and are given in table 2.2 for Y, Ba, Cu and O atoms, s is the scattering parameter andγ is the relativistic correction of the electron mass given by [34]:

$$\gamma = \frac{m}{m_0} = 1 + \frac{eU}{m_0 c^2} \tag{2.7}$$

The atomic scattering factors for Y, Ba, Cu and O atoms in dependence of the scattering angle (θ) are shown in figure 2.2.

Z	Element	Fitting factors (a_i) [Å]	(b_i) [Å^2]
16	O	[0.4548, 0.9173, 2.1440, 0.1384]	[23.7803, 7.6220, 2.1440, 0.2959]
29	Cu	[1.5792, 1.8197, 1.6576, 0.5323]	[62.9403, 12.4527, 2.5042, 0.3331]
39	Y	[5.8478, 4.0026, 2.3420, 0.8795]	[104.9721, 19.3666, 3.7368, 0.4142]
56	Ba	[7.8212, 6.0040, 3.2803, 1.1030]	[117.6575, 18.7782, 3.2634, 0.3760]

Table 2.2: Fitting parameters for calculating the atomic scattering factors of Y, Ba, Cu, O [32].

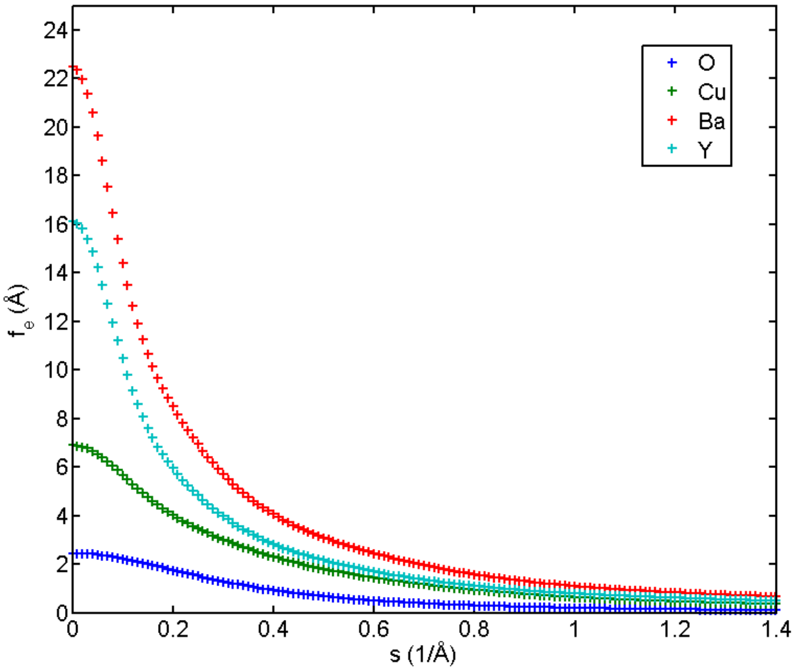

Figure 2.2: Relativistically corrected atomic scattering factors in dependence of the scattering angle for 120 keV.

When considering scattering of a crystalline material the kinematical structure factor is given by:

$$F_{hkl} = \sum f_j(s) \exp[2\pi \cdot i(h \cdot x_j + k \cdot y_j + l \cdot z_j] \tag{2.8}$$

Debye Waller factors are set to unity and (h, k, l) are the Miller-Bravais indices (of the scattered beam) and (x_j, y_j, z_j) are the atomic positions. The atomic positions for YBCO are given in table 1.2 and the calculated kinematical structure factors for YBCO are given in table 2.3.

hkl	$d_{hkl}(nm)$	$g_{hkl}(nm^{-1})$	$s_{hkl}(nm^{-1})$	$F_{hkl}(nm)$
001	1.168	0.856	0.584	0.366
002	0.584	1.712	0.856	1.532
003	0.389	2.568	1.285	3.886
010	0.387	2.582	1.291	4.309
100	0.3823	2.615	1.307	4.308
011	0.367	2.720	1.362	0.488
101	0.363	2.752	1.377	0.643
012	0.322	3.098	1.552	1.345
110	0.272	3.675	1.838	8.754
111	0.264	3.774	1.893	1.399

Table 2.3: Structure factor calculation for YBCO using an accelerating voltage of 120 keV. d_{hkl} are the lattice spacings, g_{hkl} is the reciprocal lattice vector, s_{hkl} the deviation from the Bragg condition and F_{hkl} the Kinematical scattering factor.

Dynamical theory of diffraction contrast

There are two basic modes of CTEM operation, namely the bright-field mode, where the objective aperture is set so that the transmitted beam contributes to the image formed and the dark-field mode in which a specific diffracted beam is selected. In both cases the specimen is oriented with respect to the electron beam to excite a particular diffracted beam, or a systematic row of reflections, and the image is sensitive to the differences in specimen thickness, distortion of crystal lattices due to defects, strain and bending. Diffraction contrast imaging and selected area diffraction (SAD) were used to (i) determine the grain size and (ii) to study the grain tilting mechanisms in LZO buffer layers, (iii) to determine the size of secondary phases in TFA-YBCO, (iv) to identify crystal defects in TFA-YBCO and (v) to study the interfaces between the layers.

Diffraction contrast imaging was done under two-beam conditions where the sample was oriented with repect to an incoming electron beam such that only the direct beam and a specific diffracted beam (g_{hkl}) were strongly excited. The theory of dynamical contrast diffraction imaging describes the rate of change of the amplitudes of both the diffracted and the direct beam with respect to a thickness Z of a thin sample and is described by the first order Howie-Whelan coupled differential equations [35, 36]:

$$\frac{d}{dz}\begin{pmatrix}\phi_0(z)\\ \\ \phi_g(z)\end{pmatrix} = i\pi\begin{pmatrix}\frac{1}{\xi_0} & \left(\frac{1}{\xi_g}\right)e^{-2\pi i(\vec{g}+\vec{s})\cdot\vec{r}}\\ \\ \left(\frac{1}{\xi_g}\right)e^{2\pi i(\vec{g}+\vec{s})\cdot\vec{r}} & \frac{1}{\xi_0}\end{pmatrix}\cdot\begin{pmatrix}\phi_g(z)\\ \\ \phi_0(z)\end{pmatrix} \tag{2.9}$$

where ξ_0 and ξ_g are the extinction lengths of the direct and the diffracted beams. The extinction length is defined as:

$$\xi_g = \frac{\pi V_c \cos(\theta_B)}{\lambda F_{hkl}} \tag{2.10}$$

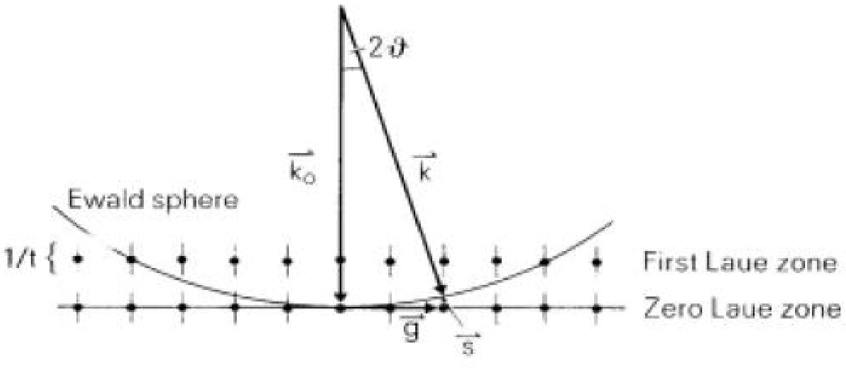

Figure 2.3: Scattering of an electron beam on the lattice planes of a crystal, $\vec{s}$ is the excitation error, (deviation from the perfect Bragg condition).

Where $\vec{k_0}$ and $\vec{k}$ are the incident and diffracted wave vectors as shown in figure 2.3, $\vec{g}$ is the diffraction vector and $\vec{s}$ is the excitation error and is defined by: $\vec{s} = (\vec{k}_0 - \vec{k})\ -\vec{g}$.

The rate of change is proportional to the change of amplitudes of the direct and the diffracted beams. The solution of these equations for a two beam case give the intensities of the diffracted and direct beams and are given by:

$$|\phi_g^2| = \left(\frac{\pi}{\xi_g}\right)^2 \left(\frac{\sin^2(\pi t S_{eff})}{(\pi S_{eff})^2}\right) \tag{2.11}$$

where

$$|\phi_0|^2 = 1 - |\phi_g|^2 \tag{2.12}$$

Where ϕ_0 is the direct beam andϕ_g is the diffracted beam and t the specimen thickness.

For equation 2.10, θ_B is the Bragg angle, V_C is the volume of the unit cell, F_{hkl} is the kinematical structure factor and S_{eff} is the effective excitation error which is given by:

$$S_{eff} = \frac{\sqrt{s^2\xi_g^2 + 1}}{\xi_g} \tag{2.13}$$

These equations explain thickness fringes due to the periodicity with repect to t and the bending contours in the sample due to the variation of the excitation error, but fails to describe the non-complementaries observed in bright and dark field imaging in TEM since inelastic scattering and absorption of the scattered electrons by the objective aperture are not taken into account these effects can be considered by introducing the complex terms, $\frac{i}{\xi_0^{'}}$, $\frac{i}{\xi_g^{'}}$ to the terms $\frac{i}{\xi_0}$, $\frac{i}{\xi_g}$ in the Howie Whelan equations according to [35]. Introducing these into equation 2.9 we have the Howie-Whelan equations including absorption:

$$\frac{d}{dz}\begin{pmatrix} \phi_0\left(z\right) \\ \\ \phi_g\left(z\right) \end{pmatrix} = i\pi \begin{pmatrix} \frac{1}{\xi_0} + \frac{i}{\xi_0'} & \left(\frac{1}{\xi_g} + \frac{i}{\xi_g'}\right) e^{-2\pi i(\vec{g}+\vec{s})\cdot\vec{r}} \\ \\ \left(\frac{1}{\xi_g} + \frac{i}{\xi_g'}\right) e^{2\pi i(\vec{g}+\vec{s})\cdot\vec{r}} & \frac{1}{\xi_0} + \frac{i}{\xi_0'} \end{pmatrix} \cdot \begin{pmatrix} \phi_g\left(z\right) \\ \\ \phi_0\left(z\right) \end{pmatrix} \tag{2.14}$$

By transforming the functions ϕ_0 , $\phi_g$and by approximating the unit of length $\xi_0^{‘} = \xi_g^{‘}$ we can re-write the Howie-Whelan equations as:

$$\frac{d}{dz}\begin{pmatrix} \phi_0\left(z\right) \\ \\ \phi_g\left(z\right) \end{pmatrix} = i\pi \begin{pmatrix} (-A + 2iw) & (i - A) \\ \\ (i - A) & -A \end{pmatrix} \cdot \begin{pmatrix} \phi_g\left(z\right) \\ \\ \phi_0\left(z\right) \end{pmatrix} \tag{2.15}$$

Where the anomalous absorption is defined as $A = \xi_0^{'}/\xi_g^{'}$ and the excitation parameter is given by $w = s \cdot \xi_g = \cot\beta$. The intensity of the direct and diffracted beams can be expressed analytically as:

$$|\phi_g|^2 = \left| -\cos(\beta/2)\sin(\beta/2)(\exp(-iXz) - \exp(iXz))\exp(-\pi z/\xi_0^{'}) \right|^2 \tag{2.16}$$

$$|\phi_0|^2 = \left| (\cos^2(\beta/2)\exp(-iXz) + \sin^2(\beta/2))\exp(-iXz/\xi_0^{'}) \right|^2 \tag{2.17}$$

Where

$$X = \frac{\pi\sqrt{1+w^2}}{\xi_g} + \frac{\pi i\sqrt{1+w^2}}{\xi_g^{'}} \tag{2.18}$$

In the case of uniformly thin and defect free crystalline sample no variation in the intensity is observed, but in the case of crystals containing defects variations are observed if they cause a local displacement of the atoms from their original position defined as $R(\vec{r})$. This causes bending of the lattice planes and variations of the local excitation error values in the sample. The corresponding Howie-Whelan equations are given by [37]:

$$\frac{d}{dz}\begin{pmatrix} \phi_0(z) \\ \phi_g(z) \end{pmatrix} = i\pi \begin{pmatrix} \frac{1}{\xi_0} + \frac{i}{\xi_0'} & \left(\frac{1}{\xi_g} + \frac{i}{\xi_g'}\right) e^{-2\pi i(sz+\vec{g})\cdot\vec{R}} \\ \left(\frac{1}{\xi_g} + \frac{i}{\xi_g'}\right) e^{2\pi i(sz+\vec{g})\cdot\vec{R}} & \frac{1}{\xi_0} + \frac{i}{\xi_0'} \end{pmatrix} \cdot \begin{pmatrix} \phi_g(z) \\ \phi_0(z) \end{pmatrix} \tag{2.19}$$

As in the case of a perfect crystal, after transforming ϕ_0 and ϕ_g and the unit of length, the Howie-Whelan equations are given by[37]:

$$\frac{d}{dz}\begin{pmatrix} \phi_0(z) \\ \phi_g(z) \end{pmatrix} = i\pi \begin{pmatrix} (-A + 2i(w + \pi\vec{g}\cdot\frac{d\vec{R}}{dz})) & (i - A) \\ (i - A) & -A \end{pmatrix} \cdot \begin{pmatrix} \phi_g(z) \\ \phi_0(z) \end{pmatrix} \tag{2.20}$$

Where the effective excitation parameter for the distorted crystal is defined as:

$$w_{eff} = w + \pi\vec{g}\cdot\frac{d\vec{R}}{dz} \tag{2.21}$$

Due to the term $\vec{g}\cdot\frac{d\vec{R}}{dz}$, these equations can only be solved numerically as shown by Hirsch *et al.* [35]. The term $\frac{d\vec{R}}{dz}$ describe the local tilt of lattice planes projection in $\vec{g}$ direction. These equations are the basis of any defect anlysis by diffraction contrast. Not $\vec{R}$ itself enters the Howie-Whelan equtions but $\vec{g} \cdot \frac{d\vec{R}}{dz}$, i.e. the projection of $\vec{R}$ in $\vec{g}$ direction and from this the derivative with respect to Z, the direction of the electron beam.

2.2.2 Inelastic scattering

Relativistic mechanics: energy and momentum conservation

In order to correctly describe the physics of inelastic electron scattering it is necessary to use the concepts of energy and momentum conservation of relativistic mechanics. According to relativistic mechanics the total energy of an incident electron is given by:

$$W = \gamma m_0 c^2 \tag{2.22}$$

and the incident momentum is given by:

$$p = \gamma m_0 v = \hbar k_0 \tag{2.23}$$

One can define a relativistic equation for the total energy and this leads to a wave vector – energy relationship of the form:

$$W = [(M_0 c^2 + p^2 c^2]^{1/2} = [(m_0 c^2)^2 + \hbar^2 k_0^2 c^2]^{1/2} \tag{2.24}$$

According to energy conservation we can write:

$$W - E = W' = [(M_0 c^2 + p^2 c^2]^{1/2} = [(m_0 c^2)^2 + \hbar^2 k_1^2 c^2]^{1/2} \tag{2.25}$$

where W and $W\acute{}$ are the total energy before and after the collision and $\vec{k_0}$ is the incident wave vector and $\vec{k}$ is the scattered wave vector. The wave vector after the collision is given by:

$$k_1^2 = k_0^2 - 2E[m_0^2/\hbar^4 + k_0^2/(\hbar c)^2]^{1/2} + E^2/(\hbar c)^2 \tag{2.26}$$

$$k_1^2 = k_0^2 - 2\gamma m_0 E/\hbar^2 + E^2/(\hbar c)^2 \tag{2.27}$$

After the collision the wave vector depends from the wave vector before the collision and from an energy-loss where $k_1^2 < k_0^2$. Multiplying with the squared from the Bohr radius we obtain:

$$(k_1 a_0)^2 = (k_1 a_0)^2 - (E/R)[\gamma - E/(2m_0 c^2)] \tag{2.28}$$

$$(k_1 a_0)^2 = (E_0/R)[1 + E_0/2m_0 c^2] = (T/R)/(1 - 2T/m_0 c^2) \tag{2.29}$$

with $T = m_0 v^2/2$, where R is the Ryberg constant, which is a energy unit ($R = 13.6eV$) and is given by:

$$R = \frac{\hbar^2}{2m_0 a_0^2} \tag{2.30}$$

According to figure 2.4 (a) and from momentum conservation we can write:

$$q^2 = k_0^2 + k_1^2 - 2k_0 k_1 cos\theta \tag{2.31}$$

where $\vec{q}$ is the scattering vector and $\vec{k_0}$ and $\vec{k_1}$ are the wave vector before and after the collision. The scattered wave vector $\vec{k_1}$ correponds to a wave vector $\vec{k_0}$, but ends at S. The difference to $\vec{k_0}$ is called

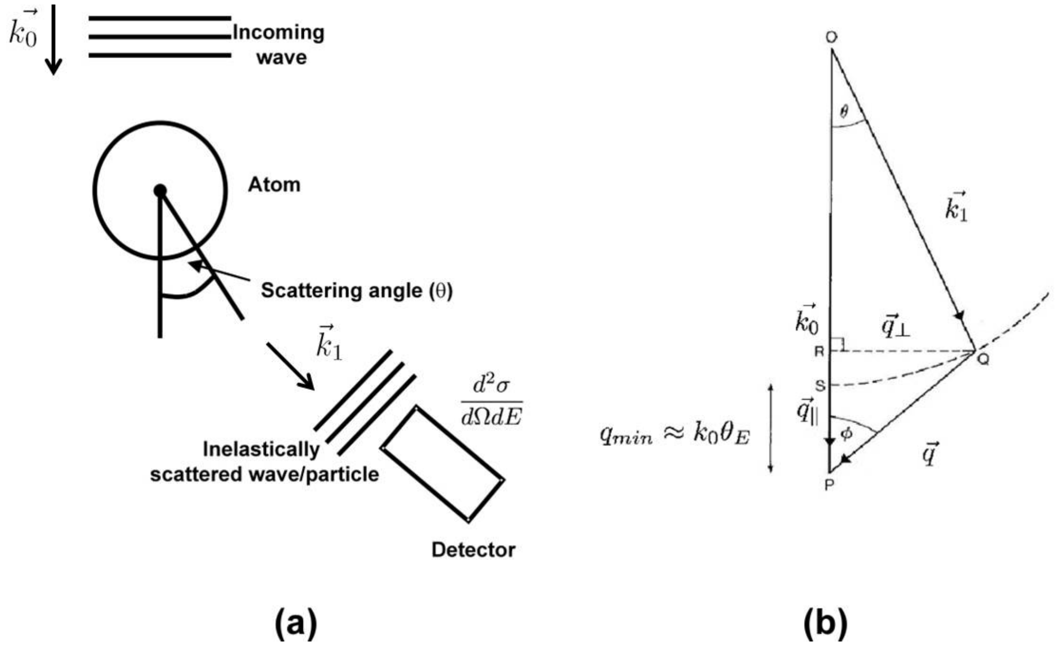

Figure 2.4: (a) Inelastic scattering process (b) Schematic of the inelastic scattering process from an atom.

$\vec{q}_{min}$, which depends from the energy-loss and the primary energy only.

Due to energy conservation we have that:

$$(k_1a_0)^2 = (k_1a_0)^2(E/R)[\gamma - E/2m_0c^2] \tag{2.32}$$

This can be written as:

$$(qa_0)^2 = (qa_0)^2_{min} + 4\gamma(T/R)\sin^2(\theta/2) \tag{2.33}$$

So we have two terms, where only one depends on the scattering angle (θ). From figure 2.3 (b) we have that $q^2 = q_{\|}^2 + q_{\perp}^2$.

For small angles we have that:

$$(qa_0)^2 = (qa_0)^2_{min}4k_0^2[(\theta/2)]^2 \tag{2.34}$$

$$q^2 = k_0^2(\theta_E^2 + \theta^2) \tag{2.35}$$

Where θ_E is the characteristic angle and is defined as:

$$\theta_E = \frac{E}{2E_0} \tag{2.36}$$

and q_{min} is defined as:

$$q_{min} \sim k_0\theta_E \tag{2.37}$$

The characteristic scattering angles (θ_E) for elements concerning YBCO coated conductors are calculated in table 2.4 for $E_0 = 120$ keV (acceleration voltage for the Zeiss 912 omega TEM) and the corresponding energy-losses of interest.

Z	Element	Level	Energy-loss (eV)	$\theta_E = \frac{E}{2E_0}$ (mrad), $E_0 = 120\ keV$
8	O	K	532	2.21
28	Ni	$L1, L2, L3$	1008, 872, 855	4.20, 3.63, 3.56
29	Cu	$L1, L2, L3, M2, 3M4, 5$	1096, 951, 931, 74.3, 72	4.56, 3.96, 3.87, 0.31, 0.30
39	Y	$M3, M4, N2, N3$	301, 160, 29, 26	1.25, 0.66
40	Zr	$M3, M4, N2, 3$	331, 183, 29	1.37, 0.76, 0.12
56	Ba	$M4, M5, N4, N5$	796, 781, 93, 90	3.31, 3.25, 0.387, 0.375
57	La	$M4, M5, N4, N5$	849, 832, 99, 97.7	3.53, 3.46, 0.41, 0.40
58	Ce	$M4, M5, N4, N5$	902, 884, 111, 107.6	3.75, 3.68, 0.46, 0.44

Table 2.4: Characteristic scattering angles (θ_E) for elements concerning YBCO coated conductors.

2.2.3 Summary of relevant relationships for elastic and inelastic scattering

Table 2.5 sumarizes the relevant relationships for the elastic and inelastic scattering processes: (1) describes the relationships between the wave vectors $\vec{k}_0$ and $\vec{k}_1$ and the scattering vector $\vec{q}$, (2) the relationship between the scattering vector $\vec{q}$ and the scattering angle θ and in the case of inelastic scattering the characteristic angle θ_E (3) no energy-loss for the elastic scattering case and an energy-loss for inelastic scattering, (4) the differential scattering cross-section for elastic scattering and the double differential sacttering for inelastic scattering and (5) the atomic scattering factor in function of the Fourier transform of the atomic potential and the transition probability form an intial state $|i>$ to a final state $|f>$ for an inelastic scattering process described by the double differential scattering cross-section.

2.2.4 Differential scattering cross-sections for inelastic scattering: low-loss

Calculating inelastic scattering differential scattering cross-sections for the low-loss region involves the description of inelastically scattered valence electrons i.e. outer shell scattering and is complicated since the valence electron wave functions are modified by chemical bonding. Collective excitations, plasmons, play a major role and involve many atoms. This part of the energy-loss spectrum gives information on the electronic band structure of the material.

Figure 2.5 shows a sketch of the band structure for YBCO derived from electron energy-loss spectroscopy, photoemission, inverse photoemision, X-ray absorption spectroscopy and band structure calculations given by [38]. Energy levels that are interesting for YBCO and are accesible via Low-Loss EELS are found in the sketch i.e. Cu 3 p, Ba 4 d, Y 4 p and 0 2p levels.

	Elastic scattering	Inelastic scattering
Definition of q	$\vec{k_0} + \vec{q} = \vec{k_1}$	$\vec{k_1} + \vec{q} = \vec{k_0}$
q and the small scattering angle	$\frac{\lvert\vec{q}\rvert}{2} = \frac{\theta}{\lambda}$	$q^2 = k_0^2(\theta^2 + \theta_E^2)$
Wave functions	$\vec{k_0},\, \vec{k_1},\, E = 0$	$(\vec{k_0}, i), (\vec{k_1}, f), E \neq 0$
Functions introduced	f ... atomic scattering factor	$\frac{\partial f}{\partial E}$ ... Generalized Oscillator Strength
Differential cross-sections	$\frac{d\sigma}{d\Omega} = \lvert f(\theta)\rvert^2$	$\frac{\mathrm{d}^2\sigma}{\mathrm{d}\Omega \mathrm{d}E} = \frac{4\gamma^2 R}{Eq^2} \frac{k_1}{k_0} \frac{\partial f}{\partial E}(q, E)$
Atomic scattering factor and the Generalized Oscillator Strength	$f(\theta) = \frac{8\pi m_0 e}{h^2} \int V(\vec{r}) e^{-i\vec{q}\cdot\vec{r}} d^3r$	$\frac{df}{dE} \propto \frac{1}{q^2} \left\lvert < f \rvert e^{i\vec{q}\cdot\vec{r}} \lvert i > \right\rvert^2$

Table 2.5: Relationships for the elastic and inelastic scattering processes.

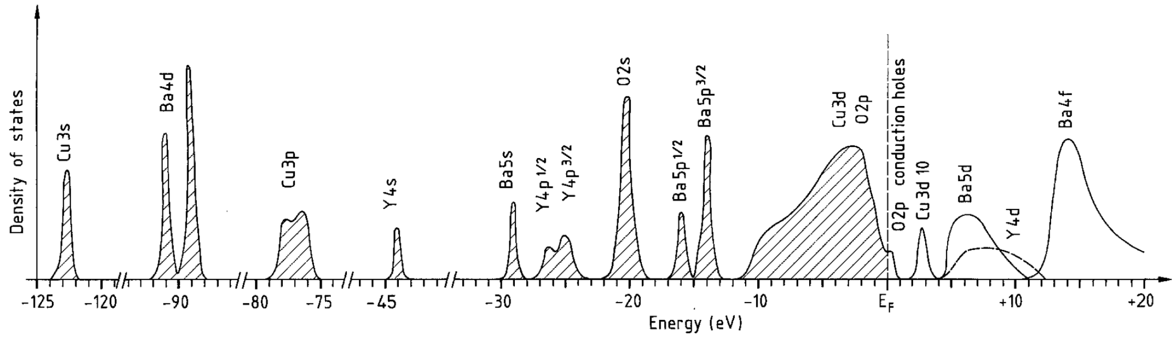

Figure 2.5: Sketch of the band structure for YBCO derived from photoemission, inverse photoemision, X-ray absorption spectroscopy, electron energy-loss spectroscopy and band structure calculations. Cu 4s, 4p and 0 3s levels are not shown [38].

The interaction of the transmitted electron with the entire solid can be described in terms of a dielectric response function $\varepsilon(q, w)$, where q is the scattering vector and w is the frequency.

The same response function describes the interaction of photons with a solid, so that this formalism allows energy-loss data to be correlated and compared with results of optical measurements ([39] and references therein). Ritchie [40] derived an expresion for the electron-scattering power of an infinite medium, where the transmitted electron is represented by a point charge $-e\delta(r-vt)$ where r is coordinate and v the velocity in the z-direction. The charge generates within the medium a spatially dependent, time-independent electrostatic potential $\phi(r, t)$ that satisfies Poisson´s equation:

$$\varepsilon_0 \varepsilon(q, w) \nabla^2 \phi(r, t) = e\delta(r, t) \tag{2.38}$$

The stopping power, $\frac{dE}{dz}$, is equal to the force on the electron in the direction of motion, which is also the electronic charge multiplied by the potential gradient in the z-direction. Using Fourier transforms, one can show that [39]:

$$\frac{\mathrm{dE}}{\mathrm{d}z} = \frac{2\hbar^2}{\pi a_0 m_0 v^2} \int\int \frac{q_y w Im[-1/\varepsilon(q, w)]}{q_y^2 + (w/v)^2} dq_y dw \tag{2.39}$$

where the angular frequency w is equivalent to $E/\hbar$ and q_y is the component of the scattering vector in a direction perpendicular to v. The imaginary part of $[-1/\varepsilon(q, w)]$ is the energy-loss function and provides a description of the response of the medium through which the electron is travelling. This related to the double differential scattering cross-section (per atom) for inelastic scattering by the following expression [39]:

$$\frac{\mathrm{d}^2\sigma}{\mathrm{d}\Omega \mathrm{d}E} = \int\int n_a E \frac{d^2\sigma}{d\Omega dE} d\Omega dE \tag{2.40}$$

where n_a are the number of atoms per unit volume of the medium. Using $dq_y \approx k_0\theta$ and $d\Omega \approx 2\pi\theta d\theta$ and equation 2.38 and 2.39 we can write:

$$\frac{\mathrm{d}^2\sigma}{\mathrm{d}\Omega \mathrm{d}E} \approx \frac{Im[-1/\varepsilon(q, E)]}{\pi^2 a_0 m_0 v^2 n_a} \left(\frac{1}{\theta^2 + \theta_E} \right) \tag{2.41}$$

where θ_E is the characteristic angle. The double differential scattering cross-section can be given in terms of the loss function in the following form [39]:

$$\frac{\mathrm{d}^2\sigma}{\mathrm{d}\Omega \mathrm{d}E} = Im\left[-\frac{1}{\varepsilon(q,w)}\right] \tag{2.42}$$

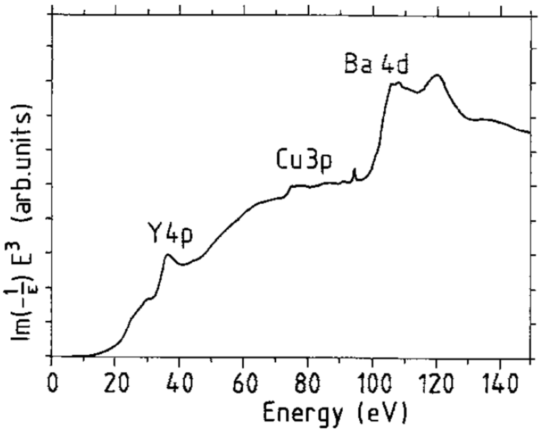

Figure 2.6: Loss-function multiplied by $(energy)^3$ in function of the energy-loss for YBCO according to [38]. The Y 4p (YN2,3 edge), Cu 3p (Cu N4,5 edge) and Ba 4d (Ba N4,5 edge) levels are shown.

Figure 2.6 shows the low-loss function for YBCO according to [38]. The Y 4p, Cu 3p and Ba 4d levels are shown, these correspond to the Y N2,3, Ba N4,5 and Cu N4,5 absorption edges.

Fourier-Log deconvolution of EELS Low-Loss spectra

In order to correct for multiple scattering Fourier-Log deconvolution can be used to remove plural scattering from the low-loss region (<50 eV) [39] in order to understand data from this region. In this region the main energy-loss mechanism involves excitation of outer-shell electrons, this is described by a Plasmon model which has its origin in the valence-electron excitation and occurs wih a high probability because the plasmon free path is comparable to the sample thickness.

Fourier-Log deconvolution.

The technique is based on the Fourier transform, it allows to remove plural scattering from the Low-loss region of the EELS spectrum ([39] and references therein). The deconvolution method applied by Johnson and Spence [41] assumes that the scattering events are independent and that the probability of plural scattering is described by Poisson statistics according to:

$$I_n = IP_n = \left(\frac{I}{n!}\right)\left(\frac{t}{\lambda}\right)^n \exp\left(\frac{-t}{\lambda}\right) \tag{2.43}$$

where I_n is the intensity, P_n the probability of n scattering events within a specimen of thickness (t), ! denotes a factorial and λ is the mean free path for inelastic scattering, this characterizes all inelastic scattering in the energy range over which the intensity is integrated. The case $n = 0$ corresponds to the absence of inelastic scattering and is represented in the energy-loss spectrum by the zero-loss peak:

$$Z(E) = I_0R(E) = I\,exp(-t/\lambda) \tag{2.44}$$

where the resolution function or instrument response$R(E)$ has unit area and a FWHM equal to the experimental resolution ΔE. Single scattering corresponds to $n = 1$ and can be described by an intensity distribution $S(E)$. From equation 2.42 we obtain:

$$I_1 = \int S(E)dE = I(t/\lambda)\exp(-t/\lambda) = I_0(t/\lambda) \tag{2.45}$$

Due to limited energy resolution ΔE. Single scattering occurs within the experimental spectrum $J(E)$ as a broadened distribution $J^1(E)$ defined as:

$$J^1(E) = R(E) * S(E) = \int R(E - E')S(E')dE' \tag{2.46}$$

where * denotes a convolution over an energy-loss. Double scattering has an energy dependence of the form $S(E) * S(E)$.

and is given as:

$$J^2(E) = R(E) * D(E) = R(E) * S(E) * S(E)/2!I) \tag{2.47}$$

Accordingly multiple scattering would be given by $J^3(E) = R(E) * T(E)$

The observed spectrum, including the zero-loss peak can be written as:

$$J(E) = Z(E) + J^1(E) + J^2(E) + J^3(E) + ... \tag{2.48}$$

The Fourier transform of $J(E)$ is defined according to Bracewell [42] as :

$$j(v) = \int j(E)\exp(2\pi ivE)dE \tag{2.49}$$

taking the transforms of both sides of equation 2.47, the convolutions become products:

$$j(v) = z(v)\{1 + s(v)/I_0 + [s(v)]^2/(2!I^2) + [s(v)]^3/(3!I^3) + ...\} \tag{2.50}$$

$$j(v) = z(v)\exp[s(v)/I] \tag{2.51}$$

according to Johnson and Spence [41], equation 2.49 can be inverted by taken the logarithm of both sides giving:

$$s(v) = I_o[j(v)/z(v)] \tag{2.52}$$

Within single scattering distribution (SSD) inverse transform is given by:

$$j^1(v) = g(v)s(v)I_0 exp(-\pi^2\sigma^2v^2)ln[j(v)/z(v)] \tag{2.53}$$

this can be written as:

$$j^1(v) = r(v)s(v) = z(v)ln[j(v)/z(v)] \tag{2.54}$$

These equations are implemented for Fourier-Log deconvolution of Low-Loss EELS spectra of YBCO using ESIVISION software [43].

2.2.5 Differential scattering cross-sections for inelastic scattering: core-loss

Introduction

In order to calculate differential scattering cross-sections from inner-shell ionizations (core-loss) it is necessary to use quantum mechanics. A primary electron is scattered by an atom with a change in the scattering vector, $\vec{k}$ to $\vec{k'}$, and the electrons of the atom undergo a transition from a Ψ_{1s} state to Ψ_n state. Hans Bethe was the first to calculate inelastic scattering cross-sections for the collision of a fast electron with an atom [44]. His treatment is based on the wave mechanical theory of Born and is applied to collisions of electrons with a hydrogen-like atom. Shown in table 2.6 is equation 7 of reference [44] where Bethe defines the differential cross-section as $d\Phi_n(q)$ with dimensions of area and $V_n(q)$ is the Coulomb potential responsible for the interaction. Equation 10 of the same reference gives the differential cross-section in terms of a matrix element $\varepsilon(q)$ which defines the exchange interaction.

In 1971 Inokuti [45] revised Bethe´s quantum mechanical theory based on the Born approximation that allowed to calculate collision cross-sections and stopping powers for hydrogen like atoms and re-defined Bethe´s equation without mayor changes as given in table 2.6. Egerton [39] defines the differential scattering cross-section similarly, but in terms of the wave functions, where $V(r)$ is the potential responsible for the interaction, Ψ_0 is the wave function and the Ψ^* is the complex conjugate of the wave function and the integration is done over all the volume elements $d\tau$ within the atom. Finally, Schattschneider defines the differential scattering cross-section as equation 2.8 of reference (see tablee 2.6-2.7)[46], where V_n represents the interaction potential between the probe and the target charges where $\mid a >$ is an unperturbed state and $\mid b >$ is a perturbed state and the transition is given by the matrix element $\varepsilon(q)$. The matrix element is defined in equation 2.59 and the interaction potential (V_n) in equation 2.56.

In the relativistic case, not only the inelastic collision of an electron with a hydrogen like atom has to be taken into account, but also the collision of two relativistic electrons gives rise to a retardation potential first mentioned by G. Breit in 1929 [47]. Møller [48] gave a simplification of the Born collision theory in terms of relativistic invariant expressions for the scattering of two very fast particles and defined a differential scattering cross-section as shown in table 2.6. Bethe and Fermi [49] proved the connection between the Breit and Møller works and showed that the Breit equations for the effect of retardation on the interaction of two relativistic particles can be deduced from Møller´s equations and using quantum-electrodynamics.

The physical origins of the retardation potential takes into account the interaction between two charges. Since these are non-static, a scalar potential V and a vector potential A at a same time t cannot correspond exactly to the charge and current distributions at that particular moment, unless the charges are fixed in space, therefore retarded potentials have to be defined that indicate the charge and current distributions at that particular moment $t - (r/c)$, where r is the distance between the two charges and c the speed of light, this is the physical origin of the retardation potential.

In 1956 Fano [50] revisited these works and showed that the retardation induces a transition with dipole moment transverse to the momentum transferred in the scattering and that the spins of the electrons play a role in the retardation effect. This effect was then included in the calculation of the differential scattering cross-section. The definition from Fano is given in equation 5 of reference [50] (see table 2.7). The first term describes the three body problem and the second term accounts for the retardation interaction of two relativistic electrons. Egerton adopts Fano´s description and defines the retardation term as $G(\beta, \gamma, \theta)$, which is the second term of equation equation 404 of reference [39] as shown in table 2.7.

	Problem	Differential scattering cross-section	Relativistic treatment	Ref.	Eq. no.	Page
Bethe	Inelastic collision of an electron with a hydrogen like atom	$d\phi_n(q) = \frac{4\pi^2}{h}\frac{m_0^2}{h^3}\frac{k_1}{k_0} \cdot 2\pi \sin\vartheta d\vartheta \cdot e^4 z^2 \cdot \lvert V_n(q)\rvert^2$	No	*[44]*	*7*	*331*
		$d\phi_n(q) = \frac{8\pi\alpha^2}{q^4}\,(m_0 z)^2\,\frac{k_1}{k_0}\,\lvert\varepsilon_n(q)\rvert^2 \sin\vartheta d\vartheta$			*10*	
Inokuti	Inelastic collision of an electron with a hydrogen like atom	$d\sigma_n = (2\pi)^{-2} m_0^2 \hbar^{-4} (\frac{k_1}{k_0}) \left\lvert \int e^{iK\cdot r} u_n * (r_1, ..., r_z) \times V_n(r_1, ...r_z) dr_1 ... dr_z dr \right\rvert^2 dw$	No	*[45]*	*1*	*298*
		$d\sigma_n = 4z^2 (m_0 e^2/\hbar^2)^2 (k_1/k_0)\,\lvert\varepsilon_n(q)\rvert^2\, dw$			*2.4*	
Egerton I	Inelastic collision of an electron with a hydrogen like atom	$\frac{\mathrm{d}\sigma_n}{\mathrm{d}\Omega} = (\frac{m_0}{2\pi h^2})^2 \frac{k_1}{k_0} \left\lvert \int V(r)\Psi_0\Psi_0^* e^{iq\cdot r} d\tau \right\rvert^2$	No	*[39]*	*3.20*	*147*
		$\frac{\mathrm{d}\sigma_n}{\mathrm{d}\Omega} = \left(\frac{4\gamma^2}{a_0^2 q^4}\right) \frac{k_1}{k_0}\,\lvert\varepsilon_n(q)\rvert^2$			*3.22*	
Schattschneider	Inelastic collision of an electron with a hydrogen like atom	$\frac{\mathrm{d}^2\sigma}{\mathrm{dEd}\Omega} = (\frac{2\pi}{\hbar})^4 m_0^2 \Sigma \frac{k_1}{k_0} \lvert< b \lvert V_n\rvert\, a >\rvert^2 \delta(E_a - E_b)$	No	*[46]*	*2.8*	*17*
		$\frac{\mathrm{d}^2\sigma}{\mathrm{dEd}\Omega} = \left(\frac{2me^2}{(\hbar q)^2}\right)^2 \frac{k_1}{k_0}\,\lvert\varepsilon_n(q)\rvert^2$			*2.14*	

Table 2.6: Definition of the differential scattering cross-section according to various authors.

	Problem	Differential scattering cross-section	Relativistic treatment	Ref.	Eq. no.	Page
Møller	collision of two relativistic electrons	$dQ(\theta) = \frac{e^4 sin2\theta \cdot 2d\theta d\varphi}{m^2 v^4} \cdot$ $\left\{ \frac{1}{sin^4\theta} + \frac{1}{cos^4\theta} - \frac{1}{sin^2\theta cos^2\theta} - \frac{\beta^2}{4} \left[\frac{4}{sin^4\theta} + \frac{3}{cos^4\theta} - \frac{2}{sin^2 \cdot cos^2\theta} - \frac{5}{cos^2\theta} \right] \right\}$	Yes	[48]	14	793
Fano	Inelastic collision of an electron with a hydrogen like atom + collision of two relativistic electrons	$\frac{\mathrm{d}\sigma}{\mathrm{d}\Omega} = z^2 (\frac{e^2}{\hbar c})^2 \frac{4}{\beta^2} \frac{x_n^2}{\theta_0^2} \times \left[\frac{\theta_0^2}{\theta_0^2 + \theta^2} + \frac{\beta^2 \theta^2}{\theta_0^2 + \theta^2} \frac{\beta^2 \theta_0^4}{[\theta_0^2 (1-\beta^2) + \theta^2]^2} \right]^2$	Yes	[50]	5	386
Egerton II	Inelastic collision of an electron with a hydrogen like atom + collision of two relativistic electrons	$\frac{\mathrm{d}\sigma}{\mathrm{d}E} = \frac{4\pi a_0^2}{(E/R)(T/R)} \cdot$ $\frac{df}{dE} \left[\ln \left(1 + \frac{\beta^2}{\theta_E^2} \right) + 2 \ln \gamma - \ln \left(\frac{\beta^2 + \theta_E^2}{\beta^2 + \theta_E^2 / \gamma^2} \right) - \frac{v^2}{c^2} \left(\frac{\beta^2}{\beta^2 + \theta_E^2 / \gamma} \right) \right]$	Yes	[39]	404	A.5

Table 2.7: Definition of the differential scattering cross-section including retardation.

In order to describe precisley the inelastic scattering of electrons by an atom and the dependence of scattered intensity on an energy-loss, the behavior of each atomic electron must be specified in terms of the transition form an initial state of wavefunction ψ_0 to a final state of wave function ψ_n. This involves interaction in a three body problem that includes (i) the primary electron (ii) the nucleus of an hydrogen like atom (iii) $1s$ electron of an hydrogen like atom. Where ψ_0 is the product state of two electrons.

According to the first Born approximation, the differential cross-section for the transition according to Egerton [39] is:

$$\frac{\mathrm{d}\sigma_n}{\mathrm{d}\Omega} = (\frac{m_0}{2\pi h^2})^2 \frac{k_1}{k_0} \left| \int V(r) \Psi_0 \Psi^* \ e^{iq \cdot r} d\tau \right|^2 \tag{2.55}$$

Where $\vec{k}_0$ and $\vec{k}_1$ are wavevectors of the fast electron before and after scattering, $\hbar\vec{q} = \hbar(\vec{k}_0 - \vec{k}_1)$ is the momentum $\vec{q}$ transferred to the atom, r is coordinate of the fast electron, $V(r)$ is the potential responsible for the interaction, Ψ_0 is the initial wave function,$\Psi^*$is the complex conjugate of the wave function and the integration is done over all the volume elements $d\tau$ within the atom.

Table 2.8 sumarizes the relevant relationships for the elastic and inelastic scattering processes: (1) describes the relationships between the wave vectors $\vec{k}_0$ and $\vec{k}_1$ and the scattering vector $\vec{q}$, (2) the relationship between the scattering vector $\vec{q}$ and the scattering angle θ and in the case of inelastic scattering the characteristic angle θ_E (3) no energy-loss for the elastic scattering case and an energy-loss for inelastic scattering, (4) the differential scattering cross-section for elastic scattering and the double differential sacttering for inelastic scattering and (5) the atomic scattering factor in function of the Fourier transform of the atomic potential and the transition probability form an intial state $|i>$ to a final state $|f>$ for an inelastic scattering process described by the double differential scattering cross-section.

Table 2.6 shows equivalent definitions of the differential cross-section found in the literature according to various authors.

The electrostatic interaction potential representing the electrostatic forces between an incident electron and an atom is given by:

$$V(r) = \frac{Ze^2}{4\pi\varepsilon_0 r} - \frac{1}{4\pi\varepsilon_0} \sum_{j=1}^{Z} \frac{e^2}{|r - r_j|} \tag{2.56}$$

Although generally referred to as a potential, V(r) is actually the negative of the potential energy of the fast electron and is related to the true potential ϕ by $V = -e\phi$.

The first term in equation 2.55 represents the Coulomb attraction by the nucleus where the charge is Ze (interaction from the primary electron with the nucleus); the second term is a sum of the repulsive effects of each atomic electron, coordinate r_j (primary electron with the $1s$ electron).

Because the initial and final states are orthogonal, the nuclear contribution integrates to zero in equation 2.54, so that inelastic scattering involves only interaction with the atomic electrons. It is advantageous to perform first the integration over r by using the relation [45, 49]:

$$\int |r - r_j|^{-1} \exp(iK \cdot r) dr = 4\pi K^{-2} \exp(iK \cdot r_j) \tag{2.57}$$

Thus, equation 2.55 transform into:

$$\frac{d\sigma_n}{d\Omega} = \frac{4\gamma^2}{a_0^2 q^4} \frac{k_1}{k_0} \left|\varepsilon_n(q)\right|^2 \tag{2.58}$$

	Elastic scattering	Inelastic scattering
Definition of q	$\vec{k_0} + \vec{q} = \vec{k_1}$	$\vec{k_1} + \vec{q} = \vec{k_0}$
q and the small scattering angle	$\frac{\lvert\vec{q}\rvert}{2} = \frac{\theta}{\lambda}$	$q^2 = k_0^2(\theta^2 + \theta_E^2)$
Wave functions	$\vec{k_0},\, \vec{k_1},\, E = 0$	$(\vec{k_0}, i), (\vec{k_1}, f), E \neq 0$
Functions introduced	f ... atomic scattering factor	$\frac{\partial f}{\partial E}$ ... Generalized Oscillator Strength
Differential cross-sections	$\frac{d\sigma}{d\Omega} = \lvert f(\theta)\rvert^2$	$\frac{\mathrm{d}^2\sigma}{\mathrm{d}\Omega \mathrm{d}E} = \frac{4\gamma^2 R}{Eq^2} \frac{k_1}{k_0} \frac{\partial f}{\partial E}(q, E)$
Atomic scattering factor and the Generalized Oscillator Strength	$f(\theta) = \frac{8\pi m_0 e}{h^2} \int V(\vec{r}) e^{-i\vec{q}\cdot\vec{r}} d^3 r$	$\frac{df}{dE} \propto \frac{1}{q^2} \left\lvert < f \rvert e^{i\vec{q}\cdot\vec{r}} \lvert i > \right\rvert^2$

Table 2.8: Relationships for the elastic and inelastic scattering processes.

where the first term is the Rutherford cross-section for scattering from a single free electron, $\frac{k_1}{k_0}$ is a term close to unity and the final term, known as the inelastic form factor or dynamical structure factor, $|\varepsilon_n(q)|^2$ is the absolute squared of the transition-matrix element defined by:

$$\varepsilon_n = \int \psi_n^* \sum_j \exp(i\vec{q}\cdot\vec{r_j})\psi_0 d\tau = < \psi_n \left| \sum_j \exp(i\vec{q}\cdot\vec{r_j}) \right| \psi_0 > \tag{2.59}$$

The inelastic form factor is a dimensionless factor that modifies the Rutherford scattering which would take take place if the atomic electrons were free, it is a property of the atom and is independent of the incident electron velocity.

A dimensionless quantity known as the generalized oscillator strength (GOS) is defined as:

$$f_n(q) = \frac{E_n}{R}\frac{(|\varepsilon_n(q)|)^2}{(qa_0)^2} \tag{2.60}$$

Where R is the Rydberg energy and E_n is the energy loss associated with the transition from the inital to the final state. The differential cross-section can be written as:

$$\frac{d\sigma_n}{d\Omega} = \frac{4\gamma^2 R}{Eq^2}\frac{k_1}{k_0} f_n(q) \tag{2.61}$$

The angular and energy dependence of scattering can be specified by a double-differential cross-section:

$$\frac{d^2\sigma}{d\Omega dE} = \frac{4\gamma^2 R}{Eq^2}\frac{k_1}{k_0}\frac{df}{dE}(q,E) \tag{2.62}$$

And taking into account that $q^2 = k_0^2(\theta^2 + \theta_E^2)$ and $\theta_E = E/2E_0$, the double-differential can be written as:

$$\frac{d^2\sigma}{d\Omega dE} = \frac{4\gamma^2 R}{Eq^2}\left(\frac{1}{\theta^2+\theta_E^2}\right)\frac{df}{dE} = \frac{8a_0^2R^2}{Em_0v^2}\left(\frac{1}{\theta^2+\theta_E^2}\right)\frac{df}{dE} \tag{2.63}$$

Calculation of the Generalized Oscillator Strength (GOS): The Hydrogenic Model

The double differential cross-section was given in equation 2.62 and consists of two terms, the first can be understood by classical mechanics, the second $\frac{df}{dE}$ modulates the first and has a quantum mechanical origin and is called the Generalized Oscillator Strength (GOS). The unit of the first term is $\frac{area}{Sr}$, whereas the unit of the second term is $\frac{1}{Energy}$, f in equation 2.60 is dimensionless. The matrix element $< \Psi' \left| e^{i\vec{q}\vec{r}} \right| \Psi_0 >$ depends on the direction of $\vec{q}$ is most easily understood in terms of the electron wave functions within the hydrogen approximation.

The calculation of the GOS within the the hydrogen model will be given below. Although the Hydrogen model can be used to calculate the GOS for a surprisingly large number of edges, more advanced methods have been applied to include relativistic wave functions in the matrix elements [46].

The GOS describes the response of an atom when a given momentum and energy are supplied from a collision of an fast electron. In order to calculate the GOS, it is necessary to know the initial- and final-state wave functions of the inner-shell electron. The most simple way of donig this is by using the Hydrogenic model as shown by Bethe [44]. This takes into account an inelastic collision of a fast electron with a hydrogen like atom and provides realistic values for K-shell ionization cross-sections.

The Schrödinger equation for the hydrogen atom is given by:

$$H\psi = E_t\psi \tag{2.64}$$

Where H is the Hamiltonian defined by:

$$H = \frac{-\hbar^2}{2m_0}\nabla^2\psi - \frac{e^2}{4\pi\varepsilon_0 r}\psi \tag{2.65}$$

and E_t is the net energy of the atomic electron. In order to use equation 2.64 to an inner-shell electron within an atom of atomic number Z, the electrostatic term must be modified to take into account the actual nuclear charge Ze and the screening of the nuclear field remaining $(Z-1)$ electrons. In the case of K-shell excitation, the second 1s electron screens the nucleus and reduces its effective charge by approximatly 0.3e giving an effective atomic number that is defined by $Z_s = Z - 0.3$, (this values corresponds to K-shell excitation) where Z is the atomic number. The net energy, E_t, of the excited electron is related to its binding energy E_k and the energy lost by the primary electron by:

$$E_t = E - E_k \tag{2.66}$$

Considering an effective atomic number Z_s, E_k is defined by:

$$E_k = Z_s^2 R - E_s \tag{2.67}$$

Z	Ionization edge	$E_s(eV)$	$Z_s = Z - 0.3$	$Z_s^2 R(eV)$	$E_k = Z_s^2 R - E_s(eV)$
6	C-K	284	5.7	441.86	157.86
8	O-K	532	7.7	806.34	274.34

Table 2.9: Calculated values for C-K and O-K according to the Hydrogenic model.

Table 2.9 shows calculated values for O-K and C-K ionization edges.

For convenience two variables are defined that are related to the scattering vector q and the energy loss E of the fast electron and are given by $Q = (qa_0/Z_s)^2$and $k_H^2 = E/(Z_s^2 R) - 1$

The GOS per atom for $E > Z_s^2 R$ and for k-shell ionization is defined acording to Madision et.al. [51] as:

$$\frac{\mathrm{d}f_k}{\mathrm{d}E} = \frac{256E(Q' + k_H^2/3 + 1/3\exp(-2\beta'/k_H)}{Z_s^4 R^2[(Q' - k_H^2 + 1)^2 + 4k_H^2]^3[1 - \exp(-2\pi/k_H]} \tag{2.68}$$

For energy ranges of $E_k < E < Z_s^2 R$. the GOS per atom for K-shell ionization is given according to Egerton by [52] :

$$\frac{\mathrm{d}f_k}{\mathrm{d}E} = \frac{256E(Q' + k_H^2/3 + 1/3\exp(y)}{Z_s^4 R^2[(Q' - k_H^2 + 1)^2 + 4k_H^2]^3} \tag{2.69}$$

where

$$y = -(-k_H^2)^{-1/2} log_e \left[\frac{Q' + 1 - k_H^2 + 2(-k_H^2)^{1/2}}{Q' + 1 - k_H^2 + 2(-k_H^2)^{1/2}}\right] \tag{2.70}$$

The generalized oscillator strength is a function of both the energy E and the momentum $\hbar q$ supplied to the atom and can be shown by a 3-D plot known as the Bethe surface.

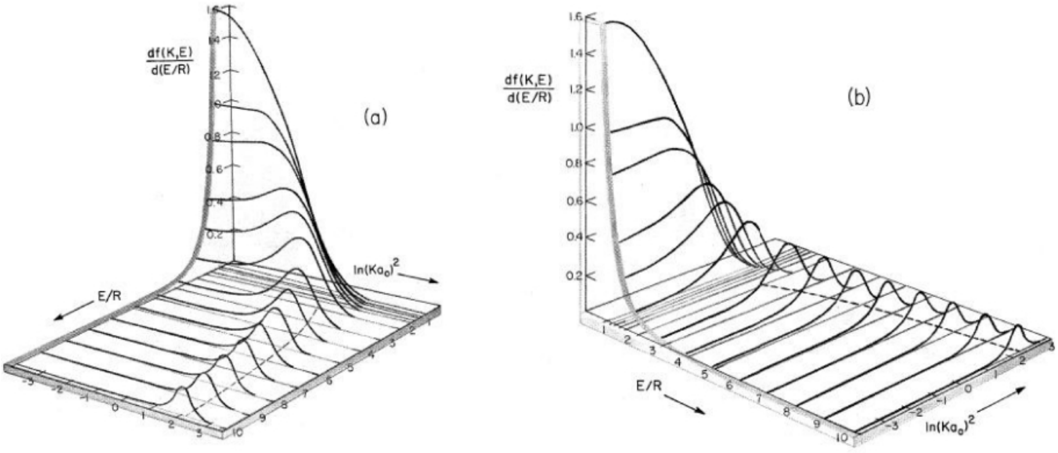

Figure 2.7: Bethe surface for hydrogen [46].

In figure 2.7 we show the calculated Bethe surface for H-K shell ionization and calculated for both regions $E > Z_s^2 R$ and $E_k < E < Z_s^2 R$ and using equations 2.68 and 2.69.

For applying this for other atoms than H, the actual nuclear charge $Z_s e$ and the screening of the nuclear field by the remaining electrons must be taken into account.

Calculation of ionization cross-sections: Relativistic Bethe Theory [39]

The angular and energy dependence of inelastic scatttering was given in section 2.2.2 and is defined by the double-differential scattering cross-section (equation 2.62):

$$\frac{d^2\sigma}{d\Omega dE} = \frac{4\gamma^2 R}{Eq^2}\frac{k_1}{k_0}\frac{df}{dE}(q,E) \tag{2.71}$$

Where γ is the relativistic correction factor. R is the Rydberg constant, q is the scattering vector, k_0 the incoming wave vector, k_1 scattered wave vector, E an energy-loss and $\frac{df}{dE}(q,E)$ is the differential oscillator strength. At high incident energies (above 200 keV) an additional relativistic effect (collison of two relativistic electrons) becomes significant and is given in the form of a retarded interaction (See table 2.7, Egerton and Fano) so that equation 2.71 can be replaced by [53]:

$$\frac{d^2\sigma}{d\Omega dE} = 4\gamma^2 a_0^2 R^2 \left(\frac{k_1}{k_0}\right)\left[\frac{1}{Q^2} - \frac{2\gamma - 1}{\gamma^2 Q(E_0 - Q)} + \frac{1}{(E_0 - Q)^2} + \frac{1}{(E_0 + m_0 c_2)^2}\right] \mid \eta(q,E) \mid^2 \tag{2.72}$$

Where $\gamma = 1/(1 - v^2/c^2)^{1/2}$, v is the incident velocity, a_0 is the Bohr radius and R is the Rydberg energy. The quantity Q has dimensions of energy and is defined as:

$$Q = \frac{\hbar q^2}{2m_0} - \frac{E^2}{2m_0 c^2} = R(qa_0)^2 - \frac{E^2}{2m_0 c^2} \tag{2.73}$$

The first term has dimensions of "energy", and the second term is a dimensionless quantity. Quantities with different dimensions cannot be added. q is the scattering vector and E represents the energy loss. The term $\frac{E^2}{2m_0c^2}$ is significant at small scattering angles.

According to Inokuti *et al.* [45], $\mid \eta(q,E) \mid^2$, is an energy-differential relativistic form factor that is equal to the non-relativistic form factor $\mid \varepsilon(q,E) \mid^2$ for high angle collisions and is defined as:

$$\mid \eta(q,E) \mid^2 = \frac{1}{E}\left(\frac{df}{dE}\right)\left[Q - \frac{E^2}{2\gamma^2 m_0 c^2}\right] \tag{2.74}$$

Fano *et al.* [50] showed that the differential cross-section can be written as the sum of three independent terms within the dipole regime $\theta \ll \left(\frac{E}{E_0}\right)^{1/2}$ and is given as:

$$\frac{d\sigma}{dE} = \frac{4\pi a_0^2}{(E/R)(T/R)}\frac{df}{dE}\left[\frac{1}{\theta^2+\theta_E^2} + \frac{(v/c)^2\theta^2\theta_E^2}{(\theta^2+\theta_E^2)(\theta^2+\theta_E^2/\gamma^2)^2}\right] \tag{2.75}$$

where $T = m_0 v^2/2$ and $\theta_E = E/(2\gamma T)$.

Integration up to a collection angle β gives:

$$\frac{d\sigma}{dE} = \frac{4\pi a_0^2}{(E/R)(T/R)}\frac{df}{dE}\left[\ln(1+\beta^2/\theta_E^2) + G(\beta,\gamma,\theta_E)\right] \tag{2.76}$$

where $G(\beta,\gamma,<\theta_E>)$ is a retardation term that accounts for relativistic effects and is defined as:

$$G(\beta,\gamma,<\theta_E>) = 2ln\gamma - ln\left(\frac{\beta^2+\theta_E^2}{\beta^2+\frac{\theta_E^2}{\gamma^2}}\right) - \frac{v^2}{c^2}\left(\frac{\beta^2}{\beta^2+\frac{\theta_E^2}{\gamma^2}}\right) \tag{2.77}$$

For an ionization edge with a threshhold energy E_k and integrated over an energy range $(\triangle)$ which is small compared to E_k gives:

$$\sigma(\beta,\Delta) = \frac{4\pi a_0^2}{(<E>/R)(T/R)}f(\Delta)\left[ln(1+\left(\frac{\beta^2}{<\theta_E>^2}\right) + G(\beta,\gamma,<\theta_E>)\right] \tag{2.78}$$

where $<E>$and $<\theta_E>$ are the average values of E and θ_E and $<E>$ is defined as an expectation value and is givens as [39]:

$$<E> = [E_k(E_k+\triangle)]^{1/2} \tag{2.79}$$

Equation 2.78 was implemented for calculating differential scattering cross-sections in this thesis.

2.3 Experimental Implementation

In this section the various electron microscopy methods used for coated conductor characterization on different length scales and specimen preparation techniques for TEM will be briefly described. Figure 2.8 is a flow diagram describing the strategy used for the micro and nano-structural analysis of YBCO coated conductors. SEM and SEM-EDX play a major role in the identification of micro-meter scaled defects and chemical inhomogenities after which it can be decided to procede or not to TEM specimen preparation, which is very time consuming, and to further characterization by advanced TEM techniques.

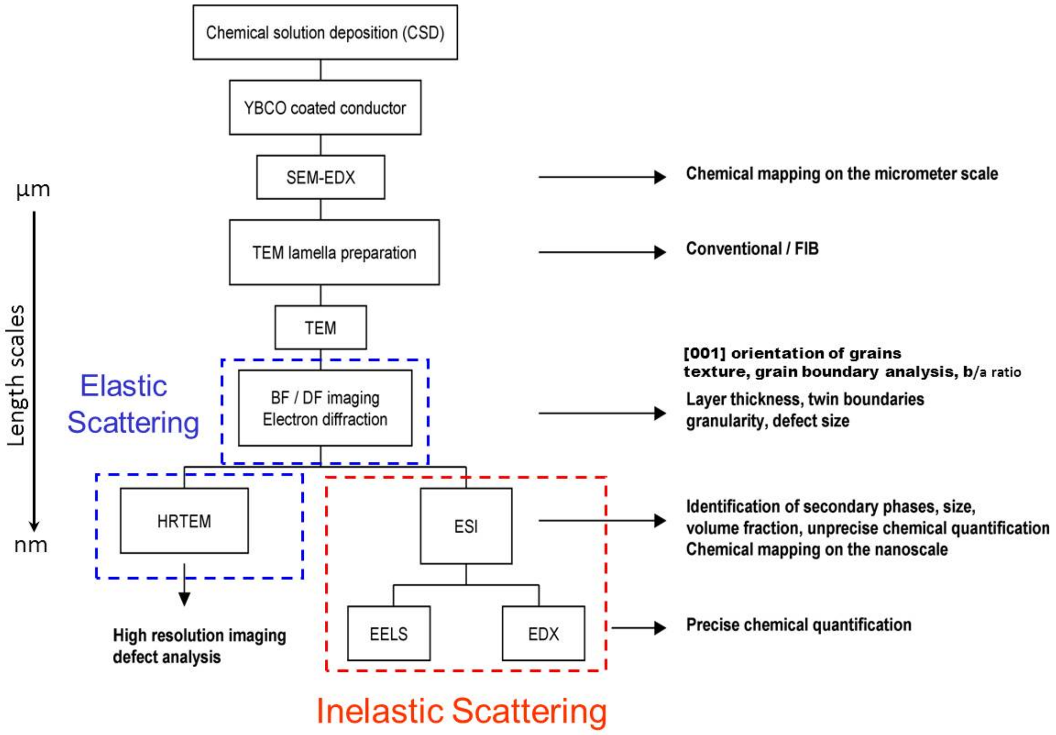

Figure 2.8: Methodology used for the characterization of YBCO coated conductors by electron microscopy.

2.3.1 Challenges of coated conductor TEM analysis

Among the mayor challenges for TEM studies of chemically deposited YBCO-coated conductors are:

1.) TEM lamellae preparation: The preparation of cross-sectional TEM lamellae of oxide thin films on flexible nickel tungsten substrates presented a mayor challenge for specimen preparation because of the high compresive misfit (7.6 %) between the LZO buffer layers and the substrate and the multi-phase nature of chemically prepared TFA-YBCO superconducting films. Two methods were established for preparing TEM cross-sectional samples of YBCO-coated conductor samples: (a) the first method relied on conventional grinding and polishing and (b) the second on the in-situ lift-out Focused Ion Beam (FIB) technique.

2.) Understanding the micro- and nanostructure of LZO buffer layer growth on flexible nickel tungsten substrates: Understanding the biaxial texture and grain growth process of the LZO buffer layers was relevant since the buffer layers act as diffusion barriers and transfer the biaxial texture to the superconducting layer, this has important implications for long-length scaled coated conductor technology.

Chemically deposited LZO buffer layers showed exciting structural features such as (i) biaxial texture on substrates with large misfit and atomically rough surfaces (ii) a high-density of small-angle grain boundaries yielding grain sizes in the buffer layer of 100 nm compared to 40 µm in the substrate (iii) nanoporosity and void formation and (iv) carbon content.

For investigating these features TEM was the method of choice. Conventional diffraction contrast imaging, which includes Moiré fringes analysis, gave insight into the small-angle grain boundary network in the LZO buffers and the biaxial texturing and grain tilting mechanisms. TEM is the only method to probe the voids since TEM is a volume sensitive technique. EDX in the TEM provided quantitative information on the carbon content after pyrolysis.

3.) Establishing a structure-property-chemistry correlation for superconducting TFA-YBCO films: (a) TFA-YBCO superconducting films showed distinct features: (i) a large number of secondary phases on various length scales, i.e. Y_2O_3, CuO and Ba-rich phases (ii) surface segregation of secondary phases relevant for multilayer deposition and (b) a large density of crystal defects which are relevant for pinning. The study of (i) intrinsic Y_2O_3 precipitates and (ii) extrinsic $BaZrO_3$ nanoinclusions by energy-filtered TEM was shown to be of importance.

2.3.2 Scanning electron microscopy (SEM)

In a scanning electron microscope (SEM), a focussed electron beam is scanned on points in a sample in an array manner and the response signal is then measured by a detector. Secondary electron images are formed by combining the array point to a 8-bit pixel grey value that is proportional to the magnitude of the response signal.

2.3.3 EDX spectroscopy and EDX chemical mapping using a SEM

EDX spectroscopy and EDX chemical mapping using a SEM characterization of YBCO coated conductors involves both EDX-spectroscopy and EDX-chemical mapping. For a reliable control of film thickness and homogeneity, a quick non-destructive quantification method with a high spatial resolution is neccessary and SEM-EDX is the method of choice. Micro-meter scaled defects and chemical secondary phases were quantitatively studied by EDX-chemical mapping. For EDX mapping of using a specific element the energy window has to be set to a particular X-ray line. The X-ray intensity detected in this window is used as a signal. The elemental map gives qualitative information on the spatial distribution of an element in the sample. For a quantitative study SEM-EDX spectroscopy is needed. The characteristic X-ray lines used for elemental mapping and EDX spectroscopy are given in Table 2.10.

X-ray line	Energy (eV)	Transition
$Ni - K\alpha_1$	7478,2	KLIII
$La - L\alpha_1$	4651,0	LIIIMV
$Ce - L\alpha_1$	4840,2	LIIIMV
$Zr - L\alpha_1$	2049,4	LIIIMV
$Cu - L\alpha_1$	8048,0	KLIII
$Ba - L\alpha_1$	4466,0	LIIIMV
$Y - L\alpha_1$	1922,0	LIIIMV
$O - K\alpha_1$	525,0	KLIII

Table 2.10: Characteristic X-ray lines used for SEM-EDX quantification and elemental mapping.

The scanning electron microscopes used were a Jeol 6500 F SEM and a Philips XL 30 both provided with a FEG, and SE-detector and Si(Li) EDX detectors from Oxford Instruments and EDAX. The accelerating voltage can be adjusted from 10 to 30 kV. For elemental mapping in a SEM various parameters are of importance (i) counts/sec (ii) acquisition time (iii) mapping size in pixels (iv) counts per peak (v) total counts and (vi) number of frames. Using INCA software [35] the possible mapping sizes [pixel] are 128 x 88, 256 x 176, 512 x 352 and 1024 x 704. The process time can be chosen from 6 different levels where 1 is the fastest mapping time and 6 the slowest. For choosing the process time, the sample drift and sample charging have to be taken into account. The size of the details that can be mapped are usually larger than 1 µm. For chemical mapping of smaller details electron spectrocopic imaging or STEM-EDX in a TEM are better options. The following equation allows to calculate the intensity (cts) per pixel for a specific elemental map:

$$\frac{I}{pixel} = \frac{\frac{cts}{sec} t \frac{Int.\,cts\,under\,the\,peak}{total\,cts\,per\,spectrum}}{M} \tag{2.80}$$

where t is the acquisition time and M is the total number of pixels in the image. An example is shown in table 2.11.

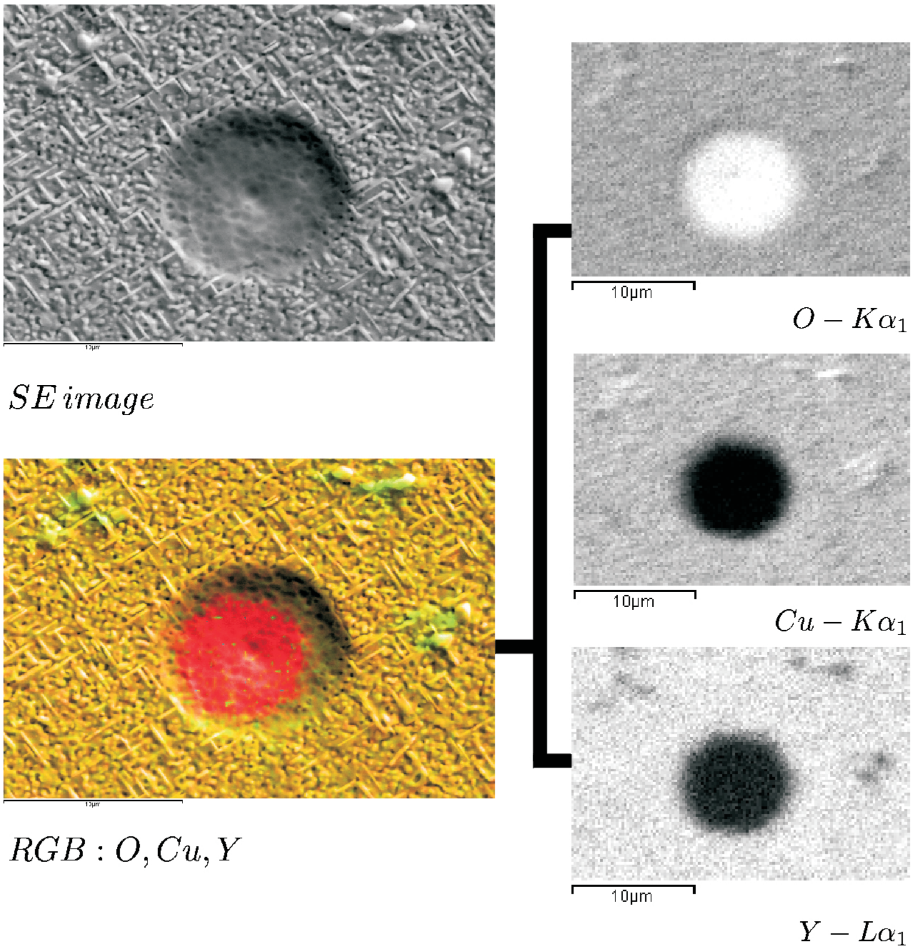

Figure 2.9: a) Secondary electron image of a YBCO/LAO sample b) RGB image and elemental maps: c) Cu-La1,2 d) Y-La1,2, e) O-Ka1 (All scale bars are 10 µm).

Parameters	$O - K\alpha_1$	$Cu - L\alpha_1$	$Y - L\alpha_1$
cts per peak	133316	55001	25861
Total cts	7093163	7093163	7093163
cts /sec	4000	4000	4000
Acq. time [sec]	3000	3000	3000
Number of pixels [256x176]	45056	45056	45056
cts / pixel	100.11	19.42	41.30

Table 2.11: Calculated values for SEM-EDX mapping of a YBCO/LAO sample.

Figure 2.9 is are the SE, RGB images and elemental maps of a YBCO/LAO test sample. Figure 2.10 is the corresponding histogram (grey value in function of pixel counts) of and and the concentration histogram (CHI). The intensity in CHI is proportional to the number of pixels with a combination of Cu-grey values and Y-grey values, this corresponds to the YBCO matrix. The crater is an oxygen rich area (red) as seen in the RGB image and corresponds to the LAO substrate. EDX point measurements confirmed Al and La content. Table 2.11 are the calculated parameters expected. Volume fractions of chemical phases can be determinated by quantitative phase analysis as described in [54].

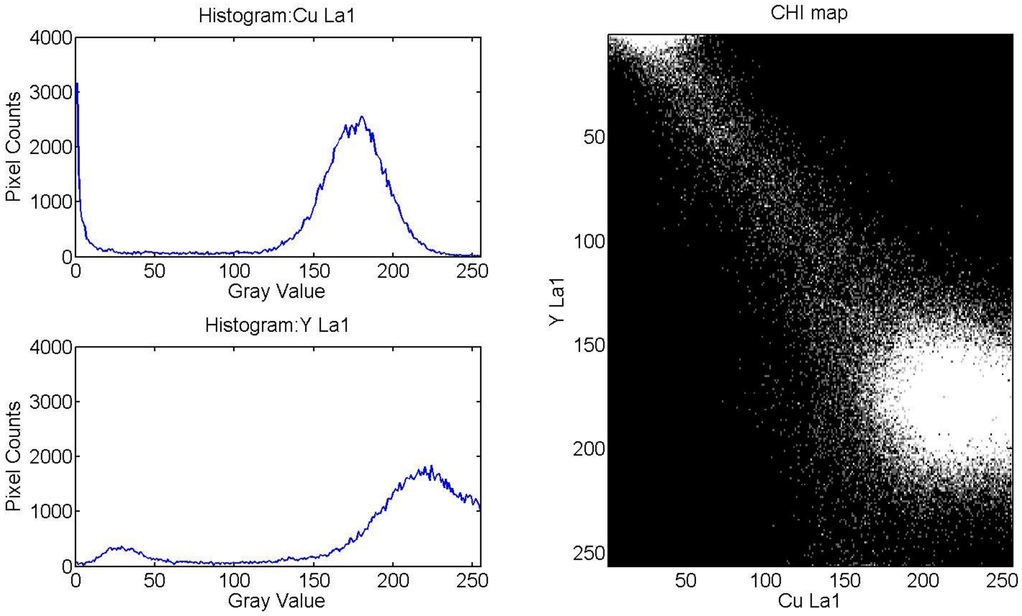

Figure 2.10: Histograms and CHI map of $Y - Ka_1$ and $Cu - La_1$.

2.3.4 Electron diffraction

Selected area electron diffraction patterns were acquired with a 290 mm camera length and allowed to study the crystallinity of the samples. The experimental inteplanar spacing d_{hkl} are given by:

$$d_{hkl}R_{hkl} = CL \cdot \lambda \tag{2.81}$$

Where CL is the camera length and λ is the wavelength of electrons with and energy of 120 keV.

In order to calculate interplanar spacings for YBCO we need to use the following lattice parameters: $a = 0.3817$ nm, $b = 0.3882$ nm and $c = 1.1671$ nm. d_{hkl} will be given by the following expression:

$$\frac{1}{d_{hkl}^2} = \frac{h^2}{a^2} + \frac{k^2}{b^2} + \frac{l^2}{c^2} \tag{2.82}$$

were hkl are the Miller-Bravais indices describing the lattice plane of interest. Shown already in table 2.3 are the interplanr spacings (d_{hkl}) and corresponding (hkl) planes for YBCO are given.

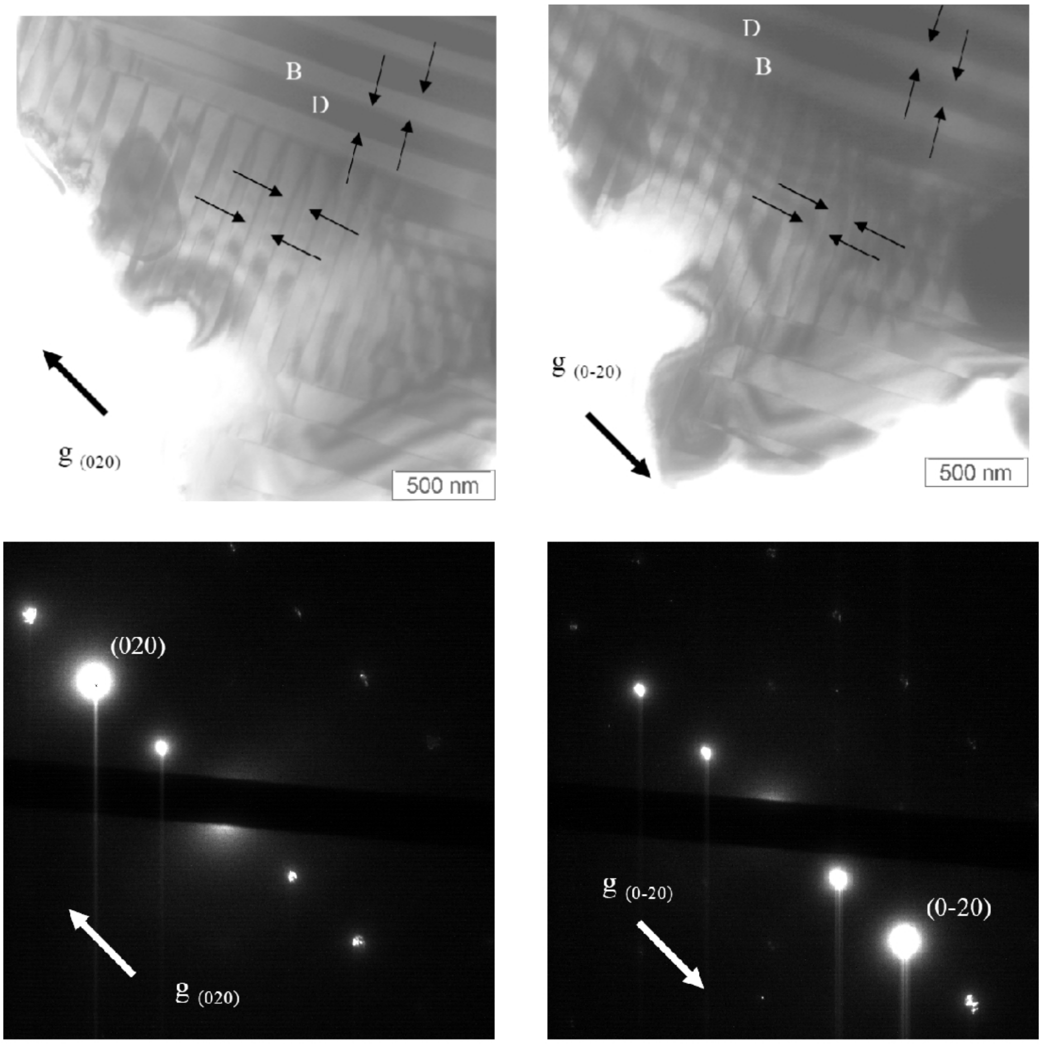

Figure 2.11: Bright-field imaging and electron diffraction of bulk YBCO using (020) and (0-20) reflections.

Figure 2.11 are examples bright-field images using the $g_{(020)}$ and $g_{(0-20)}$ reflections for YBCO. Twin boundaries are visible.

2.3.5 Energy-filtered transmission electron microscopy (EFTEM)

Shown in figure 2.12 (a) are the components of the Zeiss 912 omega transmission electron microscope (TEM) used for EELS and ESI. Figure 2.11 (b) is an schematic of the electron beam path emphasizing the omega energy filter which is the principal component of the EFTEM.

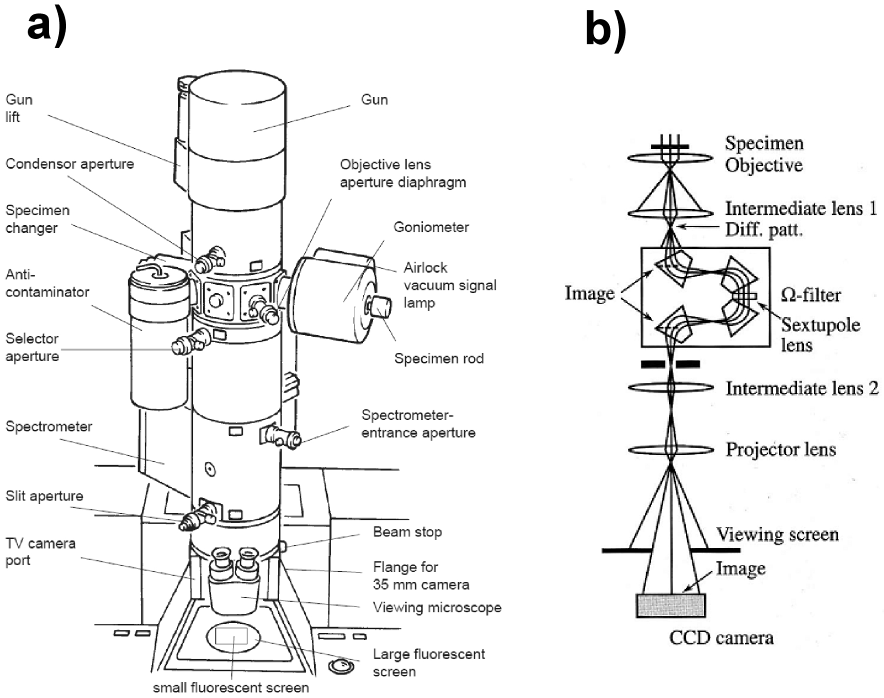

Figure 2.12: (a) Schema of the Zeiss Omega 912 TEM, (b) the electron beam path and the omega energy filter.

Electron energy-loss spectroscopy (EELS)

Electron energy-loss spectroscopy in the transmission electron microscope requires very thin sample areas. For EELS quantification a single scattering process in very thin sample area is assumed and is taken as a K-type absorption edge. For the quantification of a specific element of interest the following has to be taken into account (i) a probability of ionization (P_K) (ii) the ionization cross-section (σ_K) (iii) the number of atoms per unit area (N) (iv) the intensity of the edge of interest (I_K) (v) the collection angle (β) (vi) the energy slit (δ) (vii) the intensity of the whole spectrum (I_T) and the edge of interest (K).

The intensity of the edge of interest is given by:

$$I_k = P_K I_T \tag{2.83}$$

And the probability of ionization is:

$$P_K = N\sigma_k exp(t/\lambda_K) \tag{2.84}$$

The intensity of the edge of interest can be written as:

$$I_K \approx N\sigma_K I_T \tag{2.85}$$

Where the number of atoms per unit area is:

$$N = \frac{I_K}{\sigma_K I_T} \tag{2.86}$$

and the ionization cross-section is σ_k which can also be written as an interpreted cross-section $\sigma_K(\beta, \Delta)$, where β is the objective aperture angle and Δ is the size of the energy slit.

Relevant ionization edges for elements in YBCO and LZO and CeO_2 are given in table 2.12.

Element	Z	K	Edge (eV)								
		K	L 1	L 2	L 3	M 2	M 3	M 4	M 5	N 2,3	N 4,5
O	8	532	-	-	-	-	-	-	-	-	-
Cu	29	8979	1096	951	931	87	87				
Y	39	-	2373	2155	2080	300	300	160	160	36	-
Zr	40	-	2532	2307	2222	335	335	181	181	29	
Ba	56	-	-	-	-	-	-	796	781	-	93
La	57	-	-	-	-	-	-	849	832	-	99
Ce	58	-	-	-	-	-	-	902	884	-	110

Table 2.12: Relevant ionization edges for elements concerning CSD processed YBCO coated conductors

Acquisition conditions for EELS with the Zeiss 912 omega TEM

The acquisition conditions for electron energy-loss spectroscopy (EELS) using the Zeiss 912 omega TEM are given in table 2.13.

Spec.	Bias	Emision current (µA)	Spot size (nm)	Obj.aper. (mrad)	Spec.mag (x)	Acq. time	Time Int.
Low-Loss	8-9	2-3	10-20	3.5	19.5, 40, 63, 125	50-100 ms	yes
Core-Loss	9	4	100	8.1/13.5	19.5, 40, 63, 125	1-10 s	no
Wide-range	9	4	100	13.5	19.5, 40, 63, 125	1-10 s	no

Table 2.13: Acquisition conditions for EELS and parameters used for obtaining Low-Loss, Core-Loss and Wide-range spectra of YBCO samples.

Electron spectrocopic imaging (ESI)

Elemental maps: acquisition and the three window method

EELS has to be performed before EFTEM for a certain ionization edge in order to identify the available signal to noise (SNR) and signal to background (SBR) ratios. The signal to noise ratio (SNR) is especially important for electron spectroscopic imaging since the signal of interest is obtained by extrapolation. Energy filtered images are much more difficult to acquire than conventional TEM images. EFTEM imaging is limited by the SNR and the maximum magnification possible of the microscope used. Higher resolution means less accuracy.

Thus, signal optimization is important for obtaining low noise elemental maps. The SNR is given by [55]:

$$SNR = \frac{I_k}{\sqrt{I_k + hI_B}} \tag{2.87}$$

I_k is the net core-loss signal for an energy window of width Δ, h is a dimensionless parameter that accounts for statistical uncertainties associated with thhe background extrapolation and is taken as unity and I_B is the background signal intensity at the post-edge.

We used the three window technique for the background estimation of the ESI elemental maps [15]. For two energy windows below the ionization edge of interest the corresponding pixel signals were recorded. The background was calculated from two pre-edge images taken before the ionization edge and assuming power law dependencies of the from [55, 39, 56]:

$$Y_{B1} = AE_1^{-r} \tag{2.88}$$

$$Y_{B2} = AE_2^{-r} \tag{2.89}$$

See figure 2.13, A and r are fitting constants obtained from pre-edge 1 ($E1$) and pre-edge 2 ($E2$).

The fitting factor r is calculated by:

$$r = \left(\frac{log \frac{Y_{B1}}{Y_{B2}}}{log \frac{E_2}{E_1}} \right) \tag{2.90}$$

After background subtraction the remaining elemental map displays the spatial distribution of the element within the analyzed specimen area. The signal of interest is then given by [14]:

$$S_N = S(E_3) - AE_3^{-r} \tag{2.91}$$

Where E_3 is the energy loss of window number three.

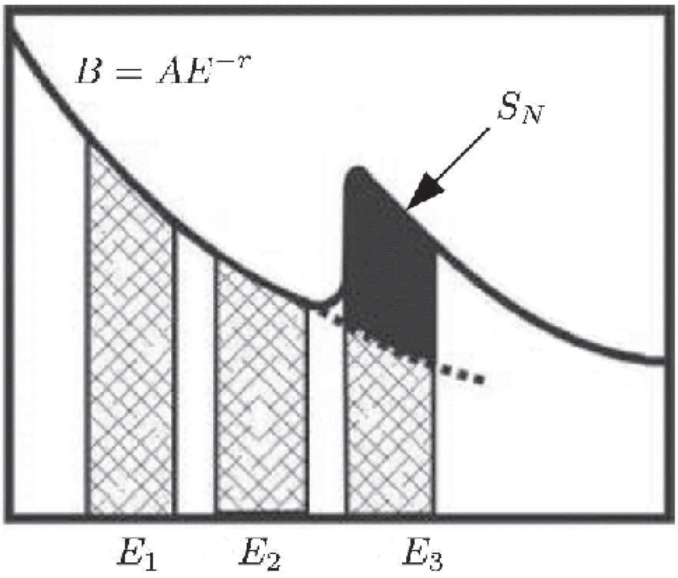

Figure 2.13: Schematic diagram of an energy loss spectra with a core loss edge.

The strategy followed for applying ESI with the three window method was to first optimize the acquisition conditions with respect to the intensity per pixel in the elemental maps. The microscope to our disposal was a Zeiss 912 TEM operating at 120 kV equipped with omega energy-filter and a LaB_6 thermal emitter limiting the possible lateral resolution due to noise in the images.

2.3.6 Energy-dispersive micro-analysis in the TEM (TEM-EDX)

EDX in the TEM allows for specific element quantification through point measurements and is a relatively straight foreward to use method in comparision to EELS. EDX in combination with other spectroscopic methods are essential for identifying secondary phases in YBCO. The TEM used was a Zeiss 912 omega provided with a Si(Li) EDX detector from Oxford instruments provided with INCA software. For EDX quantification in the TEM, the Cliff-Lorimer equation of interest [57]:

$$\frac{C_A}{C_B} = K_{A-B}\frac{I_A}{I_B} \tag{2.92}$$

Where C_A and C_B are the weight procent of elements A and B, I_A and I_B are the above background characteristic intensities, which we can measured. It is assume that the sample is thin enough so that absorption or fluorescence can be ignored. The weight percents can be related to the measured intensities by the Cliff-Lorimer equation, is the Cliff-Lorimer factor, which depends on the EDX system and the acceleration voltage of the TEM used. The factor can be calculated by:

$$K_{A-B} = \frac{Q_B w_B a_B \varepsilon_A}{Q_B W_A a_A \varepsilon_B} \tag{2.93}$$

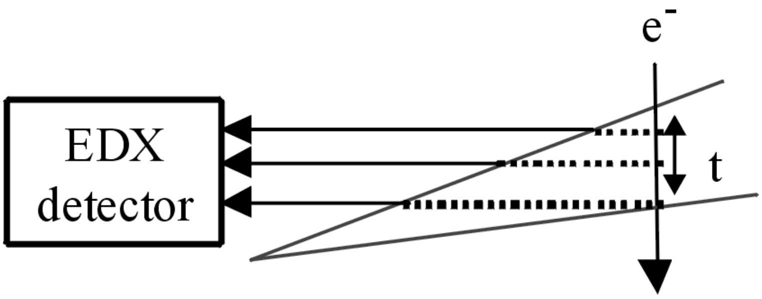

Figure 2.14: EDX in the TEM.

Where Q is the ionization cross-section, w the fluorescence yield of the characteristic X-rays, a is the relative probability for a transition $K\alpha$ and ε is the detector efficiency for characteristic X-ray of elements A and B. Figure 2.14 is the geometry used for TEM-EDX on a wedge shaped sample prepared by conventional mechanical polishing and ion beam milling. The EDX detector is tilted 45° to the specimen, t is the sample thickness.

2.3.7 TEM specimen preparation

Conventional method

TEM specimens were prepared from coated conductor samples by conventional polishing and ion etching. TEM plan-view and cross-sections were preparation procedures are shown in figure 2.15 and 2.16 respectively. Samples were ion milled from the substrate side only for plan-view preparation and from both side in the case of cross-sections.

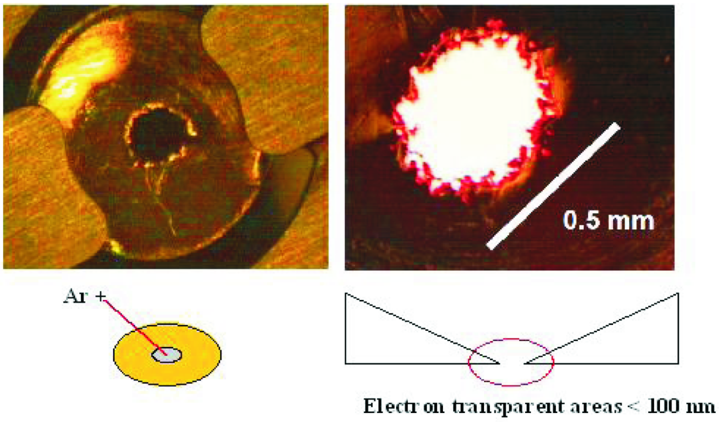

Figure 2.15: Conventional TEM cross-section sample preparation.

The samples were mechanically thinned from the substrate side only using diamond foils of decreasing grain size (from 30 µm to 1 µm) until reaching a thickness of 25 µm. Further thinning up to 100 nm thickness was done by using a BALTEC RES 100 ion etching machine. Typical etching values were 4.5 kV and 3.5 mA and angles of 12° and a final polishing stage at 6°. This why wedge shaped samples are obtained and regions near the hole are thin enough for TEM ($<$100 nm).

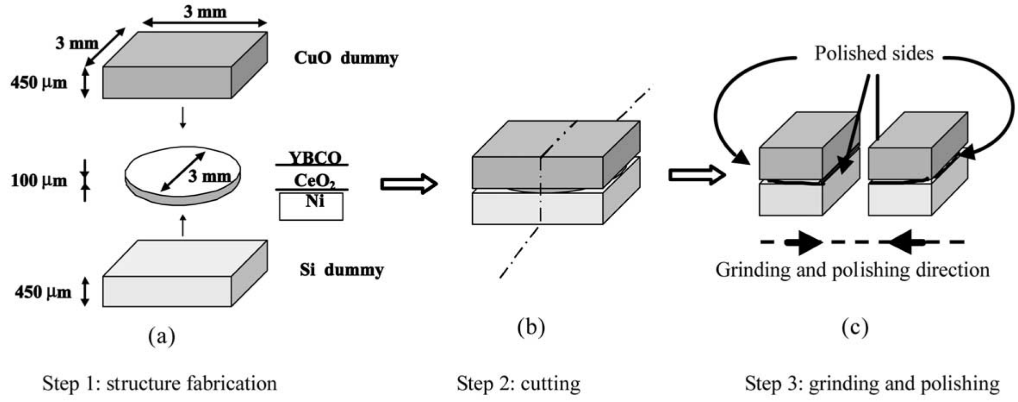

Figure 2.16: Conventional TEM cross-section sample preparation.

Focused Ion Beam (FIB)

The FIB is commonly used to prepare samples for the transmission electron microscope [58, 59]. The TEM requires very thin samples, typically less than 100 nanometers. Other techniques, such as ion milling or electropolishing can be used to prepare such thin samples. The FIB used was a Zeiss Crossbeam 1540 XB FIB, which is a two-beam machine. It has an electron beam and a ion beam, which allows to simultaneously observe and work on a specific sample region, the nanometer-scale resolution of the FIB allows the exact thin region to be chosen. The drawback to FIB sample preparation is surface damage and ion implantation, which produces noticeable effects when using techniques such as high-resolution TEM (HRTEM) or electron energy-loss spectroscopy (EELS). The layer damaging can be minimized by FIB milling with lower voltages, or by further milling with a low voltage argon ion beam after completion of the FIB process.

Figure 2.17 shows the beam geometry used. The adjustment of the FIB machine includes (i) eucentric point adjustment of both Z-height 1 (SEM FE-Gun) and and Z-height 2 (FIB (Ga+)) beams. (ii) Pt protection layer deposition on the zone of interest (100 pA) using W Pt gas (iii) trapezoid selected area (1nA, 500 pA) for step cuts. (iv) clean cut using a Ga+ source at 5 kV (v) Final side cuts (vi) in-situ lift out of the sample using the nano-manipulator.

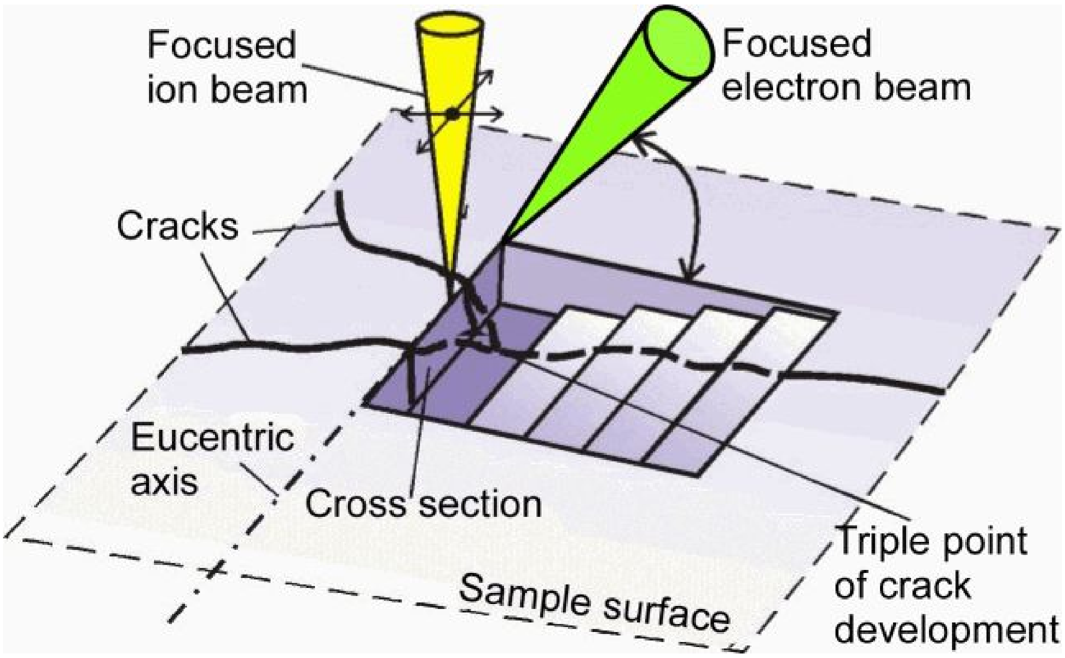

Figure 2.17: Focused Ion Beam (FIB)

Figure 6.4 (page 107) shows a dark-field TEM image of a fully CSD processed YBCO coated conductor sample in cross-section. The different layers of YBCO coated conductors can be clearly identified. By this method (FIB) large thin electron transparent areas of a few microns ($> 4\mu m$) could be obtained.

Chapter 3

Chemically deposited LZO buffer layers for YBCO coated conductors: film growth and microstructure

3.1 Introduction

An adequate buffer layer architecture is of great importance for$YBa_2Cu_3O_{7-\delta}$ (YBCO) coated conductor fabrication. We present a transmission electron microscopy (TEM) analysis of $La_2Zr_2O_7$ (LZO) buffer layers on biaxially textured Ni-5at.%W substrates for YBCO-coated conductors prepared by chemical solution deposition (CSD). The LZO thin films were heat-treated at 900°C and 1050°C, respectively. Electron diffraction patterns, bright and dark-field images were used to determine the micro-structure, texture and the nanoporosity of the films. By X-ray diffraction the films were found to be [100] oriented and strongly biaxially textured. Although X-ray diffraction suggests an epitaxial growth of LZO on Ni it was shown by TEM that this was not the case.

The grain size of the films is between 100-300 nm and therefore much smaller than the Ni grain size of 40 µm. Appropriate acquisition conditions for SEM and TEM imaging are given to identify the nanogranularity of the films. For the film annealed at 1050°C high-resolution SEM images clearly show a poly-crystalline LZO micro-structure and the grain size can readily be determined. Electron diffraction rings are more pronounced than for the film annealed at 900°C indicating a higher level of polycrystallinity in the film. SEM images of the film annealed at 900°C yield no evidence of a polycrystalline micro-structure; only single misoriented LZO grains separated by 500 nm are observed. Nanovoids 10-40 nm in size were found in the LZO buffer layers with a high density. The voids had approximately cuboid shape indicating an anisotropy of the surface energy in LZO. The surface planes of the voids were identified as {111} lattice planes. Despite the nanoporosity, which is a typical feature of CSD grown buffer layers, the LZO buffer layers act as efficient Ni diffusion barriers. Energy dispersive X-ray microanalysis (EDX) in the transmission electron microscope yielded the composition of the films no Ni-rich secondary phases were detected and significant C contamination occurred during spectrum acquisition.

Since high critical current carrying conductors are needed for applications using YBCO coated conductors, so called second generation conductors are prepared by thin film deposition techniques on metallic substrates [2]. A coated conductor consists of a metallic substrate tape, in most cases a Ni-alloy, coated with one or more buffer layers and a superconducting layer on top in such a way as to obtain both in-plane and out-of plane texturing of the grains. Thereby a biaxial texture of the YBCO layer insures high superconducting transport currents due to small-angle grain boundaries that act as strong links [60].

The buffer layers behave as diffusion barriers and transfer the texture from the biaxially textured metallic Ni-alloy substrate to the YBCO film. Coated conductor technology relies on the development of low-cost preparation methods especially towards the production of long lengths. This has proven to be a great challenge, since one of the desirable properties of the tapes for applications, notably magnet winding, is that they are mechanically flexible. At present, next to physical deposition methods such as Ion Beam Assisted Deposition (IBAD)[61], Rolling Assisted Biaxially Textured Substrates (RaBiTS) [19], and Inclined Substrate Deposition (ISD)[62] cost efficient chemical deposition routes within the chemical solution deposition (CSD) method are investigated [29]. CSD can be applied to grow both buffer and superconducting layers, allowing a control of the stoichiometry in the precursor solution, modification of the composition and the possibility to coat large areas [63, 23].

Over the years various materials have been investigated as buffer layers deposited on Ni substrates, most extensively cerium oxide (CeO_2) and yttria-stabilized zirconia (YSZ) [61]. $La_2Zr_2O_7$ has more recently been used as a buffer layer material due to its structural compatibility with YBCO and its biaxial growth on Ni-W substrates [64]. The crystal structure of LZO is cubic pyrochlore space group Fd3m with a lattice parameter a = 10.79 Å. Considering a 45° rotated growth of LZO on Ni the pseudocubic lattice parameter or matching distance is a_m = 3.81 Å, resulting in a lattice mismatch to Ni (cubic, a = 3.52 Å) of 7.6 %, nonetheless leading to biaxially textured growth on Ni-W [63]. Two of the lattice parameters of orthorhombic $YBa_2Cu_3O_{7-\delta}$ are a = 3.83 Å and b = 3.88 Å, when compared to the lattice parameter of LZO this yields only a small lattice mismatch of 0.5% and 1.8 % respectively.

Transmission electron microscopy plan-view and cross-section analysis of CSD grown $La_2Zr_2O_7$ buffer layers on flexible Ni-5at.%W substrates are summarized in this paper to investigate the microstructure of CSD buffer layers grown on Ni-5at.%W substrates. The small number of investigations in the literature can be attributed to the difficult and challenging TEM sample preparation of these thin coated metallic samples, which has been eased by the development of a simple preparation technique by Eyidi and Eibl [65]. TEM investigations provide detailed information that is essential for the understanding of the growth and microstructure of CSD prepared buffer layers and their Ni-W substrates, such as layer thickness, texture, roughness of the boundary surface, grain boundaries, nanovoids, dislocation density in the substrate, elastic strain, cracks, secondary phases and reaction layers.

3.2 Experimental details

Two types of CSD grown buffer layers on biaxially textured Ni-5at.%W tapes (evico) were studied in this work, see table 3.1. Samples were prepared by depositing the buffer layers by chemical solution deposition on Ni-5at.%W substrates, but using different concentrations for the precursor solutions of LZO. Also the heat treatment of the samples was done at different temperatures. Sample 1 was a double coated LZO buffer layer on a Ni-5at.%W substrate annealed at T = 900°C and sample 2 consisted of a single coated LZO buffer layer with a thin CeO_2 buffer layer on top and was annealed at 1050°C.

These temperatures were chosen because LZO formation (nucleation) starts at T > 850°C [23] and therefore the film properties were studied for different annealing temperatures. T = 900°C was choosen because this was the lowest annealing temperature at which the layers showed a very good biaxial texture (low full-width-at-half maximum (FWHM) values in-plane and out-of-plane), a smooth surface

	Substrate	Buffer layer architecture (nominal thicknesses)	Heat-treatment Temperature [°C]
sample 1	$Ni-5at\%W$	2 X LZO (160 nm)	900
sample 2	$Ni-5at\%W$	1 X LZO(280 nm)/CeO_2 (70 nm)	1050

Table 3.1: Description of the samples investigated in this section.

structure with RMS roughness values about 2 nm (1µm x 1µm scan size with atomic force microscopy (AFM) [66]. At lower temperatures, e.g. 800°C, the FWHM values were higher. At higher temperatures, the roughness increased.

3.2.1 Preparation of $La_2Zr_2O_7$ buffer layers on biaxially textured Ni-5at%W substrates

Cube textured Ni-5at%W substrates with the dimensions of 80 µm in thickness and 1 cm width were used as substrates. Details of the substrate preparation were reported in [27, 67]. The recrystallized substrates were cleaned in both an ultrasonic acetone and a isopropanole bath for 20 minutes.

In order to obtain the coatings for the double coated LZO buffer layer sample (sample 1) the dip coating method was applied at room temperature. The Ni-5at.% W substrates were dipped into the precursor solution, held immersed for 30 s and withdrawn with a speed of 0.3 cm/s. The solution preparation for the precursor solution to obtain the double coated LZO buffer layer sample was described in detail previously [63]. The concentration of the solution was adjusted to c(La^{3+}) = c(Zr^{4+}) = 0.4 mol l^{-1}. Coating was directly followed by an annealing step in a quartz tube furnace at a maximum temperature of 900°C. To increase the film thickness the coating and annealing step was repeated once. Double coating was done to avoid cracking and to improve Ni diffusion barrier quality.

A similar preparation procedure was used to prepare the single coated LZO buffer layer sample with an additional CeO_2 buffer layer (sample 2) except that the concentration of the LZO solution was adjusted to c(La^{3+}) = c(Zr^{4+}) = 0.6 moll^{-1} and a maximum Temperature of T = 1050°C was used. The CeO_2 cap layer was deposited by dip coating. The concentration of the precursor solution was adjusted to c = 0.1 mol $l^{-1}$and a withdrawal speed of v =0.2 cm s^{-1} was applied. Details of the precursor solution preparation process can be found in [68].

TEM cross-section and plan-view sample preparation of $La_2Zr_2O_7$ buffer layers

A reliable method for preparing TEM cross-sectional samples of LZO buffer layers on Ni substrates has been established. The relatively short preparation time, the simple equipment used and the large electron transparent areas obtained make this procedure particularly appropriate for the preparation of TEM cross-section samples of LZO buffer layers.

The TEM cross-section samples investigated in this work were prepared by gluing the sample of interest between barium titanate and silicon dummies followed by mechanical polishing and conventional ion beam milling in order to obtain electron transparent sample areas of less than 100 nm in thickness. Details of TEM cross-section sample preparation methods and ion beam milling techniques are found in [65]. TEM cross-section samples were thinned using Ar^+ ions in a Baltec Res 100 rapid ion beam milling machine operated at 4.5 kV and 3.5mA with an angle of ± 6° for 40 h. TEM plan-view samples were obtained by mechanical grinding and polishing from the substrate side down to 20 µm and ion beam milling at 4.5 kV and 3.5 mA with an angle of 12° for up to 25 h.

All samples were investigated using a Phillips Field Emission (FE) XL 30 scanning electron microscope (SEM) working at 10 kV and an emission current of 174 µA provided with an energy dispersive X-ray (EDX) detector and a Zeiss Leo 912 Ω energy filter transmission electron microscope (TEM) operating at 120 kV and provided with an energy dispersive x-ray detector (EDX). Spectra obtained by the EDX detector mounted on the Zeiss 912 Ω TEM were analysed using the INCA 4.01 software package from Oxford Instruments [69]. All TEM EDX spectra were acquired under following acquisition conditions: spot size of 20 nm, 100 s measurement time, 20° tilting angle of the specimen towards the detector and an energy range of 0-20 keV in the EDX spectrum.

3.3 Results

3.3.1 LZO buffer layer annealed at 900°C

SEM analysis of sample 1 revealed a homogenous and crack free surface as shown by the secondary electron images in Figure 3.1. The surface topography of the LZO buffer layer reflects the surface topography of the Ni substrate. Due to grain boundary grooving the position of grain boundaries of the Ni substrate can still be identified on the surface of the LZO layer. Figure 3.1 (a)-(c) show secondary electron images of the LZO surface at different magnifications: in figure 3.1 (b) the position of the Ni grain boundaries of the underlying substrate are identified at low magnification. At higher magnification as seen in figure 3.1 (c), the microstructure of the LZO film can be imaged and the grain size is between 100-200 nm as denoted by the areas enclosed by circles.

Figure 3.2 presents pole figures of (a) Ni (111) and (b) LZO (222) reflections of the double coated LZO buffer layer annealed at T = 900°C. The LZO pole figure is rotated by 45° with respect to the underlying Ni tape due to an improved lattice match in this orientation between LZO and Ni and the mismatch in this orientation yields 7.6 %. The LZO buffer layer shows very good in-plane alignment on Ni with full-width-at-half-maximum (FWHM) values of 6.7° for LZO (222) and 6.2° for Ni (111) [7].

Figures 3.3 (a) shows a TEM bright-field image of sample 1 in plan-view. The contrast changes according to specimen thickness. In the bright areas nanovoids can be identified. Figure 3.3 (b) shows an insert of figure 3.3 (a), the size of the nanovoids is about 10–20 nm. Figure 3.3 (c) is the corresponding electron diffraction pattern under almost two-beam conditions of the area shown in figure 3 (a). The selected area diffraction aperture (SAD) had a diameter of 760 nm and the (222) and (444) reflection of LZO can be identified.

Figure 3.3 (d) is an intensity line scan of the nanovoid shown in figure 3 (b) denoted by the vertical white line, also denoted in figure 3 (a) by the black arrow. The strong contrast of the nanovoids is due to diffraction contrast close to two-beam diffraction conditions.

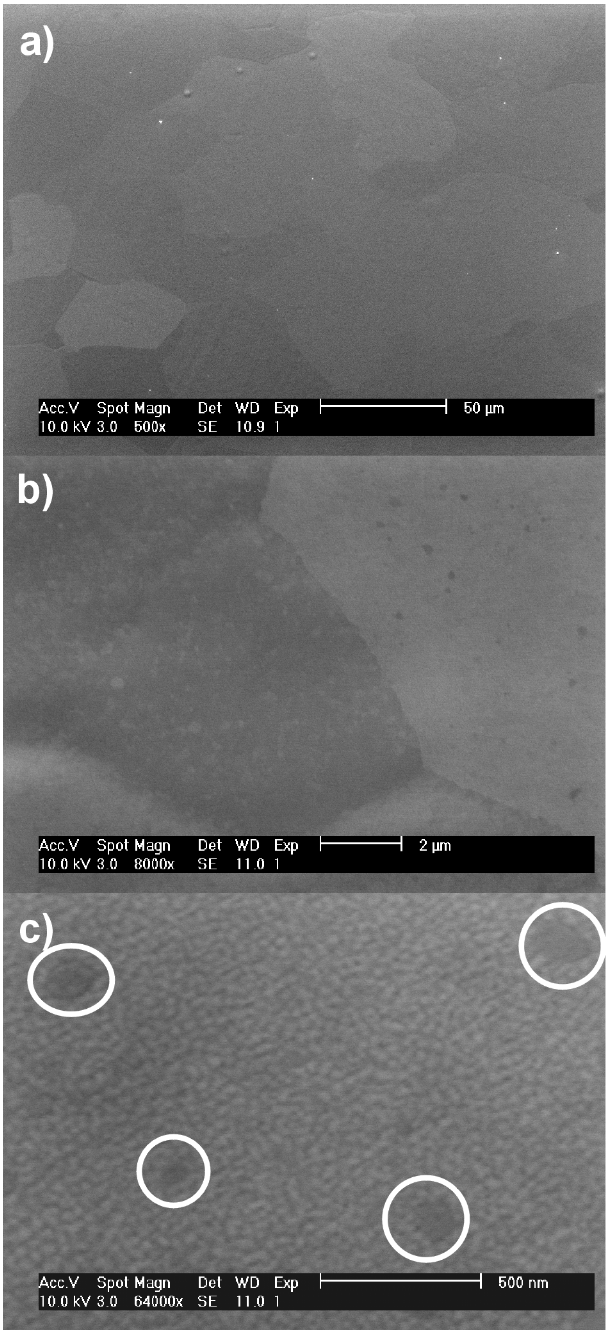

Figure 3.1: SEM secondary electron images of the LZO buffer layer annealed at T=900°C: (a) overview, (b) the underlying Ni grain boundaries are transferred as roughness in the LZO buffre layer. (c) Higher magnification image in which misoriented LZO grains are visible.

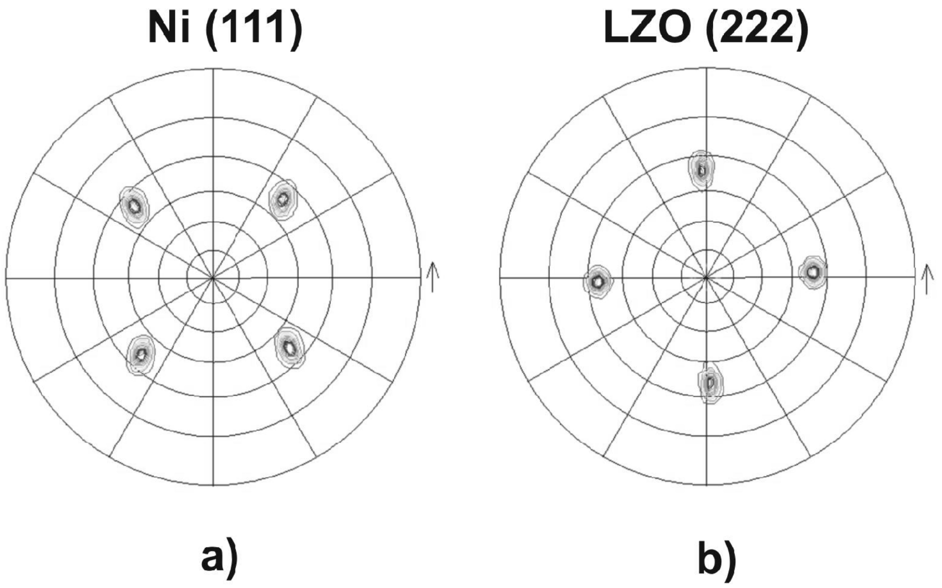

Figure 3.2: X-ray pole figures (Cu Kα) of (a) Ni (111) and (b) LZO (222) reflections of an LZO buffer layer annealed at T = 900 °C.

Figure 3.4 (a) shows an area of sample 1 where individual LZO grains of 100-200 nm in size can be seen. Figure 3.4 (b) is the corresponding electron diffraction pattern using an illumination of 2 µm (diameter) where the (222), (440) and (444) reflection of LZO can be indexed. A diffraction ring corresponding to the (222) reflection is observed. Figures 3.4 (c) is a TEM bright-field image of a single LZO grain at higher magnification. Figure 3.4 (d) is the corresponding dark-field image of figure 3.4 (c). The strong contrast within grains is due to nanoporosity, individual voids are seen and are 10 nm in size. The LZO films were also imaged by high-magnification SEM.

Using diffraction contrast LZO grains were imaged. Shown in figures 3.5 (a) to 3.5 (f) are bright-field images and corresponding electron diffraction patterns taken at following tilt positions: θ=0°, -1.3° and -2.6° and with an automatic illumination aperture selection (AIS) of 2 µm. The (440) and (222) reflexes of LZO can be indexed and ring like reflections can be observed.

Figure 3.6 (a) is a TEM bright-field image of sample 1 in cross-section. Two layers of LZO separated by a thin porous layer (white arrow no.2) are observed. Both layers, the upper and the layer close to the Ni substrate had a thickness of ~160 nm.

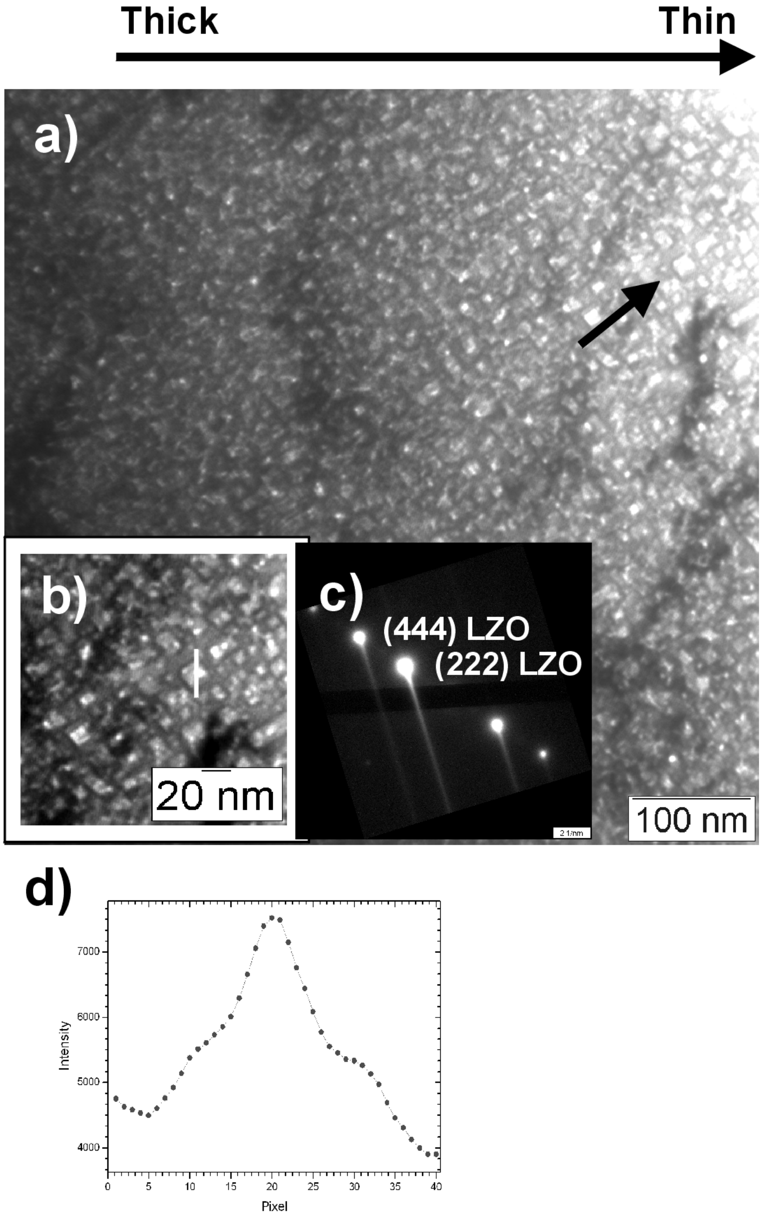

Figure 3.3: a) TEM plan-view bright-field image of sample 1 in plan view. b) Insert of figure 3 (a) where nanovoids are visible. c) Corresponding electron diffraction pattern of the area shown in figure 3 (a). d) Line scan of the nanovoid shown in figure 3 (b).

Figure 3.6 (b) shows the electron diffraction pattern under two beam conditions for the LZO buffer layer area shown in 3.3 (a). The (200) reflection of Ni and the (400) of LZO are indexed. The interface between the LZO buffer layer and the nickel substrate is clearly identified as seen in figures a and c (white arrow no.1). Nanovoids, 10-20 nm in size (diameter) are found and they appear to be distributed homogeneously throughout the sample.

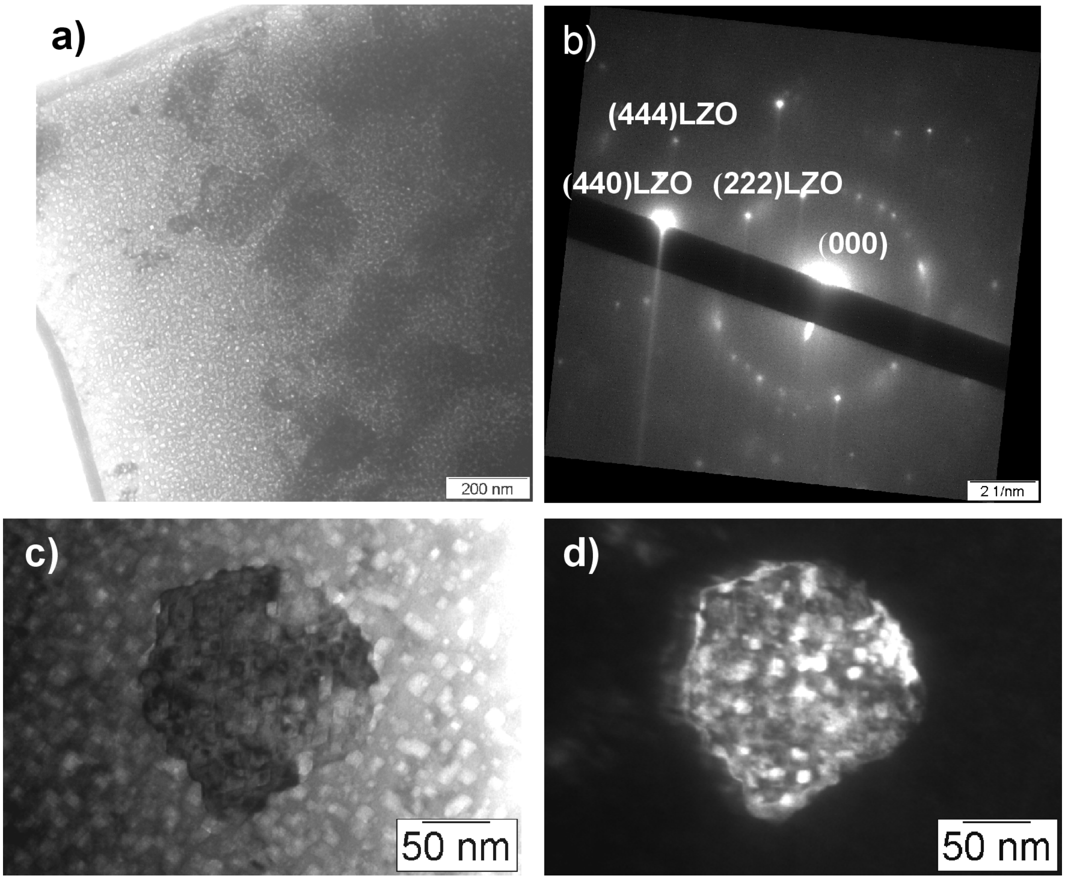

Figure 3.4: a) TEM bright-field image of sample 1 in plan view. b) Corresponding electron diffraction pattern. c) Corresponding dark-field image. d) Higher magnification TEM bright-field image.

Figure 3.6 (c) shows a TEM cross-sectional energy-filtered image of sample 1 using electrons with an energy-loss of 13 eV. A large density of nanovoids with a size of 10-20 nm are observed and they have a rectangular shape, which is surprising. The surfaces confining a void are bound to crystallographic planes, presumably of {111} type, due to the anisotropy of the surface energy in this material. Note that [111] planes are close packed planes in this structure. These voids are not identified in SEM images. Dark regions in the Ni substrate (figure 6 (c)) are due to diffraction contrast of strain fields of dislocations.

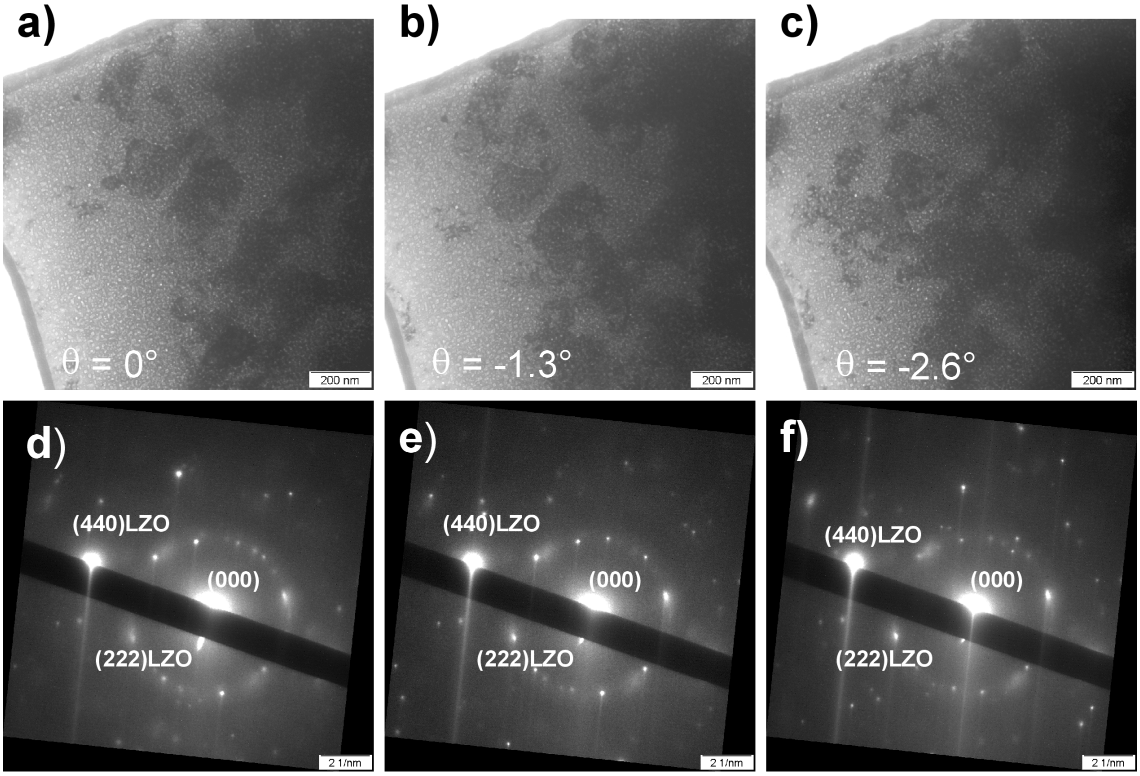

Figure 3.5: (a)-(c) TEM bright-field images of sample 1 in plan-view for different tilt angles. Figures (d)-(f) are the corresponding electron diffraction patterns. Note the diffraction rings present in (d)-(f).

3.3.2 The single coated LZO buffer layer sample annealed at 1050°C

Figures 3.7 (a) presents a SEM secondary electron image of sample 2. Seen in the image is a typical grain boundary network originating from the Ni substrate. Figure 3.7 (b) is an insert of an area of figure 3.7 (a). Figure 3.7 (c) is an area from figure 3.7 (b) where LZO grains with average grain size of 200-300 nm (diameter) can be seen. Similar pole figures as for sample 1 were also obtained for sample 2 as seen in figure 3.8.

The LZO pole figure is rotated by 45° with respect to the underlying Ni tape due to an improved lattice match in this orientation between LZO and Ni. The LZO buffer layer shows a good in-plane alignment on Ni with full-width-at-half-maximum (FWHM) values of 5.4° for Ni (111) and 5.5° for LZO (222). Detailed information on X-ray measurements of LZO and LZO/CeO_2 buffer layers is described in [68].

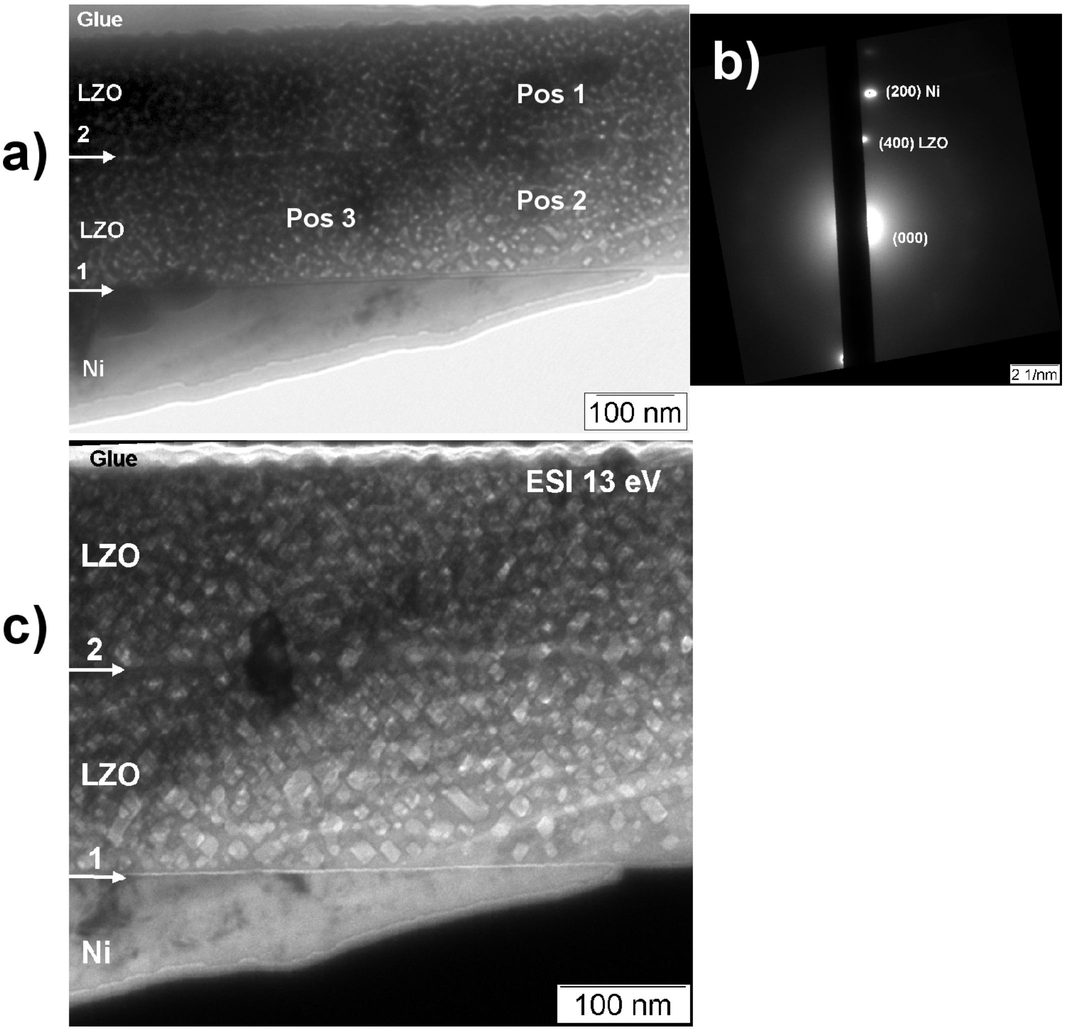

Figure 3.6: a) TEM bright-field images of sample 1 in plan-view. b) Corresponding electron diffraction pattern. c) Corresponding dark-field image. d) Energy-filtered image (ESI) taken at an energy-loss of 13 eV.

Figure 3.9 (a) and (b) shows a TEM plan-view bright field image of sample 2 where LZO grains and nanovoids are visible. Figure 3.9 (c) is the corresponding electron diffraction pattern of the area shown in figure 3.9 (a) taken with a selected area diffraction aperture (SAD) of 760 nm. Diffraction rings corresponding to LZO (222) and LZO (400) type reflections are observed. Figures 3.9 (d) is a bright-field image of a LZO grain. Figure 3.9 (e) is the corresponding dark-field image. This confirms that LZO grain size is 200-300 nm.

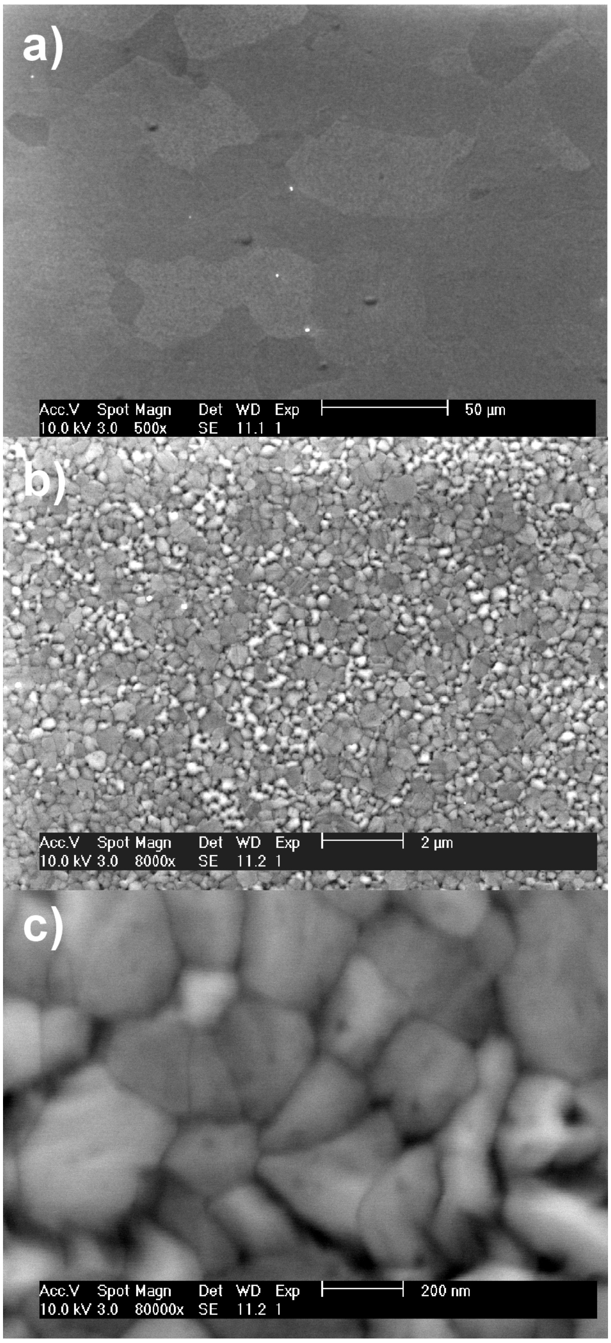

Figure 3.7: a) SEM secondary electron image of the LZO buffer layer annealed at T = 1050°C. b) Insert of an area of figure 6 (a) at a magnification of 8000. c) Insert of an area of figure 6 (b) at a magnification of 80,000.

Figure 3.10 (a) is a TEM bright-field image of sample 2 in cross-section. Nanovoids are found with a size of 30-40 nm (diameter). Figure 3.10 (b) is the corresponding diffraction pattern of the LZO buffer layer region taken with a SAD aperture of 760 nm under almost two-beam conditions. The (200) reflection of LZO is indexed. Figure 3.10 (c) is the corresponding dark-field image. This sample was dip-coated once and the LZO buffer layer thickness was found to be 350 nm. The CeO2 buffer layer could not be identified on top of the LZO layer. Figure 3.10 (d) is a TEM energy filtered image taken at an energy-loss of 30eV of the same area shown previously in 3.10 (a) and 3.10 (c). Nanovoids of 30-40 nm can be clearly identified and despite the increase in size a preferred 45° orientation with respect to the nickel substrate interface can still be observed. Figure 11 shows a series of bright-field images of the interface area for the untilted and tilted sample. In the LZO buffer layer in figure 3.10 (a) nanovoids can be identified in the untilted position, however, when tilted by 18°, nanovoids are hardly observable (See figure 3.11 (a)). This is due to the rectangular or cuboid shape of the nanovoids.

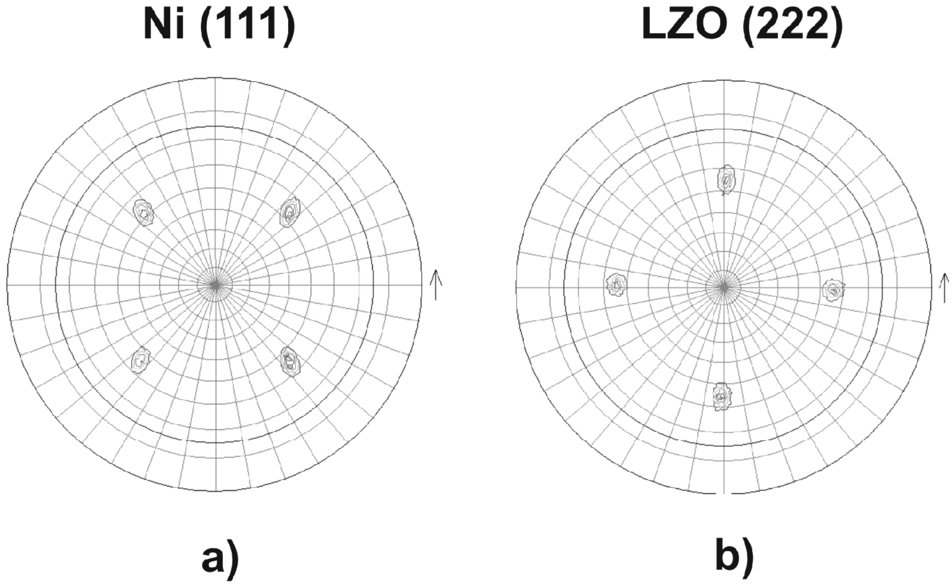

Figure 3.8: X-ray pole figures (CuKα) of (a) Ni (111) and (b) LZO(222) of an LZO buffer layer annealed at T = 1050 °C.

3.3.3 Quantitative chemical analysis of the buffer layers

Energy dispersive x-ray microanalysis (EDX) yielded the chemical composition of the LZO buffer layers. Figure 3.12 (a) is a EDX spectrum from position 1 (Pos1) in sample 1 of figure 3.5 (a). The EDX spectra shown in Figure 3.12 (b) corresponds to position 1 (Pos 1) shown in figure 3.9 (a) of sample 2.

Table 3.2 shows the results of a quantitative EDX analysis of the investigated sample areas (Pos 1-3) shown in figures 3.6 (a) and 10 (a) of sample 1 and 2. These results confirm approximately the mole fraction of La:Zr 1 : 1 of the $La_2Zr_2O_7$ compound. The values shown in table 2 take into account the standard deviation (SD) for each measurement. No Ni peak was found in the EDX analysis of both LZO buffer layer samples at Pos 1-3.

3.4 Discussion

3.4.1 TEM analysis of LZO buffer layers

TEM analysis of biaxially textured LZO buffer layers was performed by diffraction contrast and requires special attention with respect to the acquisition conditions. Two microstructural features of the films are of special interest, i.e.,

i) grain size and biaxial texture

ii) nano-porosity

Sample	Sample 1		Sample 2	
	900 [°C]		1050 [°C]	
Atom %	La	Zr	La	Zr
Position 1	52.62 ± 1.2	47.38 ± 1.3	51.50 ± 1.2	48.50 ± 1.1
Position 2	51.68 ± 1.2	48.32 ± 1.3	46.83 ± 1.1	53.17 ± 1.1
Position 3	54.03 ± 1.1	45.97 ± 1.2	55.44 ± 1.3	44.56 ± 1.1

Table 3.2: Results of the EDX quantitative analysis performed on sample 1 and 2.

In these films it is difficult to determine the grain size unambiguously, particularly for sample 1. In this sample small-angle grain boundaries do exist and the misorientation of adjacent grains on the sub-µm scale is small. The diffraction contrast is sensitive to even slight misorientation of adjacent grains, but yields significant contrast only, if strong diffracting conditions are established among the grains of interest.If this is not the case only poor contrast (no contrast) between the grains is observed. Bright-field images of the same area were acquired at different sample tilts along with electron diffraction patterns with varying illumination areas to study the sub-µm texture.

The strong contrast of the voids is best observed in two-beam images, in which the intensity of the transmitted and diffracted beams oscillate with the extinction distance in the sample [70]. The sample thickness is about 100 nm, the nanovoid size 10-40 nm and the extinction distance is about 30 nm for dynamic electron diffraction in LZO.

Because the void size is of the order of the extinction length, a strong contrast is found in the images. TEM is the only method that is able to detect the voids, since TEM is probing the volume of the sample. AFM or SEM probe the surface and, therefore, only the effect of the nanovoids on the surface roughness can be imaged. Nanovoids of a few nm in size, but less dense, were previously observed in CeO2 thin films deposited on biaxially textured nickel substrates by PVD methods [71] and on metal organic deposition (MOD) prepared LZO films on Ni-W substrates [72].

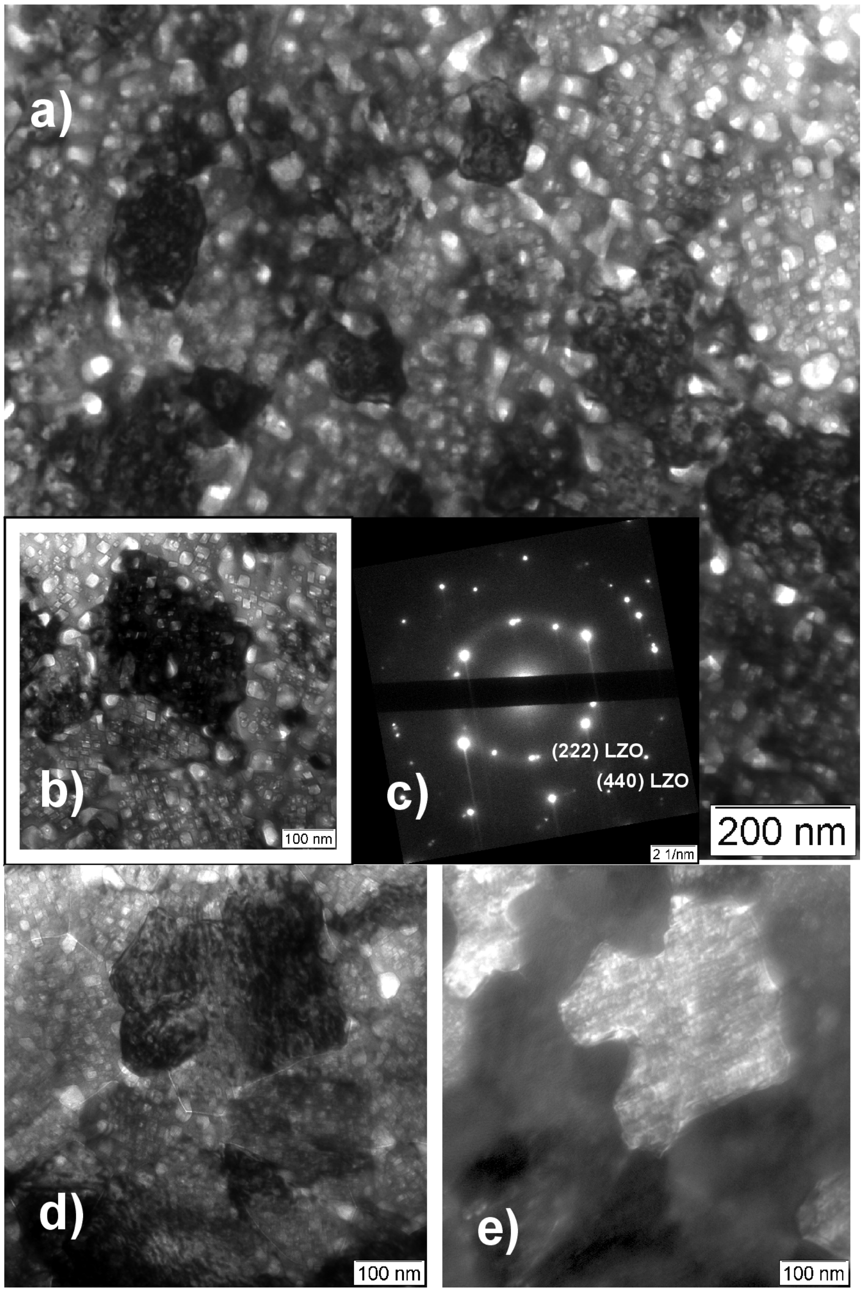

Figure 3.9: a) TEM bright-field image taken of sample 2 in plan view. b) TEM bright-field image of a single LZO grain showing nanovoids. c) Corresponding electron diffraction pattern of the area shown in figure 8 (a). d) TEM bright-field image. e) TEM dark-field image.

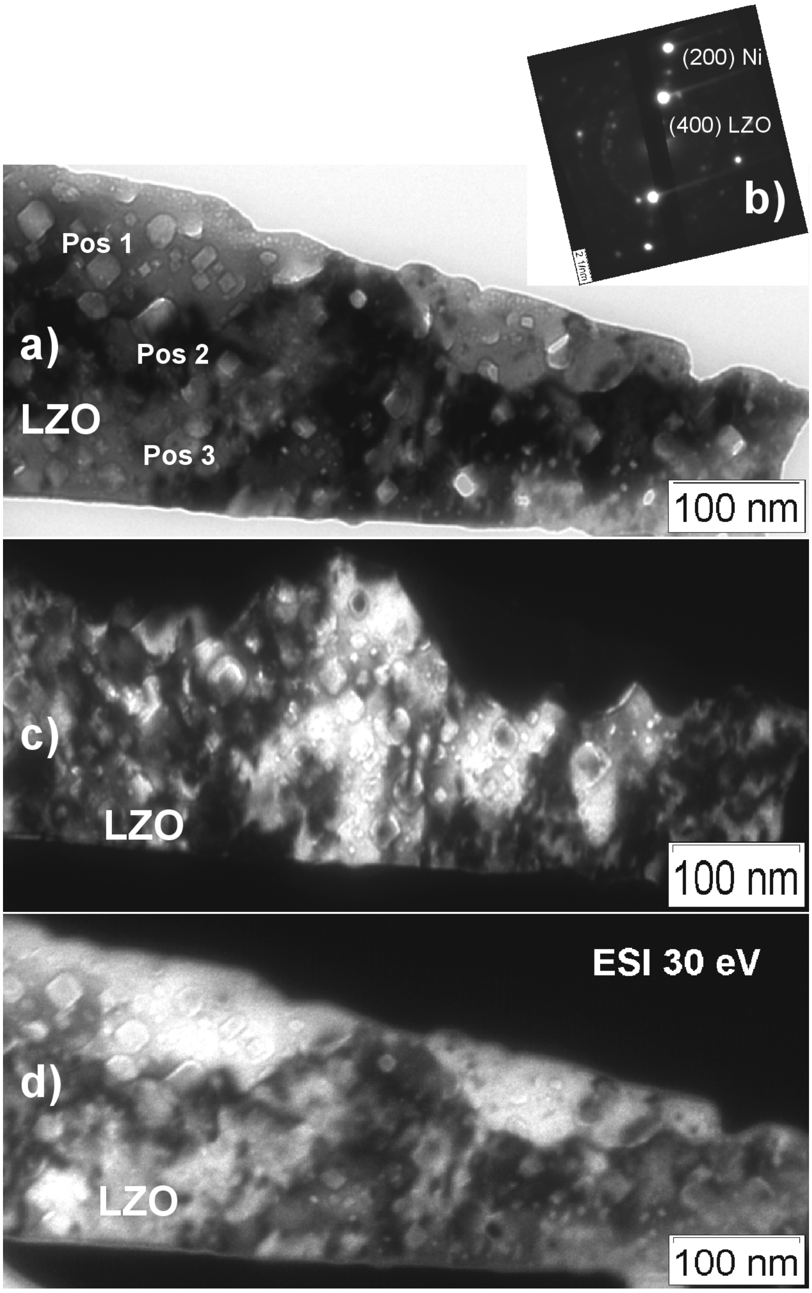

Figure 3.10: a) TEM bright-field image of sample 2 in cross-section b) Electron diffraction pattern of the area shown in figure 9 (a). c) Corresponding dark-field image of figure 9 (a). d) Energy-filtered image taken at an energy-loss of 30 eV.

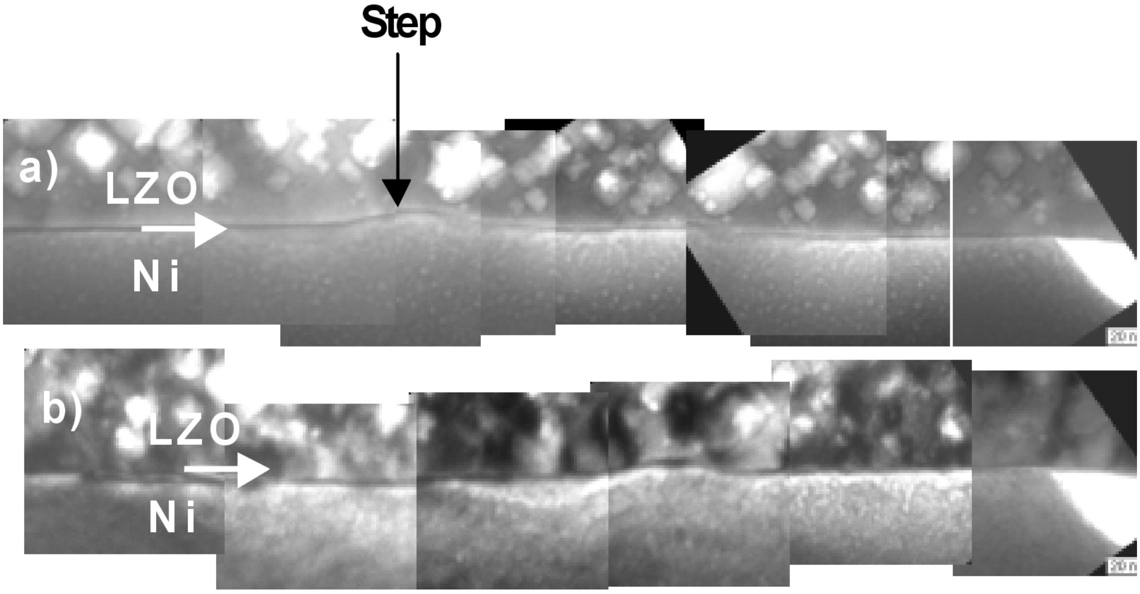

Figure 3.11: Sample 2: a) TEM bright-field images of the LZO buffer layer-nickel substrate interface at a tilt angle of 0° along the surface normal. b) and of 18°.

TEM is the only method that is able to detect the voids, since TEM is probing the volume of the sample. AFM or SEM probe the surface and, therefore, only the effect of the nanovoids on the surface roughness can be imaged. Nanovoids of a few nm in size, but less dense, were previously observed in CeO_2 thin films deposited on biaxially textured nickel substrates by PVD methods [14] and on metal organic deposition (MOD) prepared LZO films on Ni-W substrates [72].

3.4.2 Microstructure of CSD prepared LZO buffer layers

The LZO buffer layer thickness of sample 1 was determined to be 160 nm for both the top and the bottom layer. The sample was dip-coated twice and two layers were observed by TEM. The total thickness of the LZO buffer layer is then 320 nm. Sample 2 had a single layer of 350 nm. This single layer thickness corresponds nicely to the nominal thickness of the films: LZO (280 nm) + CeO_2 (70 nm).

The roughness (RMS) of the LZO buffer layers annealed at T = 900°C was determined to be RMS = 2 nm (1µm x 1µm scan size, AFM) for a 160 nm thick LZO sample. For a 320 nm thick layer the value is about the same [66]. The second layer was always processed under the same conditions as the first layer. Cracks were never observed in the layers when tehy produced under the given conditions. The double coating was necessary to increase the thickness mainly because there is a thickness limit for single coatings. At too high solution concentrations or withdrawal speeds the layers tend to crack.

TEM plan-view images of both samples yielded the LZO grain size, i.e. 100-200 nm for sample 1 and 200-300 nm for sample 2. The increase in LZO grain size is due to the higher temperature during the annealing process. Consequently, the LZO grain size is much smaller than the Ni grain size, the latter being about 40 µm. Also, electron diffraction patterns reveal diffraction rings when the LZO films are illuminated with a beam size of 2 µm. This indicates that the sub-µm texture is less pronounced and the good texture observed in X-ray diffraction patterns comes from averaging over large areas of the films.

Although the pole figures acquired by X-ray diffraction (figures 3.2 and 3.8) suggest epitaxial growth of the LZO on Ni-W we have shown experimentally that this is not case. The reasons/arguments for the biaxial, but not-epitaxial growth are: (i) the misfit between LZO and Ni is very large (7.6 %), (ii) the Ni-W substrates have a rough surface on the atomic scale and (iii) the formation of the LZO starts presumably at the top part of the film rather than from the bottom (iv) EBSD patterns from Ni and LZO surfaces differ significantly and many unindexed LZO areas appear (v) most directly TEM images and diffraction patterns yield polycrystalline microstructures on the 100 nm scale. The growth of the films and the chemical reaction yielding LZO have to be understood in more detail. Therefore, temperature series of intermediate states of the reaction have to be analysed by the methods described here.

Both, sample 1 and 2 are highly nanoporous which is found to be a typical feature for CSD grown LZO buffer layers. Voids are identified and are a dominating feature of the microstructure. The nanovoid size has been exactly determined by transmission electron microscopy. For the LZO buffer layer annealed at 900 °C, sample 1, the nanovoid size was found to be 10- 20 nm. Sample 2 annealed at 1050 °C had larger nanovoids of 30-40 nm. This was determined in both cases by taking into account the voids with the largest diameter observed in the cross-sectional TEM images. For both cases nanovoids had a rectangular or cuboid shape and the surfaces had a preferred 45° orientation with respect to the nickel tungsten substrate. The form and orientation of the nanovoids are due to the anisotropy of the LZO surface energies. The voids might form during the chemical reaction, in which the organic precursors react to inorganic $La_2Zr_2O_7$ and the voids might be filled with C-rich gas. Nanovoids are important for buffer layer properties since they can be centers of crack generation and favour crack propagation. However, until now the LZO buffer layers studied fulfil the requirements as biaxially textured layers and effective diffusion barriers [66, 73].

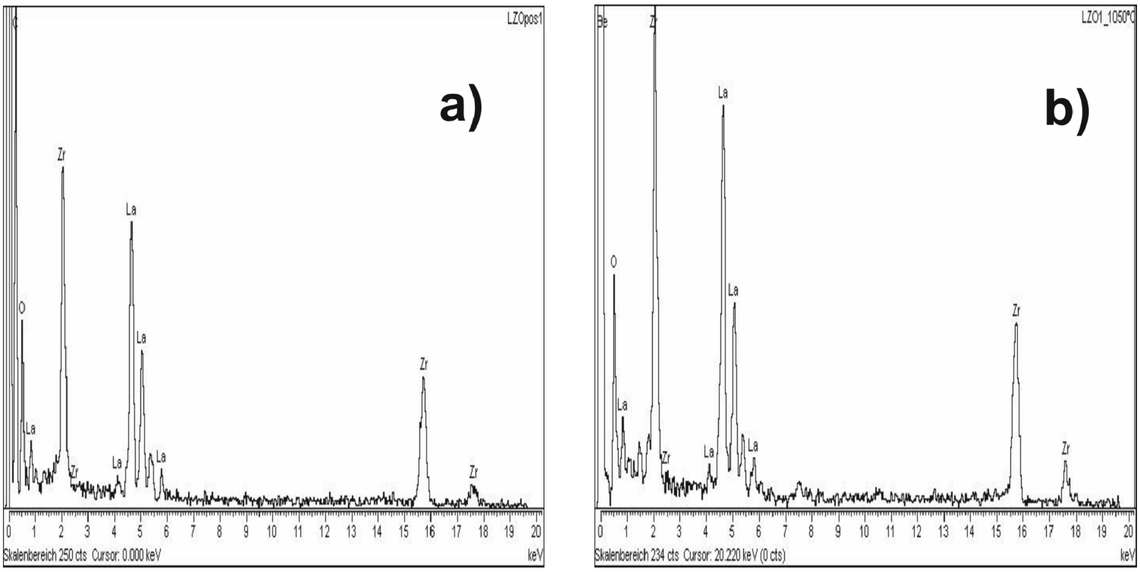

Figure 3.12: a). EDX spectra of position 1 on the LZO buffer layer annealed at 900°C, see Figure 5 (a). b). EDX spectra of position 1 on the LZO buffer layer annealed at 1050°C, see figure 10 (a).

EDX in the TEM yields a quantitative analysis of the main constituents of the films and the variation of the stoichiometry in the films. The microstructure of the buffer layers is homogeneous, no Ni-rich compounds could be identified. The minimum detectable mass fraction for Ni is beyond 1 at.% for EDX analysis of cross sections due to stray radiation. Therefore, Ni diffusion into the buffer layers Ni mole fractions lower than 1 at.% cannot be detected by EDX in the TEM.

LZO phase formation was found to start at $T > 750°$ in 20 nm thick LZO films grown by CSD and studied by *in-situ* XRD [23], in which an X-ray diffraction peak corresponding to LZO (004) was clearly observed starting at T=850°C and beyond, indicating that LZO starts to nucleate at this temperature. Similar temperatures in resembling studies were also reported by Obradors et al.[24], as well as for the samples investigated in this work annealed at T = 900°C and 1050°C respectively, temperatures at which LZO phase formation has already started [63, 68].

These previously mentioned studies showed that the films had a smooth and crack-free microstructure with a crystalline surface and also the high performance of the LZO layers as efficient buffer layers. However, it is still unclear whether the LZO phase starts to form at the interface to the substrate or at the surface of the film yielding a biaxially textured LZO buffer layer. Critical thicknesses for introducing misfit dislocations would be smaller than 1 nm for 7.6 % misfit.

3.5 Conclusions

The microstructure of $La_2Zr_2O_7$ thin films deposited on biaxially textured 5 at.% tungsten alloyed nickel substrates prepared by chemical solution deposition (CSD) and annealed at 900°C and 1050°C were characterised by scanning and transmission electron microscopy. The LZO thin films were prepared as TEM cross-section and plan-view samples. The buffer layer thickness for the double coated LZO annealed at 900°C was found to be 160 nm for each layer. For the 1050°C sample the layer thickness was found to 350 nm. Both values confirm the layer thickness estimated during the CSD preparation process. The LZO grain size (100-300 nm) for both samples was found to be much smaller than the grain size of Ni which is about 40 µm in size. Electron diffraction patterns and images show that the films have a grain size between 100 and 300 nm. Compared to the X-ray diffraction results the sub-µm texture is poor and the strong texture observed by X-ray comes from averaging over large areas.

At present we understand the established microstructure as a result of a growth mechanism during the annealing of the film, in which nucleation presumably starts at the surface of the film rather than at the substrate interface. This is in contrast to an epitaxial growth which occurs in a layer-by-layer or Stranski-Krastanov growth mode and starts from the substrate interface. The established microstructure in the film depends on the following energy contributions: (i) surface energy, (ii) film-substrate interface energy, which includes the strain energy of misfit dislocations, (iii) grain boundary energy, (iv) strain energy in the volume of the film. The established microstructure yields a minimization of the sum of these energies. However, it remains open what the driving force for the long-range biaxial texture of the film really is. It is important to note that on the sub-µm (probed by TEM) scale the texture is less perfect than on larger length scales (probed by XRD).

LZO on Ni-W is a system with a high misfit of 7.6%, that even so leads to a biaxially textured growth of the film on the substrate. The underlying Ni-W substrate is essential for the growth mechanism because it provides the biaxial texture that is transferred to the LZO buffer layer. The transfer of texture is reached however without epitaxy. It is well known that for epitaxy to occur the substrate must be atomically planar and the film will grow in a layer-by-layer mode yielding the same grain size in the film as in the substrate. This is, however, not observed: the grain size of the LZO film is about 100 nm and the grain size of the Ni substrate is 40 µm.

The large misfit between the LZO film and the Ni substrate might be compensated by tilting the grains of the film, rather than by misfit dislocations. Such a mechanism was found for GaAs films on a Si substrate [74]. The driving force for this tilting of grains is strain relief, since it would be energetically more favourable to introduce grain boundaries with widely spaced dislocations rather than closely spaced misfit dislocations. Another system is $CeO_{2-\delta}$ on MgO, where the mechanism for the titling was also observed and arises from a strain-relieving mosaic growth [75]. This type of behaviour has also been observed in CeO_2 films deposited on biaxially textured nickel substrates [71].

Nanovoids (10-40 nm in size) were found to be a typical feature for CSD grown buffer layers. Nanovoids had a rectangular or cuboid shape indicating an anisotropic surface energy of LZO. The preferred surfaces are crystallographic (111) planes, which are hexagonally close packed planes in this structure. Despite the presence of nanovoids in both samples no Ni diffusion into the buffer layers has been observed, indicating that they act as efficient barriers between the Ni-5at.%W substrate and the LZO film and no crack formation has been found.

Chapter 4

Temperature series of LZO buffer layers on flexible nickel tungsten substrates

4.1 Introduction

Chemically deposited LZO thin films are currently of great interest for the fabrication of YBCO coated conductors for their use as low cost buffer layers. These are crucial for coated conductor production since they transfer the texture from a highly biaxially textured nickel substrate to the YBCO superconducting layer and act as nickel ion diffusion barriers. The LZO buffer layers studied in this work were deposited on biaxially textured Ni-5at%W substrates by chemical solution deposition (CSD) using the same precursor starting solutions and heat-treated at temperatures ranging from 600 to 1000°C. Samples were studied by scanning electron microscopy (SEM), X-ray diffraction (XRD) and conventional transmission electron microscopy (TEM) in plan-view and cross-section.

By combined TEM and XRD investigations on the same samples we found a clear difference in the microstructure of the LZO thin films: (i) a nanocrystalline or amorphous state for T $<$ 800°C with grains of 5-10 nm in size (ii) and a polycrystalline state at higher temperature with an average grain size of up to 200 nm. Grain growth starts at 800°C and nanovoid formation has been confirmed and occurs during the grain growth process. The nanovoid size was determined to be 10-20 nm and small-angle grain boundaries were observed in the LZO buffer layers. The facetting of the LZO grain boundaries play an important role in the grain growth process, samples annealed at higher temperatures have grain boundaries that are less strongly facetted than at lower temperatures. The misfit of LZO with respect to Ni is 7.6% and as a result the LZO grain size is much smaller than the Ni grain size.

Thus, although the LZO buffer layers are highly biaxially textured, no epitaxial growth occurs. Grain growth started at 800°C and nanovoid formation and growth occurred during the grain growth process. The nanovoid size was determined to be 10-20 nm and small-angle grain boundaries were observed in the LZO buffer layers. The facetting of the LZO grain boundaries play an important role in the grain growth process, samples annealed at higher temperatures had less strongly facetted grain boundaries than at lower temperatures. On top of the LZO buffer layers YBCO thin films were deposited by PLD and CSD yielding critical current densities of $>$ 1 MA/cm2 at 77 K.

The LZO buffer layers were prepared by chemical solution deposition (CSD): a Ni-5%W substrate is successively dip-coated in a LZO precursor solution at room temperature followed by a heattreatment. The misfit of LZO with respect to Ni is 7.6% (compressive), a tilting mechanism is believed to play an important for strain relief in this highly strained system [76]. LZO on YSZ has a similar (compared to LZO on Ni) misfit of 5% and growth of LZO films on (001) YSZ was investigated by Lu C J et.al. [77]. The arrangement of misfit dislocations and the formation of slightly tilted domains was analysed in the LZO pyrochlore islands grown on YSZ substrates. Also in this case misfit yielded tilting of neighbouring domains/grains.

4.2 Experimental

Sample preparation Biaxially-textured Ni-5at.%W tapes were dip coated using a 0.15 M solution, pyrolyzed and annealed at temperatures ranging from 600-1000°C. The pyrolysis was performed at 600°C with a heating rate of 10K/min. After the pyrolysis the samples were brought to room temperature and annealed with a heating rate of 10 K/min. Annealing time was 60 min and cooling was done at 2-3 K/min. For details on preparation procedures see [66, 63].

The LZO film thickness was between 150 to 170 nm for all samples investigated in the temperature series. The sample preparation and superconducting properties of a full YBCO(PLD)-coated conductor shown in this section is described in [78]. A Zeiss 912 Omega EF-TEM operating at 120 keV and equipped with an EDX detector (Oxford) was used in this study, all images shown here were energy-filtered (EF). The EDX spectra were acquired for 100 s with a spot size of 10-40 nm. The Cliff-Lorimer method was used for quantitative analysis of the spectra no absorption correction was applied.

4.2.1 TEM specimen preparation

Samples were prepared for TEM investigations by conventional mechanical polishing and grinding methods followed by ion milling using a Res 100 Baltec ion milling machine operated at 4.5 kV and 3.5 mA for several hours. Plan-view samples were ion milled from one side only at an angle of 12°. Cross-section samples were prepared by the method described in [65] and then ion milled from both sides using angles of 12°.

4.3 Results

4.3.1 Biaxial texturing and grain growth

Understanding the biaxial texturing of the buffer layer is of key importance for coated conductor preparation technology. Therefore, detailed TEM diffraction contrast studies were preformed to image small misorientations of the LZO grains with respect to the underlying Ni substrate. TEM diffraction contrast is more sensitive to small misorientations of the grains than electron diffraction patterns.

Electron diffraction patterns are useful to obtain diffraction rings of the nanocrystalline microstructure prior to annealing, and spot patterns of individual grains that are 100-200 nm in size after grain growth occurred. Figure 4.1 shows a tilt series of an LZO thin film in plan view annealed at 900°C, the LZO film thickness was 80 nm. The sample was tilted such that two-beam diffraction conditions were established in a number of grains of the area that appear in dark contrast (fig. 4.1 top left).

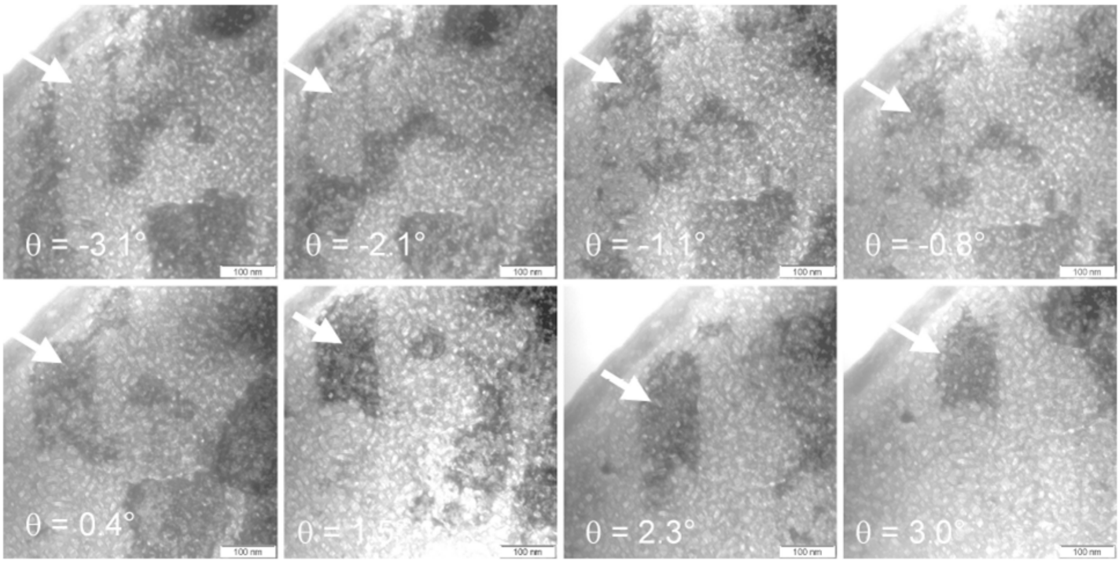

Figure 4.1: TEM bright-field images of a 900°C LZO buffer layer sample in plan-view taken at different tilt angles θ. Granularity is visible. Scale bar is 100 nm.

From this position the sample was further tilted and different grains were brought into diffraction condition. By such experiments small tilts of neighbouring grains can be determined and the grain size was found to be 100-200 nm. The contrast in these images is sensitive to the out-of-plane tilt of the crystallites. Within the grains the diffraction contrast is determined by nanovoids, which were determined to be 10-20 nm in size [76].

4.3.2 XRD and TEM measurements on $La_2Zr_2O_7$ buffer layers annealed from 600°C to 1000°C

Figure 4.2 shows XRD pole figures, TEM bright field images and corresponding electron diffraction patterns at different annealing temperatures. For T= 700°C no LZO(222) reflection in the pole figure can be observed and nm sized LZO grains are observed in the bright-field TEM image.

The electron diffraction pattern shows a ring that corresponds to LZO (222). At T= 800°C grain growth and biaxial texture started as seen in the pole figure where LZO(222) reflections are observed. In the BF-TEM image grains of ~100 nm grain size are found. At T=900°C and T=1000°C the grain size increases to 100-200nm, pole figures yield less background and more defined peaks and corresponding electron diffraction patterns show distinct spots instead of rings.

The micro-structure of the of the films prior to the annealing was studied in detail. Figures 4.3 (a-b) show bright and dark-field TEM images in plan-view and (c) the corresponding electron diffraction pattern of the sample annealed at T=600°C. In the electron diffraction pattern rings corresponding to LZO(222), LZO(422) and LZO(444) can be identified indicating that the sample is nanocrystalline. The LZO grains were found to be ~5 nm in size by dark field images.

Figure 4.3 (e) shows a single LZO grain of 100 nm and the corresponding dark-field image 4.3 (f) in a sample annealed at 800°C. Within the LZO grain nano-granularities of 10-20 nm can be identified. The electron diffraction pattern, figure 4.3 (g), shows a diffraction ring corresponding to LZO(222). Within the ring diffraction spots can be identified. The ring segment circled was used to obtain the dark-field image shown in figure 4.3 (f). Figure 4.3 (d and h) show EDX spectra from which the cation mole fraction and the C mole fraction were determined.

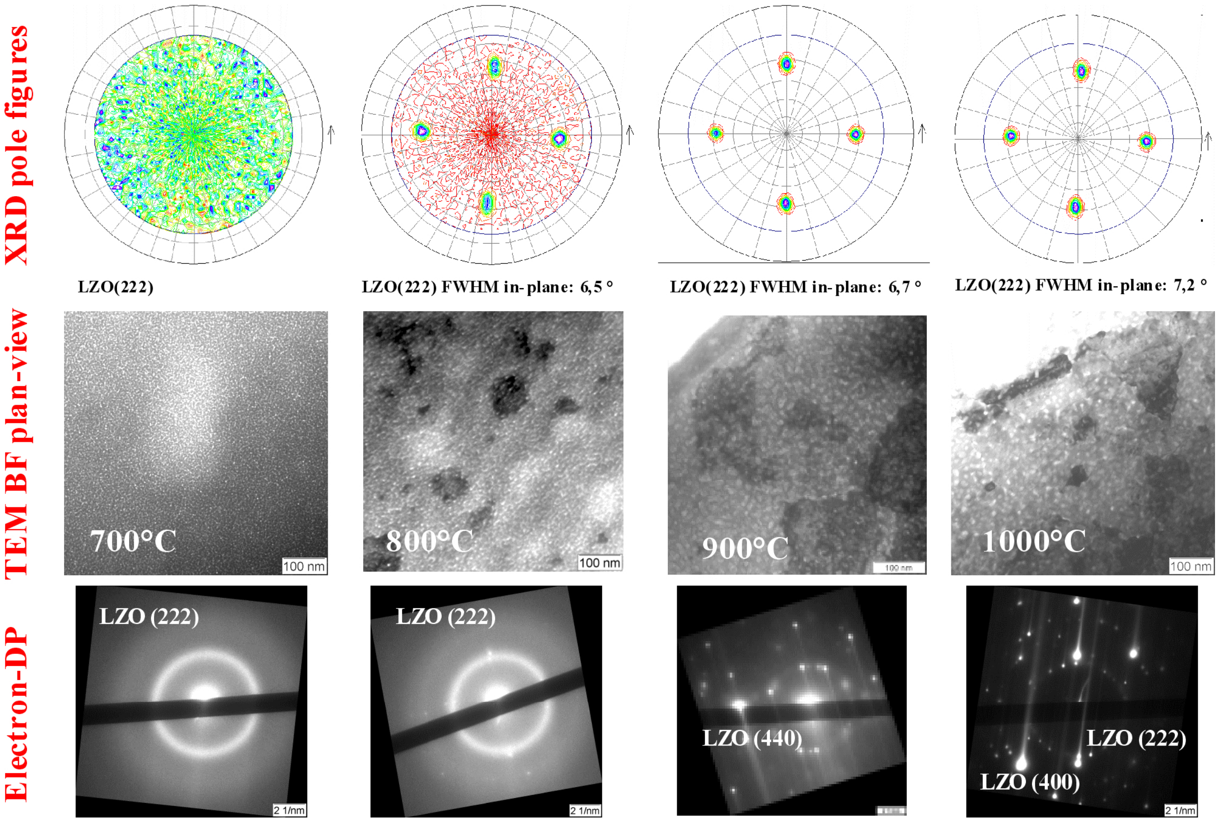

Figure 4.2: XRD pole figures and TEM measurements of LZO buffer layers.

Table 4.1 summarises data obtained by TEM for all samples. The nanocrystalline state appeared at T< 800°C with grains of ~5 nm and polycrystalline grain growth starts above 700°C where LZO grain boundaries were found to be strongly facetted at T =800°C and 900°C. In samples prepared at T=1000°C grain boundaries were less strongly facetted.

Temperature (°C)	600	700	800	900	1000
Grain size	5nm	5nm	50-100nm	50-100nm	100-200nm
Grain boundaries	-	-	strongly facetted	strongly facetted	less facetted
Voids	-	-	-	10nm	10nm
Bright and dark areas	yes	yes	yes	yes	dark only
Diffraction patterns	ring	ring	ring + spots	ring + spots	spots only

Table 4.1: Microstructural parameters of the LZO films annealed at different temperatures.

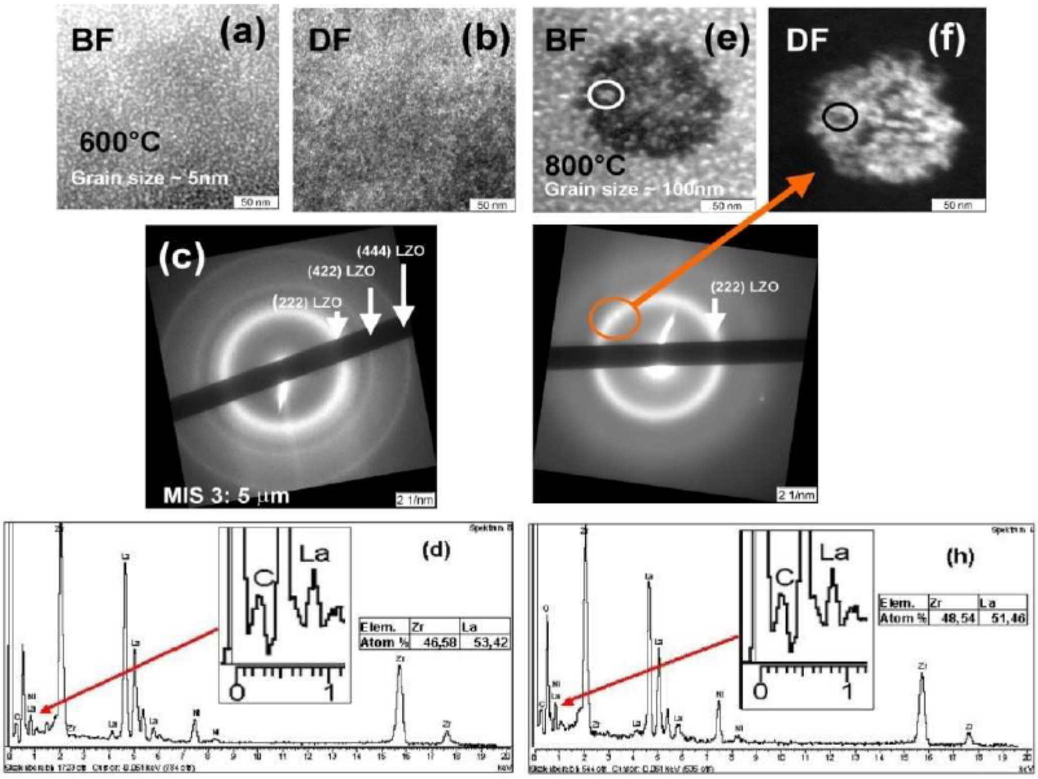

Figure 4.3: (a) Bright-field image of the LZO sample annelaed at 600°C (b) corresponding dark-field image (c) diffraction pattern of the LZO sample annelaed at 600°C (d)corresponding EDX spectrum (e) Bright-field image of the LZO sample annelaed at 800°C (f) corresponding dark-field image (g) diffraction pattern of the LZO sample annelaed at 800°C (h) corresponding EDX spectrum.

4.3.3 Moiré contrast and in-plane rotations of LZO grains

Moiré contrast in TEM occurs when the electron beam penetrates consecutively two crystals with different orientation and/or lattice parameters. Shown in figure 4.4 is the sample geometry needed for observing Moiré contrast. $\vec{g_1}$ is a reciprocal lattice vector of LZO denoted as crystal 1 and $\vec{g_2}$ is a reciprocal lattice vector of Ni denoted as crystal II. Z is the sample thicknes ($Z = Z_1 + Z_2$).

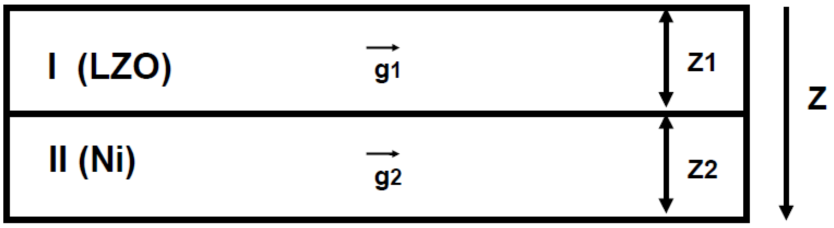

Figure 4.4: Geometry needed for observing Moiré contrast, Z denotes sample thickness and $\vec{g_1}$ is a reciprocal lattice vector of LZO and $\vec{g_2}$ is a reciprocal lattice vector of Ni.

Several types of Moiré contrast can occur as shown schematically in figure 4.5 where Translational

Moiré fringes, Rotational Moiré fringes and mixed type Mixed Moiré fringes are presented [70]. The simplest type of Moiré fringe is a translational Moiré, in this case two lattices with different lattice parameters overly. Areas with match appear bright and areas with worse lattice match appear dark.

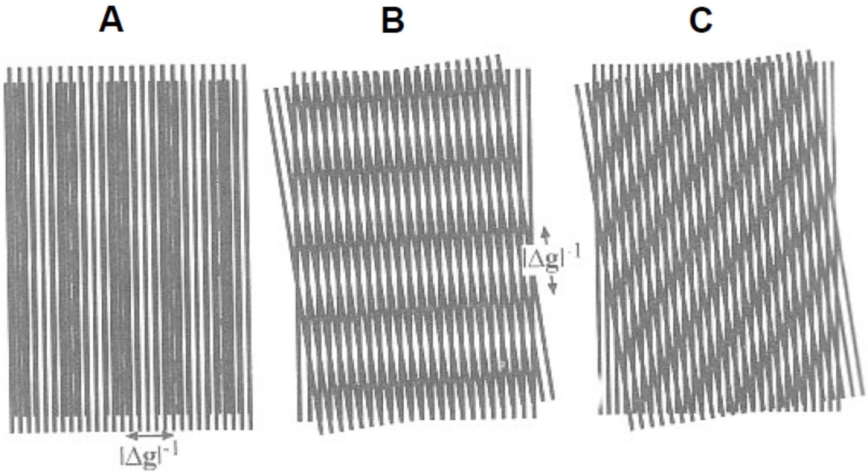

Figure 4.5: The different types of Moiré fringes(A) Translational Moiré fringes. (B) Rotational Moiré fringes. (C) Mixed Moiré fringes

Due to the existence of two lattices with different lattice parameters reflexes appear as peairs in electron diffraction patterns. One reflexion belongs to crystal I and the second belongs to cyrstal II. The difference is$\Delta\vec{g}$, which lies perpendicular to the observed Moiré pattern.

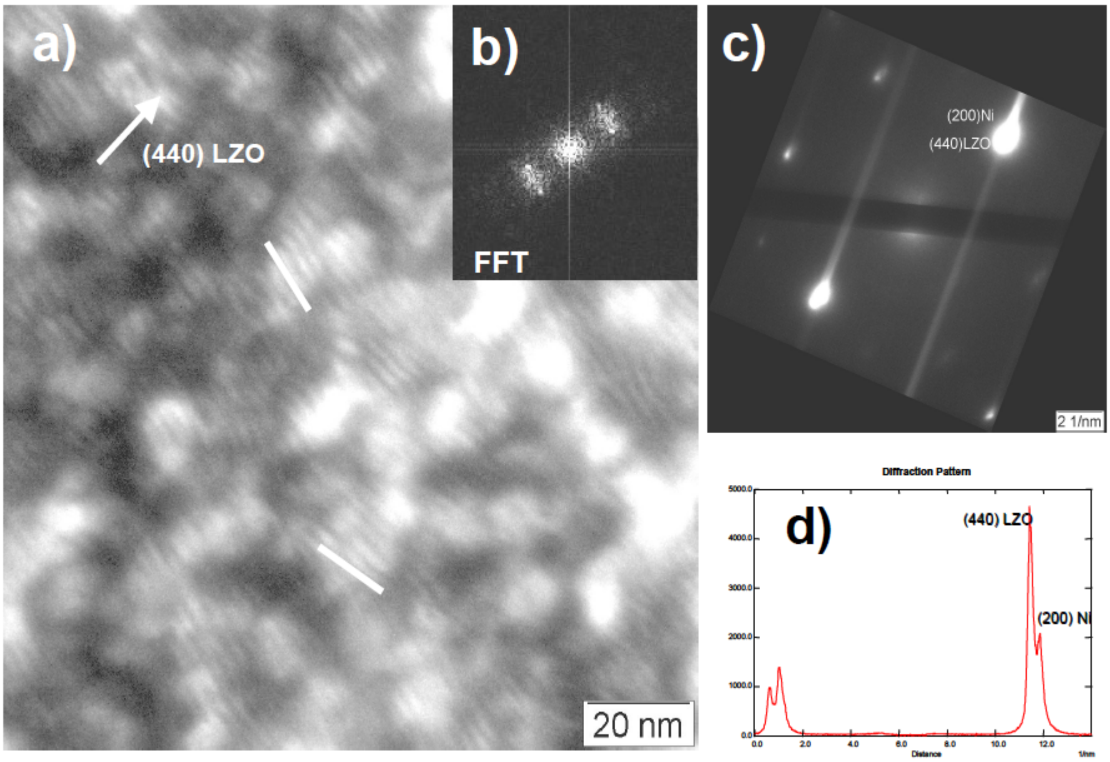

Figure 4.6: TEM plan-view of a LZO-Ni sample (900°C) a) Bright-field image in a thick region of the sample. Moiré fringes are observed due to the overlapping of the LZO film and the Ni substrate in the beam direction. Note the different orientations of the fringes in the image (white bars). The bright areas observed in the figure correspond to nanovoids of 10-20 nm that are found to be present in chemically deposited LZO buffer layers [76]. Fast-Fourier transform (FFT) of the selected region in (a). b) Electron diffraction pattern under two beam conditions showing adjacent reflections corresponding to the (440) LZO and (200) Ni reflections c) Intensity profile of the electron diffraction pattern shown in figure 3 (c).

The Moiré fringes spacing is given by:

$$d_{Fringes} = \frac{(d_{440(LZO)}Film)\,(d_{200(Ni)}Substrate)}{(d_{440(LZO)}Film) - (d_{200(Ni)}Substrate)} \tag{4.1}$$

The calculated value of the Moiré fringes spacing is 1.01 nm, this is in agreement with the measured value of 1.2 ± 0.5nm

Figures 4.7 (a-c) shows a bright-field TEM tilt series from = -5.0° to -6.3° of the same sample area shown in figure 4.1, but at higher magnification. Figures 4.7 (d-f) show the corresponding electron diffraction patterns where the (200)Ni and the 440(LZO) reflections can be indexed. Due to the overlapping of the LZO film and the Ni substrate in the electron beam direction Moiré contrast is observed, note the different orientations of the fringes in the image (white bars in 4.4 c).

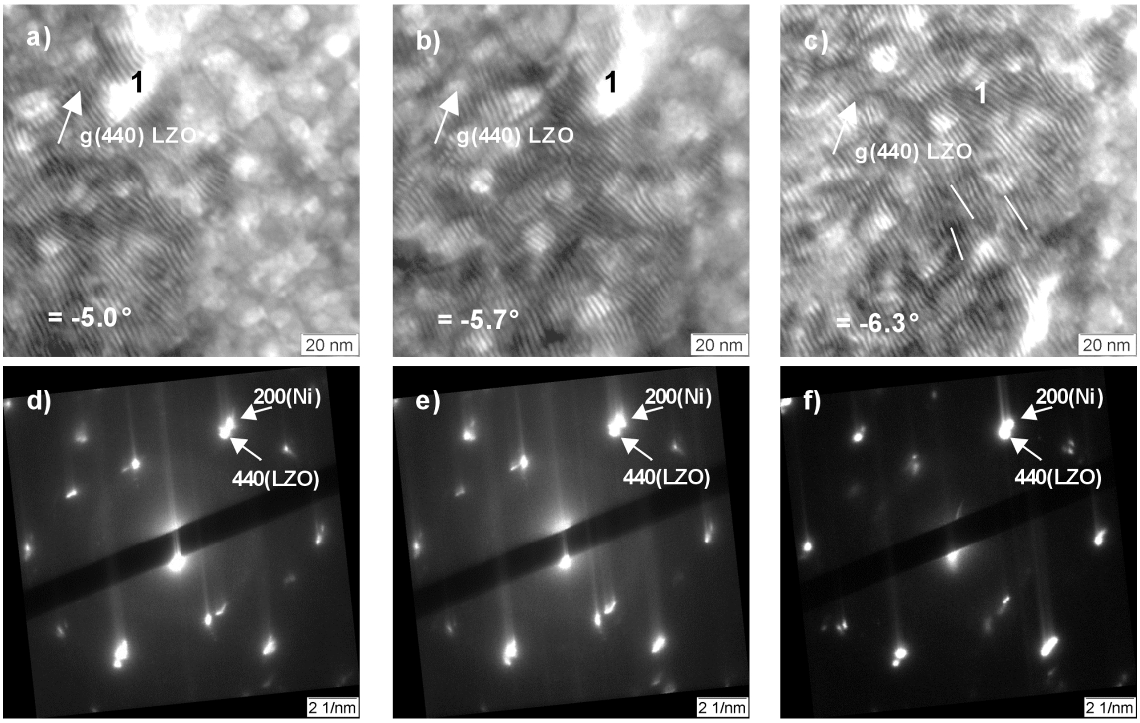

Figure 4.7: (a)-(c) TEM bright-field images for different tilt angles (ϑ). Figures (d)-(f) are the corresponding electron diffraction patterns.

This Moiré contrast magnifies the misorientation of LZO grains with respect to the underlying Ni grain by a factor of 13 and small rotations of the LZO grains of less than 3° can be determined. The bright contrast in the images is due to the nanovoids present in the film. The Moiré fringe imaging is sensitive to the in-plane-rotation of the crystallites. The splitting of the (200) Ni and the (440) LZO reflections is the reason for the Moiré fringe contrast to appear and shows that the lattice parameter for LZO is close to the intrinsic value. The misfit of the film with respect to the substrate was compensated by strain relaxation, misfit dislocations that were expected to be arranged in a two-dimensional grid were, however, not observed in these images.

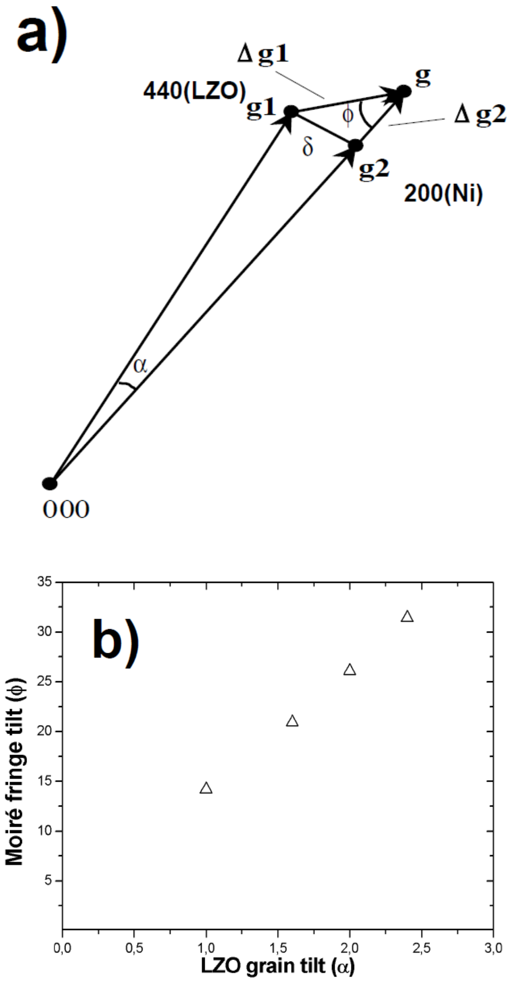

Figure 4.8: a) Schematic representation of a mixed Moiré fringe [71](b) Moiré fringe tilt vs.LZO grain tilt (with respect to the underlying Ni grain) for a LZO buffer layer on a nickel tungsten substrate with a misfit of 7.6%.

The relationship between angles is given by:

$$\sin\frac{\phi}{2} = \frac{1}{2}\frac{|\vec{g_1}|}{|\Delta\vec{g_1}|}\alpha \tag{4.2}$$

$$\frac{\phi}{2} \approx \frac{1}{2}\frac{|\vec{g_1}|}{|\Delta\vec{g_1}|}\alpha \tag{4.3}$$

$$\phi \approx 13.1 \cdot \alpha \tag{4.4}$$

If the electrons are first scattered in the LZO film and then in the Ni substrate, translational Moiré fringes appear. Considering such Moiré fringes Δg can be calculated according to:

$$\Delta g = |\vec{g_1} - \vec{g_2}| \tag{4.5}$$

4.3.4 Facetting of LZO grain boundaries

Figure 4.9 is a schematic of LZO grain facetting. At lower annealing temperatures (T = 800 °C) grains are more strongly facetted than at higher annealing temperatures (T=1000°C), where grain boundaries are straighter. Figure 4.10 are bright field image of a small-angle grain boundary in LZO. Figure 4.10 (a) shows a strongly diffracting grain at 50 K magnification. (b) at 100 K and (c) at 200 K. Moiré spacing is ~1nm.

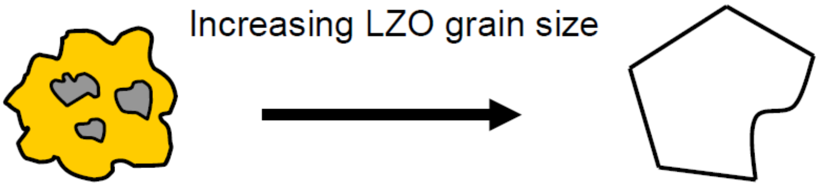

Figure 4.9: (a) TEM bright-field image. Dark region corresponds to a strongly diffracting grain. (b) Same region at higher magnification, LZO small-angle grain boundaries are visible. (c) Rotational Moiré fringes are visible at the grain boundary.

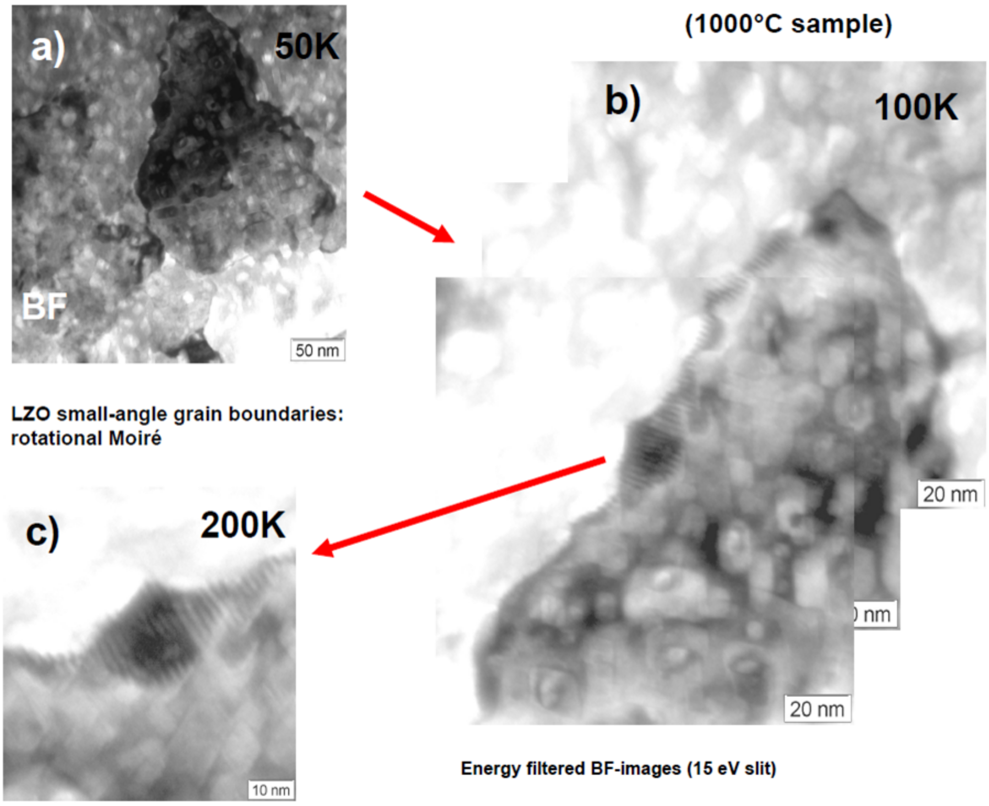

Figure 4.10: (a) TEM bright-field image. Dark region corresponds to a strongly diffracting grain. (b) Same region at higher magnification, LZO small-angle grain boundaries are visible. (c) Rotational Moiré fringes are visible at the grain boundary.

4.3.5 LZO-Ni interfaces

Figure 4.11 (a-c) shows a LZO-Ni cross-section TEM bright-field tilt series of the same sample area at tilt angles ranging from θ = 9.6°, φ=4.6° to θ = 10.8°, φ=4.6° . Figure 4.11 (a) shows a strongly diffarcting grain over the full layer thicknes. Figures 4.11 (b-c) show that slight tilts 0.4° are enough to bring the grain out of a perfect Bragg condition. Figure 4.11 (d) is a centered dark-field image of the same area. Intensity profiles with the transmitted beam and the diffracted $g(400)$LZO beam are shown.

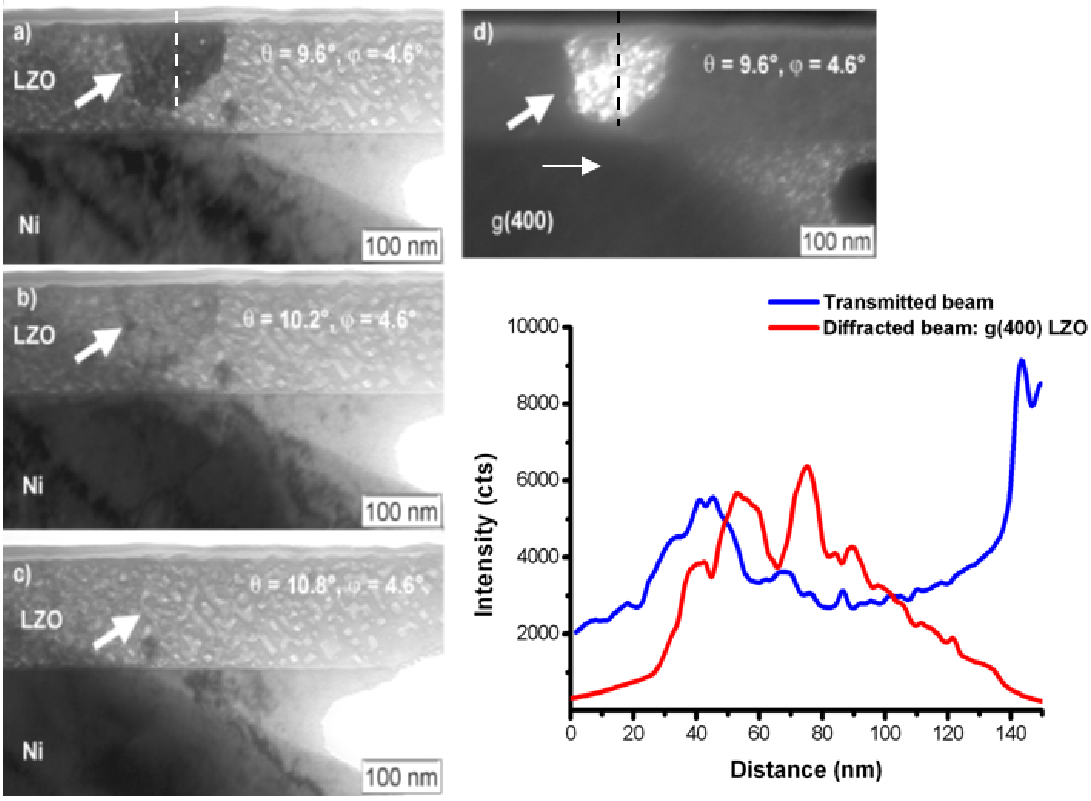

Figure 4.11: Tilt series of a TEM cross-section prepared LZO sample annealed at 900°C.

Figure 4.12 is astudy TEM DF of a LZO buffer layer in cross-section (T=1000°C). An interface roughness with a wavelength of ~ 60 nm and an amplitude of ~10 nm was found. Total film thickness is ~100 nm. Strongly diffracted grains are denoted by 1, 2, 3 and 4 in the image.

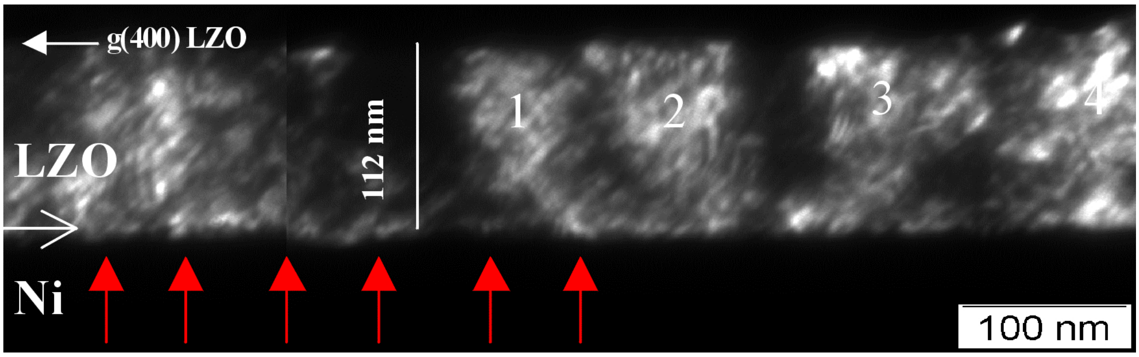

Figure 4.12: Dark-field image of a LZO/Ni interface.

Figure 4.13 is a HRTEM image of an LZO-Ni interface. HRTEM analysis is difficult since LZO on Ni is a highly strained system (compressive misfit of 7.6 %) has a very rough interface on the nanometer scale and the underlying flexible nickel-tungsten substrate has a high density of dislocations. The small lattice parameters of the Ni substrate requires a point resolution of significantly better than 0.2 nm.

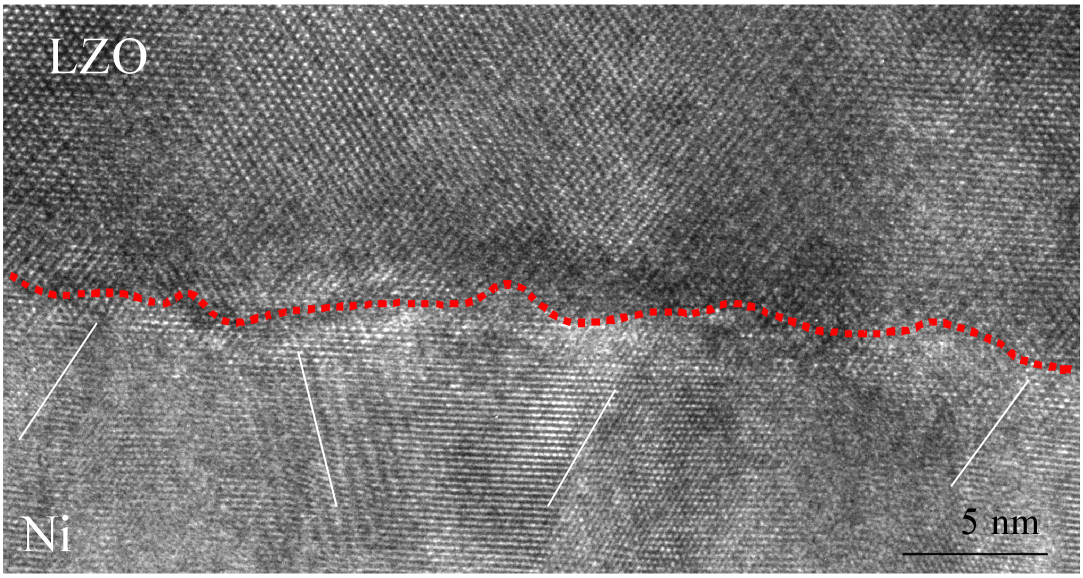

Figure 4.13: HRTEM image of a LZO/Ni interface. Obtained with an external TEM operated at 300 kV (TITAN Cube equipped with a Cs corrector yielding a point resolution of better than 0.1 nm).

After having identified the various structural defects in LZO buffer layers, the growth of PLD-YBCO films on these buffer layers was studied. Figure 4.14 (a) shows a YBCO coated-conductor in cross-section, in which the various layers could be identified. Nanovoids are visible within the LZO buffer layers. Figures 4.14 (b-d) are the corresponding electron diffraction patterns, fig.4.14 (e-f) are TEM-EDX spectra obtained within the LZO and CeO_2 buffer layers.

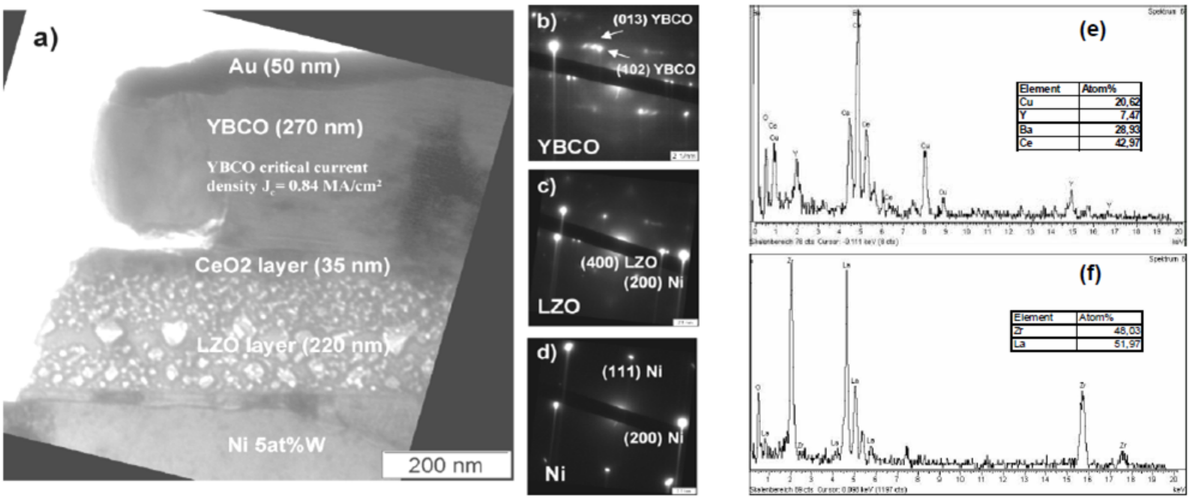

Figure 4.14: (a) TEM bright-field image of a YBCO(PLD)-coated conductor. (b-d) Corresponding electron diffraction patterns of the YBCO layer, the LZO buffer layer and the Ni substrate. (e) EDX spectra taken within the CeO_2 buffer layer and (f) within the LZO buffer layer. In (e and f) the cation mole fractions are given.

Figure 4.15 shows Convergent beam electron diffraction (CBED) measurement at a LZO-Ni interface. CBED is a technique that is very sensitive to local changes of the lattice parameters and strain in a sample. Images were energy-filtered in order to avoid background from inelastically scattered electrons. The images where obtained directly at an interface tiltting the Ni substrate into the [103] pole where fringes could be clearly observed. However, CBED patterns from the LZO area of the cross-sectional sample were strongly disturbed, indicating the presence of a high density of strain fields at the interface.

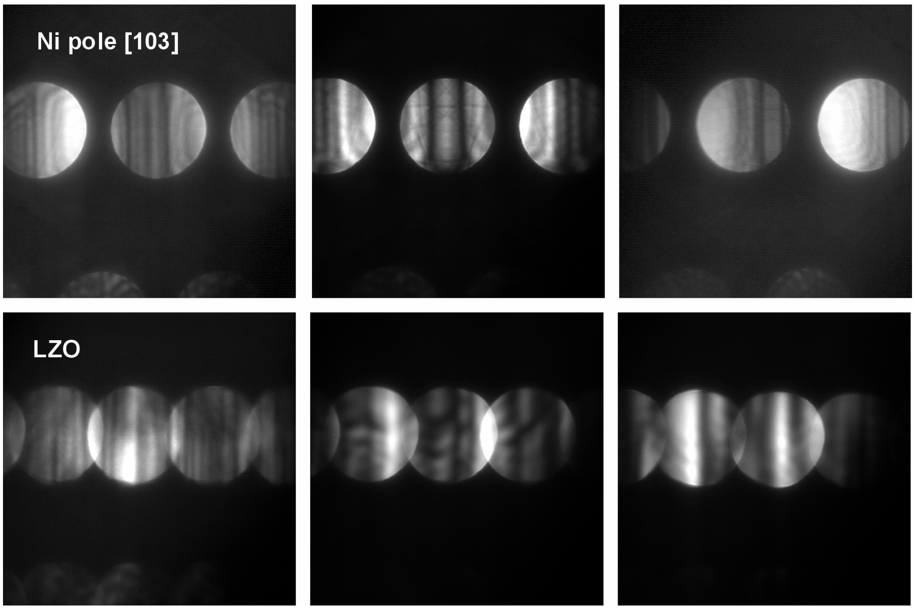

Figure 4.15: Convergent beam electron diffraction at a LZO-Ni interface.

4.3.6 Quantitative TEM-EDX of LZO buffer layers

A EDX thickness measurement series was performed on samples annealed at T=600°C, 800°C and 1000°C. Acquisition time for all EDX spectra was 200 seconds, spot size was 20 nm. Special care was taken to avoid contamination, for this purpose a cold finger was maintained at liquid nitrogen temperature and the same probe current was used. In the following sections (4.3.6.1-3), the integrated counts for C-K, Zr-L and La-L are given as well has quantitative EDX data.

LZO sample annealed at T = 600°C

Table 4.2 correspond to the Integrated counts for the EDX measurement on the T=600°C sample and respective quantitative EDX data (table 4.3).

Integrated cts			
Spectrum number	C-K	Zr-L	La-L
1	442,1	10668,3	14117
2	499,2	15118,2	20056,5
3	632,4	18418,8	23956,2
4	902,3	20465,6	24926,9
5	727,9	20456,2	24659,5
6	1095,8	25871,6	37454,4

Table 4.2: Integrated counts for the EDX measurement on the T=600°C sample.

Spectrum number	at %					
1	C	Err (±)	Zr	Err (±)	La	Err (±)
2	16,11	4,75	40,96	0,96	42,93	0,84
3	13,25	4,4	42,3	0,81	44,45	0,71
4	13,83	3,9	42,45	0,73	43,73	0,64
5	17,55	3,3	41,96	0,69	40,48	0,63
6	14,73	3,7	43,62	0,69	41,65	0,63
7	15,77	3,01	39,24	0,62	44,99	0,51

Table 4.3: Quantitative EDX measurements on the T=600°C sample.

LZO sample annealed at T = 800°C

Table 4.4 correspond to the Integrated counts for the EDX measurement on the T=800°C sample and respective quantitative EDX data (table 4.5).

Integrated cts			
Spectrum number	C-K	Zr-L	La-L
1	263,1	5104,5	6707,4
2	319,5	6648,1	8945,6
3	406,6	7938,8	10623,6
4	455,9	5396,3	12588,1
5	555,8	11455,6	15135,7
6	500,7	12651,3	15525,1

Table 4.4: Integrated counts for the EDX measurement on the T=800°C sample.

Spectrum number	at %					
1	C	Err (±)	Zr	Err (±)	La	Err (±)
2	19,33	6,1	39,53	1,39	41,14	1,2
3	18,08	5,5	39,65	1,22	42,26	1,05
4	19,09	4,9	39,28	1,1	41,63	0,97
5	18,2	4,6	39,86	1,3	41,94	0,89
6	18,36	4,2	39,89	0,93	41,75	0,81
7	16	4,4	42,6	0,88	41,41	0,80

Table 4.5: Quantitative EDX measurements on the T=800°C sample.

LZO sample annealed at T = 1000°C

Table 4.6 correspond to the Integrated counts for the EDX measurement on the T=800°C sample and respective quantitative EDX data (table 4.7).

Integrated cts			
Spectrum number	C-K	Zr-L	La-L
1	279,9	4071,2	5644
2	265	4562,6	6254,7
3	265,8	4410,4	6613,3
4	274,1	7356	10677
5	305,7	7079,7	10513,9
6	307	12952,8	18614,3

Table 4.6: Integrated counts for the EDX measurement on the T=1000°C sample.

Spectrum number	at %					
1	C	Err (±)	Zr	Err (±)	La	Err (±)
2	23,72	5,9	36,6	1,5	39,92	1,3
3	20,24	6,1	38,17	1,4	41,58	1,2
4	42,96	3,6	26,07	1,5	30,97	1,2
5	14,12	6,04	39,95	1,16	45,93	0,96
6	15,84	5,7	38,67	1,1	45,49	0,97
7	9,52	5,7	42,32	0,87	48,17	0,73

Table 4.7: Quantitative EDX measurements on the T=1000°C sample.

Summary of the EDX measurements.

Figure 4.16 show the data for integrated counts for Zr-L and La-L peaks for samples annealed at 600°C, 800°C and 1000°C. By confirming the linear dependence of Zr-L counts (blue squares) Vs. La-L counts (red dots) a extremely reliable carbon content measurement by EDX in the TEM was established. The measured integrated counts of the C-K peak could be used to determine the rest carbon content of the samples after pyrolysis even though carbon is a light element and is extremely difficult to measure reliably by TEM-EDX.

At T=600°C it was showed a volume carbon content of 15% with a slope of $m = 0.031$. At the T=800°C the slope changes to m=0.021 and carbon contents decreases to 10.6% indicating a volume and surface carbon content and at T=1000°C the slope is nearly 0 and the carbon content is at the surface of the film.

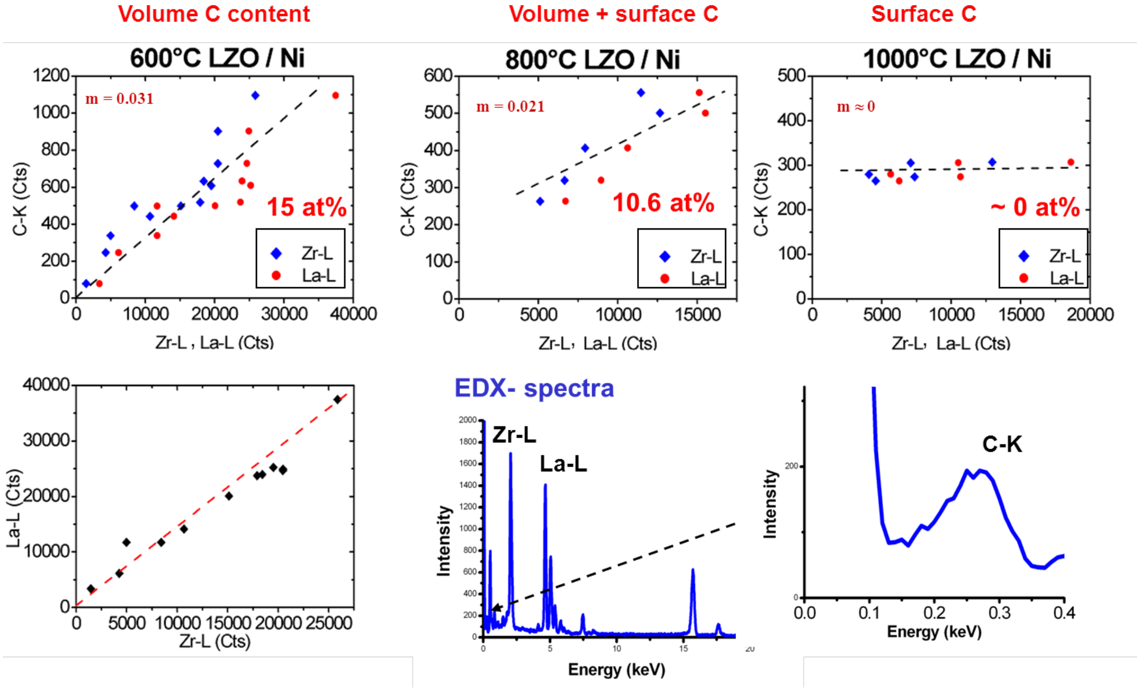

Figure 4.16: Quantitative TEM-EDX of LZO buffer layers.

4.3.7 Nanovoid formation in LZO

By TEM diffraction contrast the LZO grain growth and biaxial texturing was proved. At 600°C grains are not yet formed, at 800°C grain formation starts and grain size is 50-100 nm and are strongly facetted and at T=1000°C grains increase in size up to 200 nm filling the whole cross-sectional volume of the film and are less facetted than at lower temperatures. LZO grain boundaries with a LZO films act has carbon diffusion paths.

At lower temperature the rest carbon remains in the volume of the film and nanovoids form. At T > 1000°C grains increase in size and the rest carbon diffuses to the surface of the film leaving rectangular shaped nanvoids with {111} preferential planes due to the strong surface anisotropy of LZO [76, 77, 79]. Figure 4.17 is a schematic diagram of nanovoid formation showing carbon impurities as volume and surface fractions for samples annealed at 600°C, 800°C and 1000°C under (Ar5%H_2) reducing conditions.

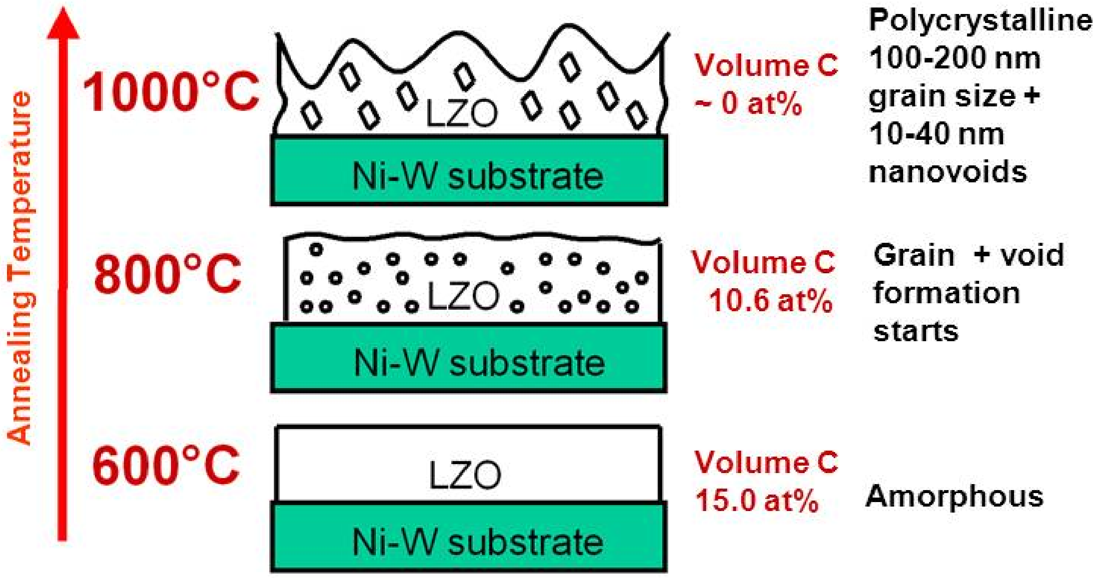

Figure 4.17: Nanovoid formation in LZO thin films.

Table 4.8 summarizes misfit, grain size and nanovoid size observed by several authors and deposition methods in LZO, GZO and CeO_2 buffer layers.

4.4 Conclusions

Although XRD pole figures of the LZO samples annealed at T>800°C suggest epitaxial growth of the LZO film it has been shown by TEM that epitaxial growth does not occur. The grain size in LZO films was found to be 100-200 nm by TEM and SEM and grains are misoriented with respect to the underlying Ni. The biaxial texture of LZO observed in the pole figures comes from averaging over large areas of the sample. It was shown that plan view bright- and dark field images under two-beam conditions are sensitive to image the in-plane and out-of-plane tilt of LZO grains.

The LZO lattice parameter was close to its intrinsic value, however, misfit dislocations were not observed in the Ni/LZO interface. The tilting of LZO grains with respect to the underlying Ni grain might be a mechanism for misfit compensation. LZO films annealed at temperatures between 600° and 1000°C were systematically studied by TEM and detailed results were presented.

System	Sample preparation	Misfit	Voids	Grains	References
$La_2Zr_2O_7$	Chemical solution deposition (CSD)	7.6 %	10-20 nm	50-250 nm	Molina *et al.* [76], Molina *et al.* [80] Steffens et.al. (100-300nm) [81], Caroff *et al.* [82](30-50 nm)
$La_2Zr_2O_7$	Sol gel	7.6%	10-20 nm	50-250 nm	Cloet *et al.* (EUCAS 09)
$Gd_2Zr_2O_7$	Electro-deposition	5.7 %	10-20 nm	50 nm	Zhao *et al.* [79]
CeO_2	Thermally evaporated	9 %	few nm	20-50 nm	Eyidi *et al.* [71]

Table 4.8: Oxide thin films on flexible Ni-tungsten substrates.

Chapter 5

Structure-property correlation of CSD processed coated conductors at different length scales

5.1 Introduction

Long-length CSD fabrication technology for coated conductors impose significant challenges for the characterization.The first technological challenge is to deposit high-quality buffer layers. A complete set of quantitative SEM-EDX film thickness determination were established and used for determining LZO buffer layer thickness. For a reliable control of the film thickness and homogeneity, a quick non-destructive quantification method with a high spatial resolution is necessary and SEM-EDX is the method of choice.

We established two different SEM-EDX film thickness determination methods: (a) current dependent and (b) current independent. Calibration curves were generated which contain parameters of the EDX spectra as a function of buffer layer thickness. For establishing the calibration curves we analyzed four samples of different buffer layer thicknesses (from 80 nm to 325 nm) previously measured by alternative methods, i.e. ellipsometry, which has a poor spatial resolution and cross-sectional transmission electron microscopy, which is very time-consuming. SEM-EDX is particularly useful for quickly analyzing macroscopic defects in the films that are related to the a local variation of film thickness.

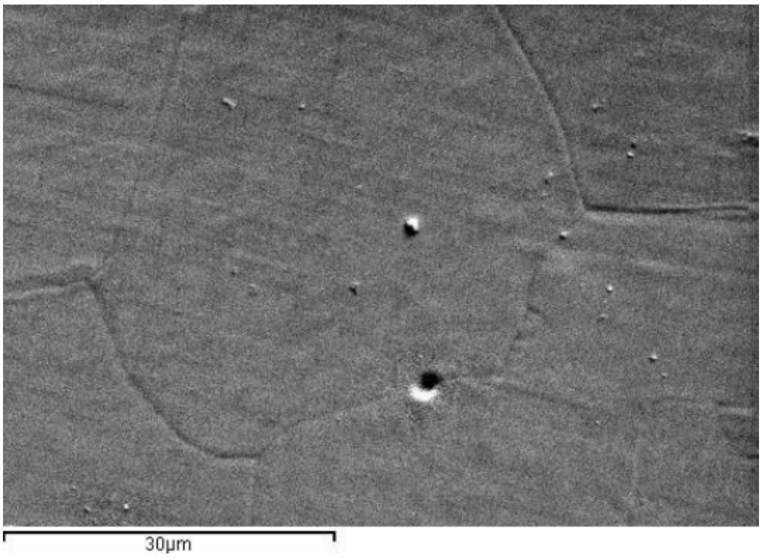

Figure 5.1: Secondary electron image of an LZO film deposited on a RaBiTS substrate.

This methodology proved to be an efficient and quick way to monitor the LZO film thickness homogeneity and quality control of the films produced at long lengths. Figure 5.1 is a secondary electron image of an LZO film deposited on a flexible nickel tunsgten substrate, the grain size of the underlying nickel substrate of ~40 µm can be seen. these are transferred as roughness to the overlying LZO film.

5.2 Experimental

Four samples of previous known thickness were choosen for generating the calibration curves (See table 5.1). Samples 1 and 2 were single layered LZO specimens and samples 3 and 4 were double layered LZO samples.

No.	Sample		Film thickness	Determined by:
1	2 x LZO Knoth (20050027)	IFW-Dresden	325 nm	TEM
2	20080019 (T231004)	ELSA	263 nm	Ellipsometry
3	2008004 (T230861)	ELSA	134 nm	Ellipsometry
4	1 x LZO (20060012)	IFW-Dresden	80 nm	TEM

Table 5.1: Four samples were chosen for the EDX measurements.

The experimental procedure included the following steps:

(i). Obtain EDX area scans (10, 20 and 30 kV) over large sample areas of 100 µm x 100 µm.

(ii). Identification of adequate EDX peaks: La-L series, Zr-L series and Zr-K.

(iii). To verify the linear dependence of netto cts vs. current for 10, 20 and 30 kV.

(iv). To measure the sample current.

Care was taken in establishing the adequate acquisition conditions. The SEM used was a Jeol JSM 6500 F provided with an Oxford EDX detector. All samples were measured under exact same probe current. Table 5.2 gives the acquisition conditions used.

Instrument	Jeol JSM 6500 F
Gun	Schottky Field emission
Emission current	~ 83 µA
Accelerating voltage (kV)	10, 20, 30
Magnification	5 K
Acquisition time (sec.)	200
Process time	4
Scan type	area
Dead time	5-30 %
Objective aperture	4

Table 5.2: SEM-EDX acquisition conditions.

5.3 Results and discussion

5.3.1 EDX spectroscopy of LZO buffer layers

The motivation for EDX spectroscopy of LZO buffer layers was (i) to obtain reliable film thickness measurements of LZO buffer layers and to (ii) check film homogeneity check over large sample areas.

The methodology used was the following (i) first we established adequate acquisition conditions for SEM-EDX, then we identified adequate EDX energy peaks in the spectra since netto counts are known to be proportional to the element concentration [83]. The goal is then to obtain a simple relationship between netto counts and film thickness.

Figure 5.2 are EDX area scans of a double layered LZO thin film on a nickel tungsten substrate taken at 10, 20 and 30 kV. Similar spectra were obtained for all sample in table 5.1. Sample areas scanned were ~100 µn X 100 µm. SEM-EDX acquisition conditions are given in table 5.2.

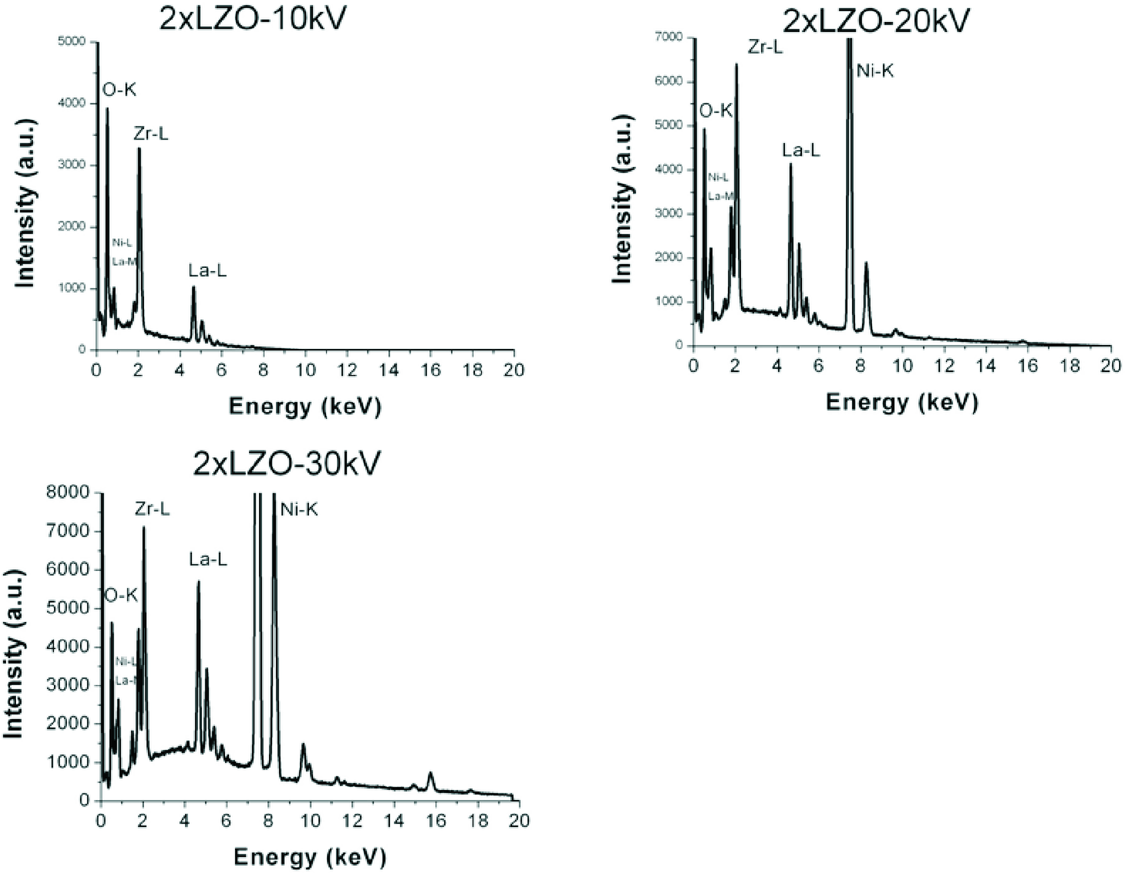

Figure 5.2: EDX area scans of a double layered LZO thin film on a nickel tungsten substrate taken at 10, 20 and 30 kV.

5.3.2 Calibration curves

Calibration curves were generated taking care to precisely measure the sample current in function of the netto counts under the La-L and Zr-L peaks. A linear dependence was shown indicating that the netto counts are proportional to the current, thus the current measurement yields reliable values consistant with EDX-line intensities (Figure 5.3).

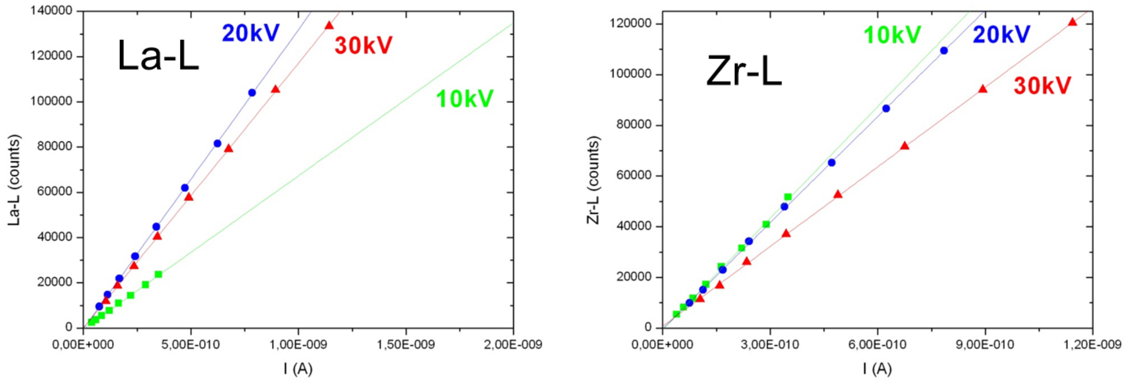

Figure 5.3: SEM-EDX calibration curves: Netto cts in function of the sample current.

5.3.3 SEM-EDX film thickness determination of LZO buffer layers

Figure 5.4 shows EDX area spectra of the La-L peaks for samples with different layer thickness.$La-L\alpha1$ lies at 4.651 keV, $La-L\beta1$ at 5.0049 keV,$La-L\beta2$ at 5.393 and $La-L\gamma1$ at 5.771 keV. Figure 5.5 is the same for the Zr-L series with $Zr-L$ at 1.798 keV and$Zr-L\alpha1$ at 2.049, due to the overlapping of the lines it is difficult to obtain netto counts under each peak.

The possible sample current independent ratios for film thickness estimation are given by the following ratios:

(i)$La-L\alpha1$ to background
(ii) $Zr-L\alpha1/Zr-L1$
(iii) $O-K/Ni-L$
(iv) $O-K/La-L\alpha1$

The $La-L\alpha1$ / background ratio is the most reliable, since La peaks can be easily resolved. Zr-peaks overlap.

Table 5.3, 5.4, 5.5 are normalized netto counts for several peaks relevant for possible ratios for film thickness estimation.

30 kV	Thickness	O-K	Ni-L	Zr-L	La-L
2XLZO	325	3.47	1.44	10.45	11.65
20080019	263	3.20	2.55	8.72	9.97
20080004	134	1.77	5.47	4.66	3.73
20060012	80	0.77	13.09	2.48	1.18

Table 5.3: Table of normalized netto counts for 30 kV. Data was normalized to sample current [10^4 cts/nA].

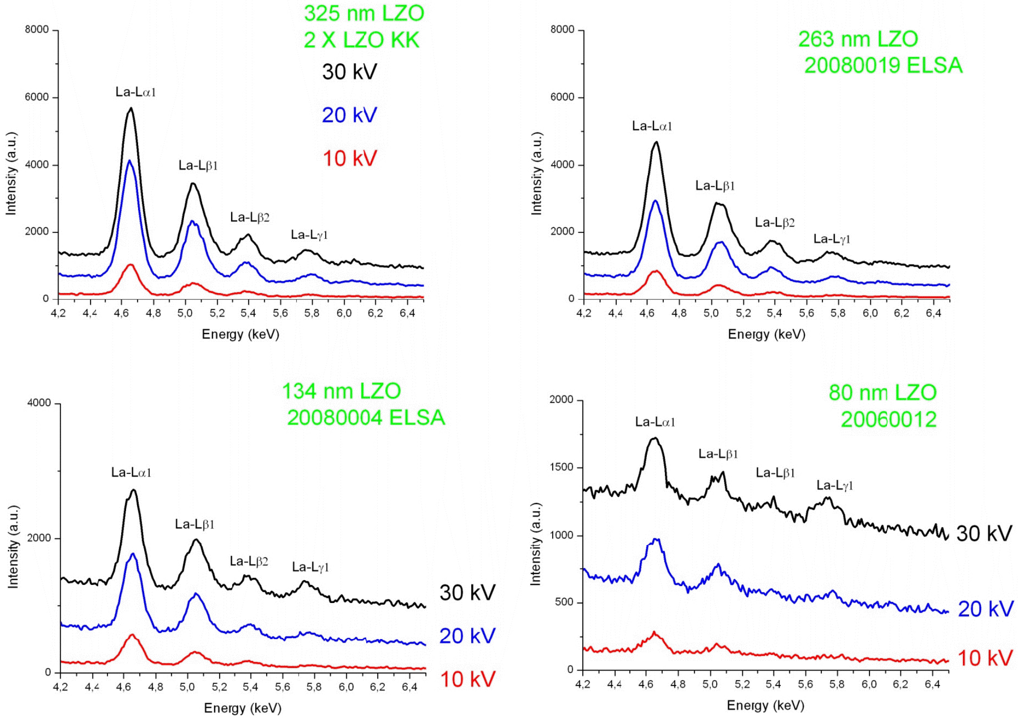

Figure 5.4: La-L series

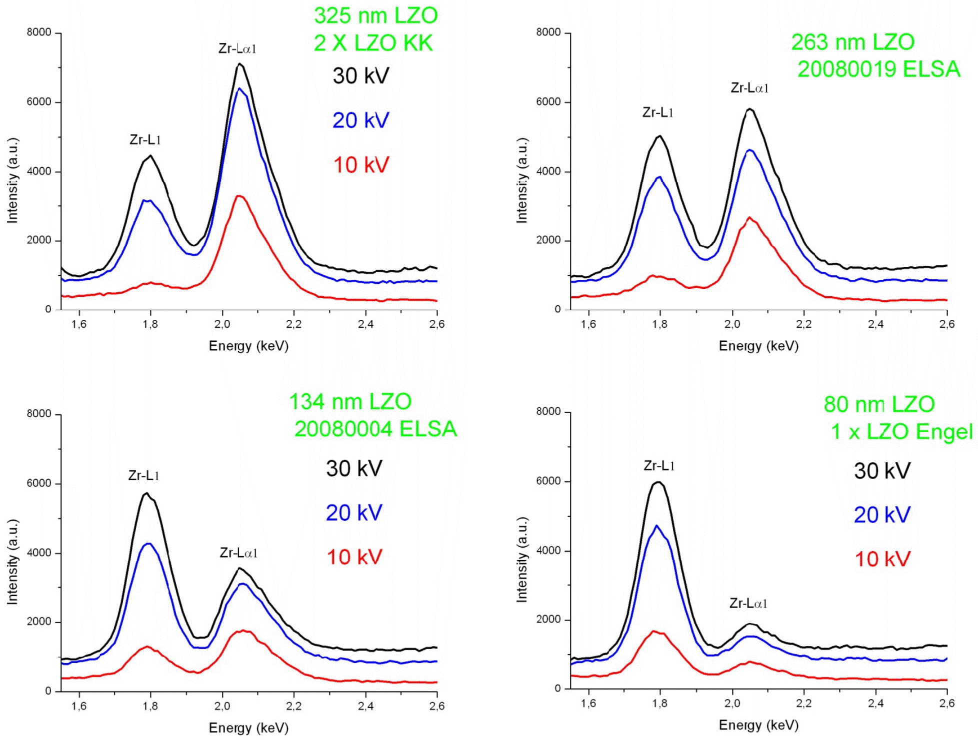

Figure 5.5: Zr-L series

20 kV	Thickness	O-K	Ni-L	Zr-L	La-L
2XLZO	325	5.40	1.58	13.54	13.02
20080019	263	4.82	3.71	10.17	8.83
20080004	134	2.71	7.14	6.24	4.24
20060012	80	1.08	17.06	3.05	1.35

Table 5.4: Table of normalized counts for 20 kV. Data was normalized to sample current [10^4 cts/nA].

10 kV	Thickness	O-K	Ni-L	Zr-L	La-L
2XLZO	325	9.08	1.01	13.90	6.29
20080019	263	9.25	2.59	12.38	5.84
20080004	134	6.04	7.11	8.23	3.47
20060012	80	0.64	6.07	1.07	0.33

Table 5.5: Table of normalized counts for 10 kV. Data was normalized to sample current [10^4 cts/nA].

Figure 5.6 are normalized counts under the La-L peak plotted in function of the film thickness. At 20 and 30 kV data can be fitted with a linear curve, giving a good estimate for the film thickness.

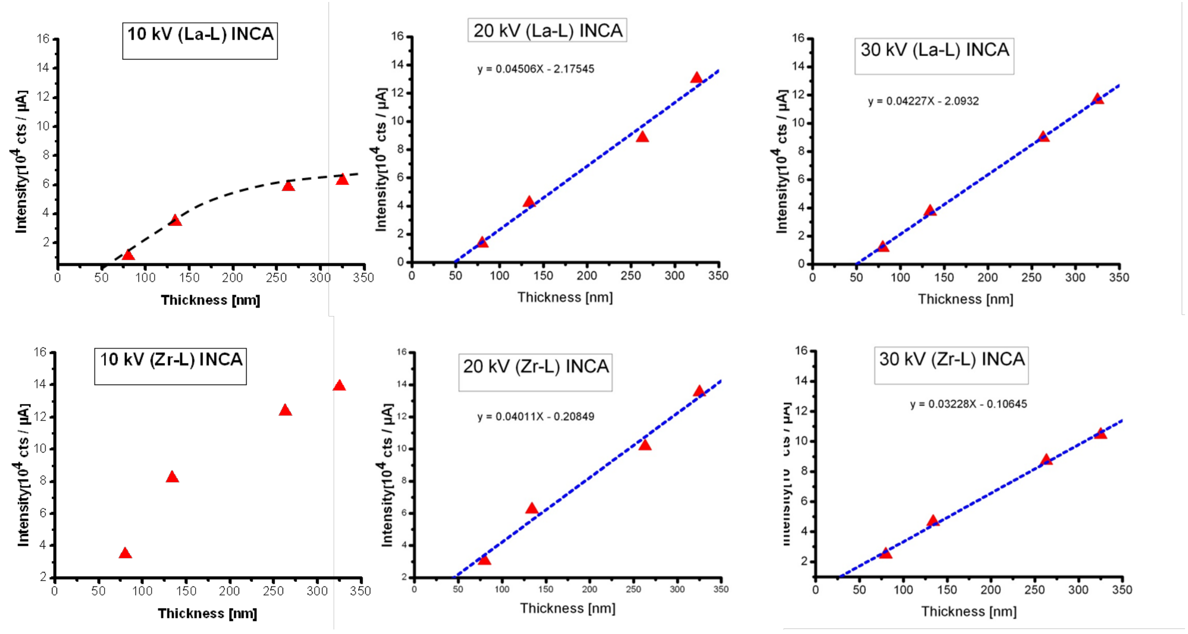

Figure 5.6: La-L and Zr-L counts in function the film thickness.

5.4 Conclusions

We performed a thickness investigation of four LZO/Ni samples (325nm, 263nm, 134nm, 80nm). All samples were measured under the same acquisition conditions using a FE-SEM provided with an Oxford EDX detector and EDX area scans were made (sample areas of 100 x 100 µm).

A linear behavior of netto cts vs. sample current was confirmed. La-L peaks can be manually evaluated, but an offset is observed. Zr-L series are more difficult to manually evaluate due to peak overlapping. Zr-K1 can be manually evaluated, but only spectra taken at 30 kV can be used (very low cts 500 cts). Zr-L and Zr-K give same offset of 25 nm. Provided a reference sample, the LZO film thickness can be determined by measuring the netto cts from the La-L peaks and La-L / Background. Overall sample homogeneity can be checked by performing EDX area scans of different sample areas.

However, still unsolved remains: (i) the reason for the offset (ii) Zr-L series behaviour is not understood (iii) detector efficiency is not taken into account and (iii) Ni-K, Ni-L series were not taken into account for the estimation. We therefore established a preliminary empirical method for film thickness determination by SEM-EDX. This is a starting point for a more reliable film thickness determination method and film thickness simulations by Monte Carlo methods.

Chapter 6

Nano-scaled chemical analysis of solution derived YBCO coated conductors

6.1 Preview

Solution derived $YBa_2Cu_3O_{7-\delta}$ (YBCO) coated conductors prepared by the chemical solution deposition process (CSD) are currently of interest for the fabrication of low cost coated conductors for long scale production using flexible nickel-tungsten substrates. In this study we present a TEM thin film and chemical phase analysis of coated conductor samples with Ni5at%W (substrate) / $La_2Zr_2O_7$ (CSD) / CeO_2(CSD) / YBCO (CSD) layer architecture.

The chemical composition and distribution within the samples was studied by inelastic electron scattering in a energy-filtered transmission electron microscope (EFTEM). Electron energy loss spectroscopy (EELS) allows to distinguish between the different phases present. By electron spectroscopic imaging (ESI) chemical distribution maps with high lateral resolution of YBCO-coated conductor samples in cross-section and plan-view were obtained. This method is suitable for identifying performance-limiting and or pinning defects found in the superconducting layer, understand their origin and develop methods to control them during sample fabrication. Layer interfaces were identified.

The samples studied in this contribution presented Y_2O_3, CuO, Y, Ba and Cu rich secondary phases. The nanostructure differs from that of PVD deposited films, i.e. (i) a larger number secondary phases on various length scales and (ii) surface segregation of secondary phases relevant for multilayer deposition are observed. By taken advantage of the finger print features in the low-loss EELS spectra, Y_2O_3 precipitates were mapped and quantified. A new and efficient chemical mapping method yielding high accuracy was established by FIB prepared TEM lamellae in combination with elemental maps acquired by energy-filtered transmission electron microscopy (EFTEM).

Electron spectroscopic imaging (ESI) was performed on both, cross-sectional TEM specimens prepared by conventional grinding, polishing and Ar+ ion milling as well as by the in-situ lift-out Focused Ion Beam technique (FIB). The TEM lamella prepared by FIB presented increased signal to background intensity ratio and less sample thickness variation in comparison to the conventionally prepared specimen, making it especially suitable for ESI. The chemical maps were assessed by point measurements using energy dispersive X-ray microanalysis (EDX) and electron energy-loss spectroscopy (EELS).

6.2 Introduction

Large attention has been given to the chemical solution deposition process (CSD) as a cheap way of preparing $YBa_2Cu_3O_{7-\delta}$ (YBCO) coated conductors deposited on flexible nickel-tungsten substrates for industrial applications [29]. Efforts have concentrated in understanding the complex growth process of such solution prepared thin oxide films on flexible nickel-tungsten substrates, especially the growth and biaxial texturing of $La_2Zr_2O_7$ (LZO) and CeO_2 buffer layers have been studied in detail [76, 66, 78, 84, 85, 80, 65, 86]. A Ni5at%W substrate is dip coated twice in a LZO precursor solution, afterwards a single CeO_2 layer is deposited and finally a superconducting YBCO double-layer is grown on top. In this study we present a detailed nano-scaled chemical analysis of complete solution derived YBCO coated conductor samples.

Chemically deposited YBCO superconducting films have a large density of defects and secondary phases which have to be identified and quantified in order to determine if they are performance limiting defects and/or improve the pinning properties of the film. Performance limiting secondary phases have to be eliminated or minimized during film deposition. Thus, a chemical phase analysis at the nanometer scale is essential in order to identify these. Reports found in the literature deal mainly with scanning transmission electron microscopy (STEM) X-ray mapping [87, 88, 89] and Z-contrast imaging of coated conductors [25].

Images formed by elastic scattered electrons are limited mainly to diffraction contrast imaging and there is no change in the internal energy of the probe and the specimen. On the other hand, inelastic scattering deals with momentum transfer and electron energy-loss. Energy-filtering transmission electron microscopy (EFTEM) relays on the analysis of inelastic electron scattering in the TEM [90, 39, 46]. By choosing an appropriate energy window the electrons that form an image can be selected according to their energy-loss providing chemical information about the sample.

For energy-filtering TEM, two types of energy filters exist, the in-column omega energy filter from Zeiss [91] and the GIF post-column filter from Gatan [92]. For this study a Zeiss 912 Ω provided with an omega energy filter and a thermal emitter was used. The omega filter is located after the objective lens, this is an advantage over TEM provided with GIF filters, since it avoids further lens aberrations, however, transmission electron microscopes provided with a FEG allow for higher spatial resolution than in the case of those with thermal emitters ($LaBa_6$).

Studies concerning electron spectroscopic imaging (ESI) applied to superconducting materials have not been widely reported in the literature. Quantitative EFTEM reports of such systems found deal mainly with multilayer structures i.e., the understanding of the growth mechanism of complex ionic oxides exhibiting superconducting properties as reported by Grogger *et al.* [93], where alternating YBCO and PBCO high-temperature superconducting multilayers were investigated. Work has also been done with STEM techniques to perform spectroscopic imaging of oxide interfaces in $YBa_2Cu_3O_{7-\delta}/PrBa_2Cu_3O_7$ [94].

The importance of quantitative electron microscopy methods for the systematic study of superconducting wires and tapes has been shown in a recent topical review from Birajdar *et al.* [95], where electron spectroscopic imaging combined with other advanced TEM techniques are used for the understanding of the thermodynamics of phase formation in MgB_2, as well as for improving the synthesis technology and superconducting properties.

A phase analysis study of superconducting polycrystalline MgB_2, by ESI can be found in [96]. The intergrowth of $(Bi,Pb)_2Sr_2CaCu_2O_{8+\delta}$ and $(Bi,Pb)_2Sr_2CaCu_2O_{10+\delta}$ superconducting phases on the nano-scale has also been investigated by electron spectroscopic imaging in the TEM [97]. The electronic and crystal structure of YBCO has been extensively studied using electron-energy loss spectroscopy (EELS) with high lateral resolution [98, 99, 38, 100]. However, few reports exist were electron spectroscopic imaging (ESI) has been applied on YBCO coated conductors [101].

6.3 Experimental details

TEM specimens from two YBCO-coated conductor tapes prepared by partners at IFW-Dresden and at Zenergy Power in Rheinbach were made (see table 6.1). In both cases, the buffer layers were prepared by chemical solution deposition (CSD) [63], and the YBCO film was prepared by the TriFluoroAcetate (TFA) process [102, 26]. The major advantage of this fluorine-based process is the suppression of the formation of the highly stable critical current degrading intermediate $BaCaO_3$ through the formation of thermodynamically more stable BaF_2. During the precursor solution synthesis, trifluoroacetates are formed from metal (metal: Y, Ba, Cu) acetates dissolved in de-ionized water and trifluoroacetic acid.

The resulting aqueous solution is refined to yield a glassy blue gel and dissolved in methanol to form the final coating solution. During pyrolysis, a film micro-structure of CuO nanocrystallites embedded in an amorphous oxyfluoride Y-Ba-O-F matrix is formed, which is subsequently converted into the highly textured YBCO phase during annealing at temperatures between 725°C and 850°C. A following oxygen annealing below 500°C is required to dope the superconductor to yield a high Tc. Reproducible high critical current carrying YBCO layers could be obtained by this process [102, 26].

Both YBCO coated conductor samples investigated in this section hadj_c´s of about 1 MA/cm² (see chapter 8, table 8.1). Two TEM lamellae of sample 1 were prepared as TEM cross-sections by conventional grinding, polishing and Ar+ ion milling [65] and by the in-situ lift-out Focused Ion Beam (FIB) technique. Sample 2 was prepared in plan-view manner by conventional ion milling.

Sample	Deposition	Architecture	Specimen preparation	Geometry	Partner
1	CSD	$Ni/2 \times LZO/CeO_2/YBCO/Au$	Conv.	Cross-section Plan-view	IFW
1	CSD	$Ni/2 \times LZO/CeO_2/YBCO/Au$	FIB	Cross-section	IFW
2	CSD	$Ni/2 \times LZO/CeO_2/YBCO$	Conv.	Plan-view	Zenergy

Table 6.1: Overview of the samples analyzed.

6.3.1 Sample preparation

Flexible cube textured Ni5at%W substrates of 80 micrometer in thickness and 1 cm in width were used as substrates [27]. Details on substrate preparation can be found in [66]. The re-crystallized substrates were cleaned in both an ultrasonic acetone and a isopropanole bath for 20 min. The substrate was dip-coated twice in a LZO precursor solution as described in [66] followed by a CeO_2 layer. TEM cross-sections of example layer architectures have been previously studied [78].

To prepare the YBCO precursor solution, metal trifluoroacetates in their stoichiometric ratios are dissolved in a 0.25 m methanol containing solution [103]. The yttrium ion concentration is 0.25 m. The coating process is then carried out at room temperature in a laminar flow box, the buffered substrate is dipped into the precursor and drawn out vertically upwards with a velocity of 1 cm/s. The tape length at this stage is 5 cm long. After 5 min the procedure is repeated. The sample is then transferred to the tube furnace and heated. In this way the first YBCO coating is deposited and pyrolysis takes place at 400°C. Afterwards, the sample is dip-coated once again and both layers are pyrolyzed at 400°C. For the Zenergy Power samples, preparation procedures were similar, but all proceses are upscaled for long length production.

6.3.2 Pre-characterization by SEM-EDX

For surface characterization of YBCO coated conductor samples on the micrometer scale a JEOL 6500 F scanning electron microscope (SEM) equipped with a field emission gun and a Si Oxford detector was used. In the examples shown here EDX elemental maps and area maps of Y, Cu, Ba and O were acquired. Typical acquisition conditions are given in table 6.2.

Peak	$Y - L\alpha_1$	$Cu - L\alpha_1$	$O - K\alpha_1$	$Ba - L\alpha_1$
Energy (keV)	1.932	0.934	0.520	4.466
Acceleration voltage	5 -20 kV			

Table 6.2: SEM-EDX example acquisition conditions.

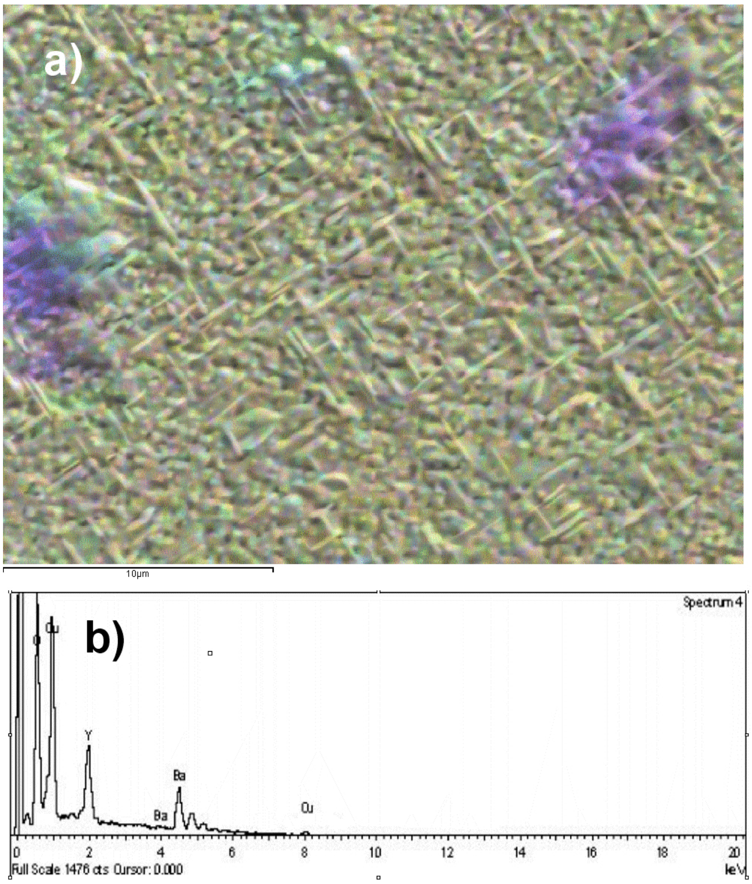

Figure 6.1: Sample 1 a.) SEM-EDX chemical mapping at 10 kV. RGB image : R (Y) G(Cu) B (Ba). Scale bar is 10 µm b.) EDX point spectrum within the YBCO matrix.

Point spectra were evaluated using INCA software [69]. RGB images were formed by combining three different elemental maps. Figure 6.1 (a) shows a R(Y)G(Cu)B(Ba) image of a CSD prepared YBCO coated conductor with an acquisition time of 3000 sec. Y-rich areas can be found and a-axis areas in the YBCO film are observed. Figure 6.1 (b) is a EDX point spectrum taken within the YBCO matrix with 10 kV, Cu-L, Y-L and Ba-L peaks are observed. Figure 6.2 is R(Y)G(Cu)Ba(O) image of sample 2 taken at 5 kV. Taking advantage of the Cu-L and O-K peaks, CuO particles of 0.5-1 µm in size could be clearly mapped.

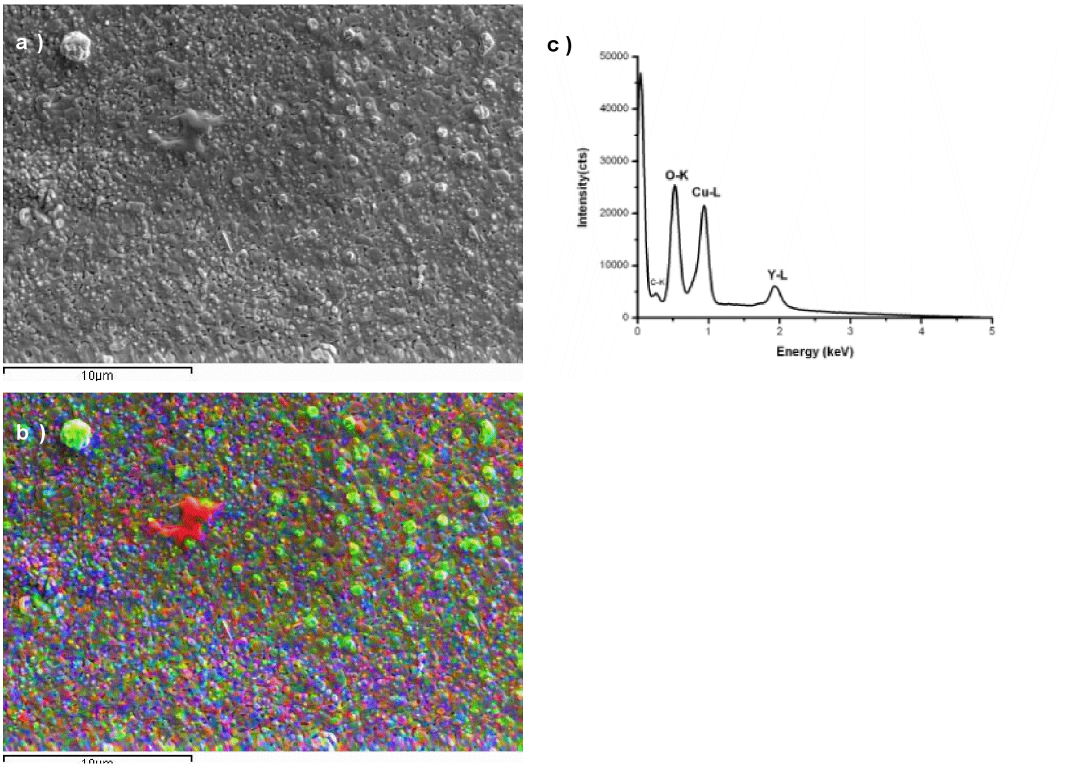

Figure 6.2: Sample 2. a.) Secondary electron image of sample 2. b.) SEM-EDX chemical mapping at 5kV. RGB image : R (Y) G(Cu) B (O). Scale bar is 10 μm, CuO rich particles can be seen (green dots, upper right). scale bar is 10μm c.) EDX area spectrum. O-K, Cu-L and Y-L peaks are seen.

6.3.3 TEM preparation

Conventional method

Sample 1 was prepared for transmission electron microscopy (TEM) by conventional mechanical polishing and ion milling in cross-section and plan-view manner. The cross-section specimen was glued between barium titanite and silicon dummies followed by mechanical polishing and grinding until reaching 20 m in thickness. Afterwards the specimen was further thinned using Ar+ ions in a Baltec Res 100 ion milling machine operating at 4.5 kV and 3.5 mA with etching angles ranging from ±12° to ±6° for up to 20 hrs.

The plan-view sample was mechanically polished and grinded from the substrate side only until reaching 20 μm in thickness, then further thinning was done using a single Ar+ ion beam operating at 4.5 kV and 3.5 mA with an etching angle of ±12° and with a final etching step at ±6° until electron transparent areas were obtained. Sample 1 had a 30 nm thick Au gold protection layer on top, before proceeding to TEM plan-view sample preparation chemical etching was done in order to remove the Au layer. During this procedure the sample was dipped in a etching solution for less than 1 min until the Au layer was removed obtaining Au free electron transparent areas. Sample 2 had no protection layer.

Focused ion beam (FIB) in-situ lift out method

Sample 1 was also prepared by the in-situ lift-out Focused Ion Beam (FIB) method at the IFW-Dresden using a Zeiss cross-beam 1540 XB operating at 30 kV. Figure 6.3 (a) shows the area of interest on the

YBCO film were a Pt protection layer was deposited. Trapezoid shaped cuts were made with a Ga-ion beam as seen in figure 6.3 (b). After thinning the lamella of the area of interest a nano-manipulator was used to lift-out the specimen and attach it to a sample holder, see figure 6.3 (c-f). After attachment, the lamella was further polished with 3 kV and 500 pA until reaching a final thickness of 100 nm as shown in figure 6.3 (f).

The advancement achieved in recent years in the implementation of the focused ion beam techniques for TEM sample preparation has proven it to be a useful technique for preparing specimens that are especially suitable for electron spectroscopic imaging (ESI) in an EFTEM because of the homogeneously thinned electron transparent lamellas obtainable.

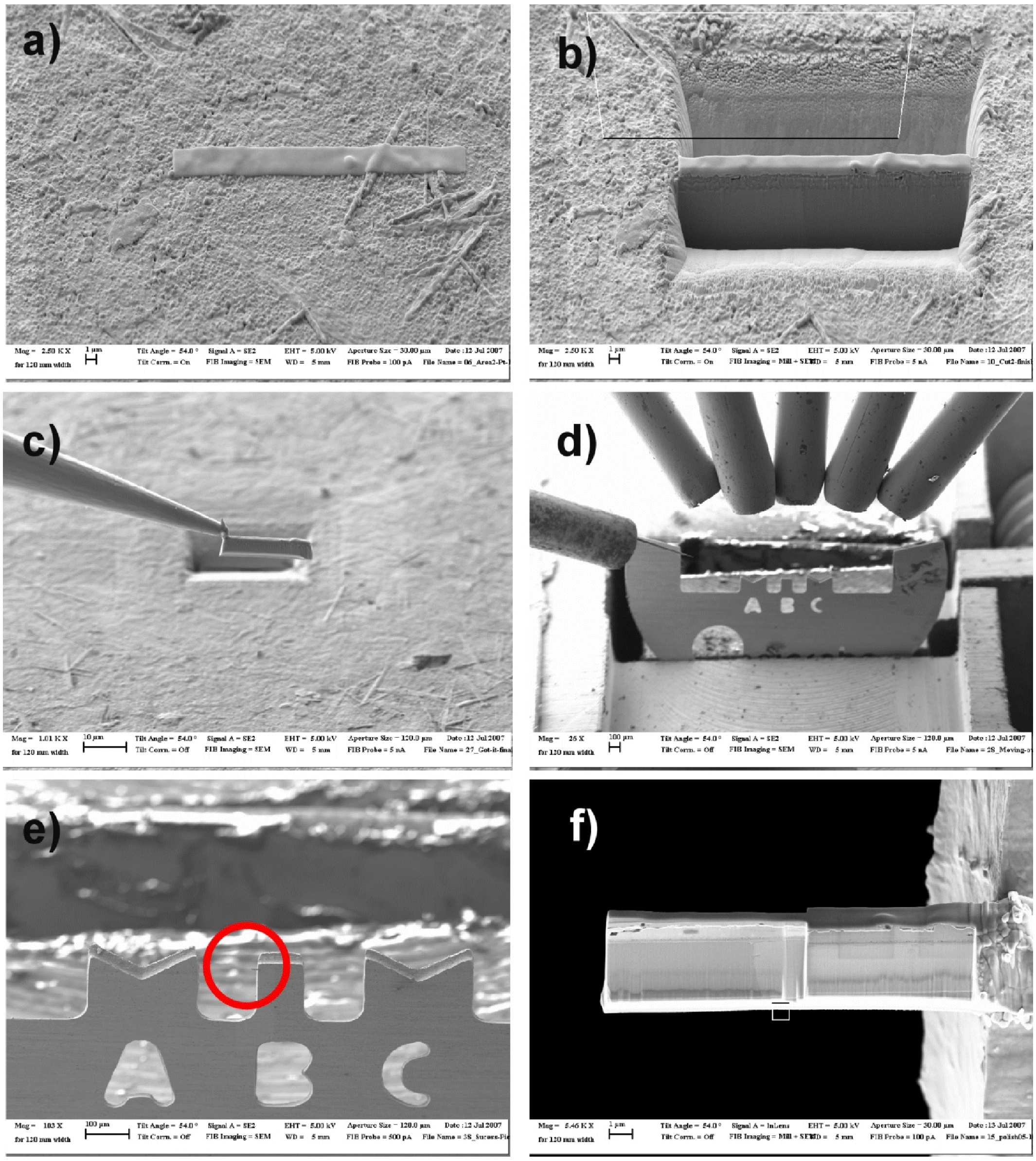

Figure 6.3: Sample number 1. FIB lamellae preparation process a.) Pt protection layer deposited on the area of interest on top of the YBCO film. Scale bar is 1 µm and a-axis growth can be observed on the area of interest. b.) Trapezoid shaped cuts made with the Ga-ion beam. Scale bar is 1 µm c.) In-situ lift out of the TEM lamella done with a nano-manipulator. Scale bar is 10 µm d.) Attachment of the TEM lamella to the half-grid sample holder. Scale bar is 100 µm e.) Encircled area shows were the sample was attached. Scale bar is 100 µm f.) Overview of the low-voltage polished final TEM lamella. Scale bar is 1 µm.

The technique is widely established for studying the microstructure of semiconductor devices with elemental mapping and energy-loss fine structure analysis [92]. However, there are no extensive studies in the literature dealing with ESI of YBCO coated conductors prepared by FIB [101]. Energy filtering benefits from FIB preparation techniques since it allows the rapid preparation of large areas of uniform thickness, as shown in figure 6.4.

However, correction for multiple scattering is needed when performing extensive quantification of large sample areas as in the case of low-magnification ESI of YBCO-coated conductors. We present results on both conventionally prepared and FIB prepared TEM cross-sections.

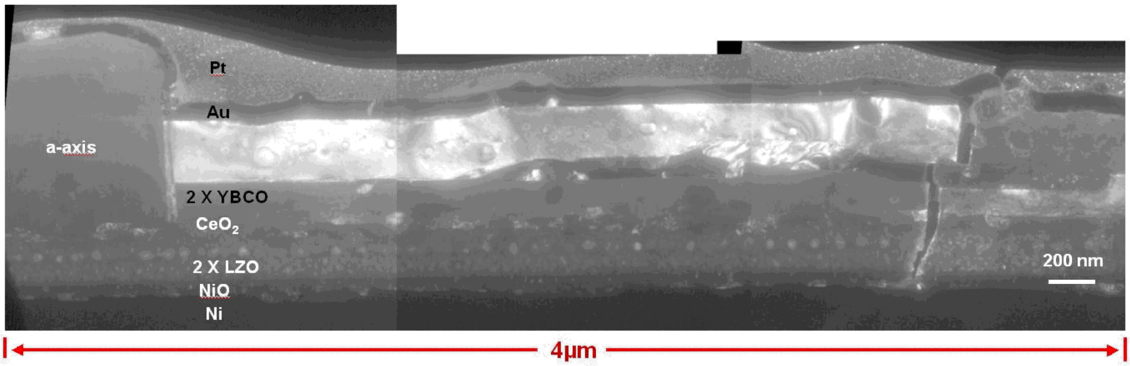

Figure 6.4: Sample 1. Dark-field TEM image under two-beam conditions of the FIB prepared lamellae (4µm in length). A-axis growth can be observed, it starts at the first YBCO layer.

6.3.4 Electron energy-loss spectroscopy (EELS) and electron spectroscopic imaging (ESI)

EELS and ESI was performed on a Zeiss 912 Ω energy-filtered transmission electron microscope operating at 120 kV. The TEM is equipped with an omega energy filter, with which parallel EELS and ESI can be performed. A $LaBa_6$ filament is used, limiting the possible lateral resolution for both methods. An energy resolution of about 1.0-1.5 eV can be achieved with this instrument.

For the acquisition of energy filtered images, the momentum transfer is controlled by the objective aperture and the energy-loss by the placement of an energy slit in the energy dispersive plane of the energy filter. For energy spectroscopic imaging the three window method was used [90]. An image is taken after a suitable ionization edge of the corresponding element (post-edge image, ΔE3), two additional images corresponding to pre-edge 1 (ΔE1) and pre-edge 2 (ΔE2) are recorded at energy losses smaller than the ionization edge of interest [55, 104]. Only the electrons passing through the selected energy slit contribute to these images. The pre-edge images are used for an approximate determination of the unspecific background which is then subtracted from the post-edge image leading to an elemental map with enhanced contrast.

All images were taken with an energy slit of 10-15 eV in width. The processing and acquisition of conventional TEM images and ESI images was done using the Esivision software (2002) from SIS. The microscope is directly connected to a PC on which the Esivision software is running.

6.3.5 Energy dispersive X-ray micro-analysis (EDX) in the TEM.

Also attached to the Zeiss 912 Ω is a Si (Li) EDX detector with an ultra-thin window. EDX spectra were acquired and quantitatively analysed using INCA 4.01 software (2001) from Oxford instruments [69]. The EDX detector operates with a digital pulse detector. The EDX spot size was 10 nm and acquisition time was 100-200 s. All EDX spectra were taken in a range from 0-20 keV. The k-factors used were 1.457 for Cu-K, 1.708 for Y-L and 2.05 for Ba-L. Due to the good vacuum within the microscope, contamination and artefacts could be avoided without cooling the sample. However, a cold finger was maintained in the microscope column at liquid nitrogen temperature.

6.4 Results

6.4.1 Bright and dark-field imaging

Figure 6.5 (a) shows a zero-loss energy filtered bright-field image of sample 1 in cross-section. The different layers (2 x LZO, CeO_2, 2 x YBCO) can be clearly distinguished. A high density of dislocations can be observed in the flexible nickel-tungsten substrate. A NiO interface layer between the substrate and the overlying LZO buffer layer could be identified. Between the two LZO layers nanovoids 40 nm in size are formed. Bright regions that correspond to secondary phases can be identified in the two YBCO layers as denoted by 1, 2 and 3 denoted in figure 6.5 (a).

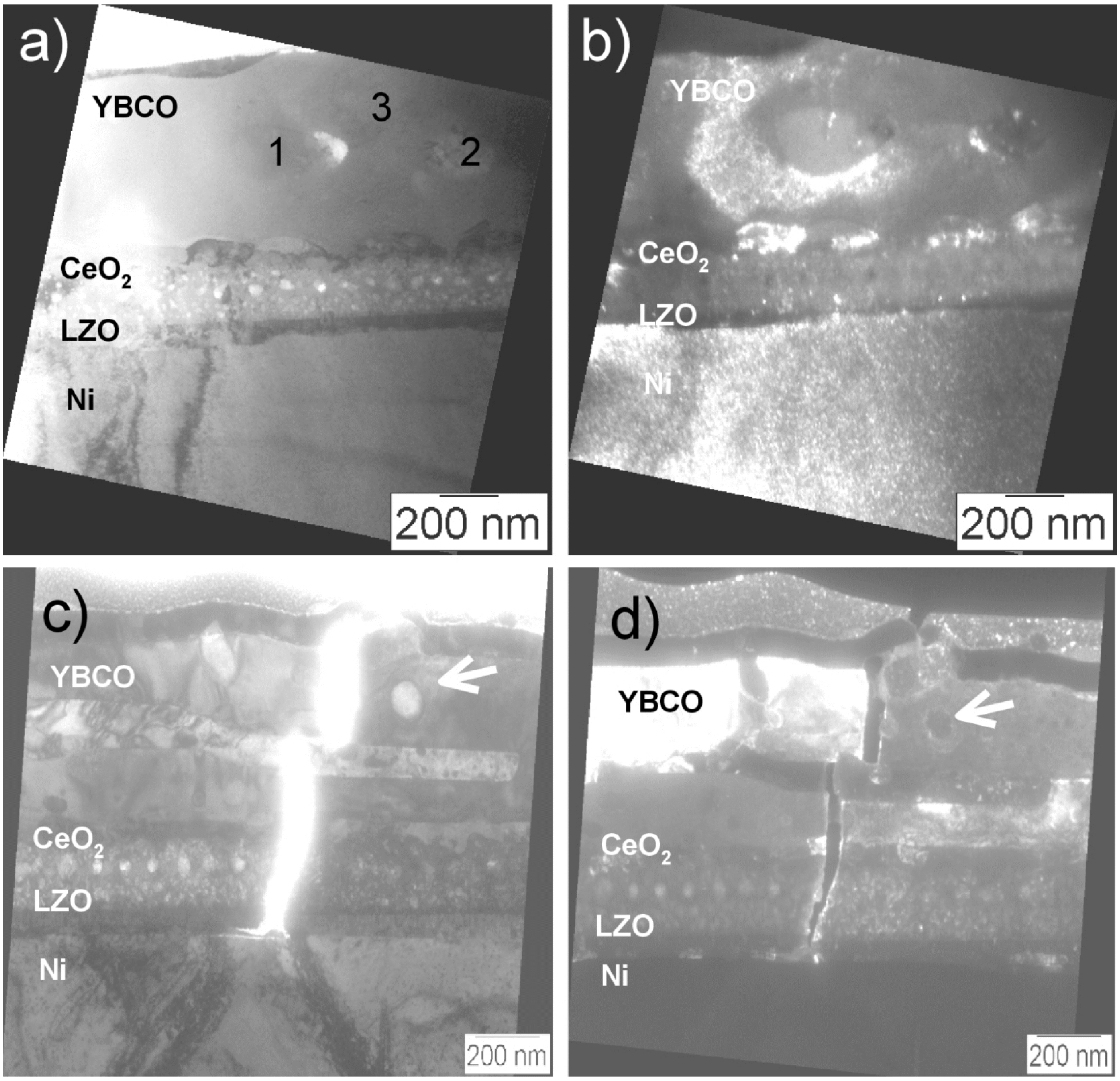

Figure 6.5: a.) Zero-loss bright-field image of sample 1 in cross-section. b.) Corresponding dark-field image. c.) Zero-loss bright-field image of sample 1 (FIB prepared TEM lamella) d.) Corresponding dark-field image.

The corresponding dark-field image taken under two-beam conditions with the (200) Ni reflection is shown in figure 6.5 (b) where this becomes more apparent. Figure 6.5 (c) is zero-loss energy filtered bright-field image of specimen 2 prepared by in-situ-lift-out FIB. Figure 6.5 (d) is the corresponding dark-field image of the same area under two beam conditions shown in figure 6.5 (c). The white arrow indicates a secondary phase. The crack observed in the images (6.5 c-d) is not due to the FIB sample preparation and appeared only after specimen transfer from the FIB to the TEM.

6.4.2 EELS

In table 6.3 are the corresponding edges, their energy losses and the characteristic angles for elements relevant to CSD YBCO coated conductors. Relevant acquisition conditions are given in table 6.4. EELS and ESI are strongly linked, before performing ESI, EELS acquisition conditions were optimized according the respective energy-loss to be used for absorption edges relevant for YBCO coated conductors.

Z	Element	Edge	Energy-loss (eV)	$\Theta_E(mrad)$
8	O	K	532	2,21
28	Ni	L1, L2, L3	1008, 872, 855	4.20, 3.63, 3.56
29	Cu	L1, L2, L3, M2,3 M4,5	1096, 951, 931, 74.3, 72	4.56, 3.96, 3.87, 0.31, 0.30
39	Y	M3, M4, N2, N3	301, 160, 29, 26	1.25, 0.66, 0.12, 0.11
40	Zr	M3, M4, N2,3	331, 183, 29	1.37, 0.76, 0.12
56	Ba	M4, M5, N4, N5	796, 781, 93, 90	3.31, 3.25, 0.387, 0.375
57	La	M4, M5, N4, N5	849, 832, 99, 97.7	3.53, 3.46, 0.41, 0.40
58	Ce	M4, M5, N4, N5	902, 884, 111, 107.6	3.75, 3.68, 0.46, 0.44
74	W	M4, M5	1872, 1810	7.8, 7.54

Table 6.3: Ionization edges, corresponding energy losses and characteristic angles relevant for the corresponding ionization edges.

The low-loss region of the EELS spectrum is useful for identifying Y and Cu secondary phases in the YBCO matrix and distiguishing between matrix areas and secondary phases, whereas the core-loss region provided useful information when investigating full YBCO coated conductors in cross-section, which included the superconducting layer, the buffer layers and the nickel tunsgten substrate.

Spec.	Bias	Spot size (nm)	Obj.aper.(mrad)	Spec. mag.	Acq. time	Time int.
Low-loss	8-9	10-20	3.5	19.5x, 40 x, 63x	50-100 ms	Yes
Core-loss	9	100	8.1/13.5	19.5x, 40 x, 63x	1-10 s	No
Wide-range	9	100	13.5	19.5x, 40 x, 63x	1-10 s	No

Table 6.4: Applied acquisition conditions for EELS.

Low-loss EELS

Low-loss EELS was performed for the phase mapping of nanometer sized Y_2O_3 precipitates and CuO nanoparticles in TFA-YBCO films. Understanding the key features in the low-energy part of the spectrum are important for optimizing ESI images when using the corresponding energy losses. Maping of nanometer sized nanoparticles using the Y-N2,3 edge found at 26 and 29 eV has been shown previously by Lozano-Pérez et.al. [105]. For all spectra shown here the smallest objective aperture with 3 mrad collection-angle was used.

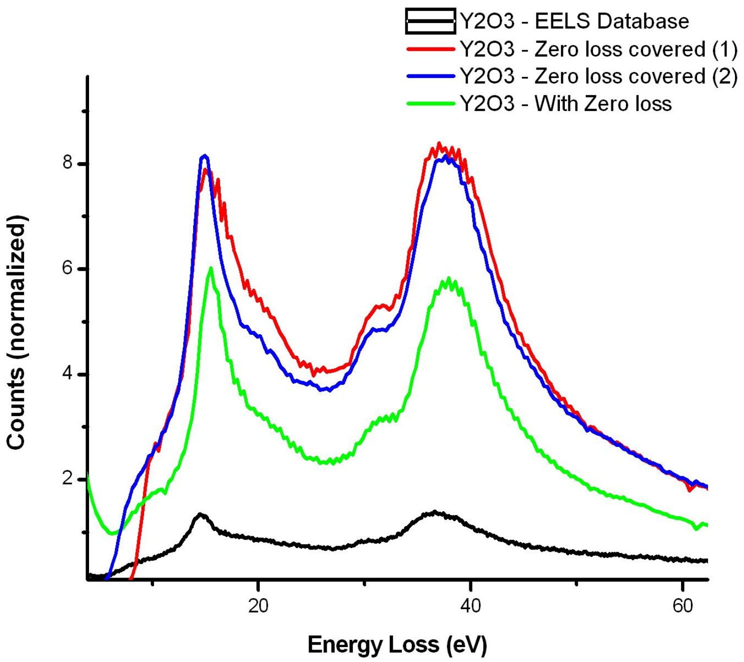

Figure 6.6: Low-loss EELS of a Y_2O_3 precipitate.

Phase	Peak position (eV)		
Y_2O_3	E_p	Shoulder	$Y\ N(2,3)$ Peak
Spectrum 1	14.9	31	37,9
Spectrum 2: with ZL peak	15.5	31.4	37.9
Spectrum 2: ZL peak covered	15.5	31.6	38
Data base	14.5	30.7	36.5

Table 6.5: Features of the Low-loss EELS spectra of Yttria.

Figure 6.6 shows the low-loss spectra of a Y_2O_3 precipitate, relevant features are denoted in table 6.5. The plasmon peaks lays at 15 eV and the Y N2,3 edge starts at 26 eV, a shoulder is found at 30 eV and a peak at 37 eV. Plotted are normalized data sets including a spectra from the EELS database [106] showing that spectra fit very well to Yttria. By covering the zero loss beam, the signal to background (SBR) could be slightly improved.

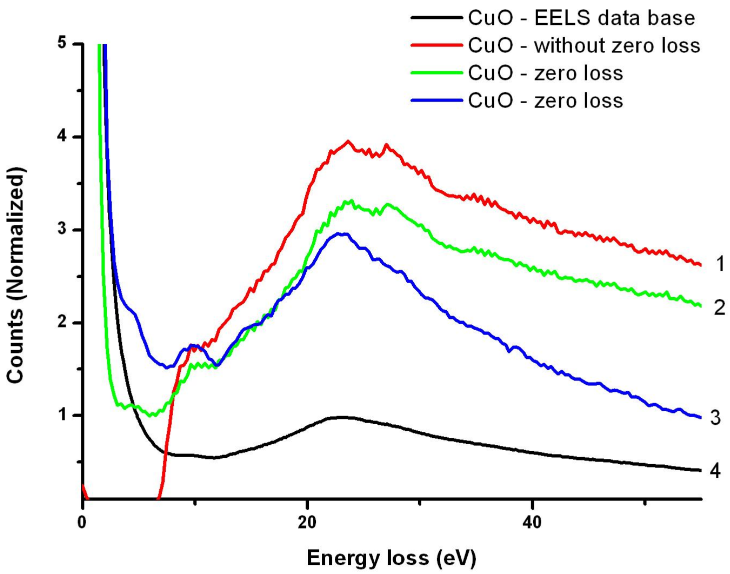

Figure 6.7: Low-loss EELS of a CuO phase.

Phase	Peak position (eV)
CuO	Peak
Spectrum 1: zero loss	23.5
Spectrum 2: zero loss	23.6
Spectrum 3: with zero loss	23.3
Spectrum 4: EELS Data base	23

Table 6.6: Low-loss EELS of CuO.

Figure 6.7 are the low-loss spectra of a CuO phase (table 6.6). Figure 6.8 are the low-loss EELS of the YBCO matrix, three characteristic features are found (Table 6.7). The Low-loss region and the correspondindg fine structure has been previously studied in detail by Fink. et.al [99] and Yuan et.al.[100] using energy resolutions of 0.1 and 0.5 eV respectively. (a) in figure 6.8 corresponds to a partial valence electron plasmon at 13.3 eV. (b) at figure 6.8 at 25.5 eV corresponds to a highly damped valence electron plasmon and (c) of figure 6.8 to a ionization edge due to a transition from Y(4p) to Y(4d) electrons. For this study we are limited by the energy resolution of the instrument used (|>1 eV)

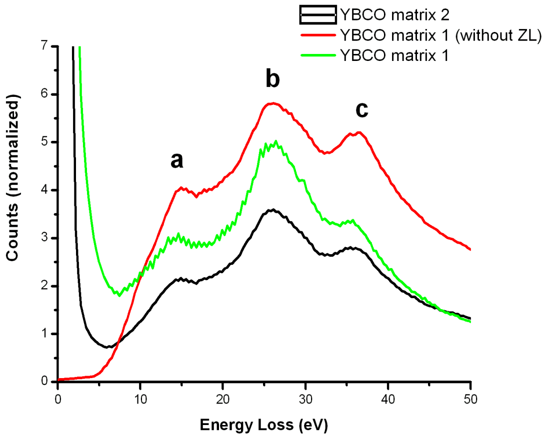

Figure 6.8: Low-loss EELS spectra of the YBCO matrix.

	Our data	Yuan et.al. (1987)	Fink et.al. (1990)	Origin
a	14.5	14.7	14	Volume plasmon
b	25.9	25.5	25.3	Volume plasmon
c	35.5	34.8	35.0	Y 4p to 4d (YN2,3 edge)

Table 6.7: Low-loss EELS of YBCO.

Figure 6.9 are spectra showing all relevant phases. From the EELS spectra local sample thickness could be estimated using the Esivision software [43]. In this case Y_2O_3 was 98 nm, $YBCO$ matrix 1 was 51 nm, $YBCO$ matrix 2 was 60 nm and CuO was 223 nm.

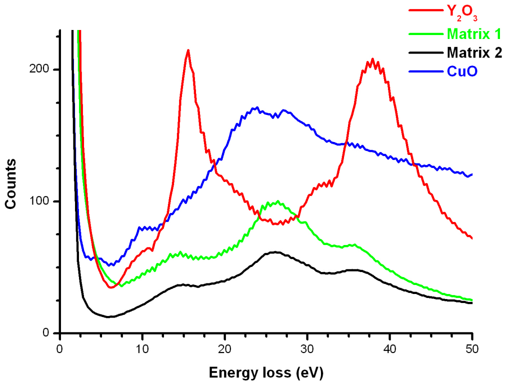

Figure 6.9: Low loss EELS of CuO, Y_2O_3 and the $YBCO$ matrix.

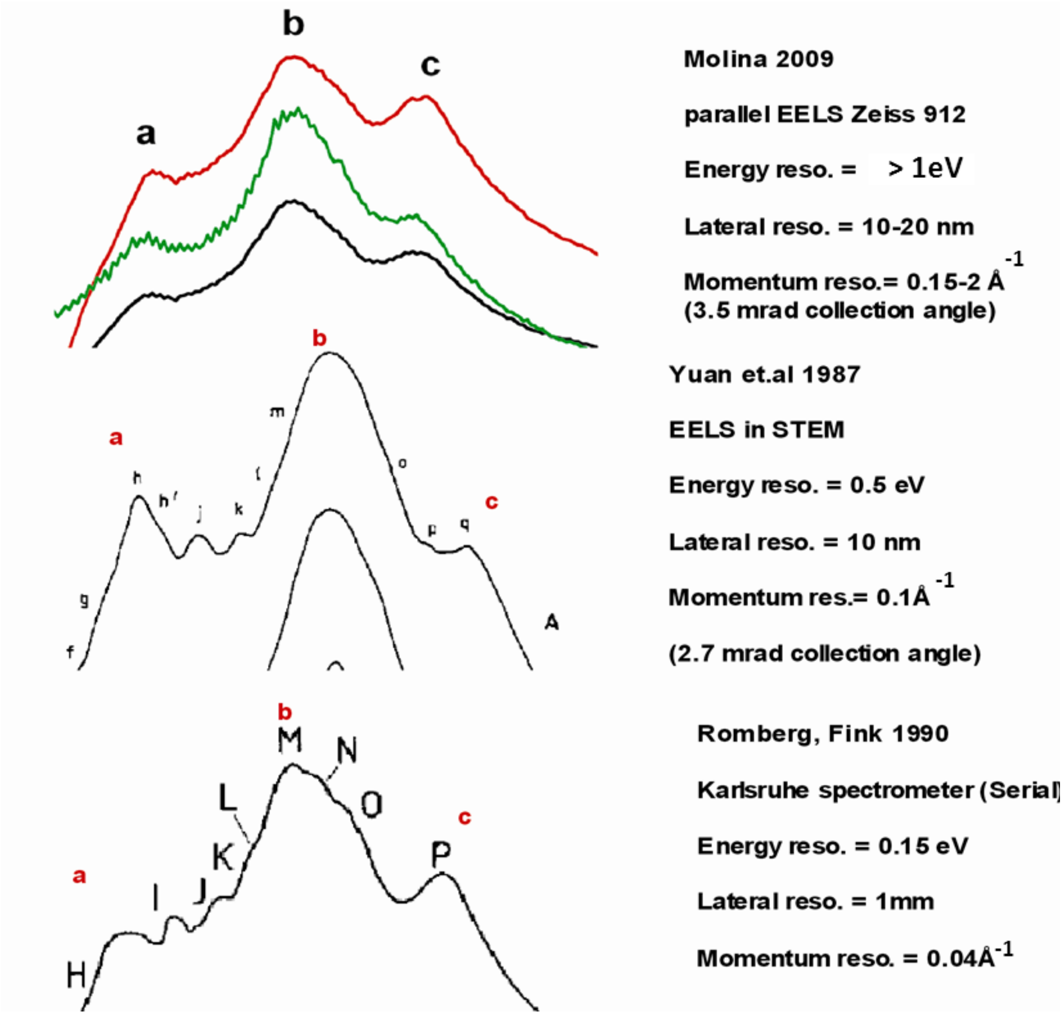

Figure 6.10: Low-loss EELS of YBCO acquired with different energy resolution own data, Yuan et.al.[100] and Romberg et.al [38]

In figure 6.10 are low-loss EELS spectra of YBCO from various authors. Important specifications include (i) energy resolution (ii) lateral resolution and (iii) momentum resolution as shown in the figure. Tabulated values for the details in the fine structure can be found in [100] and [38].

Core-loss EELS

When working with cross-sections of YBCO coated conductors, not only the identification and quantification of secondary phases and phase segregation in the YBCO film are of interest, but also the study of the interface between the superconducting layer and the buffer layer as well as the substrate-buffer layer is of importance. For this the core-loss region of the EELS spectrum is very useful.

Figure 6.11 (a) is an electron energy-loss (EELS) zero-loss spectrum from a YBCO layer. The energy regions where the windows were placed for ESI are denoted by Δ1, Δ2 and Δ3. Figure 6.11 (b) is a core-loss spectrum showing the corresponding Ba N4,5 ionization edge at 99 eV. The peaks denoted by a and b lay at 108 eV and 119.3 eV respectively. These values fit well with the ones found in the literature [107].

Figure 6.11 (c) shows the Ba N4,5 energy loss near edge structures (ELNES) taken for BaO taken from the same reference. The corresponding Ba N4,5 ionisation edge lays at 98.8 eV and the peaks a and b at 104.2 eV and 116.9 eV respectively. Figure 6.10 (d-f) corresponds to the CeO_2 N4,5 peaks are found at 107.83 eV and 112,16 eV. A broad feature is found increasing at 120 eV, as also reported by Kothleitner and Hofer in [104]. Two relevant features are found at 125.6 eV and 130.8 eV. When using N 4,5 edges for chemical mapping it is ideal to use 15-20 eV windows to fully cover the sharp peaks close to the threshold.

As reported in [104], investigations on delayed edges showed that the window can be off-set by several tens of eV in order to optimise the signal to noise ratio. The La N 4,5 peaks lay at energies lower than in the case for Ce N4,5. Peaks are found at 101,5 eV and 105,5 eV. A broad feature is found at 117,6 eV and later at 133.68 eV. Figure 6.10 (f) shows the spectrum form Y_2O_3, the Y M4,5 ionization edge lays at 160 eV. Delayed edges are observed.

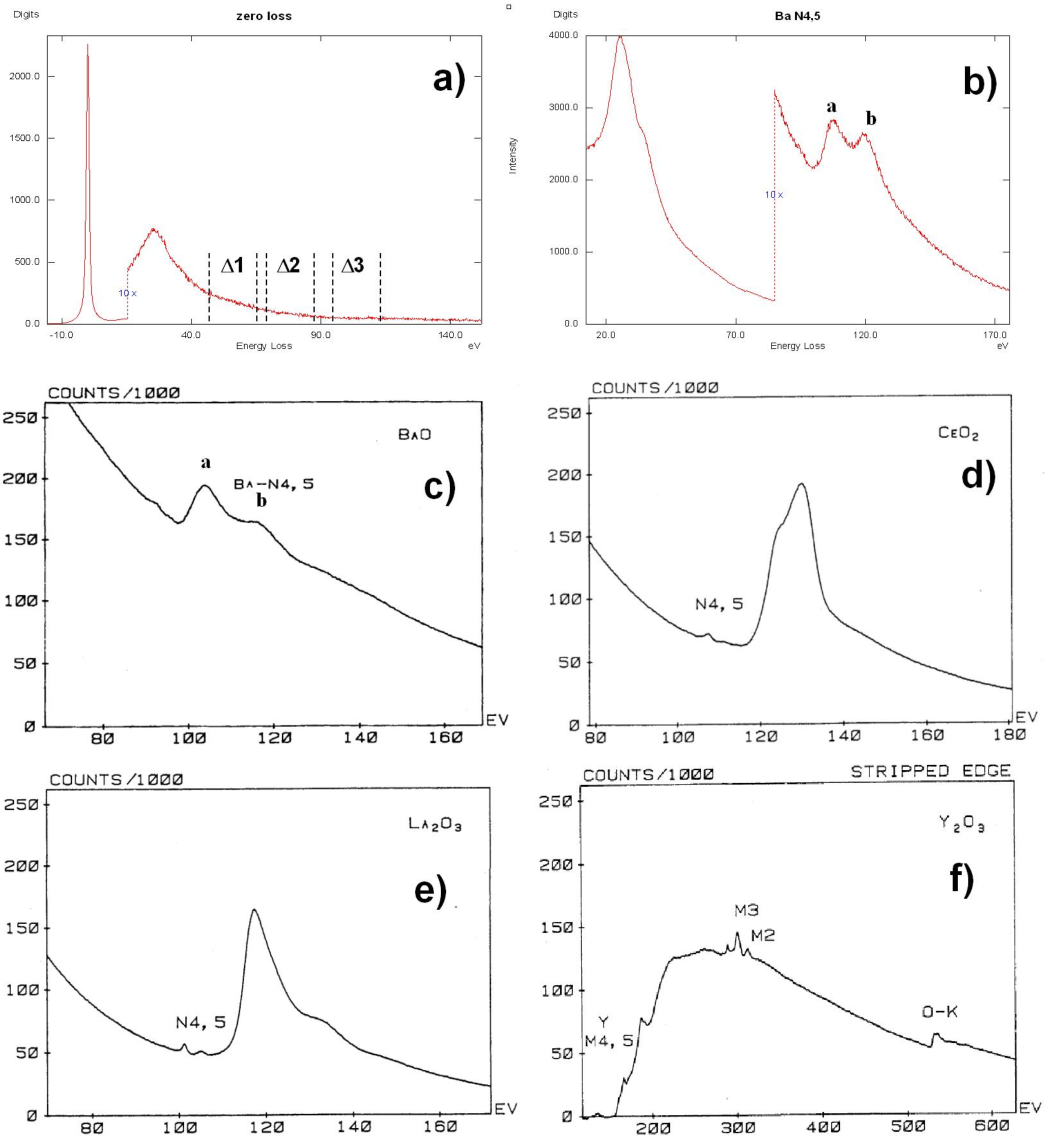

Figure 6.11: a.) Low-loss EELS spectrum. b.) Core-loss EELS of Ba N 4,5. (c-d) Ba, Ce, La and Y ionization edges between 80 eV and 300 eV, data from Ahn [41].

Wide-range EELS

Figure 6.12 (a) is a wide range EELS spectra. In fig. 6.12 (b) the Ba N4,5 peak at 93 eV is foound. Fig. 6.12 (c) are the O-K edge located at 532 eV, the Ba M4,5 at 778 eV and Cu-L at 930 eV. The values fit well with the literature. The O-K and the Ba M45 edges of figure 6.12 (c) were used for quantification and an element ratio of oxygen to barium of 3.5 could be determined by element quantification, this corresponds to the YBCO matrix.

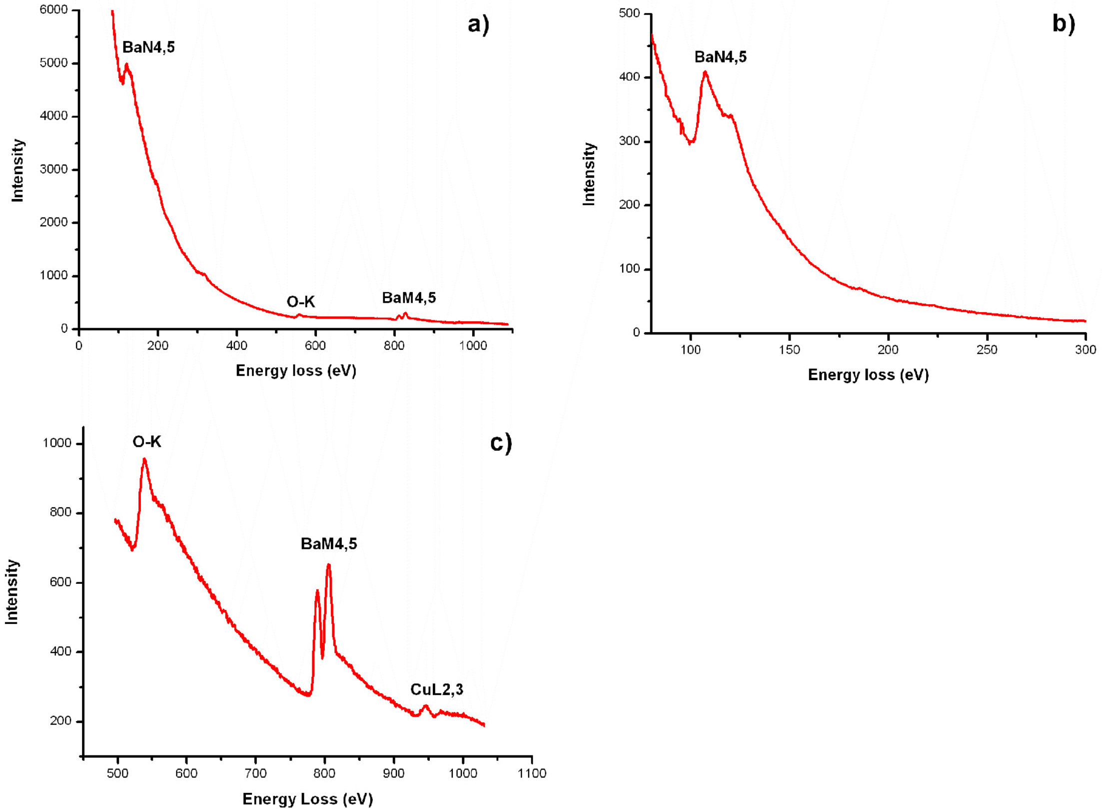

Figure 6.12: Wide-range EELS spectra of the YBCO matrix (sample number 1) a) Overview 80-1000 eV b) lower-energy-loss 80-300 eV c) higher energy-loss 500-1000 eV.

6.4.3 ESI chemical mapping

Low-loss

After identifying the features of the low-loss EELS spectra and establishing the corresponding finger prints in the spectrum these can be used for chemical mapping of precipitates in the YBCO film. From figure 6.10, the idividual characteristics of the difference phases could be identified, energy-filtered images, see figure 6.13 (a-c), where obtained from the image 1 (13 eV) , image 2 (26 eV) and image 3 (38 eV) areas with an energy slit of 10 eV.

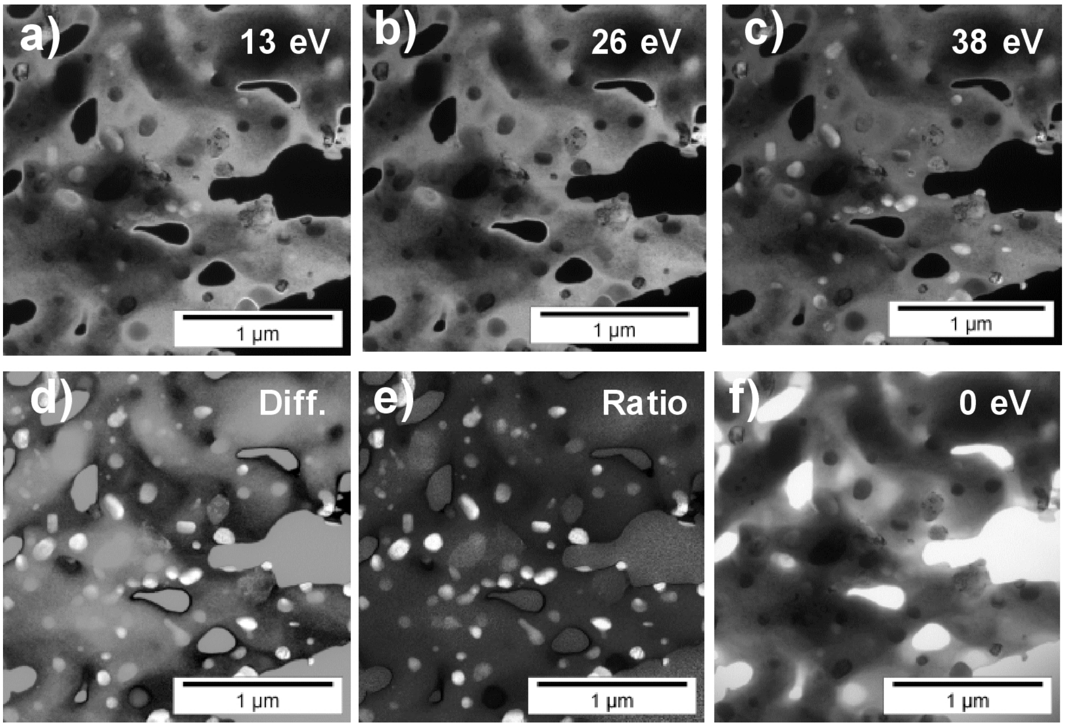

Figure 6.13: Energy-filtered imaging of sample 1, low-energy losses at 13 eV, 26 eV and 38 eV.

In the corresponding difference image (Image 3-Image 2) Y rich precipitates can be clearly distinguished from the YBCO matrix and the vaccum areas.

Area	Phase	Grey value (cts)
1	CuO	0.63
2	CuO	0.71
3	CuO	0.64
4	Y_2O_3	1.67
5	Y_2O_3	1.75
6	Y_2O_3	1.73
7	Y_2O_3	1.67
8	Matrix (YBCO)	0.58
9	Matrix (YBCO)	0.63
10	Vacuum	1.09

Table 6.8: Pixel values of the ratio image and the corresponding phases.

See table 6.8 for grey values corresponding the ratio image.Y_2O_3 areas have ratios of 1.7, whereas Cu rich areas (CuO and the YBCO matrix) have values of $0.6 - 0.7$. Thus, phases can be quantified.

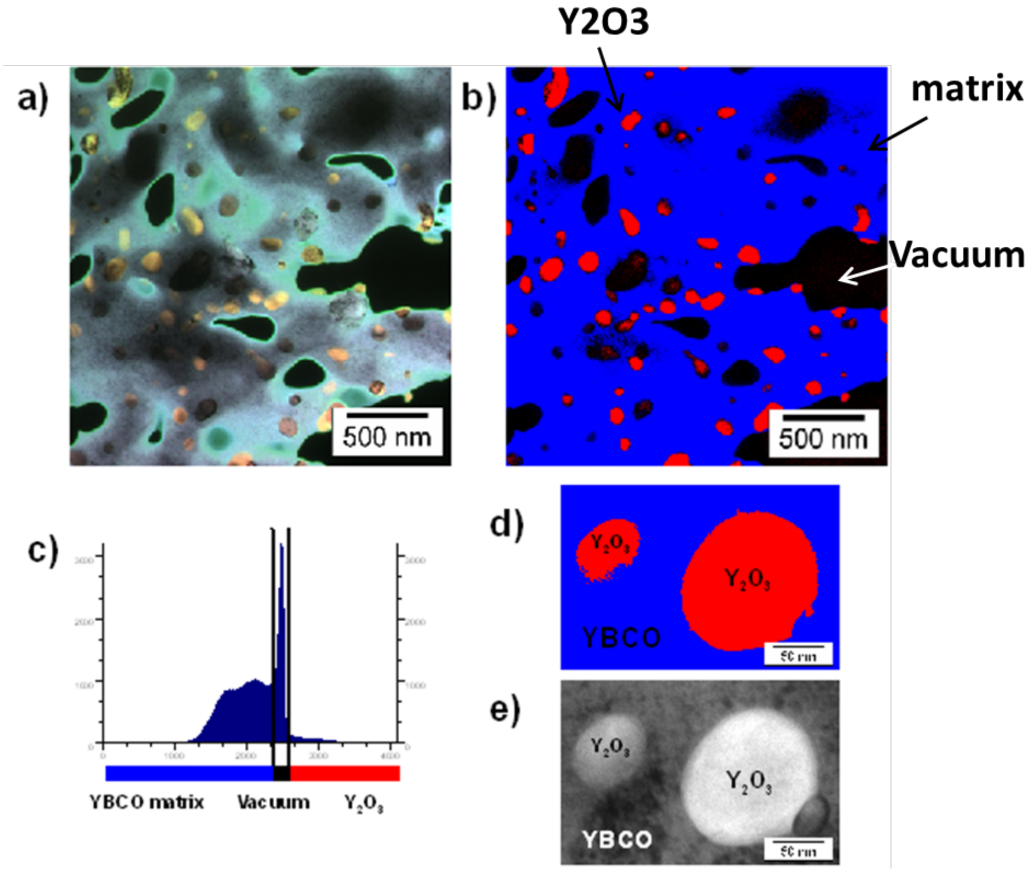

Figure 6.14: Images of sample 1 in plan-view (a) RGB and (b) color coding of energy-filtered images acquired at 13 eV, 26 eV and 38 eV. and (c) a grey values histogram of pixel values. (d-e) Y_2O_3 precipitates are clearly mapped.

Figure 6.14 (a) is an R(13eV)G(26 eV)B(38 eV) and 6.13 (b) a phase coded grey value difference image (Img2-Img1) where Y rich phases can be clearly identified, red corresponds to Y_2O_3, blue to the YBCO matrix and black to the vaccum areas. Very thick areas appear also black . The density of phase could be estimated as 5-10 % of the total area of $4\mu m^2$ shown in the image. Figure 6.14 (e) is a bright field TEM image in plan-view of sample 1.

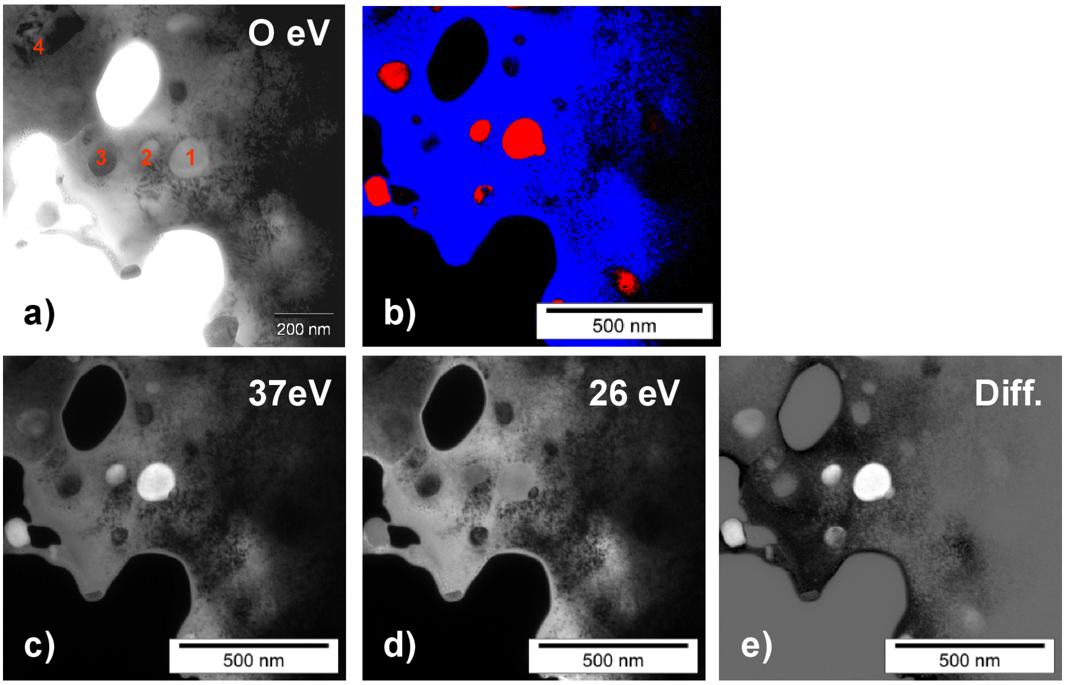

Figure 6.15: Images of sample 1 in plan-view. Chemical mapping with the Low-loss region. Area used for the EELS and EDX measurements (denoted 1-4 in figure 14 (a)).

Figure 6.15 (a) is a zero loss bright field image. Areas where EELS and EDX measurements were made are denoted as 1-4 in the figure. Where 1 correponds to the Y_2O_3, 2 and 3 to the YBCO matrix and 4 is CuO. Figure 6.15 (b) is color coding image where ~200 nm precipitates could be clearly identified. Figure 6.15 (c-d) are energy filtered images at 37 eV and 26 eV and figure 6.15 (e) is the difference between them.

Core-loss

Conventional sample Optimum acquisition conditions for ESI elemental mapping using core-loss edges are shown in table 6.9.

Edges (eV)	Y (M4,5)	Ba (N4,5)	La (N4,5)	Ce(N4,5)
	160	99	117	102
Pre-edge 1 (E_1)	127	60	76	76
Pre-edge 2 (E_2)	149	80	95	102
Pre-edge 3 (E_3)	184	111	118	137

Table 6.9: Acquisition conditions for elemental mapping with core-loss edges.

Figure 6.16 (a-b) shows pre-edge energy-filtered images obtained of the smaple in cros-section (sample 1) using the Ba N 4,5 ionization edge and acquired at 60 eV and 80 eV respectively. Figure 6.16 (c) is the corresponding post-edge image taken at 111 eV.

Figure 6.16 (d) is a contrast enhanced Ba elemental map obtained after subtracting the post-edge image from the background calculated from the pre-edge images. Similar elemental maps were obtained for the La N4,5, Ce N4,5 and Y M4,5 ionization edges.

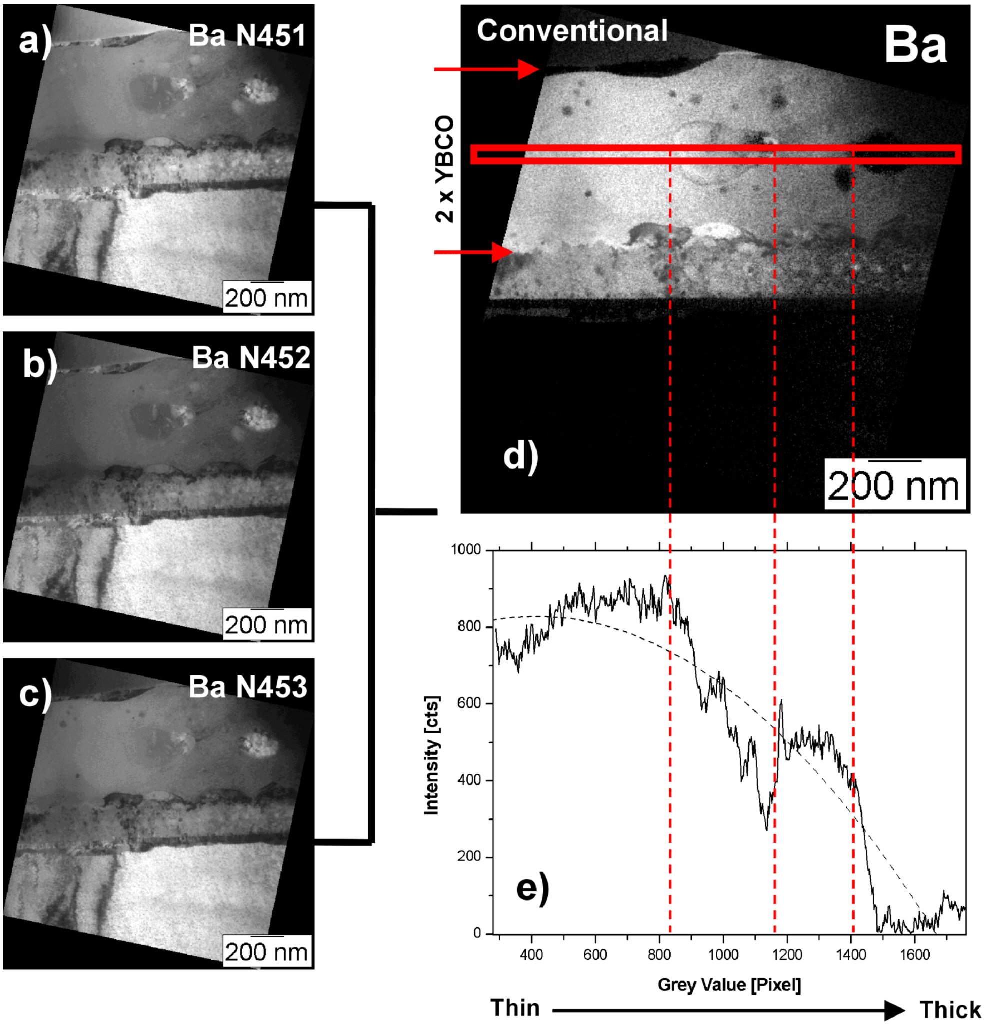

Figure 6.16: Calculating elemental maps form energy-filtered images (ESI) of the conventionally prepared sample 1 in cross-section: a.) Ba pre-edge 1 image (energy loss: 60 eV) b.) Ba pre-edge 2 image (energy loss: 80 eV) c.) Ba post-edge image (energy loss: 111 eV) d.) Ba elemental map. The image in d) is calculated by extrapolating the pre-edge background given by images a) and b) up to the energy loss of image c) and subtracting this background image from image c). e.) Line scan.

Figure 6.17 (a) shows the overlay r(Ce)G(Ba)B(La) image and figure 6.17 (b) the overlay of r(Ce)G(Ba)B(Y). All layers can be clearly identified and are denoted in the corresponding images. Secondary phases found in the YBCO layer correspond to Y, Ba and Cu-rich phases. All images were taken from the same specimen area and little sample drift was observed during image acquisition.

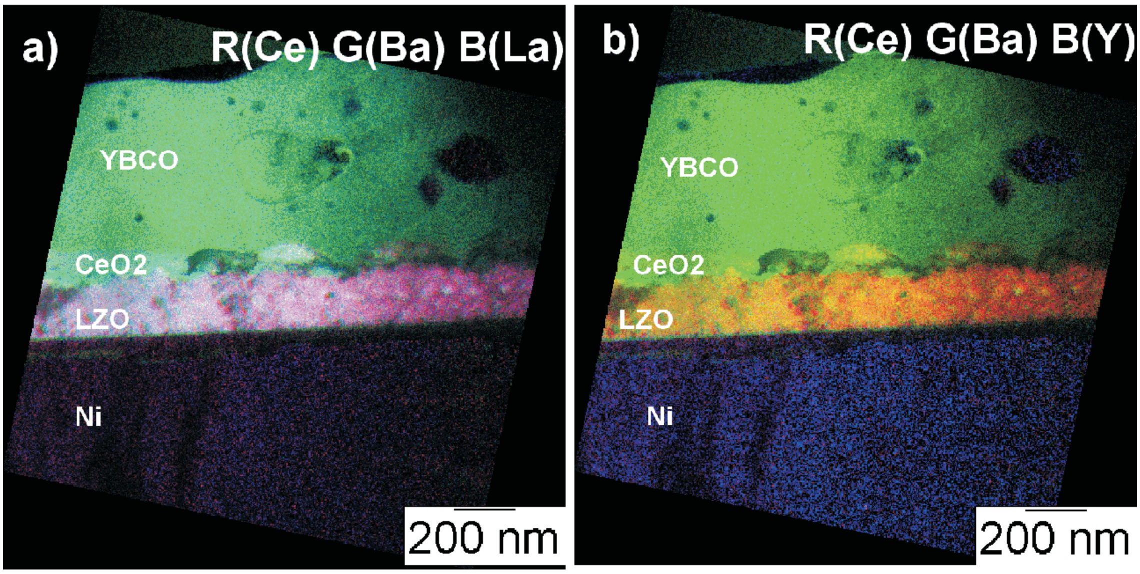

Figure 6.17: RGB overlays of elemental maps obtained by energy-filtering TEM of a coated conductor conventionally prepared cross-section a) ESI R(Ce)G(Ba)B(La) overlay image of sample 1 b) ESI R(Ce)G(Ba)B(Y) overlay image of sample 1.

FIB prepared sample Figure 6.18 shows energy filtered pre-edges, post-edge and final enhanced elemental maps taken for the Ba N 4,5 ionization edge on the FIB prepared TEM specimen. Similar elemental maps were obtained for the other elements and the energy windows. In contrast to the conventionally prepared specimen the intensity of the line scan shows only a small thickness dependence. The background substraction was done according to the equations given in section 2.3.4. For the case of Ba N 4,5 we have that:

$$Y_{B1} = AE_1^{-r} \tag{6.1}$$

$$Y_{B2} = AE_2^{-r} \tag{6.2}$$

A and r are fitting constants obtained from pre-edge 1 ($\Delta E1$) and pre-edge 2 ($\Delta E2$), which are 60 and 80 eV for Ba N4,5, as given in table 6.9. The fitting factor r is then calculated by:

$$r = \left(\frac{log \frac{Y_{B1}}{Y_{B2}}}{log \frac{E_2}{E_1}} \right) \tag{6.3}$$

after background subtraction the remaining Ba N 4,5 elemental map displays the spatial distribution of the element within the analyzed specimen area. The net signal is then given by:

$$S_{BaN4,5} = S(E_3) - AE_3^{-r} \tag{6.4}$$

The corresponding calculated image is shown in figure 6.18 d.

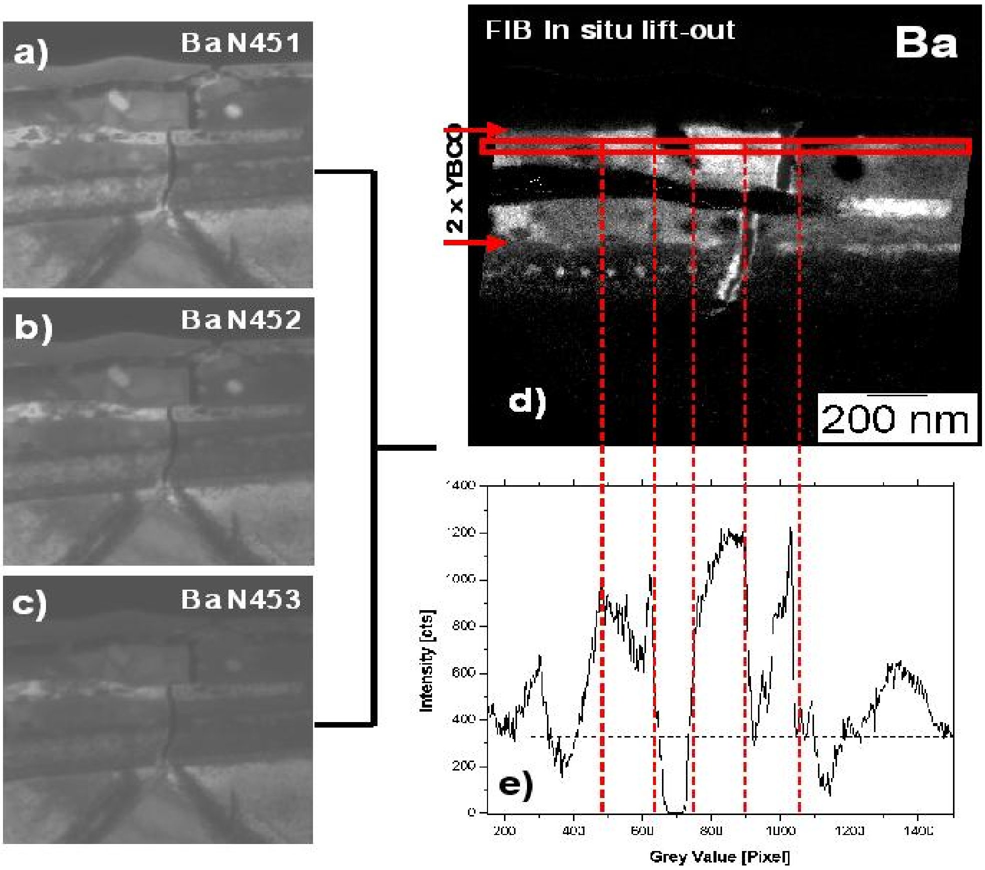

Figure 6.18: Calculating elemental maps from energy-filtered images (ESI) of the FIB prepared sample 1: a.) Ba pre-edge 1 image (energy loss: 60 eV) b.) Ba pre-edge 2 image (energy loss: 80 eV) c.) Ba post-edge image (energy loss: 111 eV) d.) Ba elemental map. The image in d) is calculated by extrapolating the pre-edge background given by images a) and b) up to the energy loss of image c) and subtracting this background image from image c). e.) Line scan.

Figure 6.19 (a) is the resulting overlay r(Ce)G(Ba)B(La) image and figure 6.19 (b) is the overlay of r(Ce)G(Ba)B(Y). The double-coated YBCO layer can be clearly identified and nanovoids in the buffer layer can be identified. Blue areas found in the YBCO film correspond to Y-rich secondary phases as determined by EDX point measurements. Note the secondary phase forming between YBCO layers. The crack observed in the images occurred after specimen FIB preparation.

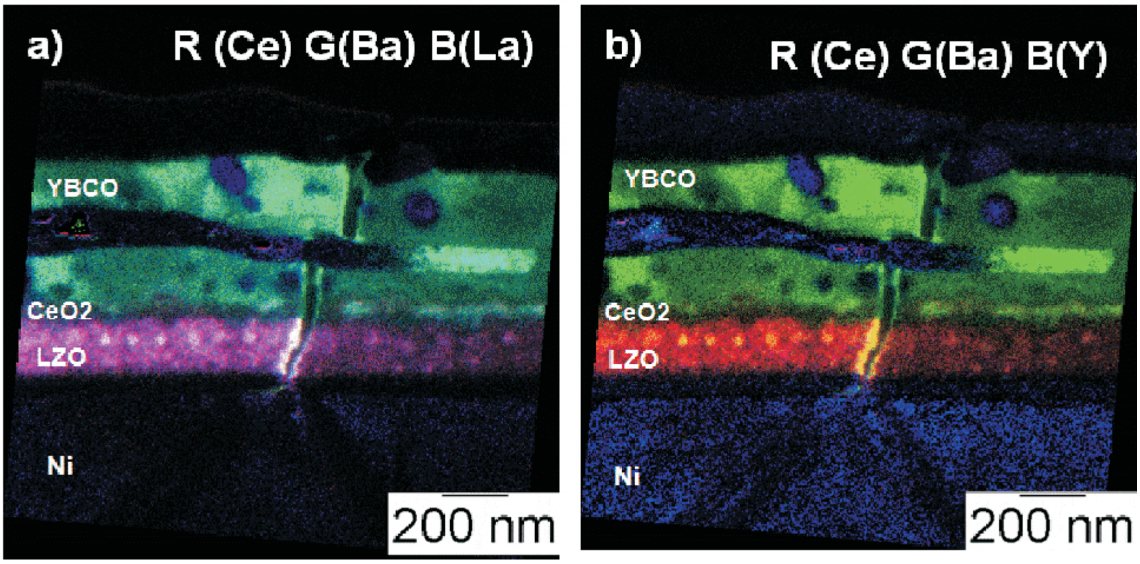

Figure 6.19: RGB overlays of elemental maps obtained by energy-filtering TEM of a coated conductor FIB prepared cross-section. a.) ESI R(Ce)G(Ba)B(La) overlay image of sample 2 b) ESI R(Ce)G(Ba)B(Y) overlay image of sample 2. Note the Nanovoids in the LZO film, the granular structure of the CeO2 film and the Y_2O_3 and Y rich secondary phases in the YBCO

All images were taken from the same sample area. Figure 6.20 shows conventionally (left side) vs. FIB (right side) prepared specimen and the corresponding enhanced Y elemental maps. As seen, the noise increases in the images due to the higher energy laying Y M4,5 ionization edges and lower signal to background ratio.

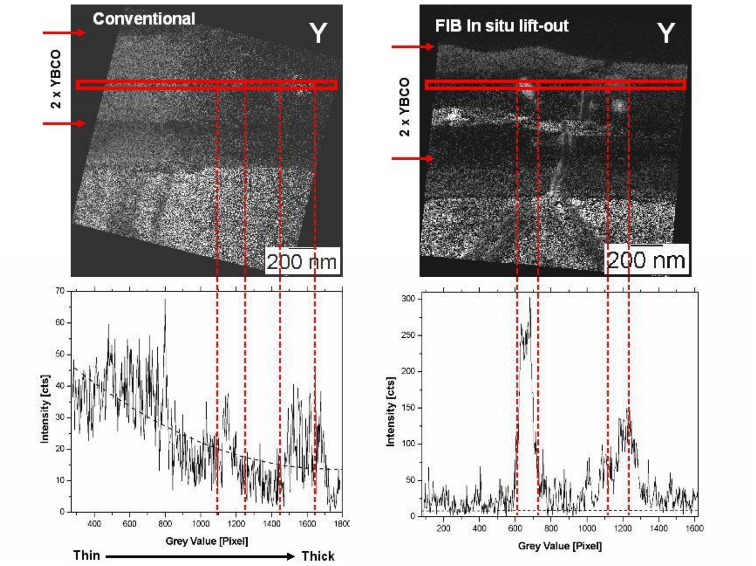

Figure 6.20: a.) Y-elemental map of sample 1 and corresponding line scan. b) Y-elemental map of sample 2 and corresponding line scan.

An intensity vs. sample thickness dependence is still clearly observed. Figure 6.21 (a-b) shows line scans over an area with nanovoids found in the LZO buffer layer [76]. The distance between the large nanovoids is 200 nm.

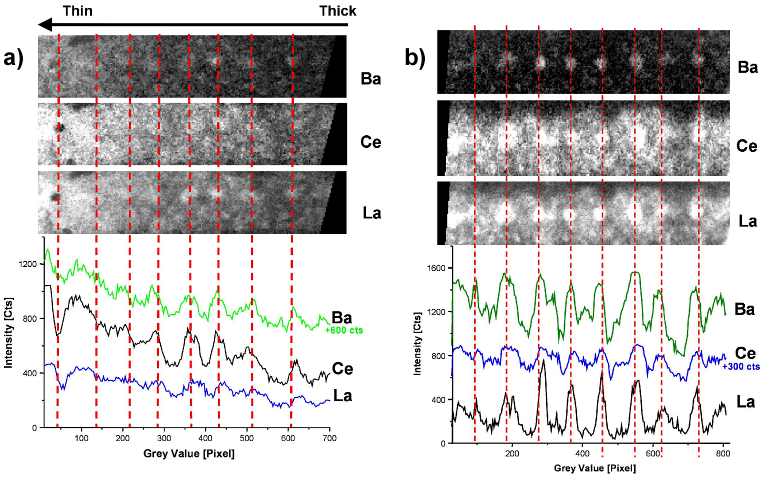

Figure 6.21: Line scans in the LZO layer in sample 1 (a) and sample 2 (b). Peaks are seen in the nanovoids present in this layer.

6.4.4 Energy dispersive X-ray microanalysis (EDX)

Figure 6.22 shows energy dispersive X-ray point measurements in a TFA-YBCO film. Y_2O_3 and CuO precipitates can be clearly distigushed from matrix areas. Quantitative EDX data are shown in table 6.10. Cliff-Lorimer K-factors used were Y-K = 2.774, Ba-L = 2.050 and Cu-K = 1.457.

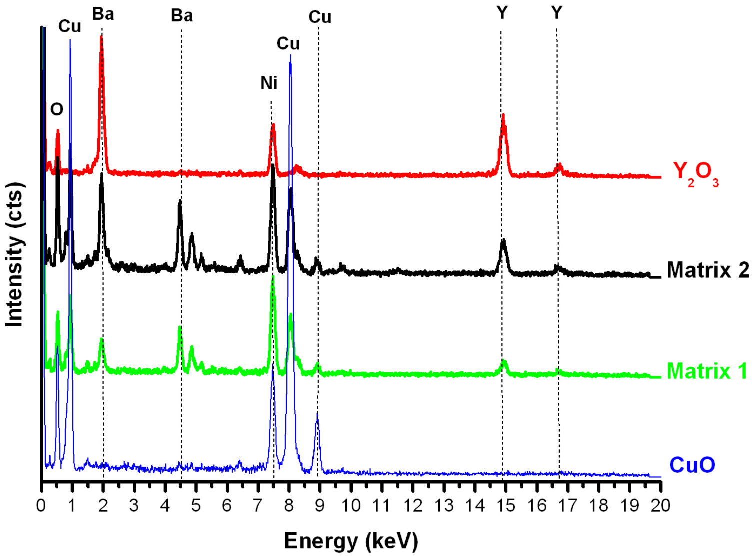

Figure 6.22: EDX spectra of Y_2O_3, matrix 1, matrix 2 and CuO of figure 12 (positions 1-4).

Spectrum No.	Y(at%)	Ba(at%)	Cu(at%)	Phase	Size (nm)
1	3.82	5.38	90.8	CuO	70
2	18.19	34.51	47.3	$YBCO$	Matrix
3	62.4	17.81	19.79	Y_2BaCuO_5	30
4	89.36	5.24	5.4	Y_2O_3	40
5	19.4	45.2	35.41	$YBCO$	30
6	48.43	21.89	29.68	Y_2BaCuO_5	40
7	0.64	0.91	98.46	CuO	$>$200
8	7.04	13.47	79.49	$BaCuO_2$	$>$100
9	22.1	32.7	45.2	$YBCO$	Matrix

Table 6.10: Quantification of EDX spectra and corresponding phases. Cliff-Lorimer K-factors used were Y-K = 2.774, Ba-L = 2.050 and Cu-K = 1.457.

6.5 Discussion: Energy-filtering TEM methodology for YBCO coated conductors

The main goal of the present analysis was to use electron energy loss spectroscopy (EELS) and electron spectroscopic imaging (ESI) for chemical quantification of YBCO coated conductors. EELS and ESI have the same physics of inelastic scattering, however the signal detection is different, i.e. EELS yields spectra with continous energy-loss, whereas EFTEM yields images at a certain energy-loss or range of energy-loss.

6.5.1 Deconvolution of Low-Loss spectra

Shown in figure 6.23 and 6.24 are example Fourier-log deconvoluted of EEL Low-Loss spectra of the Y_2O_3, CuO and $YBCO$ matrix. Figure 6.23 (a-b) correspond to areas of different thickness of the YBCO matrix. The Ba N4,5 edge and peaks at 100 and 102 eV can be clearly identified as well as the characteristic low-loss YN2,3 edge at 32 eV. Figure 6.24 (b) reveals the Cu M4,5 edge at 74 eV. Figure 6.24 (b) are the corresponding spectra for CuO, after deconvolution the Cu M 4,5 edge can be seen. Figure 6.23 (d) are the corresponding spectra were the YN2,3 is observed. The resolution obtained form the FWHM of the corresponding zero-loss peaks gave values ranging form 1.3-1.7 eV depending on the current bias used.

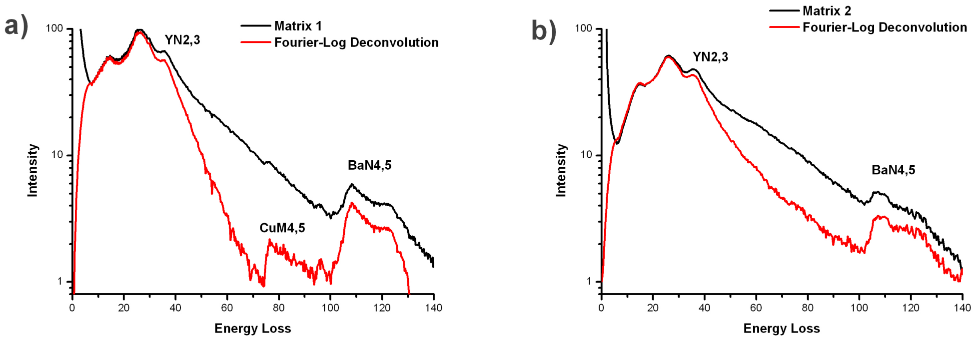

Figure 6.23: Fourier-Log deconvolution of EELS Low-Loss spectra of YBCO (sample 1).

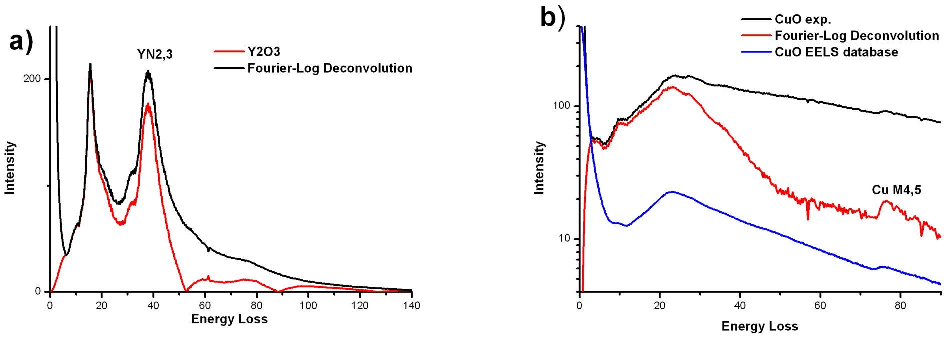

Figure 6.24: Fourier-Log deconvolution of EELS Low-Loss spectra (a) Y_2O_3 (the minima observed in the deconvolution are due to artifacts in the spectrum) and (b) CuO (sample 1).

6.5.2 Calculating differential scattering cross-sections using SIGPAR2

The ionization cross-sections were calculated for Y(M4,5), Ba(N4,5), Ba(M4,5), La(N4,5) and Ce(N4,5) using parameterized M- and N- shell cross-sections for limited $\triangle$ and β and according to equation 6.20.

Element	Z	Ec(eV)	f(50)	f(100)
Ba	56	90	7.11	9.03
La	57	103	6.43	9.46
Ce	58	109	6.6	9.65

Table 6.11: Integrated oscillator strengths, $f(\triangle)$, for N4,5 edges.

The SIGPAR2 program [108] which uses the equation 2.77 to calculate total cross sections for major ionization edges of interest for YBCO coated conductors. Given in tables 6.11 and 6.12 are the values of the dimensionless integrated oscillator strength ($f(\Delta)$) in function of a integration window (Δ), used for M4,5 and N4,5 edges. These represent the best estimates based on Hartree-Slater calculations, X-ray absorption data and EELS measurements according to [108].

Element	Z	Ec(eV)	f(50)	f(100)	f(200)
Y	39	160	0.68	2.2	
Ba	56	781	1.45	2.5	4.2
La	57	832	1.55	2.5	4.7
Ce	58	884	1.51	2.4	4.4

Table 6.12: Integrated oscillator strengths, $f(\triangle)$, for M4,5 edges.

Table 6.13 are calaculated values where β is the objective aperture (3.1, 8.1 and 13.5 mrad). Calculated values were obtained implementing equation 2.78.

Table 6.14 are the references for dipole oscillator strength estimations for fixed energy slits obtained by EELS, X-ray absorption and atomic theory calculations.

$\beta(mrad)$	$\sigma_A(\beta,\Delta)[cm^2]$	$\Delta = 15eV$	A= element (Shell)		
	$\sigma_{Y(M4,5)}$	$\sigma_{Ba(N4,5)}$	$\sigma_{Ba(M4,5)}$	$\sigma_{La(N4,5)}$	$\sigma_{Ce(N4,5)}$
3.5	2.84E-021	6.82E-020	5.49E-022	5.12E-020	4.85E-020
8.1	4.32E-021	9.52E-020	7.53E-022	7.27E-020	6.94E-020
13.5	5.23E-021	1.12E-019	1.13E-021	8.59E-020	8.23E-020

Table 6.13: Calculated total ionization cross-sections for different collection semi-angles.

Shell	EELS	X-ray absorption	Atomic theory
K	Hofer[109], Crozier [110], Malis [116], Yang [117]	Saloman [111], Henke [112], Veigele [113], del Grande [118], Barkyoumb[119]	Reilman [114], Rez [115]
L	Hofer[109], Crozier [110], Malis [116], Yang [117]	Saloman [111], Henke [112], Veigele [113],	Yeh [120], Rez [115] Reilman [114]
M	Hofer[109], Chadwick [121], Manoubi [122] Yang [117], Crozier [110]	Saloman [111], Henke [112] Luo [123], Auerhammer [124]	Rez [115], Yeh [120]
N	[109], Cukier [125]	del Grande [118], Cukier [125]	Rez [115], Cukier [125] Yeh [120]

Table 6.14: References for dipole oscillator strength estimations obtained by EELS, X-ray absorption and atomic theory [108].

Experimentally determined cross-sections

Experimental cross-section values were obtained by element ratio of the O-K and BaM4,5 edges taken from a wide-range EELS spectrum shown in figure 6.12 and are included in table 6.15 for $\sigma_{Ba(M4,5)}$, This is the only cross-section we can determine experimentally by determining the ratio of O-K to BaM4,5 ionization edges. The origins of the deviation from experimental and calculated values are due to convergent illumination and multiple scattering.

β	Experimental $\sigma_{BaM4,5}(\beta,\Delta)[cm^2]$	Calculated $\sigma_{BaM4,5}(\beta,\Delta)[cm^2]$
3.5	5.49E-022	5.45E-022
8.1	1.49E-021	7.53E-022
13.5	2.19E-021	1.13E-021

Table 6.15: Experimentally determined BaM4,5 ionization cross-sections for$\Delta = 15$ eV and different collection semi-angles.

Fitting of the cross-secction values

Calculated and experimental obtained cross-sections were fitted according to [39]:

$$\sigma(\Delta,\beta) \approx 4\pi a_0^2(R/T)(R/E_m)f(\Delta)ln\left[1+\left(\frac{\beta}{\theta_E}\right)^2\right] \tag{6.5}$$

Where R is the Rydberg energy, $f(\Delta)$ is a dipole oscillator strength andE_m a mean energy loss. For fitting purposes, this was simplfied as:

$$\sigma(\Delta,\beta) \approx c ln\left[1+\left(\frac{\beta}{\theta_E}\right)^2\right] \tag{6.6}$$

and $c = 4\pi a_0^2(R/T)(R/E)f(\Delta)$, where R is the Rydberg energy, T the primary energy, E the energy-loss and $f(\Delta)$ the integrated oscillator strength.

Such that only β and θ_E have to be known. θ_E is the characteristic angle. Both calculated and experimentally determined cross-section values are shown in figure 6.25.

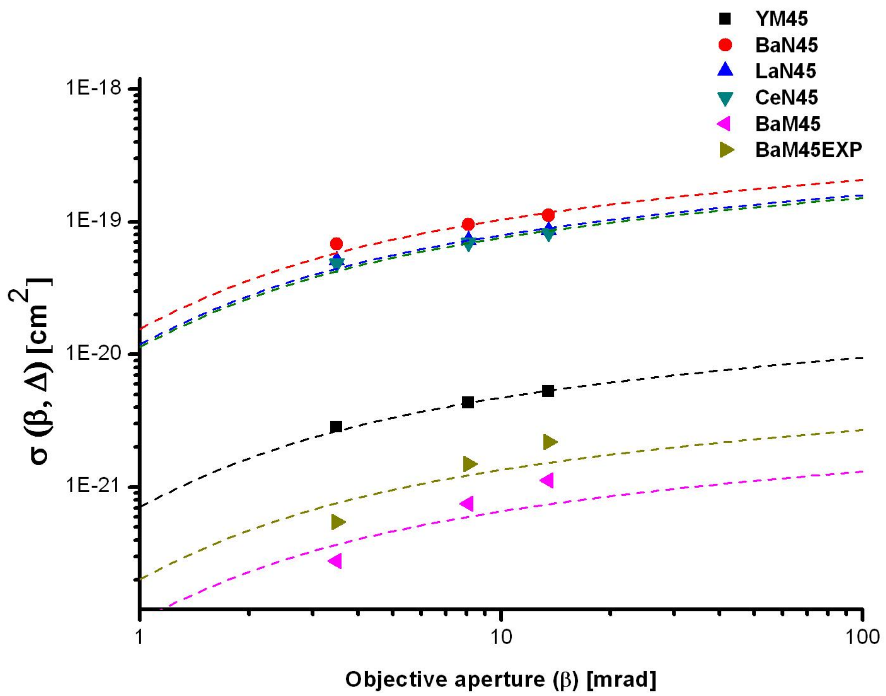

Figure 6.25: Total ionization cross-sections. Calculated and experimentally obtained values for different collection semi-angles.

Experimental and calculated EELS spectra are shown in figure 6.26. Experimental EELS spectra correspond to theBa N4,5 ionization edges ate 93 and 90 eV. The N4 corresponds to the transition from 4d3/2 to 5d3/2 and N5 from 4d5/2 to 5d5/2. Only the background can be fitted by the calculations, as shown by the blue curves.

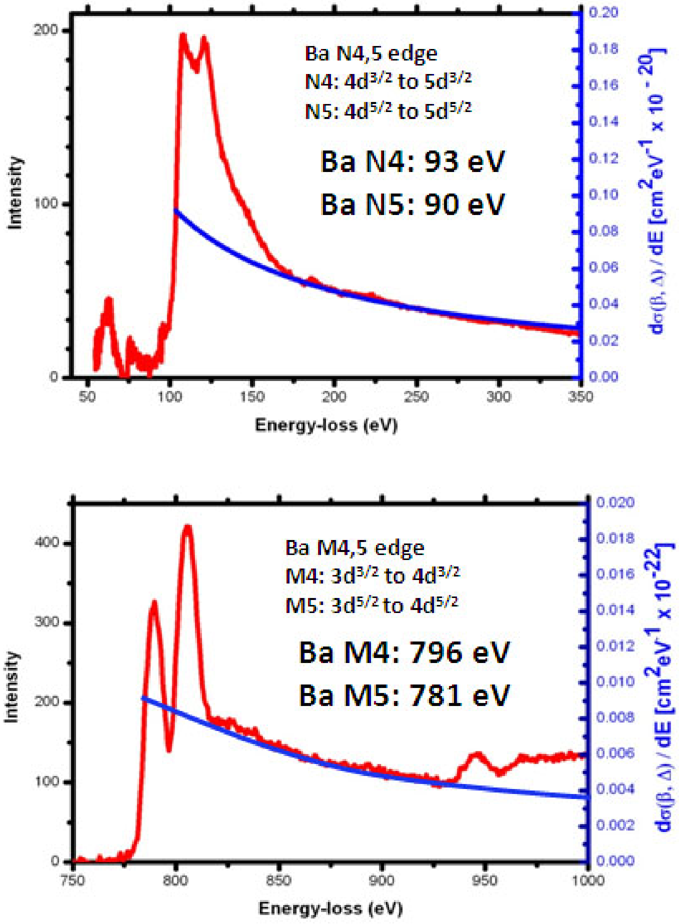

Figure 6.26: Experimental (red) and calculated (blue) EELS spectra for (a) Ba N4,5 and Ba M4,5 ionization edges.

6.5.3 Elemental mapping by electron spectrocopic imaging (ESI)

Calculation of the intensity per pixel in elemental maps

This section deals with the quantification of elemental maps within the single scattering approximation of inelastic scattering, there we use total integrated cross-sections as given quantities and calculate pixel intensities of elemental maps as a function of magnification, primary current density, acquisition time and density of atoms per area. For this calculation is is important to note what physical processes the electrons experience that contribute to the elemental maps, see table 6.16: (i) they are inelastically scattered in the sample and pass the objective aperture usually inserted (integration with respect to the scattering angle), (ii) they pass the intermediate lenses and the energy filter, where magnification and energy-loss integration occurs.

The quality of an elemental map is determined by (i) the spatial resolution and (ii) the signal to noise ratio. The spatial resolution is determined by the microscope and its electron optics and is not the resolution limiting critiria. The resolution limiting criteria is the signal to noise ratio.

The counts obtained in elemental maps are determined by: (i) fixed parameters not tunable by the microscope (ii) changeable parameters of the acquisition conditions that can be tuned during the experiment. The fixed parameters for a certain ionization edge applying the three window method are (i) the background signal (ii) the signal to background ratio (SBR) (iii) the dynamics of the inelastic cross-section with respect to the energy-loss and (iv) the camera dynamics (14 bit).

The intensity of the zero-loss electrons I_0 is given by:

$$I_0 = j_0 t A_{real} \tag{6.7}$$

I_o has a positive charge, because the negative sign is omitted for simplicity, t is the acquisition time. A_{real} is the real unmagnified area of pixels and is defined as:

$$A_{real} = \frac{A_{pixel}}{M^2} \tag{6.8}$$

A_{pixel} is the pixel area of the CCD camera and M is the magnification. The current density of the primary beam (j_0) is then:

$$j_0 = \frac{1}{t} \frac{I_0}{A_{pixel}} M^2 \tag{6.9}$$

This can also be written as:

$$I_0 = j_0 t \frac{A_{pixel}}{M^2} \tag{6.10}$$

The changeable parameters are (i) magnification of the energy-filtered image (ii) acquisition time (iii) the size of the energy slit and (iv) the size of the objective aperture. These acquisition parameters are fine tuned for reaching a maximum number of counts in the elemental maps. EELS spectra indicate how to choose the right acquisition conditions for electron spectroscopic imaging.

The number of inelastically scattered electrons for energy losses within an energy interval Δ of the ionization threshold and scattering angles up to β according to the single scattering approximation is given by [108]:

$$I_k^1(\beta, \Delta) = N I_0 \sigma(\beta, \Delta) \tag{6.11}$$

and

$$\frac{I_0}{pixel} = \frac{j_0 t}{M^2} \cdot \frac{A_{pixel}}{pixel} \tag{6.12}$$

This is the vacuum intensity and can be measured. N is the number of atoms per area. I_0 is the vacuum intensity and $\sigma(\beta, \Delta)$ is the total ionization cross-section.

The signal of interest, i.e. $\frac{I_k^1(\beta,\Delta)}{pixel}$ arriving at the CCD array can be calculated according to equation 6.7 such that:

$$\frac{I_k^1(\beta, \Delta)}{pixel} = N \cdot \sigma(\beta, \Delta) \frac{I_0}{pixel} = N \cdot \sigma(\beta, \Delta) \cdot \frac{j_0 \cdot t}{M^2} \cdot \frac{A_{pixel}}{pixel} \tag{6.13}$$

Intensity decreases with increasing magnification and that the current density (j_o) is an important parameter. A microscope with a field-emission gun has a high current density which can compensate the intensity decrease at higher magnifications. In the case of a thermal emitter magnification is limited due to the lower current density.

The role of specimen thickness is also of special importance; with increasing thickness the density of atoms per area increases leading to higher intensity per pixel values, but this also leads to increased multiple scattering, which is not accounted for in the single scattering approximation. For this study we used a Zeiss 912 omega TEM equipped with a thermal emitter (LaB_6) operating at 120 kV.

Notation	$I_K^1 \rightarrow I^{1 \leftarrow Single\ scattering\ approximation}_{A \leftarrow absorption\ edge\ (K-,\ L-\ ,M-\ ,or\ N-\ ,shell)}$		
	Equations	Physical quantities	
	$I_0 = j_0 \cdot t \cdot A_{real}$	I_0, A_{real}	Primary intensity (I_0) area real at specimen, area of pixel
	$\downarrow$		
Inelastic scattering	Sample interaction		
	$I_K^1 = N\sigma I_0$	N,σ	N are the atoms per area σ is the total cross-section
	$\downarrow$		
Energy filtering imaging	Magnification		
	$\frac{I^1(\beta,E)}{M^2}, \frac{I_0}{M^2}$	$\frac{I_0}{M^2}$	$\frac{I_0}{M^2}$, $A_pixel = M^2 A_{real}$

Table 6.16: Schematic view to explain the quantities used for the calculation of the intensity per pixel in the elemental maps.

The calculated current density according to equation 6.9 is $2.07 \times 10^7 \frac{A}{m^2}$ (with $t = 0.5$ sec, $4\mu A$ filament current and 0.16 mrad illumination angle). The maximum magnification in order to obtain a good SBR using the Zeiss 912 TEM in ESI images is limited to ∼ 8000×. In case the intensity per pixel is too low then the following can be done: (i) increase acquisition time (ii) decrease magnification (iii) increase collection angle (β). The density of atoms per area (N) used assuming a 100 nm thick sample are given in table 6.14. The area pixel is 256 µm^2.

$I_{Elemental-map}/pixel$	Charge	Number of electrons	Cts
$I_Y/pixel$	$9.987 \cdot 10^{-17} A \cdot s$	$6.234 \cdot 10^2$	∼ 200
$I_{Ba}/pixel$	$4.411 \cdot 10^{-15} A \cdot s$	$2.753 \cdot 10^4$	∼ 9000
$I_{La}/pixel$	$3.751 \cdot 10^{-15} A \cdot s$	$2.341 \cdot 10^4$	∼ 7800
$I_{Ce}/pixel$	$1.754 \cdot 10^{-15} A \cdot s$	$1.095 \cdot 10^4$	∼ 3900

Table 6.17: Calculation of expected cts in the individual elemental maps assuming a sample thickness of 100 nm according to equation 6.14. Cts are photon cts with an electron-phothon conversion factor of 3.

6.5.4 Quantification of elemental maps

Determination of integrated cross-sections

For the quantification of the individual elemental maps the number of counts according to each region of interest were quantified. (table 6.15).

Following from section 6.5.3 and assuming single scattering approximation we have that for quantification we can write:

$$\frac{I^1}{pixel} = N\sigma^1(\beta,\Delta)(j_0 t)\frac{1}{M^2} \cdot \frac{Apixel}{pixel} \tag{6.14}$$

where N is the number of atoms per area and:

$$j_0 t = \frac{I_0}{A_{pixel}} M^2 \tag{6.15}$$

Inserting into eqution 6.25 gives:

$$\frac{I^1}{pixel} = N\sigma^1(\beta,\Delta)(\frac{I_0}{A_{pixel}} M^2)\frac{1}{M^2} \cdot \frac{Apixel}{pixel} \tag{6.16}$$

$$\frac{I^1}{pixel} = N\sigma^1(\beta,\Delta)\frac{I_0}{pixel} \tag{6.17}$$

$$\sigma_k^1(\beta,\Delta) = \frac{1}{N} \cdot \frac{I^1/pixel}{I_0/pixel} \tag{6.18}$$

$$N = \frac{1}{\sigma_k^1(\beta,\Delta)} \cdot \frac{I^1/pixel}{I_0/pixel} \tag{6.19}$$

Equation 6.17 yields the total cross-sections if the intensities and vacuum intensities per pixel were known together with densities per area (Equation 6.18).

Since the specimen thickness and the primary electron current are usually not well known, it is evident that ratios of equation 6.18 will be fixed so that these quantities cancel. For the mole fraction ratios we obtain from equation 6.18:

$$\frac{N_A}{N_B} = \frac{\sigma_B}{\sigma_A} \cdot \frac{I_A/pixel}{I_B/pixel} \tag{6.20}$$

where $N = n(r)d(r)$. n(r) and d(r) represent the number of atoms per volume and the sample thickness respectively.

N can be calculated as:

$$N_{element} = \frac{atoms}{area} = \frac{atoms}{vol} \cdot d = n \cdot d \tag{6.21}$$

Table 6.16 lists the density of atoms per area for YBCO, LZO and CeO_2 assuming a thickness of 100 nm.

Layer	Element	$N_{Element}$
$YBCO$	Y	$N_Y = 5.79\,nm^{-2}$
$YBCO$	Ba	$N_{Ba} = 11.58\,nm^{-2}$
LZO	La	$N_{La} = 12.9\,nm^{-2}$
CeO_2	Ce	$N_{Ce} = 6.33\,nm^{-2}$

Table 6.18: Density of atoms per area

$I/pixel$ is the intensity per pixel of the individual elemental map and $I_0/pixel$ is the primary electron intensity per pixel under the same conditions.

In table 6.19 are the summarized counts after background substraction which can be used to distinguish between YBCO matrix, Y-rich secondary phases, LZO buffer layers and the Ni substrate.

Layer	Y(M4,5)	Ba(N4,5)	La(N4,5)	Ce(N4,5)
$YBCO$ matrix	20	250	100	0
Y_2O_3 precipitate	150	0	50	0
Y-rich phase segregation interface	250	0	30	0
LZO	20	0	200	200
LZO (voids)	20	150	250	255
CeO_2	0	50	60	60

Table 6.19: Quantification of phases using counts in the elemental maps.

Determination of mole fraction ratios

The goal of quantifying elemental maps is to determine N values for the various elements or mole fraction ratios N_A/N_B

$$\frac{N_A}{N_B} = \frac{\sigma_B}{\sigma_A} \cdot \frac{I_A/pixel}{I_B/pixel} \tag{6.22}$$

where σ_A/σ_B are k-factors and were previously calculated. For $\sigma_{YM45}/\sigma_{Ba45}$the k-factor is 0.045 assuming an aperture of 8.1 mrad. I_A and I_B are defined as $I_A = [I - I_{Background}]_A$ and $I_B = [I - I_{Background}]_B$ considering background substraction.

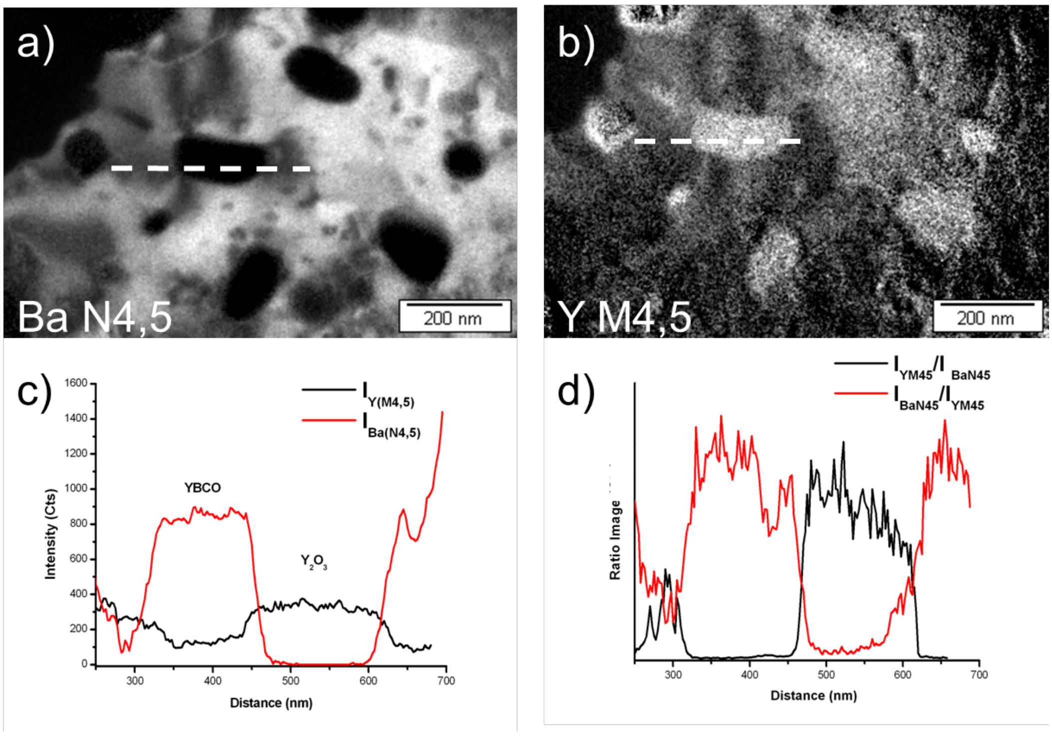

Figure 6.27: Elemental map of a TFA-YBCO plan-view sample showing pinning relevant Y_2O_3 precipiates, which are relevant for pinning in the system (a) Ba N4,5 elemental map, dark areas are precipitates (b) YM4,5 elemental map, bright areas are precipitates (c) line scans over a single Y_2O_3 precipitate and corresponding (d) image ratios.

The line scan over a Y_2O_3 precipitate shown in figure 6.27 (a) corresponds to the area shown in figure 6.15. Figure 6.28 (b) are ratio scans I_Y/I_{Ba} and I_{Ba}/I_Y and (c) the dependence of $I_{(BaN4,5)}$ in function of $I_{(YM45)}$.

Quantification: FIB vs. Conventionally prepared specimen

The FIB lamellae preparation was explained in section 6.3 and the conventional preparation in chapter 2. Conventionally prepared samples are wedge shaped, so there is a strong thickness dependence of the signal measured.

Table 6.20 and 6.21 show mean counts for the individual ESI images and the corresponding elemental maps for both the conventional and the FIB prepared TEM lamellae, more counts are obtained from the FIB specimen. For the quantification of the chemical composition, the mean values of the intensities of the elemental maps obtained by the three window method applied to both TEM lamellae are shown in the tables.

Layer	Conventional lamellae Edge used for elemental mapping	Intensity (mean cts) I(E1)	I(E2)	I(E3)	Elemental map
YBCO	Y(M4,5)	2000	1500	1000	~ 70
YBCO	Ba(N4,5)	6000	4200	2600	~ 600
LZO	La(N4,5)	4400	3000	2400	~ 600
CeO_2	Ce(N4,5)	4400	2800	2000	~ 220

Table 6.20: Intensity per pixel in the elemental maps obtained by the three window method using the conventional TEM lamellae.

The counts obtained in the FIB elemental maps are approximately double the values obtained in the conventional case. The counts also depend on the ionization edge used, for higher laying edges as in the case of $YM(4,5)$ a much weaker signal is obtained. Thus, FIB prepared lamellae are highly suitable for quantification.

Layer	FIB lamellae Edge	Intensity (mean cts) I(E1)	I(E2)	I(E3)	El.map	Calc.(d=100 nm)	Calc.(d=50 nm)
YBCO	Y(M4,5)	7000	5000	4500	~ 200	~ 200	~ 100
YBCO	Ba(N4,5)	10000	8000	5500	~ 1200	~ 9000	~ 4500
LZO	La(N4,5)	8000	6000	5000	~ 1600	~ 7800	~ 3600
CeO_2	Ce(N4,5)	8000	5500	3500	~ 600	~ 3900	~ 1800

Table 6.21: Intensity per pixel in the elemental maps obtained by the three window method using the FIB lamellae: experimental and calculated values.

6.5.5 Structural and chemical defects in YBCO films

For YBCO coated conductors two micro-structural features are of special interest (i) secondary phases and precipitates in the YBCO film and (ii) identification and chemical determination of the interfaces between the layers. ESI allows the identification of interface layers and secondary phases . The interface between both YBCO layers could be identified. Chemical solution deposited YBCO films present a large density of Y and Cu rich secondary phases.

Similar phases are well known from physical vapor deposited YBCO films [126, 127] where Y-rich, Y_2O_3, Cu-rich, CuO, $Y_2Cu_2O_5$, $CuO_x$and $BaCu_2O_2$ phases could be identified. The key microstructural features of metal organic deposited (MOD) YBCO films have also been reported by Holesinger T.G. et.al. [25] where a laminar grain structure was found for MOD prepared YBCO thins films. Grain boundary overgrowth, grain boundary meandering, colony microstructures, incoherent precipitates of Y_2O_3 and $Y_2Cu_2O_5$ and phase separations were reported.

For the chemical analysis of YBCO coated conductors it is essential to first investigate the sample over large areas (tens of microns) using SEM-EDX mapping to identify: (i) YBCO matrix (ii) sample in-homogeneities and (iii) secondary phases. This way CuO rich particles could be mapped within a YBCO matrix at the micrometer scale.

For mapping of nm sized Y_20_3 precipitates electron spectroscopic imaging is the technique of choice. By combined diffraction contrast imaging and energy-filtered imaging precipites could be identfied and imaged under two beam conditions, strain fields could be imaged as seen in figure 6.29: (a) The quaternary system YBCO (b) Two beam imaging of TFA-YBCO (c) Y_2O_3 precipitates and strain fields of dislocations. It is well known that Y-rich nanoparticles could act as pinning centers in YBCO [127]. Since the coherence length of YBCO is less than 10 nm, in the case of this study the interface between the Y_2O_3 and the YBCO matrix contributes to pinning in the system.

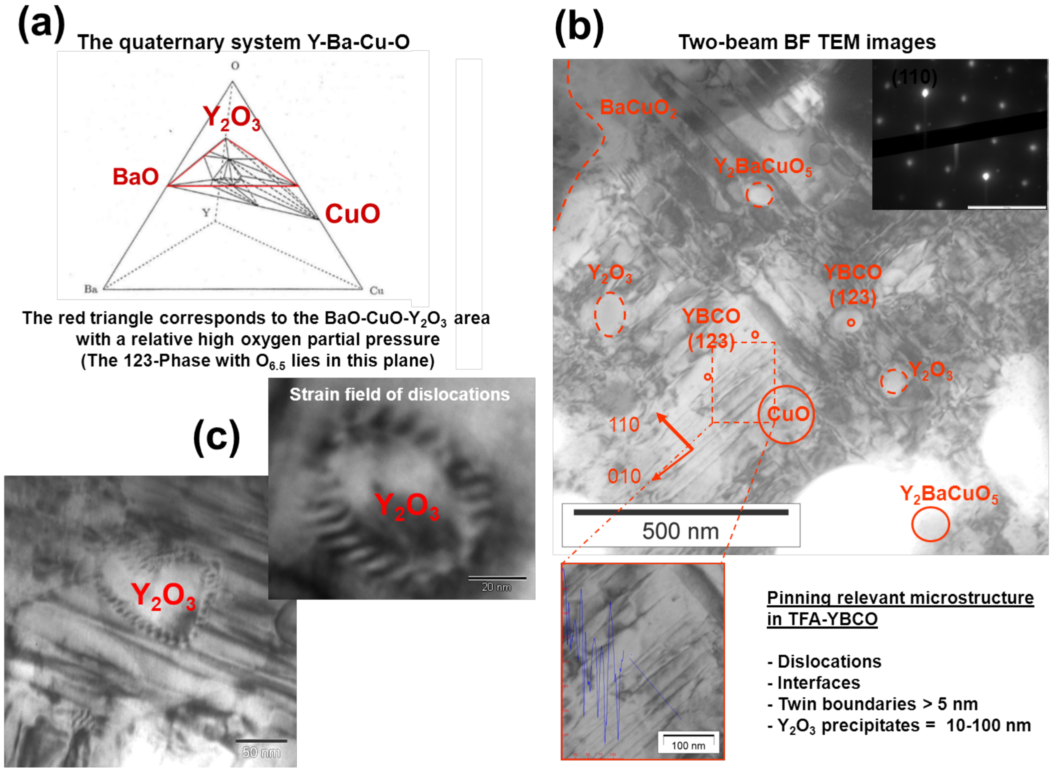

Figure 6.28: TFA-YBCO microstructure: (a) The quaternary system YBCO (b) Two beam imaging of TFA-YBCO (c) Y_2O_3 precipitates and strain fields of dislocations.

6.5.6 Relevance for superconducting properties

At least to two representative sample areas where the superconducting current density (j_c) was measured over cm wide areas of the sample were investigated. Thus, sample areas analysed are representative for the sample. All samples investigated had a $j_c \sim 1\ MA/cm^2$ at 77 K and zero-field.

The superconducting properties and j_c of YBCO coated conductors are limited by: (i) formation of secondary phases between YBCO films, that can partly block the current (ii) cracks, voids, precipitates (iii) transfer of the biaxial texture from the substrate to the YBCO film. (iv) surface roughness and (vi) the weak link effect. Minimizing and/or eliminating current limiting defects plays a central role in YBCO coated conductor sample fabrication. Chemical analysis is important for monitoring film growth and identifyng pinning relevant defects. In chapter 8 an asset on the superconducting properties of the films investigated is given

6.6 Conclusions

We have shown that both EELS and ESI in combination with EDX spectroscopy are useful tools for the quantitative chemical analysis of YBCO-coated conductors. When using the low-loss region of the EELS spectra of YBCO, attention has to be taken to identify features that are relevant for chemical phase mapping. By taking advantage of the $YN2,3$ edge and performing energy-filtering images at 13, 26 and 38 eV, the YBCO matrix could be clearly distinguished from both Y_2O_3 and CuO phases. Y_2O_3 and YBCO phases could be quantified.

EELS core-loss edges are useful when optimizing the ESI acquisition conditions for investigating all layers simultaneously in cross-sectional prepared TEM specimens. The edges used for imaging in this case were the BaN4,5, the YM4,5, LaN4,5 and CeN4,5. Energy filtered imaging is more useful than conventional diffraction contrast TEM imaging for identifying secondary phases in the YBCO layers and distinguishing the different layers. However, the images are more difficult to obtain. Special attention has to be devoted for choosing the adequate acquisition conditions. SNR has to be optimized according to the appropriate ionisation edges.

Using FIB for TEM specimen preparation homogeneously thick sample areas were obtained. Signal to background ratio increases dramatically when compared to conventionally prepared specimens. EELS measurements on the YBCO layer were done in order to determine the local sample thickness after performing fourier-log deconvolution correction for plural scattering the CuM4,5 and BaN4,5 could be identified.

We have shown that the mole fraction ratios can be calculated and only two elemental maps and the corresponding k-factor have to be known.

Chapter 7

EFTEM and EDX-spectroscopy of BZO nanocomposites in TFA-YBCO

7.1 Introduction

The increasing energy demand and depletion of fossile fuels as well as the global warming require the development of energy efficient technologies for power conversion and distribution of electrical power. Hence, there is a fast-growing worldwide interest in the second generation (2G) of high-temperature superconductor (HTS) wires for applications such as generators or high field magnets. These 2G HTS wires generally consist of a YBCO superconducting layer grown on an a biaxially textured buffer layer architecture on biaxially textured nickel tungsten substrate. Among the various deposition methods chemical solution deposition (CSD) has specific advantages such as flexibility in composition variations and the possibility to coat large area substrates. Since it is a non-vacuum method less expensive equipment is required.

Due to these advantages there is considerable interest in the development of all-solution based processes. Up to 100 m long lanthanium zirconate and cerium oxide buffered YBCO films were deposited on biaxially textured Ni5W substrates. For power applications however strong pinning of vortices is required. Thus, in the present section additional pinning is introduced by supplementary addition of various amounts of $BaZrO_3$(BZO) nanoparticle dispersions into the trifluoracetic acid (TFA) based YBCO precursor solutions in order to form nanocrystalline extrusions within the superconductor matrix.

The use of superconductors for power applications will be tremendously highlighted if an effective method for magnetic flux immobilization is discovered. It is well known that nonsuperconducting phases in the order of the coherence length of YBCO act as pinning centers. Gutierrez *et al.* [30] showed that a dense array of defects is induced in the superconducting matrix when $BaZrO_3$ nanodots are introduced by a low-cost chemical solution technique These nanodots are randomly oriented and the non-coherent interfaces are the driving forces for pinning in the system.

Angle-dependent critical-current measurements demostrated that a strong and isotropic flux-pinning mechanism is extremely effective at high temperatures and high magnetic fields leading to high-temperature superconductors with very high pinning forces. The maximum vortex-pinning force achieved at 65 K, 78 GNm^{-3}, is 500% higher than that of the best low-temperature NbTi superconductors at 4.2K and so a great wealth of high-field applications will be possible at high temperatures [30].

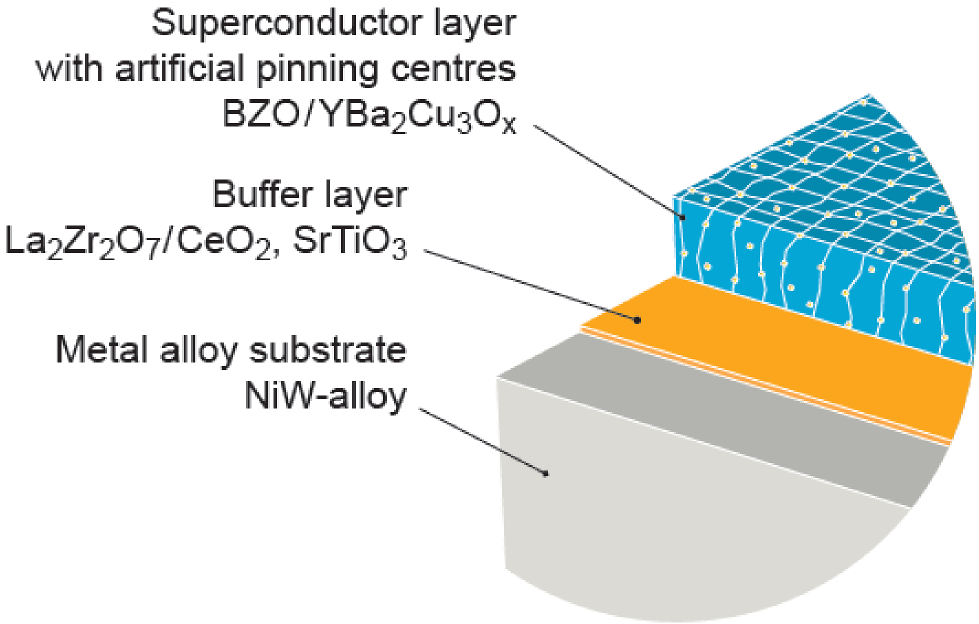

Figure 7.1: Schematic architecture of a coated conductor consisting of a highly textured Ni-5at%W tape— buffer layer (standard $La_2Zr_2O_7/CeO_2$ or alternative $SrTiO_3$), and finally the superconducting YBCO layer with nanoscale pinning centres. Figure from T. Schneller (Sol-Gel Konferenz 2009).

The system is very sensitive to the amount of nanoinclusions added into the YBCO matrix and due to the large degree of freedom in the chemical composition of TFA-YBCO, a nano-scaled chemically sensitive method at the nanometer level is fundamental for identiyfing and quantifying pinning relevant defects usch as (i) extrinsic nanoinclusions (BZO nanodots), (ii) intrinsic nanoinclusions (Y_2O_3) and (iii) secondary phases. Energy-filtering transmission electron microscopy techniques such as electron spectroscopic imaging were used for achieving this task. EDX point spectroscopy and STEM-EDX confirmed EFTEM experiements. Results relevant to the chemical imaging of BZO nanodots are presented in this chapter. Structural relevant data are also discussed when analysing electron diffraction data.

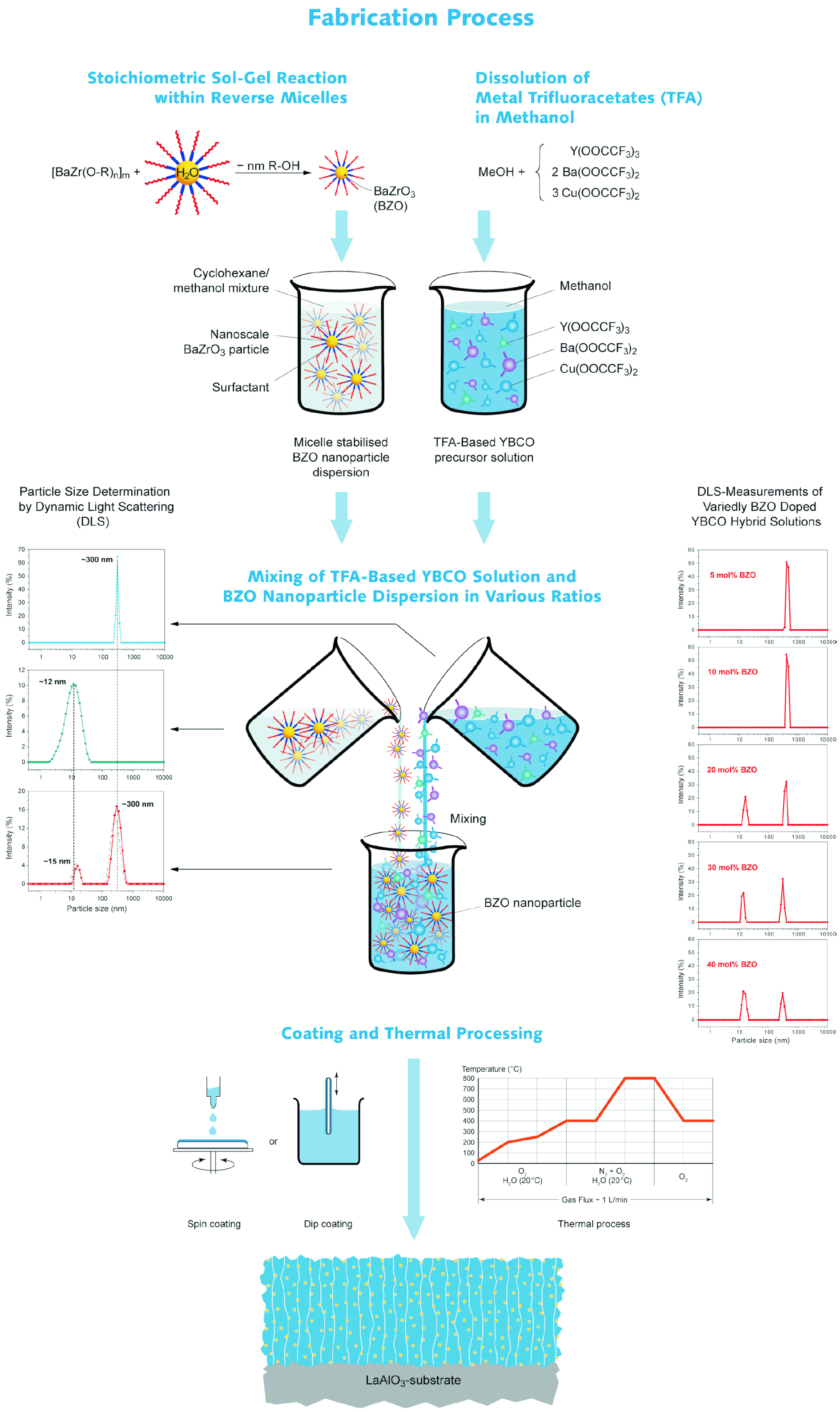

Figure 7.2: Fabrication process of a YBCO film with BZO nanoinclusions deposited on a LAO substrate. Figure from T. Schneller (Sol-Gel Konferenz 2009).

7.2 Experimental

Figure 7.2 is a flow chart of the solution synthesis and subsequent CSD Process for the BZO nano particle structured YBCO layers. The BZO nanoparticle dispersion has been prepared by a stoichiometric sol-gel reaction within nanoscaled reverse micelles. After mixing the TFA based YBCO precursor solution with various amounts of the BZO nano particle dispersion stable "hybrid solutions" were obtained. The deposition process in the present study is performed by spin coating onto single crystalline lanthanum aluminate substrate (LAO) and can also performed by dip coating for long tape substrates. Finally the as-deposited film is transformed into a BZO doped YBCO film by the thermal process described in figure 7.2.

7.3 Results and discussion

7.3.1 Diffraction contrast imaging and electron diffraction

Figure 7.3 (a) is a bright field TEM image of YBCO-10% mol BZO thin film in plan-view, twin boundaries are visible (b) is a centered dark-field image where bright spots are strongly diffracting BZO nanodots of 10-20 nm in size and (c) the corresponding electron diffraction patterns. Sharp reflections correspond to YBCO and ring patterns to BZO. Rings indicate that the nanodots are randomly oriented within the YBCO matrix. The diffraction rings could be assigned to (110), (200) and (211) reflections of BZO. Given in table 7.1 are the calculated and measured lattice distances for BZO. YBCO is [001] oriented.

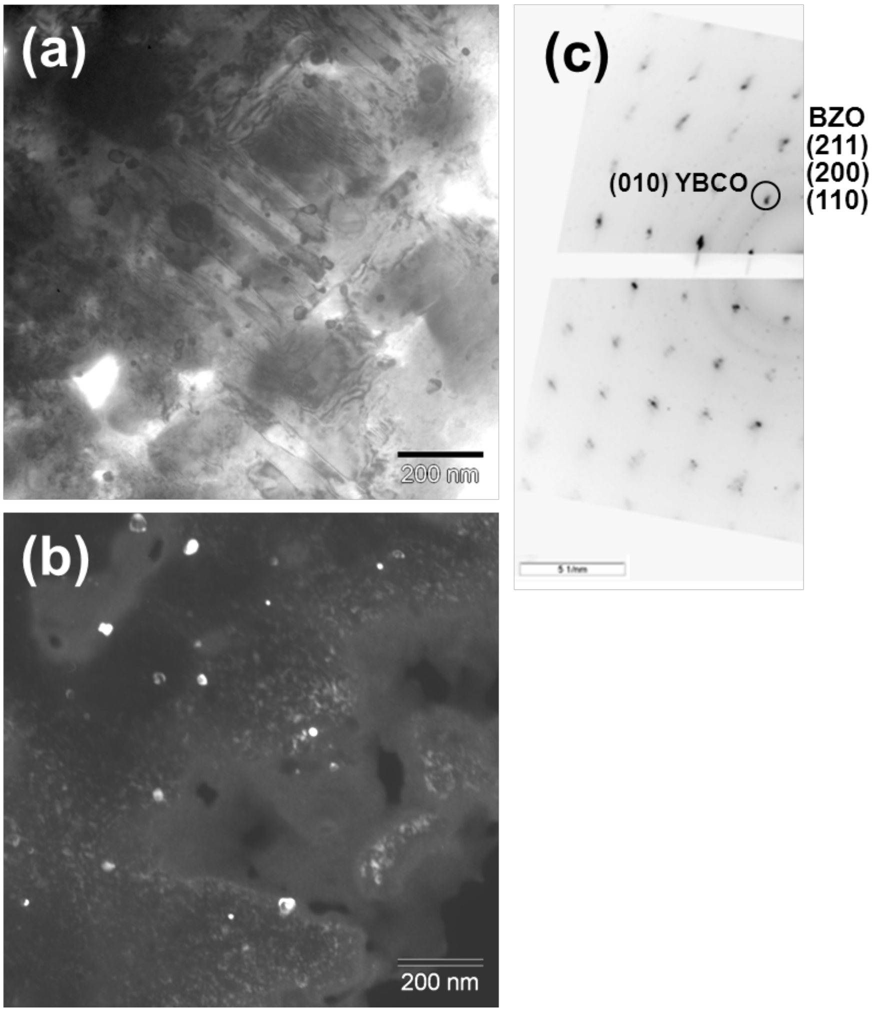

Figure 7.3: YBCO thin film with 10 % mol BZO in plan-view. (a) BF imaging (b) centered-dark field imaging and (c) corresponding electron diffraction of a 10% mol BZO doped YBCO sample. Rings correspond to BZO reflections: (110), (200) and (211). YBCO is [001] oriented.

$BaZrO_3$ Lattice parameter, a=b=c=0.4193 nm	Calc.	Exp.
d_{110}	0.292	0.311
d_{200}	0.201	0.196
d_{211}	0.171	0.175

Table 7.1: Electron diffraction of BZO.

Figure 7.4 (a) is a bright field TEM image of an YBCO thin film with 20 % mol BZO in the precursor solution. (b) is a centered dark-field image where bright spots are strongly diffracting BZO nanodots of 10-20 nm in size and (c) the corresponding electron diffraction pattern.

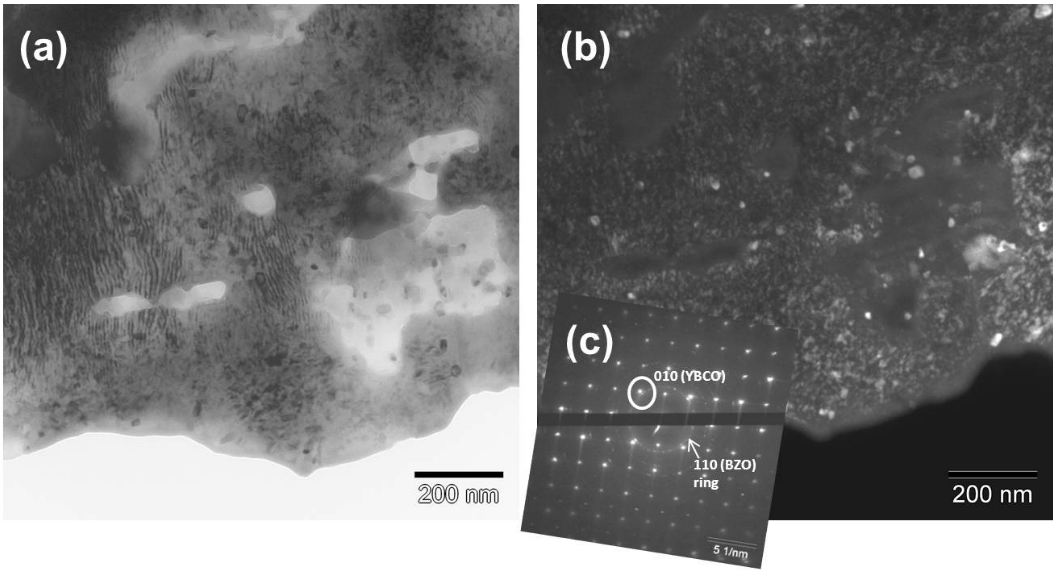

Figure 7.4: YBCO thin film with 20 % mol BZO in plan-view. a.) Bright-field TEM image (b) centered dark-field and (c) electron diffraction pattern of a 20%Mol doped TFA-YBCO sample.

7.3.2 Electron energy-loss spectroscopy (EELS) of BZO nano-dots

Figure 7.5 is an EELS spectrum of a single BZO nano-dot and the YBCO matrix. The Zr N2,3 ionization edge at 29 eV can be clearly seen. The blue EELS spectra is a reference from the YBCO (123)n phase with plasmon peaks at 14.5 eV and 25.9 eV and the YN2,3 ionization edge at 35.5 eV. The spectra were obtained with a 10 nm spot size and attention was given to avoid sample drift. Making use of the Zr N2,3 ionization edge at 29 eV, BZO nanodots within the YBCO matrix could be identified. Table 7.2 gives the acquisition conditions used for EELS.

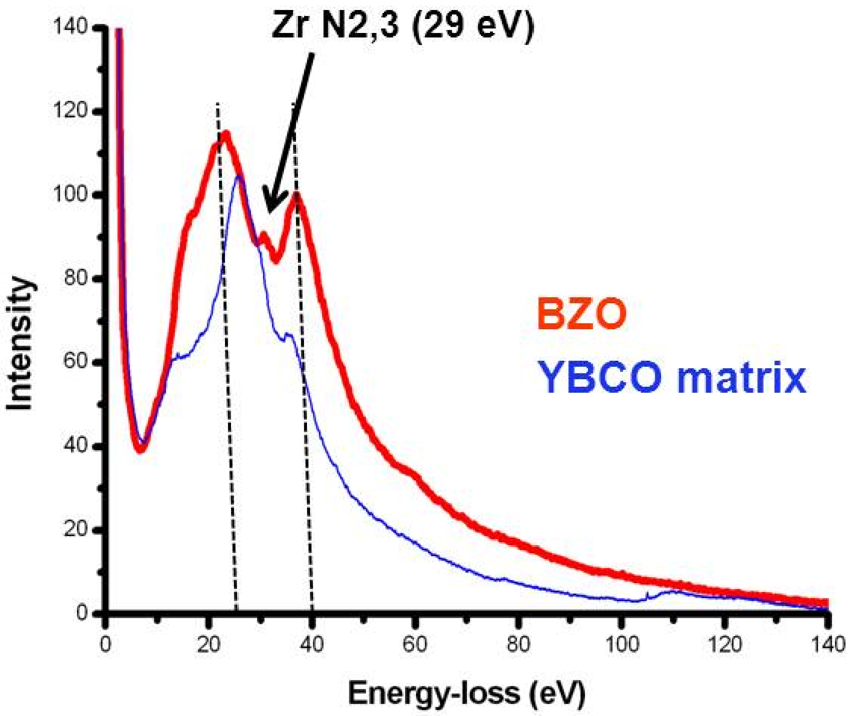

Figure 7.5: a.) EELS spectrum of a single BZO nanodot (red curve) and the YBCO matrix (blue curve).

Ionization edge	Energy-loss (eV)	Spot-size for EELS	Energy (eV):
Zr N2,3	29	10 nm	24, 40
Y N2,3	32	10 nm	25, 50

Table 7.2: Acquisition conditions for EELS and ESI of BZO nano-dot with a 3 mrad objective aperture. Energy windows with a 10 eV slit were set .

7.3.3 Electron spectroscopic imaging (ESI)

As shown in chapter 6 electron spectroscopic imaging was used for chemical imaging of defects within a YBCO matrix. Using the Zr N2,3 absorption edge it was possible to chemically image BZO nanodots within the matrix. Figure 7.6 (a) Bright-field image of a YBCO-10% mol BZO thin film. (b) Color mapping (red dots are the BZO nanoinclusions) (c) Zr N2,3 elemental mapping (d) Ba N4,5 elemental mapping (e) line scan over a single nanodot in the Zr N2,3 elemental map (f) line scan over a single nanodot in the ba N4,5 elemental map and a (g) centered dark-field featuring a single nanodot. Figure 7.6 indicates less Ba content in the BZO nanodot area than in the YBCO matrix. Quantification of elemental maps is difficult due to multiple scattering and sample drift. Nanodots appear bright in Zr N2,3 edge jump ratio images and dark in Ba N4,5 images. The sample was less than 100 nm thick.

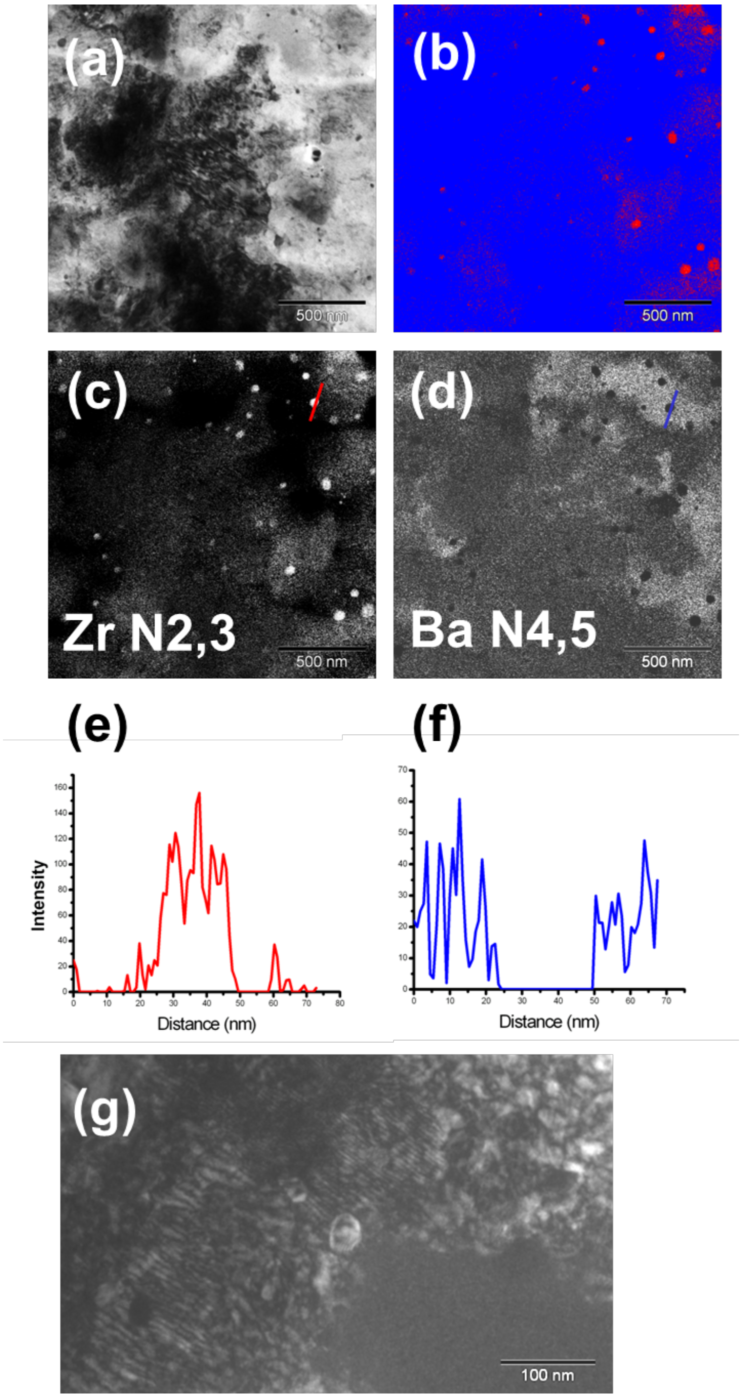

Figure 7.6: a.) Bright-field image of a 10% mol BZO doped YBCO sample(b) Color mapping (red dots are the BZO nanoinclusions) (c) Zr N2,3 elemental mapping (d) Ba N4,5 elemental mapping (e) line scan over a single nanodot in the Zr N2,3 elemental map (f) line scan over a single nanodot in the ba N4,5 elemental map and (g) centered dark-field featuring a single BZO nanodot.

7.3.4 Energy-dispersive X-ray micro-analysis (EDX)

Energy dispersive EDX spectra where obtained as point measurements, acquisition time was 50 to 300 seconds, this allowed quantification by EDX. Figure 7.7 (a) shows EDX spectra of the YBCO matrix and (b) a single BZO nanodot, where the Zr-K X-ray line is visible.

Distingushing between Y und Zr is possible only when K-lines in the spectrum are visible. Difficulties included overlapping of Y und Zr peaks i.e. Y-L (1.922 keV) and Zr-L (2.042 keV), noise, drift und detector resolution (ca. 135 eV). Given in table 7.7 are quantitative analysis of the counts under the peaks normalized to Ba-L. Due to the LaB_6 filament used (Zeiss 912 TEM) and the short acquisition time used due to sample drift, the spot size was limited to 10 nm and we obtained poor counting statistics in the EDX spectra. Note the depressed Cu peaks (Cu-L and Cu-K) and the presence of the Zr-K peak.

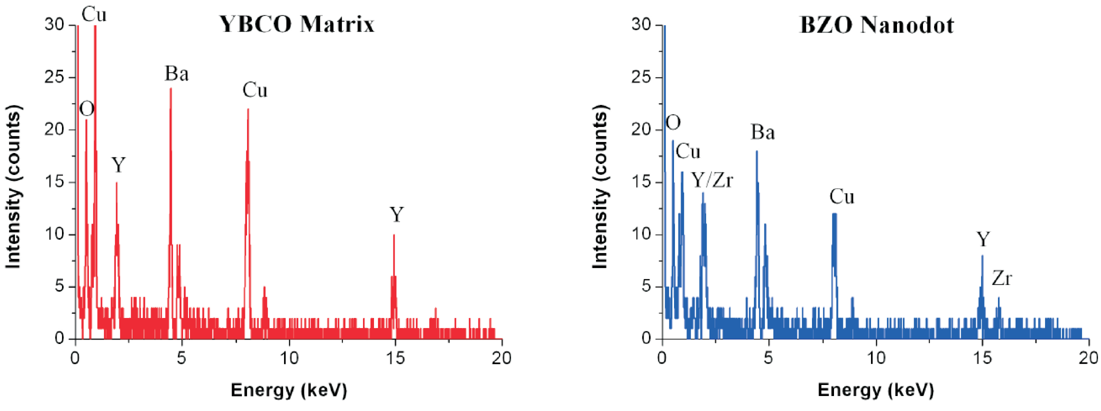

(a)

(b)

Figure 7.7: a.) EDX of the YBCO matrix (b) EDX of a BZO nanodot. Spectra were obtained with a short acquisition time (50 s) due to sample drift.

Table 7.2 are quantitative analysis of the counts under the peaks normalized to Ba-L.

Spectra	Cu-L	Y-L	Ba-L	Cu-K	Y-K	Zr-K
Nanodot	1.00	0.57	1.00	0.86	0.43	0.21
Matrix	1.36	0.68	1.00	0.95	0.45	0.00

Table 7.3: Quantitative analysis of the counts the peaks normalized to Ba-L.

7.3.5 STEM-HAADF and STEM-EDX mapping

Figure 7.7 (a) is a scanning transmission electron microscope high-angle annular dark field image (STEM-HAADF) of the sample area with a 50×50 pixel EDX mapping recorded with 0.5 s dwell time per point. This method relies on a scanning probe that rasters the sample area of interest. A Z-contrast image was obtained using a high-angle annular dark-field detector. The data was acquired with an external FEG-TEM at 200 kV. The benefit of the FEG is best seen by comparing figures 7.7 b and 7.8 d. These measurements allowed to confirm point EDX measurements and to distinguish clearly between extrinsic (BZO) and intrinsic (Y_2O_3) nanoinlclusions

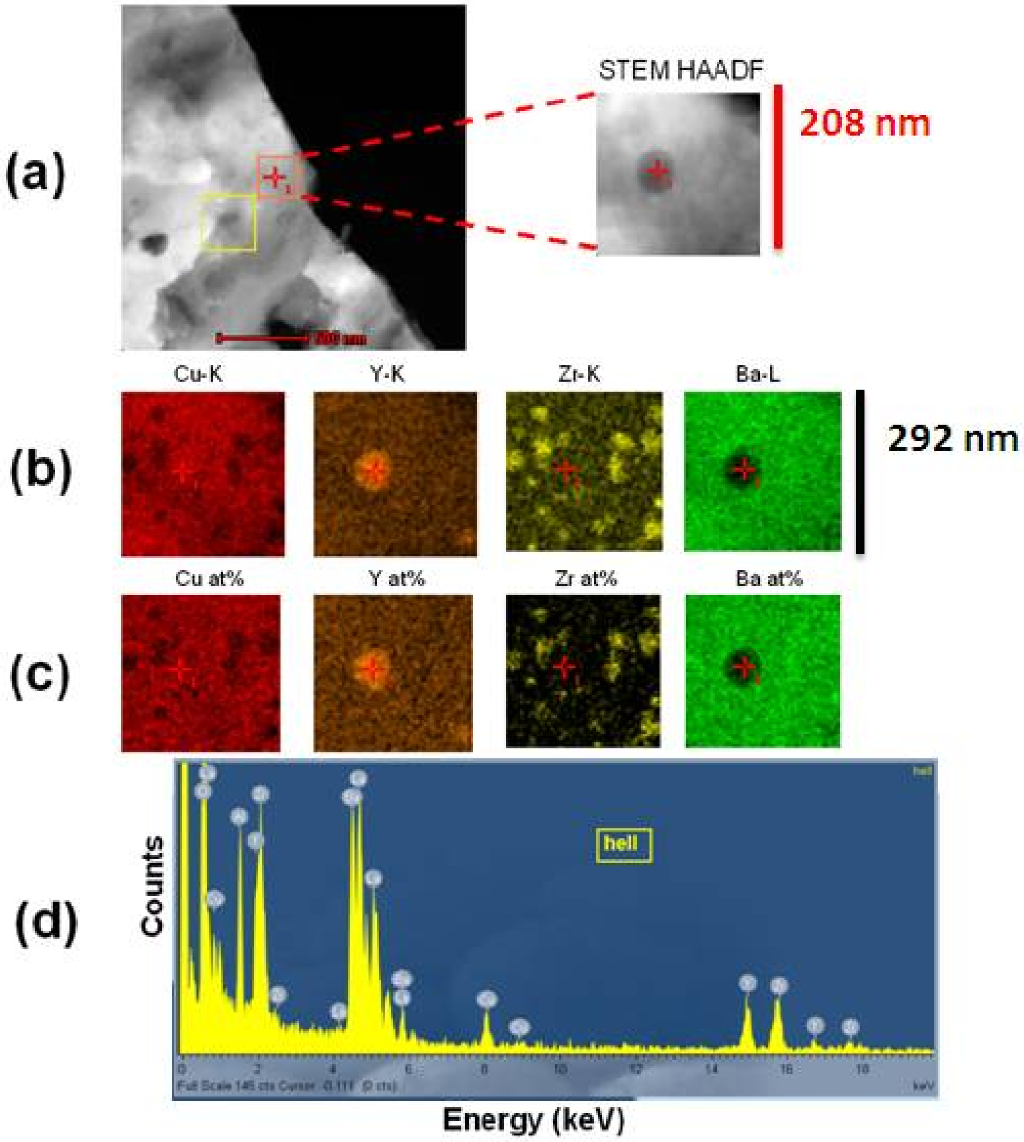

Figure 7.8: a.) STEM-HAADF image and 50×50 pixel EDX mapping recorded with 0.5 s dwell time per point. (b) The top two image rows show the integrated peak intensities and (c) the lower rows show fully quantified data as atomic percent. (d) EDX drift corrected spectrum image. Data acquired on an external 200 kV FEG-STEM.

7.4 Conclusions

The results shown in this chapter correspond to 10 and 20 % mol BZO doped TFA-YBCO thin films. TEM diffraction contrast showed that the added BZO were 10 to 20 nanometers in size and are homogeneously spread within the YBCO matrix as also previously reported by [30]. By electron energy-loss spectroscopy (EELS) single BZO nanodots could clearly chemically identificated within the YBCO matrix. Electron spectroscopic imaging using the Zr N2,3 aborption edge at 29 eV allowed to chemically image the BZO dots within a multi-phase TFA-YBCO matrix. EDX spectrocopy confirmed the Ba and Zr content of the nano-dots, however spectrum acquisition is difficult due to specimen drift during acquisition. STEM-EDX mapping allowed to cleary distinguish BZO nanoinclusions from Y_2O_3 precipitates. Electron diffraction confirmed the random oriented i.e incoherent nature of the BZO nanodots within the YBCO matrix.

Chapter 8

Final assessment on the structure-property correlation of YBCO coated conductors prepared by chemical solution deposition

8.1 Introduction

In this chapter we review the transport measurements used for determining the critical current densities of the samples investigated, give an overview on microstructural parameters of samples analyzed by TEM and discuss the limitations of the CSD process.

Holesinger *et al.* [25] gave an extensive review on the progress in nano-engineered microstructures for YBCO coated conductors based on chemical solution deposition. To obtain a tunable HTS wire technology where the performance or pinning in applied magnetic fields would be flexible to meet specific application needs, large-area YBCO deposition processes must (i) produce films with macroscopically uniform properties along the length and across the width of the wire (ii) produce a uniform, nanoscopic defect density throughout the film, and (iii) be amenable to process controls in which the nano-scale defect structures that control flux pinning, and ultimately, the intra- grain critical current density can be changed in a continuous, uniform, and reliable fashion.

Holesinger *et al.* [25] showed advances in CSD via metal organic deposition (MOD) of trifluoracetate based precursors for thick YBCO films by examining the related microstructural features and correlations to the superconducting properties. These showed that the local variations in the microstructure of the YBCO films, such as sub-grain or colony structures, YBCO film tilting relative to the interfaces, grain boundary meandering, variable porosity, and phase segregation are observed in CSD prepared films. The following phases were reported: Y_2O_3 and $Y_2Cu_2O_5$ precipitates 20-50 nm in size and a mean distance of 0.1 µm, this yields a volume density of 1000 μm^{-3}. Ba-Cu-O phases 250-500 nm in size and a mean distance of 0.357 µm yielding a volume density of 21.97 μm^{-3}.

The variations previously mentioned are averaged over all practical measurement length scales in I_c measurements and one sees macroscopically uniform I_c values and pinning properties along the length and through the thickness.

However, it is important to understand microscopic variations in the microstructure and chemistry for two reasons (i) some of the microscopic variations (precipitates, dislocations, stacking faults, etc.) in the microstructure are beneficial for the flux pinning properties (ii) variations in the connectivity caused by localized microstructural defects do have an effect on the measured I_c values through the averaging process of the measurement. Within the measurement volume, there is a distribution of inter-grain j_c values from which an average j_c value is derived. A methodology for increasing these average j_c values to identify and mitigate microscopic problems that could give rise to the lower local j_c values from which the global j_c values are determined. A common occurrence that has been observed in these types of films has been the phase segregation of Y_2O_3 and $Y_2Cu_2O_5$ precipitates. These precipitates appear to be spatially separated by Ba-Cu-O phases as also confirmed by EFTEM investigations in this thesis.

The progress in coated conductor technology is directed towards (i) enhancing self-field I_c levels (this will cut cost for all applications) (ii) developing more efficient pinning defects, and (iii) increasing the operating temperature for in-field applications (preferably to 77 K; this again will reduce cost). These cost reductions via improvements in the material properties and integration will facilitate wide-spread commercial applications of coated conductors.

8.2 Comparison between PVD and CSD grown coated conductors

The current limiting mechanisms that affect the overall performance of chemical solution deposition YBCO coated conductors include (i) the oxygen concentration (doping) and orthorhombic deformation in YBCO determining the critical temperature (ii) the texture quality and character of grain boundaries and (iii) the stoichiometry of YBCO and the presence of secondary phases and (iv) internal connectivity of superconducting layers. In point (iii) and (iv) CSD samples differ significantly from PVD prepared samples in that for CSD they yield a large fraction of secondary phases, voids and surface roughness. Only point (iii) was thoroughly studied in this work since for chemical solution deposition (CSD) prepared samples the stoichiometry can be varied easily and is important to control. Compared to PVD and CVD, the precise stoichiometry is not easily obtained in CSD-prepared samples and as a result a large density of secondary phases is usually formed.

8.3 Critical current measurements

Critical current measurements were performed by partners on all samples investigated by TEM by transport measurements for an establishment of a structure-property-chemistry correlation, this was however, limited by several factors (i.e. TEM specimen preparation, sample quality and large number of samples). As a general overview we can state that samples deposited on single crystalline samples and short lengths nickel tungsten alloy substrates gave the best results and work still needs to be done for up-scaling and a thorough correlation.

8.3.1 Measurement of the critical current density

For realizing the j_c measurements the samples had to be structured, this was done by photolithography as described in [20] and references therein. The defined measurement structure had a length of 800 µm. The width for YBCO films deposited on STO was 50 µm. For TFA-YBCO films deposited on buffered Ni-5at.%W the width was 300 µm and for PLD-YBCO samples deposited on buffered Ni-5at.%W the width was 500 µm. A thin sheet of gold was deposited on top of the samples for structuring. The system used for the measurement was a Quantum Design Physical Property Measurement System (PPMS). This system allows measurements in a temperature range from 4K to 400K under the influence of an external magnetic field of up to 9 Tesla. Rotation of the sample relative to the magnetic field direction is possible (0°-360°). All measurements were carried out under the application relevant temperature of 77 K. The samples were oriented during the measurements with the c-axis of the YBCO film parallel to the magnetic field flux $B(\vec{B} \parallel \vec{c})$. The determination of j_c and accordingly I_c from the E(j) characteristic curves was done using a field criterion of 1µV/cm which corresponds to a voltage of $0,8 \cdot 10^{-7}$ V [20]. The I-V curve or the "applied current vs the voltage drop" curve is the standard curve measured to observe a material's critical current density. The voltage drop across the superconductor material is measured as a function of the applied current, j_c is reached when the current in the superconductor yields an electric field of 1 µV/cm (see figure 1.5, chapter 1).

From the samples investigated we found that: (i) YBCO films with BZO nano-inclusions grown on LAO substrates yielded higher j_c´s ($j_c > 1\ MA/cm^2$) than the same films deposited on RABiTS ($j_c > 0.5\ MA/cm^2$) with I_c´s ranging from 20-50 A/cm. (ii) YBCO films without BZO nanoinclusions deposited on RABiTS (short-length, 10 x 10 mm) yield similar results as the same on LAO substrates ($j_c > 1 MA/cm^2$) with 280 nm and 440 nm film thickness). (iii) Values reported in the literature [30] of 10 MA/cm^2 with 200 nm film thickness and T = 77 K have not been yet reproduced on long-lengths.

Holesinger *et al.* [25] report a detailed analysis of critical current densities of CSD prepared YBCO films by investigating the magnetic field dependence and the dependence on the orientation of the magnetic field parallel to different crystallographic directions of the films, j_c measurements were carried out at temperatures between 65 and 77 K, magnetic fields between 0-7 T and usually a 1µV/cm criterion was applied for the j_c measurements. Best values for critical current densities were 5 MA/cm^2 at 65 K for zero field and 1 MA/cm^2 at 65 K and 7 T, with the field perpendicular to the c-axis. The zero field j_c values obtained for the films analyzed in this thesis can therefore be compared to those of Holesinger *et al.* [25] and the values were lower by a factor of 5-10. Since the zero field values are most sensitive to the internal connectivity of the sample it can be concluded that internal connectivity of the samples analysed in this study have to be optimized. Since critical currents were measured only at zero external magnetic field the flux pinning behavior of the material cannot be commented. It is interesting to note, however, that the short length samples with BZO nanodots yielded the largest j_c value at zero field. Thus, addition of BZO nano dots does not decrease the internal connectivity of the sample.

As will be shown in the next section large fractions of secondary phases were observed in CSD films studied in this thesis. The matrix-secondary phase interfaces could act as a two dimensional flux pinning surfaces. More detailed analysis of such interfaces are of interest. Also voids are present in the films, if these voids were connected within the samples this would yield a high surface fraction of the film. It is well known that the oxygen content and the superconducting properties at surfaces of YBCO are significantly reduced. The porosity could therefore explain the small internal connectivity, if the voids were connected to each other.

8.3.2 Micro/Nanostructural parameters of the investigated films

The transport data were correlated to the micro- and nanostructure by TEM investigations. For CSD processed YBCO films the important microstructural and chemical parameters determined by TEM methods were: (i) the chemical composition of the secondary phases, (ii) the size of the secondary phases and (iii) the density of the secondary phases. Secondary phases present included the following:

Y_2O_3 precipitates 10-40 nm in size, $Y_2Cu_2O_5$ precipitates 30-40 nm in size, $BaCuO_2$ secondary phases $>$100 nm in size, Y_2BaCuO_5 secondary phases 30-40 nm in size and CuO precipitates $>$ 200 nm in size.

From EFTEM measurements the density per area of pinning relevant Y_2O_3 precipitates and $BaZrO_3$ (BZO) extrinsic nanodots could be determined for two relevant samples: (i) a 280 nm thick CSD prepared YBCO film without BZO nandots deposited on a buffered Ni5at.%W substrate. This sample had a critical current density (j_c) of 1.0 MA/cm^2. The density of pinning relevant Y_2O_3 precipitates could be determined by EFTEM from 2-D plan-view images. The size of the Y_2O_3 secondary phases was 40 nm, the mean distance between them was 0.125 µm, from this a volume density of 512 $\mu m^{-3}$was determined. This is about half the value reported by Holesinger *et al.* [25] for a similar sample. (ii) a YBCO-CSD processed film with 10% mol BZO concentration and deposited on a LAO substrate with a critical current density (j_c) of 1.04 MA/cm^2. The sample was 200 nm thick. The BZO nanodots were 10-20 nm in size as identified by EFTEM jump ratio images of plan-view TEM specimens. The average distance between the BZO nanodots was 0.166 µm, this yields a volume density of 218.61 μm^{-3}.

Sample	j_c[MA/cm²]	I_c[A/cm]	Method	YBCO film thickness [nm]	Pinning relevant phases Origin
YBCO on Buffer layer: (2xLZO+CeO_2)	1.02	44.8	Inductive	440	Y_2O_3 Helmholtz VI
YBCO on Buffer layer: (2xLZO+CeO_2)	0.46	12.8	Inductive	280	Y_2O_3 ELSA project
YBCO (10% BZO)	1.04	20.8	Inductive	200	Y_2O_3+ BZO dots ELSA project
	j_c(77k, 0.5T) = 0.69	-	Transport (four-point, 1µV/cm)	200	Y_2O_3+ BZO dots ELSA project
(5% BZO)	1.77	35.4		200	Y_2O_3+ BZO dots ELSA project
YBCO (10 % BZO)	10	200		200	Y_2O_3+ BZO dots
	j_c(77K, 1.0T) = 2.2		Transport (four-point, 1µV/cm)		ICMAB [30]
YBCO (5% Y_2O_3+5% BZO)	j_c(7K, 1.0T) = 5.5	200	Transport (four-point, 1µV/cm)	200	Y_2O_3+ BZO dots Los Alamos [25]

Table 8.1: Superconducting properties: j_c, I_c and film thickness.

Bibliography

[1] J. Bednorz and K. Mueller, “Possible high- T_c superconductivity in the Ba-La-Cu-O system,” *Z.Phys.*, vol. B64, p. 189, 1987.

[2] D. A. Cardwell and D. S. Ginley, *Handbook of Superconducting Materials vol 2 Part E (Applications).* Bristol: Institute of Physics Publishing, 2003.

[3] S. Maekawa and M. Sato, *Physics of High-Temperature Superconductors.* Springer-Verlag Berlin and Heidelberg GmbH & Co. K, Mar. 1992.

[4] J. H. Durrell and N. A. Rutter, “Importance of low-angle grain boundaries in $YBa_2Cu_3O_{7-x}$ coated conductors,” *Superconductor Science and Technology*, vol. 22, no. 1, p. 013001, 2009. [Online]. Available: http://www.iop.org/EJ/abstract/0953-2048/22/1/013001

[5] D. Larbalestier, A. Gurevich, D. M. Feldmann, and A. Polyanskii, “High-Tc superconducting materials for electric power applications,” *Nature*, vol. 414, no. 6861, pp. 368–377, Nov. 2001. [Online]. Available: http://dx.doi.org/10.1038/35104654

[6] K. Heine, J. Tenbrink, and M. Thoner, “High-field critical current densities in $Bi_2Sr_2CaCu_2O_(x+$ 8) -Ag wires,” *Applied Physics Letters*, vol. 55, no. 23, pp. 2441–2443, Dec. 1989. [Online]. Available: http://link.aip.org/link/?APL/55/2441/1

[7] T. Schuster, H. Kuhn, A. Weisshardt, H. Kronmuller, B. Roas, O. Eibl, M. Leghissa, and H. Neumuller, “Current capability of filaments depending on their position in $(Bi,Pb)_2Sr_2Ca_2Cu_3O_{10+x}$ multifilament tapes,” *Applied Physics Letters*, vol. 69, no. 13, pp. 1954–1956, 1996. [Online]. Available: http://link.aip.org/link/?APL/69/1954/1

[8] P. Schmitt, L. Schultz, and G. Saemann-Ischenko, “Electrical properties of $Bi_2Sr_2CaCu_2O_x$ thin films prepared in situ by pulsed laser deposition,” *Physica C: Superconductivity*, vol. 168, no. 5-6, pp. 475–478, Jul. 1990. [Online]. Available: http://www.sciencedirect.com/science/article/B6TVJ-46DFBS8-4J/2/8c0d673521a4d3090e0cb99f1f18dc6e

[9] W. Buckel and R. Kleiner, *Supraleitung: Grundlagen und Anwendungen*, 6th ed. Wiley-VCH, May 2008.

[10] F. London and H. London, *Proc. Roy. Soc.*, vol. A149, p. 71, 1935.

[11] A. Abrikosov, *Zh. Eksp. Teor. Fiz.*, vol. 32, p. 1442, 1957.

[12] K. Kopitzki and P. Herzog, *Einfuehhrung in die Festkoerperphysik*, 3rd ed. Teubner Verlag, Jul. 2001.

[13] D. Christen, “Superconductors: Pumping up for wire applications,” *Nat Mater*, vol. 3, no. 7, pp. 421–422, Jul. 2004. [Online]. Available: http://dx.doi.org/10.1038/nmat1168

[14] D. Dimos, P. Chaudhari, J. Mannhart, and F. K. LeGoues, “Orientation dependence of Grain-Boundary critical currents in $YBa_2Cu_3O_{7-x}$ bicrystals,” *Physical Review Letters*, vol. 61, no. 2, p. 219, Jul. 1988. [Online]. Available: http://link.aps.org/abstract/PRL/v61/p219

[15] M. A. Beno, L. Soderholm, D. W. C. II, D. G. Hinks, J. D. Jorgensen, J. D. Grace, I. K. Schuller, C. U. Segre, and K. Zhang, “Structure of the single-phase high-temperature superconductor $YBa_2Cu_3O_{7-\delta}$,” *Applied Physics Letters*, vol. 51, no. 1, pp. 57–59, Jul. 1987. [Online]. Available: http://link.aip.org/link/?APL/51/57/1

[16] A. Goyal, D. P. Norton, J. D. Budai, M. Paranthaman, E. D. Specht, D. M. Kroeger, D. K. Christen, Q. He, B. Saffian, F. A. List, D. F. Lee, P. M. Martin, C. E. Klabunde, E. Hartfield, and V. K. Sikka, “High critical current density superconducting tapes by epitaxial deposition of $YBa_2Cu_3O_{7-\delta}$ thick films on biaxially textured metals,” *Applied Physics Letters*, vol. 69, no. 12, pp. 1795–1797, 1996. [Online]. Available: http://link.aip.org/link/?APL/69/1795/1

[17] Y. Iijima, N. Tanabe, O. Kohno, and Y. Ikeno, “In-plane aligned $YBa_2Cu_3O_{7-\delta}$ thin films deposited on polycrystalline metallic substrates,” *Applied Physics Letters*, vol. 60, no. 6, pp. 769–771, Feb. 1992. [Online]. Available: http://link.aip.org/link/?APL/60/769/1

[18] X. D. Wu, S. R. Foltyn, P. Arendt, J. Townsend, C. Adams, I. H. Campbell, P. Tiwari, Y. Coulter, and D. E. Peterson, “High current $YBa_2Cu_3O_{7-\delta}$ thick films on flexible nickel substrates with textured buffer layers,” *Applied Physics Letters*, vol. 65, no. 15, pp. 1961–1963, Oct. 1994. [Online]. Available: http://link.aip.org/link/?APL/65/1961/1

[19] D. P. Norton, A. Goyal, J. D. Budai, D. K. Christen, D. M. Kroeger, E. D. Specht, Q. He, B. Saffian, M. Paranthaman, C. E. Klabunde, D. F. Lee, B. C. Sales, and F. A. List, “Epitaxial $YBa_2Cu_3O_{7-\delta}$ on biaxially textured nickel (001): An approach to superconducting tapes with high critical current density,” *Science*, vol. 274, no. 5288, pp. 755–757, Nov. 1996. [Online]. Available: http://www.sciencemag.org/cgi/content/abstract/274/5288/755

[20] K. Knoth, “Chemisch abgeschiedene lanthanzirkonatpufferschichten auf technischen substraten zur realisierung von yttriumbariumkupferoxidbandleitern,” Ph.D. dissertation, 2006.

[21] A. Goyal, D. P. Norton, D. K. Christen, E. D. Specht, M. Paranthaman, D. M. Kroeger, J. D. Budai, Q. He, F. A. List, R. Feenstra, H. R. Kerchner, D. F. Lee, E. Hatfield, P. M. Martin, J. Mathis, and C. Park, “Epitaxial superconductors on rolling-assisted biaxially-textured substrates (RABiTS): a route towards high critical current density wire,” *Applied Superconductivity*, vol. 4, no. 10-11, pp. 403–427, Oct. 1996. [Online]. Available: http://www.sciencedirect.com/science/article/B6TW9-3TTV7NM-9/2/30eba40ca3a6192dedb451854dddc79a

[22] W. Prusseit, G. Sigl, R. Nemetschek, C. Hoffmann, J. Handke, A. Lumkemann, and H. Kinder, “Commercial coated conductor fabrication based on inclined substrate deposition,” *Applied Superconductivity, IEEE Transactions on*, vol. 15, no. 2, pp. 2608–2610, 2005.

[23] S. Sathyamurthy, M. Paranthaman, H. Zhai, S. Kang, T. Aytug, C. Cantoni, K. Leonard, E. A. Payzant, H. Christen, A. Goyal, X. Li, U. Schoop, T. Kodenkandath, and M. Rupich, “Chemical solution deposition of lanthanum zirconate barrier layers applied to low-cost coated-conductor fabrication,” *J.Mater.Res*, vol. 19, p. 2117, 2004.

[24] X. Obradors, T. Puig, A. Pomar, F. Sandiumenge, N. Mestres, M. Coll, A. Cavallaro, N. Roma, J. Gazquez, J. C. Gonzalez, O. Castano, J. Gutierrez, A. Palau, K. Zalamova, S. Morlens, A. Hassini, M. Gibert, S. Ricart, J. M. Moreto, S. Pinol, D. Isfort, and J. Bock, "Progress towards all-chemical superconducting ybco-coated conductors," *Superconductor Science and Technology*, vol. 19, no. 3, pp. S13–S26, 2006. [Online]. Available: http://www.iop.org/EJ/abstract/-link=9251230/0953-2048/19/3/003

[25] T. G. Holesinger, L. Civale, B. Maiorov, D. M. Feldmann, J. Y. Coulter, J. Miller, V. A. Maroni, Z. Chen, D. C. Larbalestier, R. Feenstra, X. Li, Y. Huang, T. Kodenkandath, W. Zhang, M. W. Rupich, and A. P. Malozemoff, "Progress in nanoengineered microstructures for tunable high-current, high-temperature superconducting wires," *Advanced Materials*, vol. 20, no. 3, pp. 391–407, Feb. 2008.

[26] M. Falter, W. Haessler, B. Schlobach, and B. Holzapfel, "Chemical solution deposition of $YBa_2Cu_3O_{7-x}$ films by dip coating," *Physica C: Superconductivity*, vol. 372-376, no. Part 1, pp. 46–49, Aug. 2002. [Online]. Available: http://www.sciencedirect.com/science/article/B6TVJ-45BCSVF-1/2/5894b60d885b940c5699a0869ec5ce2e

[27] J. Eickemeyer, D. Selbmann, R. Opitz, H. Wendrock, E. Maher, U. Miller, and W. Prusseit, "Highly cube textured Ni-W-RABiTS tapes for YBCO coated conductors," *Physica C: Superconductivity*, vol. 372-376, no. Part 2, pp. 814–817, Aug. 2002. [Online]. Available: http://www.sciencedirect.com/science/article/B6TVJ-45NPH8M-R/2/788336c2991a0108a1a782588183d916

[28] E. D. Specht, A. Goyal, D. F. Lee, F. A. List, D. M. Kroeger, M. Paranthaman, R. K. Williams, and D. K. Christen, "Cube-textured nickel substrates for high-temperature superconductors," *Superconductor Science and Technology*, vol. 11, no. 10, pp. 945–949, 1998. [Online]. Available: http://www.iop.org/EJ/abstract/0953-2048/11/10/009

[29] X. Obradors, T. Puig, A. Pomar, F. Sandiumenge, S. Pinol, N. Mestres, O. Castano, M. Coll, A. Cavallaro, A. Palau, J. Gazquez, J. C. Gonzalez, J. Gutierrez, N. Roma, S. Ricart, J. M. Moreto, M. D. Rossell, and G. van Tendeloo, "Chemical solution deposition: a path towards low cost coated conductors," *Superconductor Science and Technology*, vol. 17, no. 8, pp. 1055–1064, 2004. [Online]. Available: http://www.iop.org/EJ/abstract/-link=8702489/0953-2048/17/8/020

[30] J. Gutierrez, A. Llordes, J. Gazquez, M. Gibert, N. Roma, S. Ricart, A. Pomar, F. Sandiumenge, N. Mestres, T. Puig, and X. Obradors, "Strong isotropic flux pinning in solution-derived $YBa_2Cu_3O_{7-\delta}$ nanocomposite superconductor films," *Nat Mater*, vol. 6, no. 5, pp. 367–373, May 2007. [Online]. Available: http://dx.doi.org/10.1038/nmat1893

[31] A. V. N. ed., *Frontiers in Superconducting Materials*, 1st ed. Springer, Jun. 2005.

[32] P. A. Doyle and P. S. Turner, "Relativistic Hartree-Fock x-ray and electron scattering factors," *Acta Crystallographica Section A*, vol. 24, no. 3, pp. 390–397, 1968. [Online]. Available: http://dx.doi.org/10.1107/S0567739468000756

[33] M. A. Coulthard, "A relativistic Hartree-Fock atomic field calculation," *Proceedings of the Physical Society*, vol. 91, no. 1, pp. 44–49, 1967. [Online]. Available: http://www.iop.org/EJ/abstract/0370-1328/91/1/309

[34] L. Reimer, *Transmission Electron Microscopy: Physics of Image Formation and Microanalysis*, 2nd ed. Springer-Verlag, May 1989.

[35] R. B. N. e. a. H. P. B., A. Howie, *Electron Microscopy Of Thin Crystals.* Butterworths, 1965.

[36] B. Fultz and J. Howe, *Transmission Electron Microscopy and Diffractometry of Materials*, 2nd ed. Springer-Verlag GmbH, Nov. 2002.

[37] P. Hirsch, A. Howie, R. Nicholson, D. Pashley, and M. Whelan, *Electron microscopy of thin films.* Butterworths, 1965.

[38] H. Romberg, N. Nucker, J. Fink, T. Wolf, X. X. Xi, B. Koch, H. P. Geserich, M. Daerrler, W. Assmus, and B. Gegenheimer, "Dielectric function of $YBa_2Cu_3O_{7-x}$ between 50 meV and 50 eV," *Zeitschrift fuer Physik B Condensed Matter*, vol. 78, no. 3, pp. 367–380, Oct. 1990. [Online]. Available: http://dx.doi.org/10.1007/BF01313317

[39] R. Egerton, *Electron Energy-Loss Spectroscopy in the Electron Microscope*, 1st ed. Springer, Dec. 1995.

[40] R. H. Ritchie, "Plasma losses by fast electrons in thin films," *Physical Review*, vol. 106, no. 5, p. 874, Jun. 1957, copyright (C) 2009 The American Physical Society; Please report any problems to prola@aps.org. [Online]. Available: http://link.aps.org/abstract/PR/v106/p874

[41] D. W. Johnson and J. C. H. Spence, "Determination of the single-scattering probability distribution from plural-scattering data," *Journal of Physics D: Applied Physics*, vol. 7, no. 6, pp. 771–780, 1974. [Online]. Available: http://www.iop.org/EJ/abstract/0022-3727/7/6/304

[42] R. Bracewell, *The Fourier Transform & Its Applications*, 3rd ed. McGraw-Hill Science/Engineering/Math, Jun. 1999.

[43] *Esivision 3.2 software 2002 Soft Imaging system GmbH.*

[44] H. Bethe, "Zur theorie des durchgangs schneller korpuskularstrahlen durch materie," *Annalen der Physik*, vol. 397, no. 3, pp. 325–400, 1930. [Online]. Available: http://dx.doi.org/10.1002/andp.19303970303

[45] M. Inokuti, "Inelastic collisions of fast charged particles with atoms and molecules. the bethe theory revisited," *Reviews of Modern Physics*, vol. 43, no. 3, p. 297, Jul. 1971. [Online]. Available: http://link.aps.org/abstract/RMP/v43/p297

[46] P. Schattschneider, *Fundamentals of Inelastic Electron Scattering.* Springer-Verlag, Nov. 1986.

[47] G. Breit, "The effect of retardation on the interaction of two electrons," *Physical Review*, vol. 34, no. 4, p. 553, 1929, copyright (C) 2009 The American Physical Society; Please report any problems to prola@aps.org. [Online]. Available: http://link.aps.org/abstract/PR/v34/p553

[48] C. Moller, "Ueber den stoss zweier teilchen unter berücksichtigung der retardation der kräfte," *Zeitschrift fuer Physik A Hadrons and Nuclei*, vol. 70, no. 11, pp. 786–795, Nov. 1931. [Online]. Available: http://dx.doi.org/10.1007/BF01340621

[49] H. Bethe and E. Fermi, "Ueber die wechselwirkung von zwei elektronen," *Zeitschrift fuer Physik A Hadrons and Nuclei*, vol. 77, no. 5, pp. 296–306, May 1932. [Online]. Available: http://dx.doi.org/10.1007/BF01348919

[50] U. Fano, “Differential inelastic scattering of relativistic charged particles,” *Physical Review*, vol. 102, no. 2, p. 385, Apr. 1956. [Online]. Available: http://link.aps.org/abstract/PR/v102/p385

[51] D. H. Madison and E. Merzbacher, “Theory of Charged-Particle excitation,” Atomic Inner-Shell Processes. Volume I: Ionization and Transition Probabilities. Edited by Bernd Crasemann. Published by Academic Press, a subsidiary of Harcourt Brace Jovanovich, New York, 1975, p.2, 1975. [Online]. Available: http://adsabs.harvard.edu/abs/1975aisp....1....2M

[52] R. Egerton and D. Kenway, “An acquisition, storage, display and processing system for electron energy-loss spectra,” *Ultramicroscopy*, vol. 4, no. 2, pp. 221–225, 1979. [Online]. Available: http://www.sciencedirect.com/science/article/B6TW1-4DN98WV-9/2/7c55f2d8a373f334a56ab15ff7ffd8b9

[53] J. P. Perez, J. Sevely, and B. Jouffrey, “Straggling of fast electrons in aluminum foils observed in high-voltage electron microscopy (0.3-1.2 MV),” *Physical Review A*, vol. 16, no. 3, p. 1061, 1977. [Online]. Available: http://link.aps.org/abstract/PRA/v16/p1061

[54] A. Kenda, O. Eibl, and P. Pongratz, “Multiphase analysis with EDX elemental maps: software implementation and application to (Bi,Pb)2Sr2Ca2Cu3O10+x high-Tc superconducting tapes,” *Micron*, vol. 30, no. 1, pp. 85–97, Feb. 1999. [Online]. Available: http://www.sciencedirect.com/science/article/B6T9N-3VXYPW2-C/2/391d31de9bc8de155dd47870cc5d9e94

[55] G. Kothleitner and F. Hofer, “Optimization of the signal to noise ratio in EFTEM elemental maps with regard to different ionization edge types,” *Micron*, vol. 29, no. 5, pp. 349–357, Oct. 1998. [Online]. Available: http://www.sciencedirect.com/science/article/B6T9N-3VGDBFB-3/2/8aa7d5f74ac174caa683719ee039f1a0

[56] C. Jeanguillaume and C. Colliex, “Spectrum-image: The next step in EELS digital acquisition and processing,” *Ultramicroscopy*, vol. 28, no. 1-4, pp. 252–257, Apr. 1989. [Online]. Available: http://www.sciencedirect.com/science/article/B6TW1-46G39NC-35/2/c3727ba3a62fd1d42912c74560af1d0b

[57] D. B. Williams and C. B. Carter, *Transmission Electron Microscopy. A Textbook for Materials Science. Bd. I - IV*, 1196th ed. Springer Netherlands, Oct. 1996.

[58] N. Yao, *Focused Ion Beam Systems: Basics and Applications*, 1st ed. Cambridge University Press, Oct. 2007.

[59] N. Yao and Z. L. Wang, *Handbook of Microscopy for Nanotechnology*, 1st ed. Springer Netherlands, Nov. 2004.

[60] L. Fernandez, B. Holzapfel, F. Schindler, B. de Boer, and L. Schultz, “Grain boundary network transport properties of $YBa_2Cu_3O_{7-\delta}$ film on biaxially textured metal substrates,” *Physica C: Superconductivity*, vol. 372-376, no. Part 2, pp. 656–658, Aug. 2002. [Online]. Available: http://www.sciencedirect.com/science/article/B6TVJ-45NPH8M-B/2/114a9a09f0126f1f09bde8122f4bfd0f

[61] R. P. Reade, P. Berdahl, R. E. Russo, and S. M. Garrison, “Laser deposition of biaxially textured yttria-stabilized zirconia buffer layers on polycrystalline metallic alloys for high critical current Y-Ba-Cu-O thin films,” *Applied Physics Letters*, vol. 61, no. 18, pp. 2231–2233, Nov. 1992. [Online]. Available: http://link.aip.org/link/?APL/61/2231/1

[62] K. Hasegawa, K. Fujino, H. Mukai, M. Konishi, K. Hayashi, K. Sato, S. Honjo, Y. Sato, H. Ishii, and Y. Iwata, "Biaxially aligned YBCO film tapes fabricated by all pulsed laser deposition," *Applied Superconductivity*, vol. 4, no. 10-11, pp. 487–493, 1996. [Online]. Available: http://www.sciencedirect.com/science/article/B6TW9-3TTV7NM-J/2/828c9437a015f3e27fc8a00e38cf18bb

[63] K. Knoth, R. Huhne, S. Oswald, L. Schultz, and B. Holzapfel, "Highly textured $La_2Zr_2O_7$ buffer layers for $YBCO-$coated conductors prepared by chemical solution deposition," *Superconductor Science and Technology*, vol. 18, no. 3, pp. 334–339, 2005. [Online]. Available: http://www.iop.org/EJ/abstract/-link=8702488/0953-2048/18/3/022

[64] T. G. Chirayil, M. Paranthaman, D. B. Beach, D. F. Lee, A. Goyal, R. K. Williams, X. Cui, D. M. Kroeger, R. Feenstra, D. T. Verebelyi, and D. K. Christen, "Epitaxial growth of $La_2Zr_2O_7$ thin films on rolled ni-substrates by sol-gel process for high tc superconducting tapes," *Physica C: Superconductivity*, vol. 336, no. 1-2, pp. 63–69, Jul. 2000. [Online]. Available: http://www.sciencedirect.com/science/article/B6TVJ-40M635F-28/2/08abfb1659fdd08664c1c95bfd566976

[65] D. Eyidi and O. Eibl, "A simple, quick and reliable method for TEM cross-section preparation of ceramic oxide films on thin metal substrates," *Micron*, vol. 33, no. 5, pp. 499–505, 2002. [Online]. Available: http://www.sciencedirect.com/science/article/B6T9N-4569XNR-1/2/47e8afbe7b55676fc09a957208c878f8

[66] K. Knoth, R. Hühne, S. Oswald, L. Molina, O. Eibl, L. Schultz, and B. Holzapfel, "Growth of thick chemical solution derived pyrochlore $\mathrm{La_2Zr_2O_7}$ buffer layers for $\mathrm{YBa_2Cu_3O_{7-x}}$ coated conductors," *Thin Solid Films*, vol. 516, no. 8, pp. 2099–2108, Feb. 2008. [Online]. Available: http://www.sciencedirect.com/science/article/B6TW0-4PK7P3C-1/2/9a902606bc51330374c3dc67b86ec08a

[67] J. Eickemeyer, D. Selbmann, R. Opitz, B. de Boer, B. Holzapfel, L. Schultz, and U. Miller, "Nickel-refractory metal substrate tapes with high cube texture stability," *Superconductor Science and Technology*, vol. 14, no. 3, pp. 152–159, 2001. [Online]. Available: http://www.iop.org/EJ/abstract/0953-2048/14/3/306/

[68] S. Engel, K. Knoth, R. Huhne, L. Schultz, and B. Holzapfel, "An all chemical solution deposition approach for the growth of highly textured CeO2 cap layers on La2Zr2O7-buffered long lengths of biaxially textured Ni-W substrates for YBCO-coated conductors," *Superconductor Science and Technology*, vol. 18, no. 10, pp. 1385–1390, 2005. [Online]. Available: http://www.iop.org/EJ/abstract/0953-2048/18/10/024/

[69] *INCA 4.05 Software.* Oxford Instruments, 2001.

[70] D. B. Williams and C. B. Carter, *Transmission Electron Microscopy: A Textbook for Materials Science*, 1st ed. Springer, Aug. 2004.

[71] D. Eyidi, M. D. Croitoru, O. Eibl, R. Nemetschek, and W. Prusseit, "Growth of CeO_2 thin films deposited on biaxially textured nickel substrates," *Journal of Materials Research*, vol. 18, no. Issue 1, pp. 14–26.

[72] M. Paranthaman, *PEER Review.* Oak Ridge National Laboratory, US Department of Energy: PEER Report, 2003.

[73] K. Knoth, R. Huehne, S. Oswald, L. Schultz, and B. Holzapfel, "Detailed investigations on $La_2Zr_2O_7$ buffer layers for YBCO-coated conductors prepared by chemical solution deposition," *Acta Materialia*, vol. 55, no. 2, pp. 517–529, 2007. [Online]. Available: http://www.sciencedirect.com/science/article/B6TW8-4MC0TPX-1/2/aedb496f3f0b4b3a3a87d836e3c86670

[74] L. Schowalter, E. Hall, N. Lewis, and S. Hashimoto, vol. 130, p. 171, 1989.

[75] L. Chen, C. L. Chen, X. Chen, W. Donner, S. W. Liu, Y. Lin, D. X. Huang, and A. J. Jacobson, "Electrical properties of a highly oriented, textured thin film of the ionic conductor $Gd : CeO2 - x$ on(001) MgO," *Applied Physics Letters*, vol. 83, no. 23, pp. 4737–4739, Dec. 2003. [Online]. Available: http://link.aip.org/link/?APL/83/4737/1

[76] L. Molina, K. Knoth, S. Engel, B. Holzapfel, and O. Eibl, "Chemically deposited $La_2Zr_2O_7$ buffer layers for YBCO-coated conductors: film growth and microstructure," *Superconductor Science and Technology*, vol. 19, no. 11, pp. 1200–1208, 2006. [Online]. Available: http://www.iop.org/EJ/abstract/0953-2048/19/11/019/

[77] C. J. Lu, S. Senz, and D. Hesse, "Formation and structure of misfit dislocations at the $La_2Zr_2O_7$ - Y2O3 -stabilized ZrO2 (001) reaction front during vapour-solid reaction," *Philosophical Magazine Letters*, vol. 82, no. 4, p. 167, 2002. [Online]. Available: http://www.informaworld.com/10.1080/09500830110118058

[78] L. Molina, O. Eibl, K. Knoth, S. Engel, R. Huehne, and B. Holzapfel, "YBCO coated conductors prepared by chemical solution deposition: A tem study," *Physica C: Superconductivity*, vol. 460-462, no. Part 2, pp. 1407–1408, Sep. 2007. [Online]. Available: http://www.sciencedirect.com/science/article/B6TVJ-4NGRRVK-1K/2/5a38944d743bd7662f41dabed024bb8d

[79] W. Zhao, A. Norman, S. Phok, and R. Bhattacharya, "Transmission electron microscope study on electrodeposited Gd2O3 and Gd2Zr2O7 buffer layers for YBa2Cu3O7-x superconductors," *Physica C: Superconductivity*, vol. 468, no. 14, pp. 1092–1096, Jul. 2008. [Online]. Available: http://www.sciencedirect.com/science/article/B6TVJ-4SRW14M-2/2/5fa1827d9e0fd7892fa245bfdcf63918

[80] L. Molina, S. Engel, K. Knoth, R. Huhne, B. Holzapfel, and O. Eibl, "Grain growth and biaxial texture of chemically deposited $La_2Zr_2O_7$ buffer layers for $YBCO-$coated conductors," *Journal of Physics: Conference Series*, vol. 97, p. 012108, 2008. [Online]. Available: http://www.iop.org/EJ/abstract/-link=8702546/1742-6596/97/1/012108

[81] M. Steffens, M. Falter, M. Backer, and C. Oligschleger, "AFM investigations of the surface morphology of buffer layers for all-chemical solution coated conductors," *Journal of Physics: Conference Series*, vol. 97, p. 012165, 2008. [Online]. Available: http://www.iop.org/EJ/abstract/-link=8702549/1742-6596/97/1/012165

[82] T. Caroff, S. Morlens, A. Abrutis, M. Decroux, P. Chaudouet, L. Porcar, Z. Saltyte, C. Jimenez, P. Odier, and F. Weiss, "La2Zr2O7 single buffer layer for YBCO RABiTS coated conductors," *Superconductor Science and Technology*, vol. 21, no. 7, p. 075007, 2008. [Online]. Available: http://www.iop.org/EJ/abstract/-link=8702545/0953-2048/21/7/075007

[83] G. Love, M. G. C. Cox, and V. D. Scott, "A simple monte carlo method for simulating electron-solid interactions and its application to electron probe microanalysis," *Journal of Physics D: Applied Physics*, vol. 10, no. 1, pp. 7–23, 1977. [Online]. Available: http://www.iop.org/EJ/abstract/0022-3727/10/1/002

[84] F. Sandiumenge, A. Cavallaro, J. Gazquez, T. Puig, X. Obradors, J. Arbiol, and H. C. Freyhardt, "Mechanisms of nanostructural and morphological evolution of CeO_2 functional films by chemical solution deposition," *Nanotechnology*, vol. 16, no. 9, pp. 1809–1813, 2005. [Online]. Available: http://www.iop.org/EJ/abstract/0957-4484/16/9/066/

[85] A. Cavallaro, F. Sandiumenge, J. Gazquez, T. Puig, X. Obradors, J. Arbiol, and H.C.Freyhardt, "Growth mechanism, microstructure, and surface modification of nanostructured CeO_2 films by chemical solution deposition," *Advanced Functional Materials*, vol. 16, no. 10, pp. 1363–1372, 2006. [Online]. Available: http://dx.doi.org/10.1002/adfm.200500206

[86] M. Coll, J. Gazquez, F. Sandiumenge, T. Puig, X. Obradors, J. P. Espinos, and R. Huhne, "Nanostructural control in solution-derived epitaxial $Ce_{1-x}Gd_xO_{2-y}$ films," *Nanotechnology*, vol. 19, no. 39, p. 395601, 2008. [Online]. Available: http://www.iop.org/EJ/abstract/0957-4484/19/39/395601/

[87] J. Gazquez, F. Sandiumenge, M. Coll, A. Pomar, N. Mestres, T. Puig, X. Obradors, Y. Kihn, M. J. Casanove, and C. Ballesteros, "Precursor evolution and nucleation mechanism of $YBa_2Cu_3O_x$ films by TFA Metal-Organic decomposition," *Chemistry of Materials*, vol. 18, no. 26, pp. 6211–6219, Dec. 2006. [Online]. Available: http://dx.doi.org/10.1021/cm0617891

[88] T. Holesinger, S. Foltyn, P. Arendt, Q. Jia, P. Dowden, R. DePaula, and J. Groves, "A comparison of buffer layer architectures on continuously processed YBCO coated conductors based on the IBAD YSZ process," *Applied Superconductivity, IEEE Transactions on*, vol. 11, no. 1, pp. 3359–3364, 2001.

[89] A. P. K. H. J. Q. D. R. D. P. D. R. G. J. Holesinger T, Foltyn SR and C. JY, "The microstructure of continuously processed YBa2Cu3Oy coated conductors with underlying CeO2 and ion-beam-assisted yttria-stabilized zirconia buffer layers," *Journal of Materials Research*, pp. 1110–19, 2000.

[90] L. Reimer, *Energy- Filtering Transmission Electron Microscopy.* Springer, Berlin, Feb. 1995.

[91] H. Rose and E. Plies, "Entwurf eines fehlerarmen magnetischen Energie-Analysators," *Optik*, vol. 40, no. 336, p. 2, 1974.

[92] G. A. Botton and M. W. Phaneuf, "Imaging, spectroscopy and spectroscopic imaging with an energy filtered field emission TEM," *Micron*, vol. 30, no. 2, pp. 109–119, Apr. 1999. [Online]. Available: http://www.sciencedirect.com/science/article/B6T9N-3WMK3TF-3/2/1f2cc2dbe167bf9e0fdf72bde9548d99

[93] W. Grogger, M. Varela, R. Ristau, B. Schaffer, F. Hofer, and K. M. Krishnan, "Energy-filtering transmission electron microscopy on the nanometer length scale," *Journal of Electron Spectroscopy and Related Phenomena*, vol. 143, no. 2-3, pp. 141–149, May 2005. [Online]. Available: http://www.sciencedirect.com/science/article/B6TGC-4F0855H-3/2/d1221e0471d791145457c97359c80f88

[94] M. Varela, W. Grogger, D. Arias, Z. Sefrioui, C. Lein, C. Ballesteros, K. M. Krishnan, and J. Santamaria, "Direct evidence for Block-by-Block growth in High-Temperature superconductor ultrathin films," *Physical Review Letters*, vol. 86, no. 22, p. 5156, May 2001, copyright (C) 2009 The American Physical Society; Please report any problems to prola@aps.org. [Online]. Available: http://link.aps.org/abstract/PRL/v86/p5156

[95] B. Birajdar, N. Peranio, and O. Eibl, “Quantitative electron microscopy and spectroscopy of MgB_2 wires and tapes,” *Superconductor Science and Technology*, vol. 21, no. 7, p. 073001, 2008. [Online]. Available: http://www.iop.org/EJ/abstract/0953-2048/21/7/073001/

[96] D. Eyidi, O. Eibl, T. Wenzel, K. G. Nickel, M. Giovannini, and A. Saccone, “Phase analysis of superconducting polycrystalline MgB_2,” *Micron*, vol. 34, no. 2, pp. 85–96, Feb. 2003. [Online]. Available: http://www.sciencedirect.com/science/article/B6T9N-48DXHCH-1/2/5fac1d3edaa97a7d869b3e368b882619

[97] O. Eibl, “Electron spectroscopic imaging of $(Bi, Pb)_2Sr_2Ca_{n-1}Cu_nO_{2n+x}high - Tc$ superconducting phases in the TEM,” *Ultramicroscopy*, vol. 69, no. 4, pp. 289–296, Oct. 1997. [Online]. Available: http://www.sciencedirect.com/science/article/B6TW1-3SPX9TB-5/2/0101e36f4a6655e253c36df287770164

[98] O. Eibl, P. van Aken, and W. F. Mueller, “EELS of yba2cu3o7-x superconducting films,” *Physica Status Solidi (a)*, vol. 128, no. 1, pp. 129–137, 1991. [Online]. Available: http://dx.doi.org/10.1002/pssa.2211280115

[99] J. Fink, N. Nucker, H. Romberg, and J. Fuggle, “Electronic structure studies of high-Tc superconductors by high-energy spectroscopies,” vol. 33, no. 3, p. 372, 1989. [Online]. Available: http://domino.research.ibm.com/tchjr/journalindex.nsf/a3807c5b4823c53f85256561006324be/4952dc3ceefeb18085256bfa0067fa2c?OpenDocument

[100] J. Yuan, L. M. Brown, and W. Y. Liang, “Electron energy-loss spectroscopy of the high-temperature superconductor Ba2YCu3O7-x,” *Journal of Physics C: Solid State Physics*, vol. 21, no. 3, pp. 517–526, 1988. [Online]. Available: http://www.iop.org/EJ/abstract/0022-3719/21/3/008

[101] U. Balachandran, V. Maroni, D. Miller, S. Trasobares, Y. Lei, J. Hiller, K. Gray, V. Vlasko-Vlasov, U. Welp, H. Claus, and J. Reeves, “Characterization of coated conductors by magneto-optical imaging, raman spectroscopy, and electron microscopy,” vol. 426-431, Part2, Oct. 2005.

[102] M. Falter, K. Demmler, W. Hassler, B. Schlobach, B. Holzapfel, and L. Schultz, “Chemical solution deposition (CSD) of $YBa_2Cu_3O_{7-x}$ films and oxide buffer layers by dip coating,” *Applied Superconductivity, IEEE Transactions on*, vol. 13, no. 2, pp. 2751–2754, 2003.

[103] K. Knoth, S. Engel, C. Apetrii, M. Falter, B. Schlobach, R. Huehne, S. Oswald, L. Schultz, and B. Holzapfel, “Chemical solution deposition of YBa2Cu3O7-x coated conductors,” *Current Opinion in Solid State and Materials Science*, vol. 10, no. 5-6, pp. 205–216, 2006. [Online]. Available: http://www.sciencedirect.com/science/article/B6VS5-4PHJFFD-1/2/045559864f4d4bcd2c62fb5f0053990a

[104] F. Hofer, W. Grogger, G. Kothleitner, and P. Warbichler, “Quantitative analysis of EFTEM elemental distribution images,” *Ultramicroscopy*, vol. 67, no. 1-4, pp. 83–103, Jun. 1997. [Online]. Available: http://www.sciencedirect.com/science/article/B6TW1-3SPKX4W-J/2/4ee6cd56b971634fda1b6e225524e1bd

[105] S. Lozano-Perez, V. de Castro Bernal, and R. Nicholls, “Achieving sub-nanometre particle mapping with energy-filtered TEM,” *Ultramicroscopy*, vol. In Press, Accepted Manuscript. [Online]. Available: http://www.sciencedirect.com/science/article/B6TW1-4WB3NGF-1/2/40f6127c2644d64151f97c6589f6d62f

[106] T. Sikora and V. Serin, “The EELS spectrum database,” in *EMC 2008 14th European Microscopy Congress 1-5 September 2008, Aachen, Germany*, 2008, pp. 439–440. [Online]. Available: http://dx.doi.org/10.1007/978-3-540-85156-1_220

[107] C. C. Ahn, *Transmission Electron Energy Loss Spectrometry in Materials Science and the EELS Atlas*, 2nd ed. Wiley VCH, Oct. 2004.

[108] R. Egerton, “Oscillator-strength parameterization of inner-shell cross sections,” *Ultramicroscopy*, vol. 50, no. 1, pp. 13–28, May 1993. [Online]. Available: http://www.sciencedirect.com/science/article/B6TW1-46CC7K5-20/2/d14afcd439df501216ab6e49fb1c7ad4

[109] F. Hofer and P. Golob, “Quantification of electron energy-loss spectra with k and l shell ionization cross-sections,” *Micron and Microscopica Acta*, vol. 19, no. 2, pp. 73–86, 1988. [Online]. Available: http://www.sciencedirect.com/science/article/B6X3Y-46J055X-6K/2/a6b7d7fa4c10da2a08e23984e4a7d326

[110] P. Crozier and R. Egerton, “Mass-thickness determination by *B*ethe-sum-rule normalization of the electron energy-loss spectrum,” *Ultramicroscopy*, vol. 27, no. 1, pp. 9–18, 1989. [Online]. Available: http://www.sciencedirect.com/science/article/B6TW1-46JGMKX-DX/2/4b6554bc0f94c0f61c402c862d34a676

[111] E. Saloman and J. Hubbell, “Critical analysis of soft x-ray cross section data,” *Nuclear Instruments and Methods in Physics Research Section A: Accelerators, Spectrometers, Detectors and Associated Equipment*, vol. 255, no. 1-2, pp. 38–42, Mar. 1987. [Online]. Available: http://www.sciencedirect.com/science/article/B6TJM-473M66N-1H/2/8691ed0eeefd93510212296324fb10c0

[112] B. L. Henke, P. Lee, T. J. Tanaka, R. L. Shimabukuro, and B. K. Fujikawa, “Low-energy x-ray interaction coefficients: Photoabsorption, scattering, and reflection : E = 100-2000 eV z = 1-94,” *Atomic Data and Nuclear Data Tables*, vol. 27, no. 1, pp. 1–144, 1982. [Online]. Available: http://www.sciencedirect.com/science/article/B6WBB-4DBJ14M-34/2/6825094b1ff42381b754c31cfa39e22c

[113] W. Veigele, “Photon cross sections from 0.1 keV to 1 MeV for elements z = 1 to z = 94,” *Atomic Data and Nuclear Data Tables*, vol. 5, no. 1, pp. 51–111, 1973. [Online]. Available: http://www.sciencedirect.com/science/article/B6WBB-4H7TXYH-3/2/ebc365f91bfc0ac40867ba255a4ab20a

[114] R. F. Reilman and S. T. Manson, “Photoabsorption cross sections for positive atomic ions with z equal to or less than 30,” *The Astrophysical Journal Supplement Series*, vol. 40, p. page 815, 1979.

[115] C. C. Ahn and P. Rez, “Inner shell edge profiles in electron energy loss spectroscopy,” *Ultramicroscopy*, vol. 17, no. 2, pp. 105–115, 1985. [Online]. Available: http://www.sciencedirect.com/science/article/B6TW1-46DFCBK-3/2/69e0ee7011aafb3d7a74884c8822958a

[116] T. Malis and J. Titchmarch, *Inst. Phys. Conf. Ser. (EMAG 85)*, p. 181.

[117] Y. Yang and R. F. Egerton, “The influence of lens chromatic aberration on electron energy-loss spectroscopy quantitative measurements,” *Microscopy Research and Technique*, vol. 21, no. 4, pp. 361–367, 1992. [Online]. Available: http://dx.doi.org/10.1002/jemt.1070210412

[118] M. S. R. G. E. K. N.K. del Grande, K.G. Tirsell and S. Manson, *J.Phys. (Paris) Colloq.*, vol. 48, pp. pp. C9–951, 1987.

[119] J. H. Barkyoumb, T. I. Morrison, and D. Y. Smith, "The forward x-ray scattering factor of copper from a self-consistent data base," *Physics Letters A*, vol. 143, no. 9, pp. 462–466, Feb. 1990. [Online]. Available: http://www.sciencedirect.com/science/article/B6TVM-46S5JMX-2W8/2/8ebe05606df3706e9e58f3b0a3abef78

[120] J. J. Yeh and I. Lindau, "Atomic subshell photoionization cross sections and asymmetry parameters," *Atomic Data and Nuclear Data Tables*, vol. 32, no. 1, pp. 1–155, 1985. [Online]. Available: http://www.sciencedirect.com/science/article/B6WBB-4DBJ6HV-54/2/f1ad08f23a7d57f5adab72d3ece17af5

[121] M. Chadwick and T. Malis, "AEM characterization of sintered silicon nitride with yttria and alumina additions," *Ultramicroscopy*, vol. 31, no. 2, pp. 205–216, Oct. 1989. [Online]. Available: http://www.sciencedirect.com/science/article/B6TW1-46DFNT8-16/2/fa0bd4a0dc75d788f910347f16b55005

[122] T. Manoubi, C. Colliex, and P. Rez, "Quantitative electron energy loss spectroscopy on m45 edges in rare earth oxides," *Journal of Electron Spectroscopy and Related Phenomena*, vol. 50, no. 1, pp. 1–18, 1990. [Online]. Available: http://www.sciencedirect.com/science/article/B6TGC-44C939C-MD/2/5f12da492a705c1b87e22b8fd808c501

[123] B. Luo and E. Zeitler, "M-shell cross-sections for fast electron inelastic collisions based on photoabsorption data," *Journal of Electron Spectroscopy and Related Phenomena*, vol. 57, no. 3-4, pp. 285–295, Dec. 1991. [Online]. Available: http://www.sciencedirect.com/science/article/B6TGC-44J17NH-47/2/1eb8eaa70ed315c76d3cf22db89808f8

[124] J. Auerhammer, P. Rez, and F. Hofer, "A comparison of theoretical and experimental L and M cross sections," *Ultramicroscopy*, vol. 30, no. 3, pp. 365–370, Jul. [Online]. Available: http://www.sciencedirect.com/science/article/B6TW1-46JGMC1-B0/2/1f532bb66cc0b9ad2b496a2cf4780c77

[125] M. Cukier, P. J. C. W. P. Dhez, B. Gauthe, and F. Combet-Farnoux, *J.Phys. (Paris)*, vol. 39, pp. L–315, 1978.

[126] E. O and R. B, "Microstructure of $YBa_2Cu_3O_{7-x}$ thin films deposited by laser evaporation," *Journal of Materials Research*, pp. 2620–32, 1990.

[127] T. Holesinger, B. Maiorov, J. Coulter, L. Civale, X. Li, W. Zhang, Y. Huang, T. Kodenkandath, and M. Rupich, "Key microstructural features of MOD YBa2Cu3O7-d films on textured nickel substrates," *Applied Superconductivity, IEEE Transactions on*, vol. 17, no. 2, pp. 3259–3262, 2007.

List of Figures

List of Tables

List of Acronyms

Acronyms	Meaning
AFM	Atomic force microscopy
BF	Bright-field
CC	Coated conductor
CCD	Charged coupled device
CHI	Concentration histogram
CTEM	Conventional transmission electron microscopy
CBED	Convergent beam electron diffraction
CSD	Chemical solution deposition
DF	Dark-field
DP	Diffraction pattern
FBA	First Born approximation
EELS	Electron energy-loss spectroscopy
ELNES	Energy-loss near-edge structure
EXELFS	Extended energy-loss fine structure
EFTEM	Energy-filtering transmission electron microscopy
ESI	Electron spectroscopic imaging
EDX	Energy dispersive X-ray microanalysis
FCC	Face centered cubic
FEG	Field emission gun
FIB	Focused ion beam
FFT	Fast-Fourier Transform
FWHM	Full-width at half maximum
GB	Grain Boundary
GOS	Generalized oscillator strength
HTS	High-temperature superconductor
HRTEM	High-resolution transmission electron microscopy
IBAD	Inclined beam assited deposition
ISD	Inclined surface deposition
LAO	Lanthan aluminate
LD	Laser deposition
LZO	Lanthanum dizirconate
MOD	Metal organic deposition
ND	Normal direction
PLD	Pulsed laser deposition

RABiTS	Rolling-Assisted Biaxially Textured Substrate
RD	Rolling direction
SBR	Signal to background ratio
SNR	Signal to noise ratio
SAD	Selected area diffraction
SE	Secondary electron
SEM	Scanning electron microscopy
TAFF	Thermally activated flux-flow
TEM	Transmision electron microscopy
TD	Transverse direction
TFA	Trifluroacetate process
UHV	Ultra-high vacuum
XRD	X-ray diffraction
VD	Vapor deposition
YBCO	Yttrium-barium-copper oxide
ZAF	Atomic number, absorption, flourescence

Appendix

EFTEM result using a 300 kV TEM

Energy-filtered images obtained with a Gatan spectrometer installed on the 300 kV Titan Cube TEM at the IFW in Dresden. Figure 8.1 shows a zero-loss image of a full CSD prepared YBCO coated conductor. La and Ba elemental maps are given. Results might indicate the formation of a $BaCeO_3$ layer.

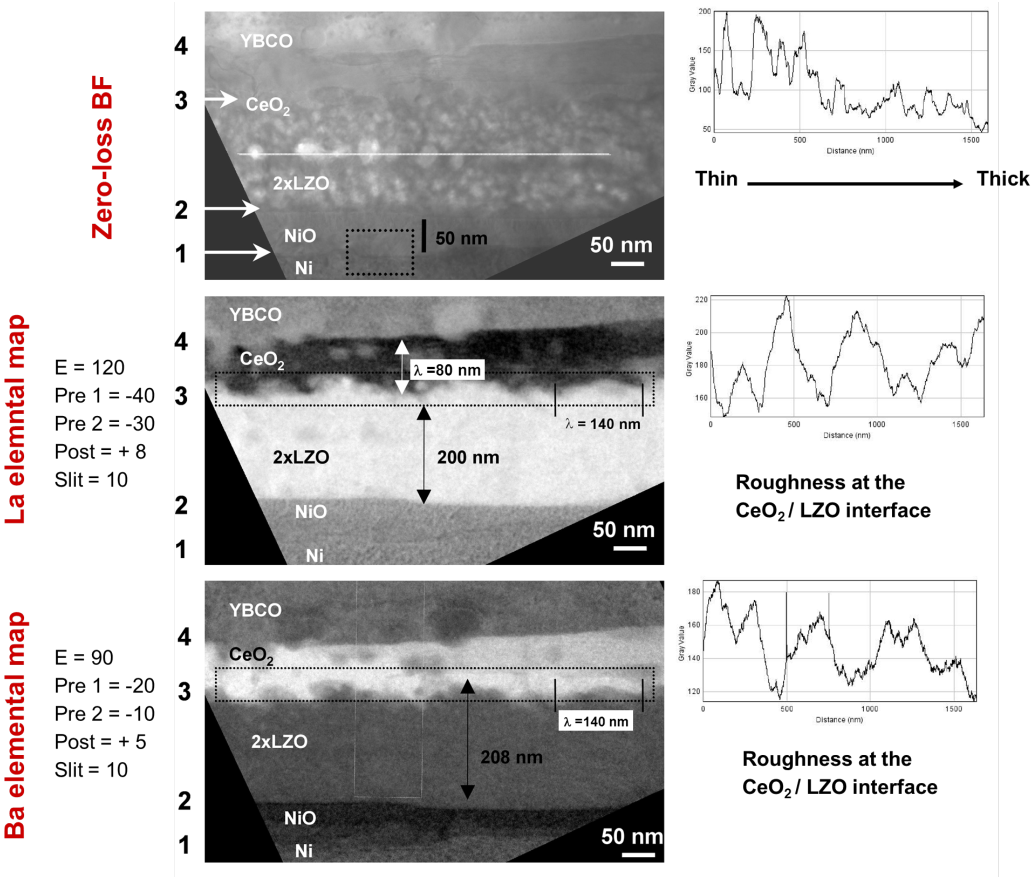

Figure 8.1: ESI of a conventionally prepared full CSD YBCO coated conductor sample in cross-section. Architecture: (1) Nickel subtrate-NiO (2) Buffer layer: 2 x LZO (3) Buffer layer: CeO_2 ($BaCeO_3$) (4) YBCO film.

Electron properties

	Non-relativistic ($E << E_0$)	Relativistic ($E \sim E_0$)
Mass	$m = m_0$	$m = \frac{m_0}{\sqrt{1-\frac{v^2}{c^2}}}$
Rel. corr. electron mass	-	$\gamma = \frac{m}{m_0} = \frac{1}{\sqrt{1-\beta^2}} = 1 + \frac{eU}{m_0c^2}$
Energy	$E = eU = \frac{1}{2}m_0v^2$	$mc^2 = m_0c^2 + eU = E_0 + E$
		$m = m_0(1 + \frac{E}{E_0})$
Velocity	$v = \sqrt{\frac{2E}{m_0}}$	$v = c\sqrt{1 - \frac{1}{\left(1+\frac{E}{E_0}\right)^2}}$
Corrected Velocity	-	$\beta = \frac{v}{c}\sqrt{1 - \frac{1}{\gamma^2}}$
Momentum	$p = m_0v = \sqrt{2m_0E}$	$p = \sqrt{2m_0E\left(\frac{1+E}{2E_0}\right)}$
		$p = \frac{1}{c}\sqrt{2EE_0 + E^2}$
de Broglie Wave length	$\lambda = \frac{h}{p} = \frac{h}{\sqrt{2m_0E}}$	$\lambda = \frac{h}{\sqrt{2m_0E\left(\frac{1+E}{2E_0}\right)}}$
		$\lambda = \frac{hc}{\sqrt{2EE_0+E^2}}$
		$\lambda = \frac{hc}{m_0c^2}\frac{1}{\sqrt{\gamma^2-1}}$

Table 8.3: Quantities of the electron for non-relativistic and relativistic energies.

Matlab script for calculating the total inelastic ionization scattering cross-section for parameterized K,L,M,N shell cross-sections

Equation (2.78) used for calculating the differential scattering cross-sections:

$$\sigma(\beta,\Delta) = \frac{4\pi a_0^2}{(<E>/R)(T/R)} f(\Delta) \left[ln(1 + \left(\frac{\beta^2}{<\theta_E>^2}\right) + G(\beta,\gamma,<\theta_E>)\right]$$

Matlab equations for calculating cross-sections	
SIGMA_Ba	1.3*10^-16*G2/(1+gamma)/EBAR_Ba/E*FD_Ba*SQUAB_Ba;
SIGMA_La	1.3*10^-16*G2/(1+gamma)/EBAR_La/E*FD_La*SQUAB_La
SIGMA_Ce	1.3*10^-16*G2/(1+gamma)/EBAR_Ce/E*FD_Ce*SQUAB_Ce
SIGMA_Y	1.3*10^-16*G2/(1+gamma)/EBAR_Y/E*FD_Y*SQUAB_Y

```
    % Basic to Matlab from SIGPAR2, Molina 2008
    % Calculates ionization scattering cross-sections
    % Values from Egerton et.al. Ultramicroscopy 50 (1993) 13-8

    % Z, EN(4,5),f(50),f(100),f(200),% ERR

    Ba = [56,90, 7.11, 9.03,6];
    La = [57,103,6.43,9.46,8];
    Ce = [58,109,6.60,9.65,6];

    1.3*10^-16*G2/(1+gamma)/EBAR_Ce/E*FD_Ce*SQUAB_Ce;
    % Z,EM(4,5),f(50),f(100),f(200),% ERR

    Y = [39,160,0.68,2.2,4.6,20]; E = 0; % Initialize to value<1

    % so it does the loop at least once prepared by chemical solution depositionif E>0 || E<400 E =

input(’Enter E’); end B = 0;
    % Initialize to value<1
    % so it does the loop at least once if B>0 || B<30 B = input(’Enter Beta in mrad’); end D = 0;
    % Initialize to value<1
    % so it does the loop at least once if D>0 || D<200 D = input(’Enter delta(eV)’); end

    % Calculate Cross-section, assuming dipole conditions if D<=50 && D>0
    FD_Ba = Ba(3).*D./50;
    FD_La = La(3).*D./50; FD_Ce = Ce(3).*D./50;
    FD_Y = Y(3).*D./50; end if D>50 && D<100
    FD_Ba = Ba(3)+(D-50)./50*(Ba(4)-Ba(3));
    FD_La = La(3)+(D-50)./50*(La(4)-La(3));
    FD_Ce = Ce(3)+(D-50)./50*(Ce(4)-Ce(3));
    FD_Y = Y(3)+(D-50)./50*(Y(4)-Y(3));
    end
```

```
if D>100 && D<250

FD_Ba = Ba(4)+(D-100)./100*(Ba(5)-Ba(4));
FD_La = La(4)+(D-100)./100*(La(5)-La(4));
FD_Ce = Ce(4)+(D-100)./100*(Ce(5)-Ce(4));
FD_Y = Y(4)+(D-100)./100*(Y(5)-Y(4));
end
EBAR_Ba = sqrt(Ba(2)*(Ba(2)+D));
EBAR_La = sqrt(La(2)*(La(2)+D));
EBAR_Ce = sqrt(Ce(2)*(Ce(2)+D));
EBAR_Y = sqrt(Y(2)*(Y(2)+D));
gamma = 1+E./511; 1.3*10^-16*G2/(1+gamma)/EBAR_Y/E*FD_Y*SQUAB_Y


G2=gamma^2;

V2=1-1/G2;


B2=B^2;

THEBAR_Ba = EBAR_Ba/E/(1+1/gamma);
THEBAR_La = EBAR_La/E/(1+1/gamma);
THEBAR_Ce = EBAR_Ce/E/(1+1/gamma);
THEBAR_Y = EBAR_Y/E/(1+1/gamma);

T2_Ba = THEBAR_Ba^2; T2_La = THEBAR_La^2;
T2_Ce = THEBAR_Ce^2;
T2_Y = THEBAR_Y^2;

GFUNC_Ba =log(G2)-log((B2+T2_Ba)/(B2+T2_Ba/G2))-V2*B2/(B2+T2_Ba/G2);
GFUNC_La =log(G2)-log((B2+T2_La)/(B2+T2_La/G2))-V2*B2/(B2+T2_La/G2);
GFUNC_Ce =log(G2)-log((B2+T2_Ce)/(B2+T2_Ce/G2))-V2*B2/(B2+T2_Ce/G2);
GFUNC_Y =log(G2)-log((B2+T2_Y)/(B2+T2_Y/G2))-V2*B2/(B2+T2_Y/G2);

SQUAB_Ba = log(1+B2/T2_Ba)+GFUNC_Ba;
SQUAB_La = log(1+B2/T2_La)+GFUNC_La;
SQUAB_Ce = log(1+B2/T2_Ce)+GFUNC_Ce;
SQUAB_Y = log(1+B2/T2_Y)+GFUNC_Y;

% Cross-section in cm^2
SIGMA_Ba =1.3*10^-16*G2/(1+gamma)/EBAR_Ba/E*FD_Ba*SQUAB_Ba;
SIGMA_La =1.3*10^-16*G2/(1+gamma)/EBAR_La/E*FD_La*SQUAB_La;
SIGMA_Ce =1.3*10^-16*G2/(1+gamma)/EBAR_Ce/E*FD_Ce*SQUAB_Ce;
SIGMA_Y =1.3*10^-16*G2/(1+gamma)/EBAR_Y/E*FD_Y*SQUAB_Y;

%output
```

```
strcat(num2str(SIGMA_Ba),’cm^2’,’+/-’,num2str(SIGMA_Ba*Ba(5)./100),’cm^2’)
strcat(num2str(SIGMA_La),’cm^2’,’+/-’,num2str(SIGMA_La*La(5)./100),’cm^2’)
strcat(num2str(SIGMA_Ce),’cm^2’,’+/-’,num2str(SIGMA_Ce*Ce(5)./100),’cm^2’)
strcat(num2str(SIGMA_Y),’cm^2’,’+/-’, num2str(SIGMA_Y*Y(5)./100),’cm^2’)
```

Eidesstattliche Versicherung

Ich erklare hiermit, dass ich die zur Promotion eingereichte Arbeit mit dem Titel "Superconducting properties and nanostructure of $YBa_2Cu_3O_{7-\delta}$ coated conductors prepared by chemical solution deposition" selbstandig verfasst, nur die angegebenen Quellen und Hilfsmittel benutzt und wortlich oder inhaltlich ubernommene Stellen als solche gekennzeichnet habe. Ich versichere an Eides statt, dass diese Angaben wahr sind und dass ich nichts verschwiegen habe. Mir ist bekannt, dass die falsche Abgabe einer Versicherung an Eides statt mit Freiheitsstrafen bis zu drei Jahren oder mit Geldstrafe bestraft wird.

Weiterhin erklare ich, dass bisher kein Promotionsversuch unternommen wurde.

Tübingen, den

Acknowledgements

First of all I would like to thank my supervisor Prof. Dr. Oliver Eibl for giving me the opportunity to work towards my PhD. in his group, for the excellent guidance during all stages, for the high level training in transmission electron microscopy applied to materials science and materials physics, for teaching me how to overcome problems and showing me the importance of good planning, things that are not only useful in science, but are also important for life in general, thank you very much. Many thanks also to Prof. Dr. Erich Plies who kindly accepted to take part in the thesis evaluation committee.

During my stay in Tübingen I had the opportunity to attend several conferences and work within two exciting research projects as an electron microscopist in the field of Applied Superconductivity. I would like to thank all the colleagues with whom I collaborated within these projects, especially Dr. Bernhard Holzapfel, Dr. Kerstin Knoth, Dr. Sebastian Engel, Dr. Bernd Rellinghaus and Thomas Thersleff from the IFW Dresden, Dr. Martina Falter and Dr. Michael Bäcker and Dr. Theodor Schneller (RWTH Aachen).

I would also like to thank my colleagues at the Institute of Applied Physics at the University of Tübingen for the great working atmosphere and support during my stay at the Institute, especially Dr. Balaji Birajdar, Dr. Nicola Peranio, Frau Imgard Meissner, Dipl. Ing. Bernard Degel, Michael Rössel, Dr. Manuela Koyuncu, Dr. Antje Bisemeier, Michael Dürrschnabel, Zainul Aabdin, Mathias Kühnle and Markus Weiler.

I would like to thank all the friends I have made over the years in Germany for their moral support and the good times during my long stay, they have made me feel at home. I want also to thank Anne for her support during the last years.

And last but not least, I would like to thank my family. This dissertation is dedicated to them. Without their help I would have never reached this stage,

¡Muchas gracias!

Leopoldo Molina-Luna

Tübingen, February of 2010

List of Publications

1. Molina L, Eibl O, Knoth K, Engel S, Hühne R, Holzapfel B. "YBCO coated conductors prepared by chemical solution deposition: A TEM study". Physica C 460-462 1407 (2007). `http://www.sciencedirect.com/science/article/B6TVJ-4NGRRVK-1K/2/5a38944d743bd7662f41dabed024bb8d`

2. Molina L, Knoth K, Engel S, Holzapfel B, Eibl O. "Chemically deposited $La_2Zr_2O_7$ buffer layers for YBCO coated conductors: film growth and microstructure".Supercond. Sci. Tech. 19 1200-1208 (2006) `http://www.iop.org/EJ/abstract/0953-2048/19/11/019/`

3. L Molina, O Eibl, S Engel, K Knoth, R Hühne and B Holzapfel. "TEM thin film analysis of chemically deposited $YBa_2Cu_3O_{7-x}$ coated conductors". Microscopy and Microanalysis. (Cambridge University Press), 13 (Suppl. 3), 412 (2007). `http://www.iop.org/EJ/abstract/-link=8702546/1742-6596/97/1/012108`

4. Molina L, Engel S, Knoth K, Hühne R, Holzapfel B., Eibl O. "Grain growth and biaxial texture of chemically deposited $La_2Zr_2O_7$ buffer layers for YBCO coated-conductors" J. Phys.: Conf. Ser.97, 012108, 2008. `http://www.iop.org/EJ/abstract/-link=8702546/1742-6596/97/1/012108`

5. L. Molina, T. Thersleff, B. Rellinghaus, B. Holzapfel and O. Eibl. "ESI and HRTEM of chemical solution deposited (CSD) YBCO-coated conductors". EMC 2008 14th European Microscopy Congress 1-5 September 2008, Aachen, Germany. Volume 2: Materials Science, page 351.`http://www.springerlink.com/content/t582510x38u3722w/`

6. L. Molina, S. Engel, B. Holzapfel and O. Eibl. "CTEM diffraction contrast of biaxially-textured LZO buffer layers on nickel substrates". EMC 2008 14th European Microscopy Congress 1-5 September 2008, Aachen, Germany Volume 2: Materials Science, p. page 355. `http://www.springerlink.com/content/p221641l13q47kp6/`

7. T. Thersleff, E. Backen, S. Engel, C. Mickel, L. Molina-Luna, O. Eibl, B. Rellinghaus, L. Schultz and B. Holzapfel. "Microstructure and self-organization of nano-engineered artificial pinning centers in $YBa_2Cu_3O_{7-x}$ coated conductors". EMC 2008 14th European Microscopy Congress 1–5 September 2008, Aachen, Germany, Volume 2: Materials Science, page 371. `http://www.springerlink.com/content/x196234t13652403/?p=a1fc47bccb644d9bb067a0ca500fa0de&pi=1`

8. Knoth K, Hühne R, Oswald S, Molina L, Eibl O, Schultz L, Holzapfel B. "Growth of thick chemical solution derived pyrochlore $La_2Zr_2O_7$ buffer layers for coated conductors".Thin Solid

Films. Volume 516, Issue 8, 29 February 2008, Pages 2099-2108 `http://www.sciencedirect.com/science/article/B6TW0-4PK7P3C-1/2/9a902606bc51330374c3dc67b86ec08a`

9. Molina L, M. Dürrschnabel, M.Falter, M. Bäcker, O. Eibl, MC 2009. "Structure-property correlation of YBCO coated conductors at different length-scales". Microscopy Conference, Graz, Austria, 30.8.-4.9.09, in: Proceedings, Volumen 3, Materials Science, W. Grogger, F. Hofer, P. Poelt (eds.), Graz: Verl. der TU Graz, 2009, Vol. 3, 481-482 (2009).

Oral conference contributions:

2009 L. Molina, O. Eibl. "Structure-property correlation of CSD grown coated conductors by electron microscopy". Talk presented at the 9th European Conference on Applied Superconductivity (EUCAS 2009), CC-Characterization session, 13-17th, September, Dresden, Germany, 2009.

2008 L. Molina, S. Engel, B. Holzapfel, and O. Eibl, “CTEM diffraction contrast of biaxially-textured $La_2Zr_2O_7$ buffer layers on nickel substrates”. Talk presented at the EMC 2008 14th European Microscopy Congress. September 2008, Aachen, Germany, 2008, pp. 353-354.

2007 L. Molina, S. Engel, K. Knoth, R.Hühne, B. Holzapfel, O. Eibl. “Grain growth and biaxial texture of chemically deposited $La_2Zr_2O_7$ buffer layers for YBCO coated-conductors”. Talk presented at the 8th European Conference on Applied Superconductivity (EUCAS 2007), Brussels, Belgium, 16th-20th September 2007.

2007 L. Molina, S Engel, B Holzapfel, O Eibl. “Temperature series to study the biaxial texturing of $La_2Zr_2O_7$ buffer layers on nickel-tungsten substrates”. Talk presented at the 71th annual meeting and DPG spring meeting of the division condensed matter, Regensburg, Germany, 2007.

Poster conference contributions:

2009 L. Molina, M. Dürrschnabel, M.Falter, M.Bäcker, O.Eibl, "Structure-property correlation of CSD coated conductors at different length scales", MC Conference, Graz, Austria, 30th August - 4th September 2009, Volume 3, Materials Science, pp.481.

2008 L. Molina, T. Thersleff, B. Rellinghaus, B. Holzapfel, and O. Eibl, “ESI and HRTEM of chemical solution deposited YBCO coated conductors”. EMC 2008 14th European Microscopy Congress 1–5 September 2008, Aachen, Germany, 2008, pp. 351- 352.

2008 T. Thersleff, E. Backen, S. Engel, C. Mickel, L. Molina-Luna, O. Eibl, B. Rellinghaus, L. Schultz, and B. Holzapfel, “Microstructure and self-organization of nano-engineered artificial pinning centers in YBCO coated conductors”. EMC 2008 14th European Microscopy Congress 1-5 September 2008, Aachen, Germany, 2008, pp. 351-352.

2008 L. Molina, T.Thersleff, C.Mickel, B.Holzapfel, O.Eibl, . “TEM sample preparation of YBCO coated conductors: conventional method and FIB”. European Microscopy Conference (EMC´08), Aachen, 1th- 5th September 2008, pp. 355-256.

2008 T. Thersleff, S.Menzel, C.Mickel, E.Backen, B.Rellinghaus, L.Schultz, B.Holzapfel, L.Molina, O.Eibl, "Targeted FIB preparation of TEM lamellae from structured YBCO coated conductors", Poster contribution Workshop Arbeitskreis FIB, Luzern 2008.

2008 T. Thersleff, L. Molina, E. Backen, S. Engel, C. Mickel, S. Menzel, B. Schlobach, O. Eibl, L. Schultz, B. Holzapfel. “Focused Ion Beam preparation of YBCO thin film TEM lamellae”, NESPA TEM Workshop, Barcelona, Spain, 5.-9.5.2008

2007 L. Molina, O. Eibl, S. Engel, K. Knoth, R. Hühne, B. Holzapfel. “TEM thin film analysis of chemically deposited YBCO coated conductors”. Microscopy Conference, Saarbrücken, Germany, 2th -7th September 2007, page 412.

2007 L. Molina, K. Knoth, B. Holzapfel, O. Eibl. “TEM analysis of biaxially textured $La_2Zr_2O_7$ thin films by the Moiré technique” in 71th annual meeting and DPG spring meeting of the division condensed matter, Regensburg, Germany, 26th -30th March 2007, page 667.

2006 L. Molina, K. Knoth, S. Engel, R. Hühne, B. Holzapfel, O. Eibl. “TEM study of YBCO coated conductors prepared by chemical solution deposition” in 8th International Conference on Materials and Mechanisms of Superconductivity and High Temperature Superconductors (M2S-HTSC-VIII), Dresden, 9th -14th July 2006, page 394.

2006 K. Knoth, R. Hühne, S. Oswald, L. Molina, O. Eibl, L. Schultz , B. Holzapfel. “Thick pyrochlore $La_2Zr_2O_7$ buffer layers prepared by CSD on cube textured Ni-W substrates for coated conductors” in Applied Superconductivity Conference (ASC) Seattle, USA, August 27th-September 1st , 2006.

2006 L. Molina, K. Knoth, S. Engel, B. Holzapfel, O. Eibl. “TEM cross-section analysis of $La_2Zr_2O_7$ buffer layers for coated conductors” in AKF Frühjahrestagung 2006 and 21th General Conference of the EPS Condensed Matter Division, Dresden, 26th - 31th March.annual meeting and DPG spring meeting of the division condensed matter, Regensburg, Germany, 26th -30th March 2007, page 667.

2006 K. Knoth, R. Hühne, S. Oswald, L. Molina, O. Eibl, L. Schultz , B. Holzapfel. “Thick pyrochlore $La_2Zr_2O_7$ buffer layers prepared by CSD on cube textured Ni-W substrates for coated conductors” in Applied Superconductivity Conference (ASC) Seattle, USA, August 27th-September 1th , IEEE Transactions on Applied Superconductivity, 2006

2006 L. Molina, K. Knoth, S. Engel, B. Holzapfel, O. Eibl. “TEM cross-section analysis of $La_2Zr_2O_7$ buffer layers for coated conductors” in AKF Frühjahrestagung 2006 and 21th General Conference of the EPS Condensed Matter Division, Dresden, 26th - 31th March.

Publications before the Ph.D thesis:

1. Raschke M B, Molina L, Elsaesser T, Kim D H , Knoll W, Hinrichs K “Apertureless near-field vibrational imaging of block-copolymer nanostructures with ultrahigh spatial resolution” ChemPhysChem. 6, 197 (2005) `http://www3.interscience.wiley.com/journal/112100392/abstract`

2. Grima-Gallardo P, Cárdenas K, Molina L, Quintero M, Ruiz J, Delgado G E, Briceño G M “A Comparative Study of $(Cu - III - Se_2)_x - (FeSe)_{1-x}$ Alloys (III: Al, Ga, In) ($0 < x < 1$) by X-Ray diffraction, differential thermal analysis and scanning electron microscopy”. Phys. Stat.sol. (a) 187, 295 (2001) `http://www3.interscience.wiley.com/journal/85515660/abstract`
3. Grima-Gallardo P, Molina L, Quintero M, Tovar R, Ruiz J, Quintero E, Delgado G, Maury L. “X-Ray Diffraction, Differential thermal analysis and magnetic susceptibility measurements on nominally $CuFeCrSe_3$”. Phys.Stat.Sol. (b) 220, 377 (2000) `http://www3.interscience.wiley.com/journal/72511007/abstract`
4. Grima-Gallardo P, Orozco E, Munoz M, Molina L, Molina I “Optical absorption measurements on $CuInS_2$ at ($T > 300$ K) high temperature”. Adv. Mat. Sci & Technol. 2, 7 (2000)

Curriculum Vitae

Personal data	Mr. Leopoldo Molina-Luna Date and place of birth: 23.09.1976, Valera, Venezuela Nationality: Venezuelan

SCHOOL

1982-1994	Bachiller en Ciencias, (Science High-school Diploma) Ministerio de Educación, Mérida, Venezuela

UNIVERSITY

1994-1999	Licenciado en Física (Bachelor in Physics) Department of Physics, Universidad de Los Andes, Mérida, Venezuela Prof. Grima-Gallardo, Prof. Quintero, Prof. Khoudeir, Prof. Percoco, Prof. Tibaire Prof. Laffaille, Prof. Naranjo, Prof. Birbal, Prof. Rosenzweig, Prof. Wasim
2000	Academic exchange student. Eberhard-Karls Universität Tübingen, Tübingen, Germany Full scholarship from the Landesstiftung Baden-Württemberg
2001-2003	Master of Science in Physics Universität Stuttgart and Max-Planck-Institute for Solid State Research, Stuttgart, Germany Prof. Keimer, Prof. Hans-Eckhardt Schaefer, Prof. Dressel, Prof. Muramatsu, PD.Dr. Hilfer, Prof. Kneissel, Prof. Fähnle, Prof. Schweizer, Prof. Mehring
Thesis	*Raman Scattering Study of High-transition Temperature Superconducting* $La_2CuO_{4+\delta}$
2004	Research assistant Max-Born-Institute for Nonlinear Optics and Short Pulse Spectroscopy, Berlin, Germany
Jan. 2005 - Jan. 2010	Institute of Applied Physics, Eberhard-Karls Universität Tübingen, Tübingen, Germany Electron Microscopy and Applied Materials Science Group. Prof. Oliver Eibl
Dissertation	*Superconducting Properties and Nanostructure of* $YBa_2Cu_3O_{7-\delta}$ *Coated Conductors Prepared by Chemical Solution Deposition*